University of Alberta

Investigation of electron beam nanolithography processes, mechanisms, and applications

by

Mohammad Ali Mohammad

A thesis submitted to the Faculty of Graduate Studies and Research
in partial fulfillment of the requirements for the degree of

Doctor of Philosophy
in
Microsystems and Nanodevices

Electrical and Computer Engineering

Fall 2013
Edmonton, Alberta

Dedicated to my parents

Abstract

Electron beam lithography (EBL) is the leading technology for versatile two dimensional patterning at the deep (10-100 nm) nanoscale. In addition to its reputation as an enabling technology for next generation advances in industry, its ease of use, accuracy, and cost has made it the technology of choice for rapid sub-micron prototyping in academia and research institutes worldwide. Advances in EBL processing have enabled sub-10 nm fabrication using a variety of materials under limited conditions. Repeatable processing at the deep nanoscale, particularly for dense nanostructure fabrication, requires a systematic quantitative study of all processing steps and their intricate interdependencies. In addition, developing future nanofabrication strategies with features approaching molecular length scales, requires a thorough examination of the molecular interactions taking place in EBL processing.

This research project investigates EBL processing using PMMA and ZEP resists through an in-depth quantitative study and analysis of process windows for dense grating fabrication. The effect of processing parameters from each EBL stage on process windows is thoroughly investigated. Through the study of process windows and contrast curves, EBL processing strategies are developed and high resolution processing limits in PMMA and ZEP resists are explored. Furthermore, the EBL development stage involving resist-solvent interactions is studied using molecular dynamics simulations in Accelrys Materials Studio software package, and analyzed using the Flory-Huggins polymer physics theory. Finally, optimized processing strategies for dense grating fabrication are demonstrated and techniques are employed for the fabrication of record ultra-narrow (8 nm) suspended SiCN cantilever structures and high aspect ratio polymer fabrication using novel SML resist.

Acknowledgements

The author was admitted to the University of Alberta (UofA) initially in 2004 in the Bachelors of Engineering program. During his undergraduate studies he was heavily involved in research at the University of Alberta Micro and Nanofabrication Facility (nanoFAB) and at the National Institute for Nanotechnology (NINT). The academic and research environment was so impressive and conducive for learning that the author decided to continue his postgraduate work at the UofA after completing his B.Sc. in Electrical Engineering in 2008. The world-class teaching and state-of-the-art facilities at these institutions enabled the author to conduct quality research which resulted in numerous research papers and presentations. The author is grateful to the UofA, nanoFAB, and NINT for the opportunity to work in these facilities and to thoroughly develop himself both intellectually and professionally.

Next, the author was fortunate to receive a number of scholarships and awards from the Natural Sciences and Engineering Research Council of Canada (NSERC), Alberta Innovates (formerly Alberta Ingenuity), and the UofA. The financial assistance received from these sources greatly helped the author in completing his research and doctoral program without any anxieties. Moreover, the generous grants provided by Alberta Innovates enabled the author to present his research at numerous national and international forums. The author gratefully acknowledges the support of all of these funding agencies and institutions.

The author is deeply indebted to his supervisors, Dr. Steven Dew and Dr. Maria Stepanova, and is also fortunate to have had the support of committee members Dr. Stephane Evoy and Dr. Phillip Choi. It is not possible to describe the contributions of each in merely a few words; however, the author would like to briefly acknowledge their highly valuable association as follows.

Dr. Dew first hired the author as a summer student in 2006 and in this way introduced him to the world of nanofabrication. Through each meeting the author increased his knowledge of the field and life in general. The author greatly cherishes his relationship with Dr. Dew and considers him a splendid teacher, mentor, and friend.

The person who is perhaps singularly responsible for the author's exposure and rise in the publishing world is Dr. Stepanova. Many of the author's key successes are attributed to her tireless encouragement and support. The author highly values Dr. Stepanova's excellent guidance and association.

The author is grateful to Dr. Evoy for the opportunity to work with his team on groundbreaking research involving an extraordinary nanomaterial 'SiCN'. The significant fame and international travel that resulted due to this collaboration will always be remembered.

The author is privileged to have had Dr. Choi join his doctoral committee. Dr. Choi's invaluable guidance in the fields of molecular dynamics and polymer

physics have enabled the author to advance significantly in a very short period of time.

In addition, there are many colleagues and friends at the University of Alberta who were very helpful in the author's research and overall training during the last several years. The author is indebted to the valuable support of Ken Westra, Eric Flaim, Mirwais Aktary, Peng Li, Daniel Salamon, Taras Fito, Kolattukudy Poulose Santo, Jiang Chen, Zsolt Szabó, Bilkiss Issack, Oliver Stueker, Luda Dorosh, David Zheng, Adegboyega Paul Adeyenuwo, Csaba Guthy, and Nathan Nelson-Fitzpatrick. The space limits mentioning many other names, however, the author is grateful for their contributions.

Last but not least; the author owes countless thanks to many friends in the administrative and technical community at the UofA, nanoFAB, and NINT for their whole-hearted support and help throughout his stay. A special note of appreciation is for Pinder Bains (UofA), Asha Rao (UofA), Efrena Garcia (NINT), and Elvira Horne (NINT).

Finally, the author is very lucky to have moral and spiritual support of his parents, Dr. and Mrs. Ali Mohammad throughout his doctoral program. Their constant prayers provided critical strength during strenuous moments. The author is also thankful to his wife, Zahra Ali for her tireless support, and to their two young children, Sakina Ali (b. 2008) and Abbas Ali (b. 2010), for their refreshing presence and energetic antics.

Table of Contents

Chapter 3. EBL Process Windows and Trends **64**

List of Tables

List of Figures

List of Abbreviations

AFM	Atomic force microscope
AlN	Aluminum nitride
AR	Aspect ratio
AZnLOF	Clariant Corp. resist
BHF	Buffered hydrofluoric acid
CAD	Computer aided design
CAR	Chemically amplified resist
CD	Critical dimension
CDU	Critical dimension uniformity
CH_4	Methane
CO_2	Carbon dioxide
CPD	Critical point drying

CVD	Chemical vapor deposition
DES	Diethyl silane
DI	Deionized
DOF	Depth of focus
DRAM	Dynamic random access memory
DRR	Dissolution rate ratio
DSA	Directed self-assembly
DUV	Deep ultraviolet
EBID	Electron beam induced deposition
EBIE	Electron beam induced etching
EBL	Electron beam lithography
EUV	Extreme ultraviolet
F–H	Flory-Huggins theory/equation
FE	Field emission

FS	Fused silica
GaAs	Gallium arsenide
Ge	Germanium
GPC	Gel permeation chromatography
GUI	Graphical user interface
H_2O_2	Hydrogen peroxide
H_2SO_4	Sulfuric acid
HF	Hydrofluoric acid
$HSiO_x$	Hydrogen siloxane (non-stoichiometric)
HSP	Hansen solubility parameter
HSQ	Hydrogen silsesquioxane
HVM	High volume manufacturing
IBL	Ion beam lithography
IC	Integrated circuit
InP	Indium phosphide

IPA	Isopropyl alcohol
ITO	Indium tin oxide
KCl	Potassium chloride
KOH	Potassium hydroxide
LiCl	Lithium chloride
LiOH	Lithium hydroxide
LER	Line edge roughness
LN_2	Liquid nitrogen
LW	Line width
LWR	Line width roughness
MALDI	Matrix assisted laser desorption ionization
MD	Molecular dynamics
MEK	Methyl ethyl ketone
MEMS	Microelectromechanical systems

MIBK	Methyl isobutyl ketone
Mw	Molecular weight
NaCl	Sodium chloride (table salt)
NaOH	Sodium hydroxide
NEMS	Nanoelectromechanical systems
NH_3	Ammonia
NIL	Nano-imprint lithography
NINT	National Institute for Nanotechnology (Edmonton, Canada)
NPT	Isothermal-isobaric ensemble
NVE	Microcanonical ensemble
NVT	Canonical ensemble
PDI	Polydispersity index
PECVD	Plasma enhanced chemical vapor deposition
PMGI	Polymethylglutarimide
PMMA	Polymethylmethacrylate

PS	Polystyrene
PVD	Physical vapor deposition
QCM	Quartz crystal microbalance
RDF	Radial distribution function
R_g	Radius of gyration
SAM	Self-assembled monolayer
SAR	Sensitivity, aspect ratio, resolution
SC	Supercritical
SEM	Scanning electron microscope
Si_3N_4	Silicon nitride
SiC	Silicon carbide
SiCN	Silicon carbon nitride
SiGe	Silicon germanide
SiN	Silicon nitride (non-stoichiometric)

SiO_x	Silicon oxide (non-stoichiometric)
SML	E M Resist Ltd. resist
SOI	Silicon-on-insulator
SPL	Single pixel line
SR	Surface roughness
TiN	Titanium nitride
TMA	Trimethyl amine
TMACl	Tetra methyl ammonium chloride
TMAH	Tetra methyl ammonium hydroxide
UV	Ultraviolet
WPH	Wafers per hour
ZED-N50	Zeon Corp. developer
ZEP	Zeon Corp. polymeric resist

CHAPTER 1

INTRODUCTION

1.1 Nanolithography technologies

In today's nanofabrication processes, a diverse variety of technological alternatives exist for performing the fundamental lithography steps. These technologies may be broadly classified as radiation-based and non-radiation-based lithographies [1]. The non-radiation based lithographies may be top-down or bottom-up in nature and employ mechanical, chemical, and mechanico-chemical approaches to form nanoscale patterns. Examples of such technologies include nano-imprint lithography (NIL) [2], soft lithography [3], scanning probe lithography [4], self-assembly [1], and directed self-assembly (DSA) [1,5]. The other category of radiation-based lithographies is top-down in nature, and includes optical and charged particle lithographies, described below. Each of the above technologies contains further variants at various stages of maturity and application in industry and academia.

The optical lithography or photolithography technologies [1] are the workhorses that enable the mass production of semiconductor chips and microelectromechanical systems (MEMS). These technologies have historically included ultraviolet (UV) lithography (λ = 436 nm, 365 nm) and deep ultraviolet (DUV) lithography (λ = 248 nm, 193 nm). Currently, advances in 193 nm DUV lithography are responsible for mass production of the latest 22 nm node semiconductor chips. Other photolithography technologies include extreme ultraviolet (EUV) lithography (λ = 13 nm), which is a candidate for future mass production, x-ray lithography (λ = 1-5 nm), and laser lithography.

The charged particle lithography technologies include electron beam lithography (EBL) [1,6], proton beam lithography [7], and ion beam lithographies (IBL) using gallium, neon, and helium ions [8]. Among charged particle lithographies, EBL is the most mature and developed technology. It is used in industry for the production of photolithography masks [9,10] and NIL templates [11]. In addition, due to its flexibility and unmatched capability to pattern the tiniest structures without the use of masks, EBL has become the technology of choice for prototyping sub-micron devices in academia and research institutes worldwide.

1.2 Electron beam lithography (EBL)

In EBL, a focused beam of electrons is precisely guided over a chemically responsive recording medium (resist) with the intent of defining micro- and nanoscale architectures in two, or sometimes three, dimensions. The beam of

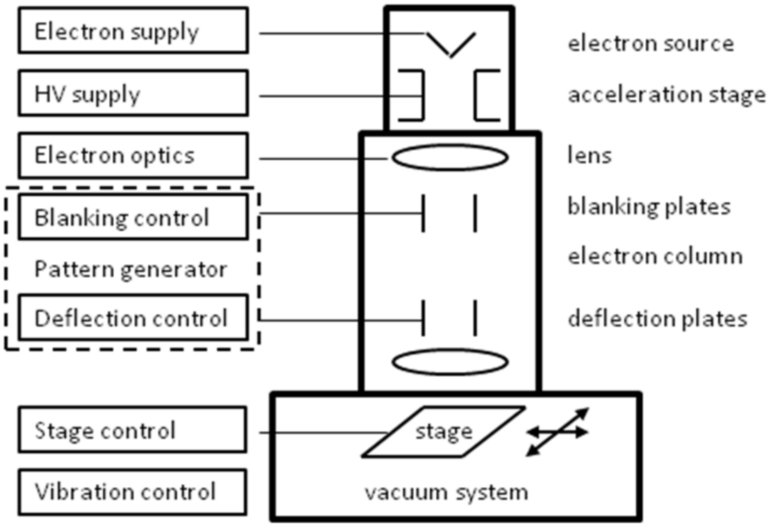

Figure 1.1 A basic direct write EBL system schematic. Reprinted with permission [12]. Copyright © 2012 Springer.

electrons may be extracted from a number of sources by applying a high voltage – among these ZrO/W field emission (FE) sources are the most popular for EBL applications [6]. As the beam passes through the EBL system column (see Figure 1.1) [12], electron lenses and apertures are used to focus the beam into a fine spot, a few nanometers wide. An assembly of electrostatic deflection plates (or electromagnetic coils) are used to guide the electron beam over the resist surface, at very high speeds, as per the intended nanostructure design. The resist dramatically changes in solubility in the locations where the electrons were exposed. After a subsequent rinsing (development) step in an appropriate chemical solution, sharp features emerge on the resist surface which can be used for further processing and analysis. Further details on the electron beam exposure and development steps are covered in chapter 2.

1.2.1 Brief history of development

The original EBL tools were developed by attaching beam blanking and pattern generation electronics to conventional scanning electron microscopes (SEMs) [6,13] more than four decades ago. The beam blanker and pattern generator, at very high speeds, control which areas of the SEM viewing field are exposed by the rastering electron beam according to the input design file. In this way, the resist surface can be patterned without the use of a mask, creating a highly flexible and widely accessible lithography technique. However, SEMs have a number of limitations (see ref. [6]), due to which dedicated Gaussian spot-beam EBL systems were introduced [6]. These formed the basis for commercial moving-stage "write-on-the-fly" mask writers [14].

The inherent serial writing nature of spot-beam systems makes it a relatively low speed (throughput) patterning technology as compared to optical lithography, and therefore shaped-beam systems were introduced [15,16,17]. In these systems, the design is broken into a composite of simple geometric shapes and patterned “on-the-fly” by shaping the electron beam. This is achieved by changing the relative positions of two sequential apertures within the electron column [16]. These systems have an order-of-magnitude faster patterning ability as compared to spot-beam systems; however, they have a more complex column, and a complex alignment, calibration, and focusing procedure [6].

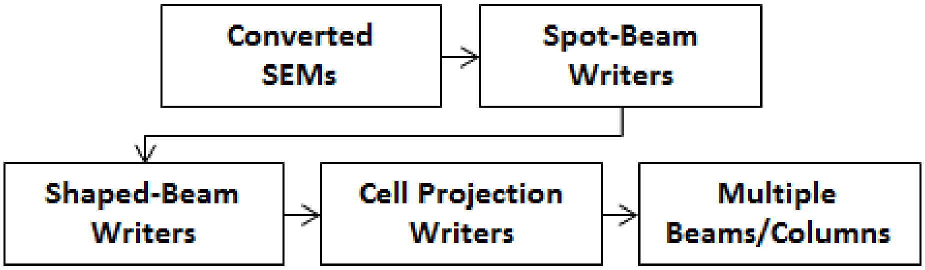

Figure 1.2 History of EBL technology architecture development.

An extension of shaped-beam systems are cell-projection lithography systems which expose a pre-defined “mask” to write de-magnified images of complete sections [18,19,20]. These systems are faster than previous EBL implementations; however, they put stringent conditions on the mask design [21] and are pattern density limited.

In order to further enhance the writing speed of EBL, parallel beam architectures have been developed [22,23,24,25]. These include systems that have multiple beams in one column [22,23,24] and multi-column [25] systems. These systems have very complicated control electronics, and require novel patterning strategies for over-coming space charge due to densely confined beams. In addition to the above, hybrid EBL systems have also been developed [25,26,27,28]. Figure 1.2 briefly summarizes the history of EBL architecture development.

1.2.2 Role of EBL in research

EBL is an enabler for leading edge research and development (R&D) in nanotechnology. Hundreds, if not thousands, of EBL units are now found worldwide in academic and research institutes used in the R&D of applications such as nanoelectromechanical systems (NEMS), opto-electronic and quantum devices, nanofluidics, molecular electronics, surface science applications, and even in revolutionary life sciences research. EBL systems for R&D require the highest flexibility and economy even at the cost of speed; therefore these systems are largely limited to Gaussian spot-beam architectures (see systems 1-2 in Figure 1.2). Manufacturers that provide SEM conversion kits (10^4 – 10^5 dollars) include JC Nabity [29] and Raith [30], whereas wholly dedicated EBL systems (10^6 dollars) for R&D are supplied by Raith [30], Vistec [31], CRESTEC [32], ELIONIX [33], JEOL [34], and NanoBeam [35]. In addition to moving stage and vector scan systems (which raster over only designed areas), new developments include hybrid EBL + IBL systems, EBL + gas injection for electron beam induced deposition/etching (EBID/EBIE), and EBL + nanomanipulation systems [30].

1.2.3 Role of EBL in manufacturing and future prospects

Since the mid 1970's, EBL tools have been used for commercial mask making [1]. In addition, electron beam technology is used for mask inspection and repair tools in industry. With the rapid scaling down in transistor device sizes and the necessity for controllably defining features at the deep nanoscale, EBL technology has become ubiquitous. Today all major integrated circuit (IC) chip manufacturing companies own large mask making facilities with industrial EBL tools (10^6 – 10^7 dollars). Such tools employ variable shaped-beam and cell projection architectures (see systems 3-4 in Figure 1.2), as high volume manufacturing (HVM) requires the highest throughput, even at the expense of flexibility (see HVM EBL tool suppliers [28,31,34]).

Considering EBL's capability to controllably and flexibly define precise nanoscale patterns beyond the capacity of other lithographic technologies, it was expected that EBL would have a major role in IC HVM as early as 1983 [36]; however, the continuous progress of photolithography and relatively low throughput (speed) of EBL has prevented this. In the 1990's, Lucent Technologies and IBM introduced the SCALPEL [18] and PREVAIL [19] cell projection systems, respectively; however these could not succeed in the IC HVM arena. Within the last decade, HVM EBL systems employing multi-beam architectures (see system 5 on Figure 1.2) such as MAPPER [23], PML2 (IMS) [27], and REBL (KLA-Tencor) [24] have undergone rapid development. MAPPER and PML2 employ programmable apertures to guide thousands of electron beams, whereas REBL projects electrons reflected from an addressable electrostatic pattern generator onto a rotary stage. Among these multi-beam tools, the MAPPER tool is claiming a pre-production throughput of 1-10 wafers per hour (WPH) [37], and up to 100 WPH in the future using clustered tools with 13,260 parallel beams per tool [38].

It is pertinent to note that the industry requirement for HVM economic viability exceeds 100 WPH.

Furthermore, continuous delays in the availability of next generation production tools based on extreme ultraviolet (EUV) lithography technology [39], primarily due to lower throughput, has compelled the chip making industry to consider a number of alternative patterning technologies [40], amongst which EBL technologies are at the forefront. Eventually, the scaling down of transistor sizes will reach single-digit nanometer dimensions, at which stage EBL technologies are expected to play an even more prominent role in the IC mass manufacturing process.

1.3 General need for further research

It is clear that EBL will continue to be a key enabler for IC HVM and non-IC applications. For many decades, the *faster, denser, and cheaper* fabrication of nanostructures has been relentlessly pursued in academia and industry. EBL technology has advanced to the stage where this technology is addressing size scales where molecular-level, or even atomic-level, mechanisms are relevant. Developing experimental techniques to forward the aforementioned pursuit requires an understanding of the pertinent mechanisms. Understanding such mechanisms further requires the usage of techniques from various fundamental-science disciplines – a key challenge in this process being the application of these techniques to an essentially engineering pursuit. In addition to driving developments in experimental techniques, gaining a fundamental understanding of molecular processes is also essential for the accurate modeling of EBL.

CHAPTER 2

ELECTRON BEAM LITHOGRAPHY PROCESSING

2.1 The EBL process

Defining nanostructures in resists using electron beam lithography (EBL) comprises of a number of sequential processes. These processes can be categorized as surface preparation, exposure, development, and post-processing. Within each process category, there are a number of process parameters that affect the EBL outcome. Altogether, a dozen or more parameters are available for creating sophisticated EBL strategies. The mechanisms and processing considerations, under each category and parameter, are elaborated upon in this chapter.

2.1.1 Sample preparation

In its very basic form, the *sample* consists of a pattern transfer or handle layer (substrate) on which a patternable material (resist) is applied. The selection of both substrate and resist layers depend upon the intended application. Commonly used EBL substrates are mask blanks (quartz, soda lime glass, etc.), silicon (Si), and silicon-on-insulator (SOI) wafers. However, other substrates have been used for niche applications such as germanium (Ge) [41], SiGe [42], gallium arsenide (GaAs) [43], indium phosphate (InP) [44], sapphire [45], fused silica (FS) [46], indium tin oxide (ITO) [47], and nitride (Si_3N_4) membranes [48], etc.

Prior to application of the resist layer, the substrate is cleaned. The cleaning procedure depends on the substrate material and may be a simple single component wash (with acetone, isopropyl alcohol, etc.) or a more complex multi-component, multi-stage routine (such as RCA clean, Piranha clean, etc.) [49]. More complicated procedures clean a larger number of contaminants and may include surface treatments. For example, Piranha (1:3 mixture of H_2O_2 and 30% H_2SO_4) cleaning removes nearly all organic materials and dust particles. Following a liquid wash and/or surface treatment, a dehydration bake is performed. The substrate preparation procedure may include a coating of a thin conductive layer [46] or a resist adhesion promotion layer [50] on the substrate. Such a layer may be a metal or a non-metal.

There exists a large selection of resists which have been used for EBL, with over two dozen resists extensively reviewed [51,52,53]. Some of these resist categories include organic and inorganic polymers, chemically amplified resists (CAR), self-assembled monolayers (SAM), metal oxides, metal halides (salts), nanocomposite resists, etc. Functionally, the resists may be either positive-tone or negative-tone. Nominally, upon exposure to electron beams, a resist may exhibit enhanced (positive-tone) or suppressed (negative-tone) solubility in a suitable solvent, relative to the unexposed areas. When exposed at non-nominal conditions, a significant number of organic-polymeric resists have exhibited a dual tone behavior. Generally these dual tone resists have distinct regimes of behavior; however under special processing conditions, they exhibit both tones simultaneously [54].

The most widely used EBL resist, and arguably one of the first, is polymethylmethacrylate (PMMA). PMMA (Fig. 2.1(a)) is well known as acrylic glass and reportedly was first used as a positive-tone EBL resist by IBM Corporation [55]. Lithography grade PMMA is supplied [56] in molecular weights (M_w) ranging from 50,000-2,200,000 g/mol as a spin-castable fluid usually in anisole solvent. The most widely used formulation has a M_w of 950,000 g/mol with a polydispersity index (PDI) of 2.25-2.75. Another very popular positive-tone EBL resist is ZEP. ZEP (Fig. 2.1(b)) is a 1:1 copolymer of α-chloromethacrylate and α-methylstyrene [57] supplied by Zeon Corp [58] as ZEP-520 and ZEP-7000 in anisole casting solvent. ZEP-520 (the more widely used formulation) has a M_w of 57,000 g/mol [59] and PDI of 2.2 [60], whereas ZEP-7000 has a M_w of 340,000 g/mol [61]. Both PMMA [54] and ZEP [62] exhibit dual tone behavior and may serve as negative-tone resists at non-nominal conditions. Hydrogen silsesquioxane (HSQ) (see Fig. 2.1(c)) is a relatively newer [63], very widely used, and high performing negative-tone EBL resist supplied in methyl isobutyl ketone

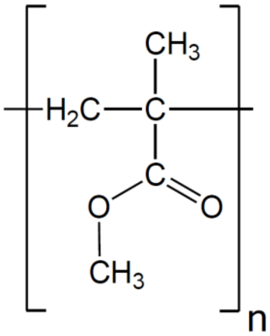

(a) **PMMA**

$[C_5H_8O_2]_n$ – 100.12 g/mol

Density 1.18 g/cm^3

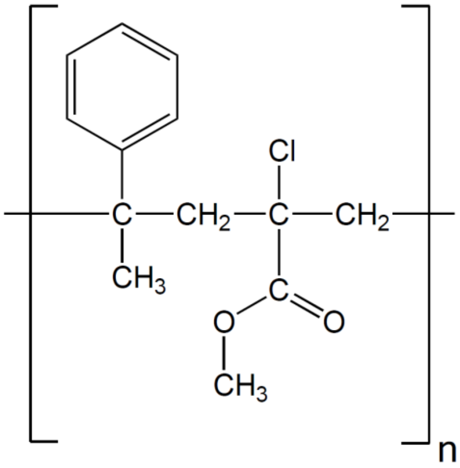

(b) **ZEP**

$[C_{13}H_{15}O_2Cl]_n$ – 238.71 g/mol

Density 1.6 g/cm^3

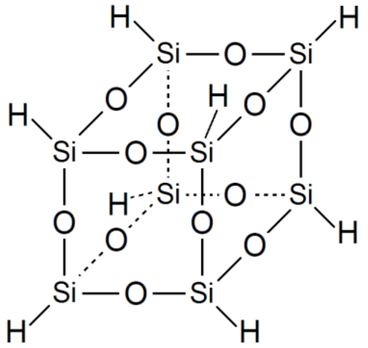

(c) **HSQ**

$H_8Si_8O_{12}$ – 424.74 g/mol

Density 1.4 g/cm^3

Figure 2.1 Molecular structure and properties of popular EBL resists

(MIBK) casting solvent [64]. Prior to its use as a resist [63], HSQ was well known as a dielectric spacer [65] for integrated circuit (IC) interconnects. The merits and performance of all three resists will be discussed and compared in later sections.

Following resist selection, resist preparation involves deposition of a layer of a proper thickness and physico-chemical treatments. Resists may be deposited by spin casting, spray coating, physical vapor deposition (PVD), or chemical vapor deposition (CVD). The thickness of spun-cast resists depends on spinning speed, time, environment, resist viscosity, etc. [66]. Liquid phase deposited resists require a *soft*-baking step, which is generally conducted on a hot plate or in a convection oven. This baking step drives off the casting solvent and, given proper selection of baking time and temperature [67], improves the resist's performance.

2.1.2 Exposure

In the exposure step, a beam of energetic electrons are directed over the sample according to a designed pattern. The penetration of the electrons into the resist layer initiates a highly complex electron transport and energy transfer mechanism. As the electrons travel through the resist material, a number of collision events occur. The *incident* electrons interact elastically with the resist atoms, which deflect the electron trajectory by small angles (Fig. 2.2) in most of the cases [68]. This is known as forward scattering. Forward scattering causes

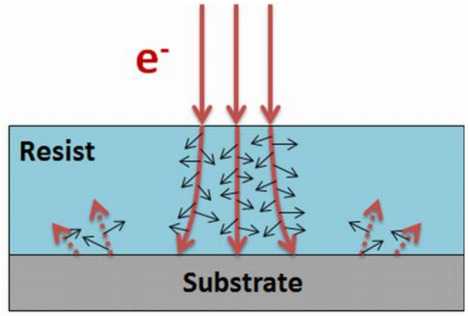

Figure 2.2 Sketch of EBL exposure showing trajectories of primary (large solid arrows), backscattered (large dashed arrows), and secondary (small arrows) electrons.

incident beam broadening depending upon the resist thickness, density, and beam energy (acceleration voltage). Generally, forward scattering is less pronounced in thin, low density resists and at high incident energies [69,70].

Most of the incident electrons pass through the resist and penetrate deep into the substrate material, where they collide with the substrate atoms. A fraction of incident electrons undergo sufficiently large-angle collisions to re-emerge back into the resist at a distance from the incident beam, a process known as backscattering [71,72] (see Figure 2.2). This distance may be on the order of microns [72,73,74], depending on the incident energy. As compared to Si, a higher atomic number substrate (such as Ge, SiGe, GaAs, InP) would cause greater backscattering, whereas the usage of membrane substrates may significantly decrease backscattering. Backscattered electrons contribute to (generally) unwanted over-exposure in nearby features, known as the *proximity effect* [75,76,77], which limits the fabrication of dense features.

Both forward (primary) and backscattered electrons contribute to the exposure of the resist. Inelastic collisions of these electrons are responsible for the creation of secondary electrons (see Figure 2.2). Most secondary electrons are of low energy (<50 eV) [68,78] resulting from the ionization events caused by the primary and backscattered electrons, and have a short range (<5 nm). Inelastic collisions of primary, secondary, and backscattered electrons are the primary cause of resist exposure related events [78,79]. Detailed accounts of the exposure from all electron species have been studied and modeled widely in the literature and can be understood through Monte Carlo [80,81,82] and analytical [68,83,84,85] modeling methods.

The exposure involves ionization of resist molecules causing physico-chemical changes such as scission (bond breakage) and cross-linking. In positive-tone regimes scission prevails. This mechanism (see Figure 2.3) drastically reduces the chain lengths in polymeric resists such as PMMA [86,87] and ZEP [88] resulting in lower average molecular weight regions. In the case of PMMA, depending on electron dose, the original unexposed chains often degrade down to single monomer units [86,89]. However, due to the nature of electron-resist interactions, a typical electron beam exposed volume will contain a distribution of chain lengths [68]. Other proposed electron beam exposure products of PMMA include gaseous and liquid volatiles such as CO_2, CH_4, CH_2OH, etc., and occasionally derivatives with one unsaturated bond; however, such unsaturated

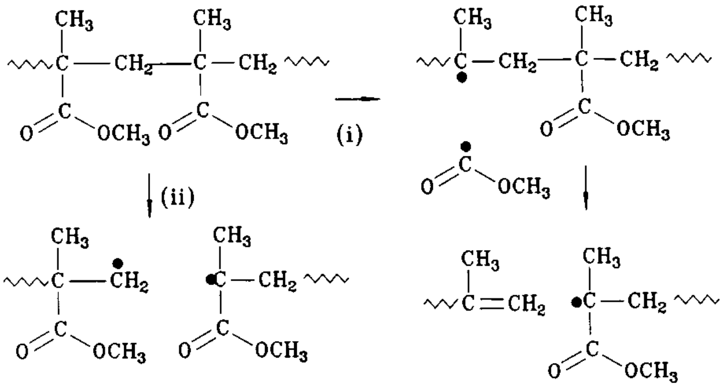

Figure 2.3 A subset of reaction pathways for PMMA decomposition following electron exposure. The main chain scission occurs by (i) removal of the ester group, leading to a terminal $=CH_2$, or by (ii) a direct process. The radical intermediates are indicated by a bullet (•) symbol and can undergo further reaction or decomposition (not shown). Reprinted with permission from [87]. Copyright © 1999, American Vacuum Society.

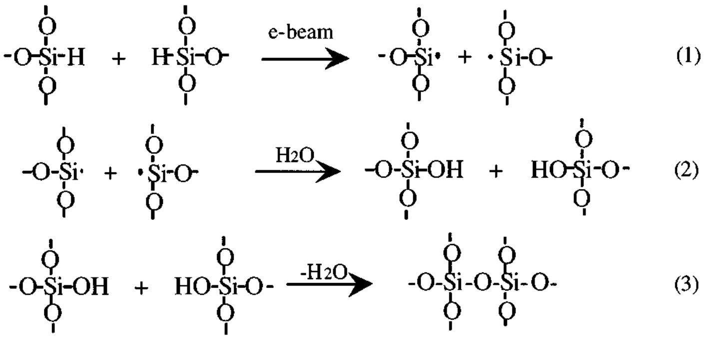

Figure 2.4 A proposed reaction pathway for HSQ cross-linking following electron exposure. Reprinted with permission from [63]. Copyright © 1998, American Vacuum Society.

species have a very low production efficiency [89]. Due to the above reasons, at nominal doses, it is safe to assume that the scission products of PMMA are shorter versions of the original unexposed chains. Similarly in the case of ZEP, the chains break down to ≤ 10 monomer units in standard exposure regimes [88].

In negative-tone regimes, bond cross-linking in the resist is the dominant mechanism and the exposed regions increase in average molecular weight. In the case of HSQ, smaller molecules are hypothesized to cross-link and form a network structure [63], see also Fig. 2.4. However, recent analytical chemistry experiments [90] have suggested that the HSQ cross-linking mechanism may be more complex. In general, the resist response to electron exposure is much less understood in comparison to electron scattering and transport physics.

From a processing perspective, the exposure stage variables include voltage, dose (charge density), EBL instrument (column) settings, and patterning conditions. The selection of specific process conditions is based on various considerations. A higher exposure voltage would cause the electrons to penetrate deeper into the sample with the penetration depth depending on voltage [91,92] and dose [93]. These trends can be seen in Figure 2.5(a). The beam diameter also reduces with increasing beam energy [94], as shown in Figure 2.5(b), both in-flight and while traveling in the resist, due to space charge and momentum considerations, respectively. Consequently, the EBL spot size decreases with increasing voltage and beam current [95]. Due to these reasons higher voltage exposures generally enable smaller feature sizes (higher resolution). However, higher voltage exposures (E) potentially cause greater damage to under layers due to greater penetration depth and also cause more heating [96]. Moreover, at higher exposure voltages, the dose requirement for

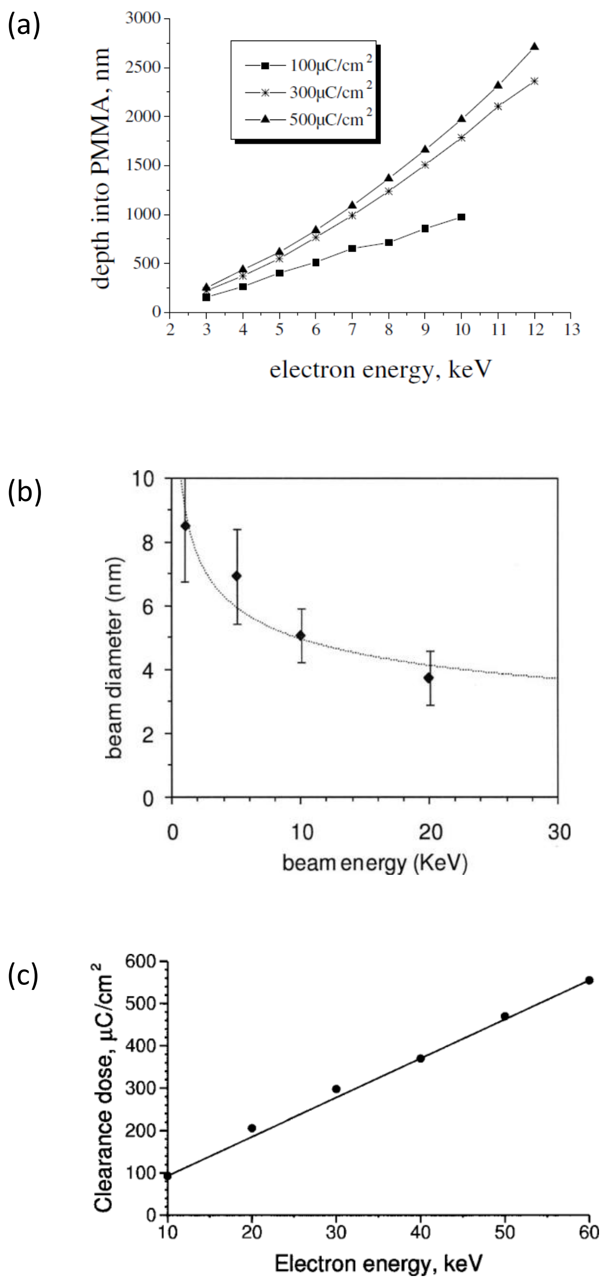

Figure 2.5 Dependencies of electron (a) penetration depth on voltage and dose, (b) beam diameter on voltage, and (c) dose on voltage. Reprinted panel (a) with permission from [93]. Copyright © 2004, Elsevier. Reprinted panel (b) with permission from [94]. Copyright © 2009, American Vacuum Society. Reprinted panel (c) with permission from [68]. Copyright © 2006, American Vacuum Society.

pattern clearance increases as shown in Figure 2.5(c) [68]. The relationship between dose and voltage can be understood through the Bethe formula $\left(-dE/dx \sim 1/E\right)$ which relates the inelastic stopping power of electrons in the sample to electron voltage [80]. Lowering the exposure voltage causes a stronger interaction of electrons with the resist in a given resist volume, resulting in a higher stopping power.

At very low exposure voltages, the strong electron stopping in resist causes an accumulation of charge, distorting the exposed features. This phenomenon is known as charging. The severity of charging is increased at very low voltages [97]; however, mitigation strategies exist [77]. Generally, lowering the voltage and increasing the dose causes an increase in the feature size [85,98] and resist thinning [99]. Finally, at lower voltages, the pattern undercut increases (see Figure 2.6) due to increased electron elastic scattering [100].

The selection of column (see Figure 1.1) and patterning parameters is also very important for high resolution electron beam lithography. Column and patterning parameters include aperture size, working distance (WD), dwell time, step size, patterning direction, etc. A smaller aperture size reduces the beam (or probe) current (i_p) and probe spread (α_p). A smaller WD enables higher resolution, by reducing the probe diameter (d_p), at the cost of reduced *depth-of-focus* (DOF). In electron microscopy, most of these relations are summarized

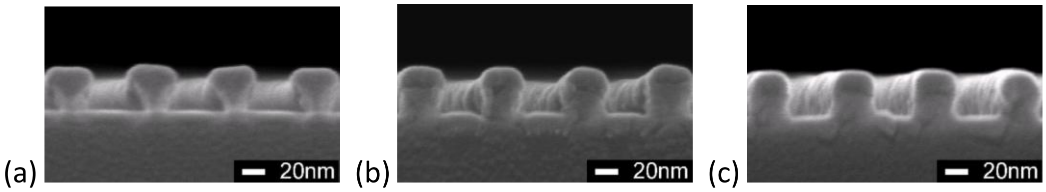

Figure 2.6 Cross section resist profiles in PMMA resist at (a) 3 keV, (b) 10 keV, and (c) 30 keV electron voltages. Reprinted with permission from [100]. Copyright © 2010 Elsevier.

in the brightness (β^*) equation $\beta^* = 4i_p / (\pi d_p \alpha_p)^2$ [101]. The dwell time, step size, and patterning direction determine the quantity of dose, and how the dose is distributed over the sample. These variables are assigned by the user depending on pattern design (geometry) [102]. In fact, nearly all of the exposure parameters discussed in this section are selected depending on the pattern. For example, exposing denser features requires a lower dose (shorter dwell time) due to the proximity effect [68,103]. Further discussion regarding the influence of pattern design on the selection of process parameters will be provided below.

2.1.3 Development

The development step involves immersing the exposed sample in a suitable *developer* solvent. A developer is a liquid or mixture of liquids whose miscibility with a solute discriminates based on the molecular weight of the solute. Therefore, it is usually not a strong solvent (or remover or stripper in microfabrication jargon). After the development step, the lower average

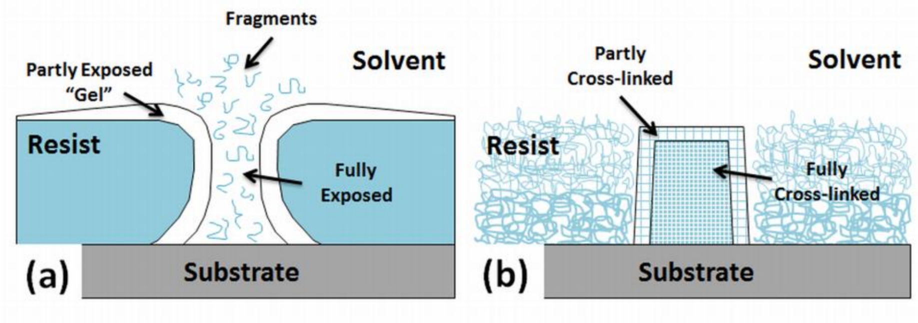

Figure 2.7 Cross-sectional profiles of EBL exposed resists during the development step showing (a) positive-tone, and (b) negative-tone feature (pattern) creation.

molecular weight regions in the resist dissolve away leaving the higher average molecular weight regions on the surface. In a positive-tone resist, the scissioned resist fragments preferentially dissolve away (Figure 2.7(a)), whereas, in a negative-tone resist (or process), the non cross-linked molecules dissolve away (Figure 2.7(b)). In order to stop the development process, an optional immersion in a very weak solvent or non-solvent (known as rinse, stopper, or quencher) may be employed prior to drying.

During resist dissolution, the developer will generally diffuse into the resist while the resist molecules diffuse into the developer. In positive-tone polymeric resists (such as PMMA, ZEP), the developer molecules penetrate the polymer matrix and surround the resist fragments, creating a gel-like swollen layer [89] as shown in Figure 2.7(a). The thickness of the gel layer depends on the strength of the developer and level of fragmentation (which is a function of the exposure dose) and the temperature. In the course of development, the resist fragments detach from the polymer matrix, and diffuse into the developer.

Longer fragments take longer to dissolve as they are less mobile [104] and are more strongly entangled to the matrix [89,105]. A smaller developer molecule [106] or a stronger solvent will enable a faster resist dissolution rate. However, stronger solvents remove longer fragments (from the gel-like layer) which may not be desirable if high resolution EBL is required.

In negative-tone resists (such as HSQ), strong solvents are used to essentially strip the sample of most non cross-linked resist leaving a fully cross-linked core and a partly cross-linked shell (Figure 2.7(b)). In contrast to positive-tone polymeric resist processes, the partly cross-linked region's width in HSQ is minimized using various dissolution rate enhancement [107] and pattern trimming techniques [108,109]. As compared to positive-tone polymeric dissolution processes, negative-tone dissolution processes are less understood.

In order to explain the development process, numerous development models have been proposed [110]. For example, the temperature dependence of the dissolution rate [111] can be described by the Arrhenius equation:

$$R = R_0 \exp\left[-\frac{E_a}{kT}\right]. \qquad (1)$$

In equation (1), E_a is the activation energy, k is Boltzmann’s constant, T is the temperature, R is the dissolution rate, and R_0 is a coefficient which is dependent on the resist and developer characteristics. Various functional forms for R_0 have been proposed in the literature, such as for polymeric positive-tone resists,

$$R_0 = R_0^* + \frac{\beta}{{M_f}^{\alpha}} \qquad (2)$$

where R_0^* is the unexposed resist development rate, M_f is the fragment molecular weight, and α and β are fitting parameters [112]. Utilizing the fact that M_f and dose d are inversely related, another model proposes [113],

$$R_0 = \eta d^{\kappa} \qquad (3)$$

where η and κ are fitting parameters. Though, in principle, the above empirical models allow for an accounting for the size of the polymer chains down to the nanometer scale, these are essentially macroscopic dissolution models and are not explicitly derived from molecular scale physico-chemical interactions taking place between the resist and developer.

To analyze the interaction of polymeric resists with developers, a suitable model is the Flory–Huggins (F–H) lattice theory [114,115]. The F–H theory has been specifically designed to handle the mixing of species with different molecular weights, in contrast with regular solution theory [116] where the solute and solvent molecular weights are identical. The F–H theory enables the prediction of resist-developer miscibility by computing the F–H interaction parameter (χ),

$$\chi = \frac{\Delta H_{mix}}{kT\phi_p \phi_s} \qquad (4)$$

where ΔH_{mix} is the enthalpy of mixing, and ϕ_p and ϕ_s are the polymer and solvent (developer) volume fractions, respectively [114]. The F–H χ parameter is a measure of polymer-solvent interaction with more negative values indicating mutual affinity. A number of researchers from the EBL community such as Sharma *et al.* [117], and Hasko *et al.* [118] have identified calculating χ using F–H theory as the route to obtaining a deeper insight into molecular interactions; however, they have stopped short of performing the actual calculations and relied on qualitative arguments. Hang *et al.* [119] have calculated χ using the Hansen solubility parameters (HSP) method for identifying strong PMMA solvents. Similarly, Olynick *et al.* [120] have used HSP for calculating χ for mixtures of calixarene resist and numerous liquids. However, the approach for calculating χ using the solubility parameter method [115],

$$\chi = \frac{V_s}{kT}\left(\delta_p^H - \delta_s^H\right)^2 \qquad (5)$$

where V_s is the molar solvent volume, δ^H is the solubility parameter, and the subscripts p, s refer to polymer and solvent respectively, is not adequate as compared to equation (4). Thus, such an approach yields only positive values of χ [115,121], and has very limited applicability in mixtures with strong polar components or mixtures having specific interactions such as hydrogen bonds

[115]. Moreover, the dissolution of exposed resist fragments is not considered in the HSP-based approach as it relies on tabulated values of bulk components. Therefore, the HSP-based calculation of χ cannot be readily extended as a consistently molecular approach.

Once the χ parameter has been calculated, the miscibility of species can be determined according to the condition $\chi < \chi_c$ where χ_c is the critical interaction parameter [115]. For a mixture of a developer and a polymer of chain length n, χ_c is given by

$$\chi_c = \frac{1}{2}\left(1 + \frac{1}{\sqrt{n}}\right)^2 . \qquad (6)$$

From equation (6), it can be observed that $\chi_c \rightarrow 0.5$ as $n \rightarrow \infty$. Therefore, in a binary mixture, segregation of components (or phase separation) occurs for long chain polymers provided χ is larger than $\chi_c = 0.5$.

Although the above models account for the resist molecular weight and the resist-developer interaction energies to quantitatively describe the development process, predictive (time-dependent) models describing such processes still need to be developed. A detailed, time-dependent mathematical description may be realized through a general mean-field theory [122] with an accounting for the intermolecular interactions between all components of a system. However, applying such a theory [122] requires the definition of a large set of parameters (including F–H χ parameters). A simpler yet quantitative development model [85] may be derived describing the *velocity* of the resist-developer interface. This interface is proportional to $\sqrt{D^*(x,y,z)t}$ where t is the development time and $D^*(x,y,z)$ is a volume average diffusivity of a local distribution of the resist's fragments. In this model, the dependence of diffusivity on the fragment size (n) is formally similar to eq. (2) as $D^*(x,y,z) \sim n^{-\alpha(x,y,z)}$; however, in contrast to eq. (2), $\alpha(x,y,z)$ is not simply a fitting parameter. The parameter $\alpha(x,y,z)$ is a fragment size dependent exponent whose value varies from ≤ 1 in a dilute solution [105] or polymer melt containing only small fragments to ≥ 2 in dense polymer melts [104,123]. In addition to the models reviewed above, molecular dynamics (MD) simulations [104,124,125] (discussed in section 2.5.2) provide detailed insight into the polymer-developer interactions.

From a processing perspective, the basic development stage variables include the developer chemistry, the development time, and temperature. For nanolithography, it is desired that the developer may strictly dissolve only the desired areas. This selectivity between the exposed and unexposed areas is referred to as the dissolution rate ratio (DRR) [126]. A strong developer (high affinity for resist) such as methyl isobutyl ketone (MIBK) for PMMA [127] enables EBL at relatively lower doses (higher sensitivity) speeding up the development process; however, a stronger developer also causes greater swelling [128]. A much weaker developer for PMMA such as isopropyl alcohol (IPA) [127,129]

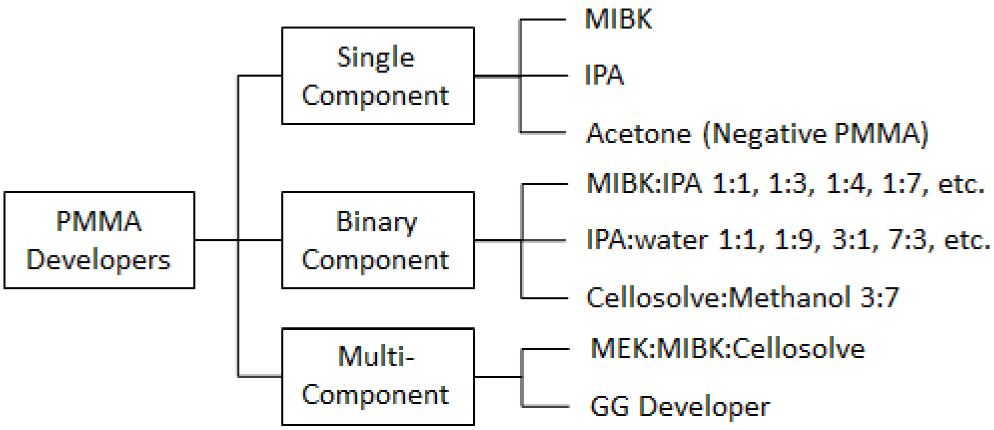

Figure 2.8 A brief review of PMMA developers.

results in less swelling. However, this occurs at the cost of significantly lower sensitivity and higher roughness [130]. In fact, IPA is used as a post-development rinse for PMMA.

In the case where process control is hard to achieve with a single component developer, binary developers are used, which are generally a combination of a strong and a weak developer (see Figure 2.8). For example, MIBK and IPA have been used in various ratios 1:1 [127], 1:3 [51,127,131,132,133], 1:4 [130], 1:7 [133], etc. Such mixtures yield processing advantages e.g., higher resolution due to non-extraction of larger exposed fragments. The soluble fragment sizes for PMMA have been estimated to be <20 monomers in MIBK:IPA 1:3 [68] versus up to 100 monomers in MIBK [134]. However, studies to conclusively determine the exact soluble fragment size (in any EBL resist) using analytical techniques such as mass spectrometry (e.g., MALDI, GPC) are greatly in need. Other binary component developers for PMMA include cellosolve:methanol [135,119], and IPA:water in various proportions 1:1 [127], 1:9 [127], 3:1 [128], 7:3 [127,128,136], etc. IPA:water is a co-solvent developer whose sensitivity is similar to MIBK – though neither of its components are strong developers. In fact, water is a non-solvent for PMMA. The nature of the behavior of IPA:water developer is not understood except for the qualitative hypothesis that the highly polar nature of water increases the developing strength of the mixture [128].

For even greater control of the development process, multi component developers can be used such as the ternary mixture of methyl ethyl ketone (MEK), MIBK, and cellosolve [137], and the GG quaternary mixture [128]. GG developer is used for the LIGA process and is a mixture of butoxy ethoxy ethanol, morpholine, amino ethanol, and water [128]. Acetone has also been used as a developer for cross-linked PMMA [138]. Of all the PMMA developers mentioned here (see Figure 2.8), MIBK:IPA 1:3 and IPA:water 7:3 are the most common, and these are also used together with advanced processing techniques mentioned below.

As a polymeric resist, similar developer selection considerations apply for ZEP as with PMMA; however, the developer chemistries are different. Common single component developers for ZEP include xylenes [139,140,141] and alkyl-acetates [60,106,139,141,142,143,144,145] (see Figure 2.9). Within the family of alkyl- (methyl-, ethyl-, propyl-, butyl-, amyl-, hexyl-, and octyl-) acetates studied

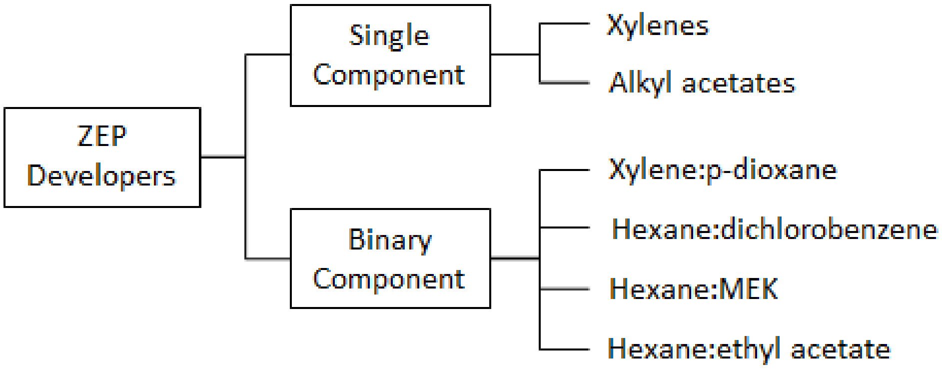

Figure 2.9 A brief review of ZEP developers.

[106], it was found that the sensitivity and dissolution rate decreases as the fragments' molecular size increases. A larger developer molecule causes the scissioned fragments to extract in aggregates, increasing the surface roughness, as opposed to molecular-level dissolution when a smaller developer molecule is used [106]. Binary component developers have also been used for ZEP such as xylene:p-dioxane (20:1) [57], hexane:dichlorobenzene, hexane:MEK, and hexane:ethyl acetate in various ratios [60]. However, in the case of ZEP, the most widely used developer is amyl- (pentyl-) acetate [141,142,145], marketed as ZED-N50 by Zeon Corp., followed by xylenes [139,140,141]. Advanced process development strategies with ZEP have also employed these very developers the most. The post-develop rinse of ZEP is conducted with MIBK or with mixtures of MIBK and IPA.

The most widely employed and developed class of HSQ developers are aqueous bases (see Figure 2.10). Initially low concentration (2.38%) tetra methyl-ammonium hydroxide (TMAH) and higher concentration (33%) potassium hydroxide (KOH) was used [63,146,147]. A number of later studies determined that a stronger (25%) TMAH developer enabled fabrication of denser and higher resolution nanostructures at the cost of sensitivity [148,149,150]. However, the development process was found to saturate due to production of a TMAH-insoluble siloxane-like ($HSiO_x$) scum, which would also remain between dense features [108,109]. This scum was removed by a two-step development process, where a dilute hydrofluoric (HF) acid dip step was employed between two 25% TMAH development runs [109]. In addition to scum removal, the dilute HF dip enabled the development to continue and provided pattern trimming (HF etches SiO_x), resulting in enhanced resolution [108].

A major development in HSQ nanolithography was the introduction of "salty development" [150,151]. Initially, 4% NaCl solution was added to 1% sodium hydroxide (NaOH) developer [150]. As a more aggressive HSQ developer, using NaOH provided a higher sensitivity. Further, the addition of salt increases the initial development rate, as the salty solution contributes to screening the resist surface charge [150]. In addition, salty development prevents cross-linked reaction products (scum) from forming [150], enabling denser and higher resolution nanolithography. In one particular study, development with four aqueous bases (TMAH, NaOH, KOH, and LiOH) and four salts (TMACl, NaCl, KCl, and LiCl) were studied to understand the interplay between bases and salts, and the effect of hydrated ion sizes and electronegativities [152]. The addition of salt also prevents the development from saturating and causes the development of

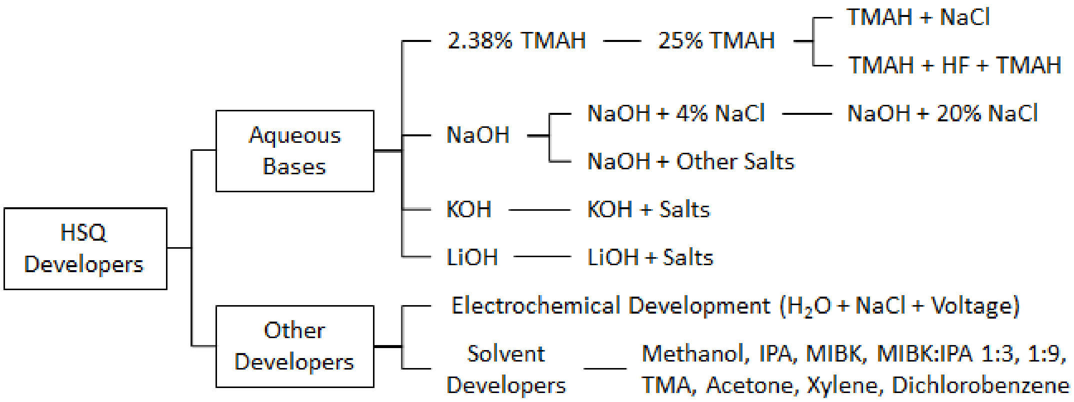

Figure 2.10 A brief review of HSQ developers.

nanostructures to be isotropic [153]. Such anisotropic development helps to improve the height to width aspect ratio (AR) of nanostructures. In yet another study, the NaCl concentration in 1% NaOH was increased to 20% and a voltage was applied to improve the development rate [154].

Other HSQ development methods include electrochemical development (H_2O + NaCl + Voltage) [155], development in organic trimethyl amine (TMA) [156], and various other “solvent developers” such as methanol, IPA, MIBK, MIBK:IPA 1:3, xylene, dichlorobenzene, and acetone [157]. The “solvent developers” were found to result in 5-17 times higher sensitivity as compared to TMAH; however, at the cost of a much lower resolution. Other issues with these developers such as gelation of HSQ in alcohols, poor pattern definition, and surface residue (scum) formation have prevented their use and further development. Therefore, further developments in EBL patterned HSQ have largely been conducted with TMAH or NaOH based salty development methods, and using water as the rinse liquid.

The development process proceeds with immersing the exposed sample in the selected developer for a certain time. This development time may range from a few seconds to tens of minutes. For nanolithography, generally the objective is to minimize the critical dimension (CD), i.e., achieve a small gap-width for positive-tone resists and a small line-width for negative-tone resists. While processing a positive-tone resist, the development time is kept to a minimum (provided it is sufficient for clearance). This is because a longer development time will widen the gap by dissolving the partially exposed gel region. Conversely, while processing negative-tone resists, it is desirable for the development to proceed for as long as possible to remove all non cross-linked and partially cross-linked resist surrounding the patterned features [149]. For both positive- and negative-tone resists, a very long development may cause either pattern collapse or excessive resist shrinking, depending on the pattern density, exposure dose, and developer strength.

The development time cannot be optimized independently of other factors, such as the exposure dose and development temperature. The optimal exposure dose and development time are related inversely, and therefore a short development after heavy exposure may be equivalent to a longer development after a less intense exposure, as shown in Figure 2.11 [85]. For polymeric positive-tone resists, the gap-width (Δx) is related to dose (d) and development time (t) according to the relation $\Delta x \sim d\sqrt{t}$ [85]. Figure 2.11 clearly

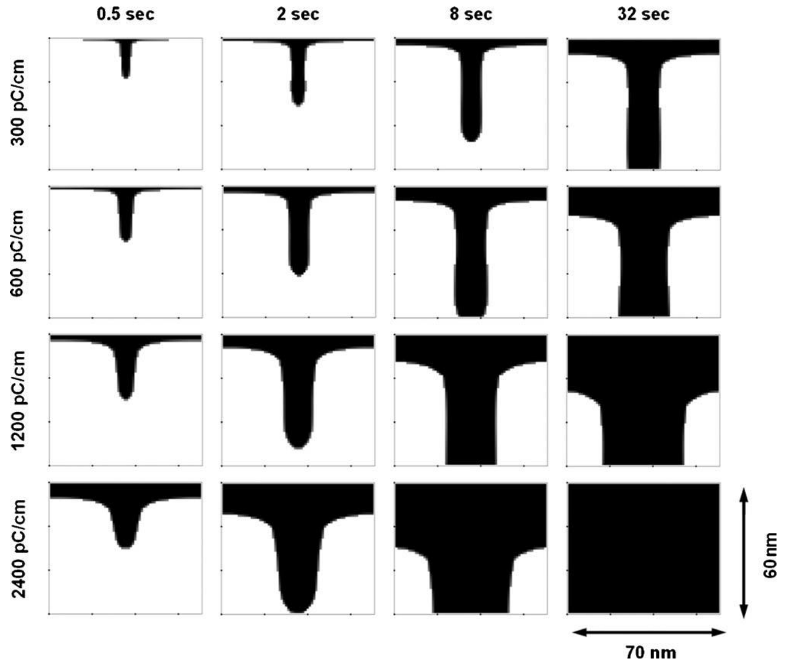

Figure 2.11 Simulated PMMA cross-section profiles in a periodic 70 nm pitch grating pattern exposed at 10 keV and developed at −15 °C in MIBK:IPA 1:3. White and black regions represent resist and cleared areas respectively [85]. This figure corresponds to increasing time horizontally and dose vertically. Reprinted with permission from [85]. Copyright © 2010, American Vacuum Society.

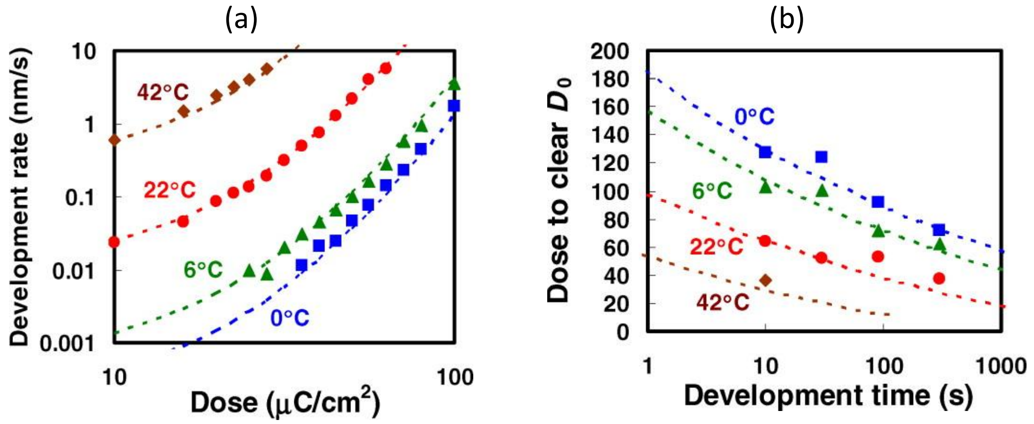

Figure 2.12 Experimental dependencies of ZEP (a) resist dissolution rate on dose, and (b) clearance dose on development time, at various temperatures. An exposure voltage of 30 keV and ZED-N50 developer was used. Reprinted with permission from [145]. Copyright © 2011, American Vacuum Society.

shows that it is necessary to simultaneously choose the dose and development time to obtain a high resolution and AR.

Similarly, the temperature (T) at which the development is conducted may be employed for improving nanolithography. According to the Arrhenius equation (see eq. (1)), increasing or decreasing the developer temperature acts to, respectively, enhance or suppress the development rate (see Figure 2.12(a)) [145]. However, varying the developer temperature also affects the sensitivity (clearance dose) and development time (see Figure 2.12(b)) [145].

In a positive-tone polymeric resist, cooling the developer has the effect of “freezing-out” [132] the resist fragments in the gel layer, enabling a higher resolution at the cost of reduced sensitivity and development rate. A number of studies have explored the temperature dependence of resist development, for example, PMMA has been developed in IPA:water 3:1 at temperatures between 0 – 20 °C [128], and in MIBK:IPA 1:3 at temperatures between 4 – 42 °C [51,131], -20 – 20 °C [133], and -65 – 15 °C [132]. For very low development temperatures, the exposure dose requirement increases sufficiently to cause tone-reversal [132]. A development temperature of around -15 °C in MIBK:IPA 1:3 was found to be optimal for high resolution nanolithography [132]. Similarly, ZEP has been developed in ZED-N50 at temperatures between -10 – 42 °C [145], -40 – 22 °C [141], in xylene between -17 – 32 °C [140], and in hexyl acetate between -60 – 30 °C [143]. Though an optimal development temperature for ZEP has not been ascertained so far, it has been observed that the clearance dose and resolution performance saturates below -20 °C [143].

In negative-tone resists, such as HSQ, elevated developer temperatures have the effect of dissolving most of the lightly cross-linked molecules on the substrate, which helps to shrink the line-widths [107]. See Figure 2.7(b) to visualize the HSQ development process. For HSQ, employing elevated developer temperatures has the effect of decreasing the sensitivity [107]; however, this result cannot necessarily be generalized to all negative-tone EBL resists [158]. HSQ has been developed in 25% TMAH at temperatures between 20 – 50 °C [141], 0 – 60 °C [107], in TMA between 18 – 50 °C [156], and in 1% NaOH + 4% NaCl salty developer between 20 – 30 °C [159]. As in the case of ZEP, no optimal development temperature has been determined for HSQ; however, 40 – 50 °C TMAH development temperatures have been used a number of times for high resolution and high AR studies [107,141,160,161,162].

In addition to the basic development stage processing variables of developer, development time, and temperature, a number of other techniques have been explored which affect the chemical and transport aspects of the development process. One of these techniques is to conduct the development while providing sonic energy [118,128,130,136,163,164,165,166,167,168]. This is a form of "mechanical agitation" which promotes mixing through shear thinning (viscosity reduction) and microstreaming effects [118]. Figure 2.13 illustrates the

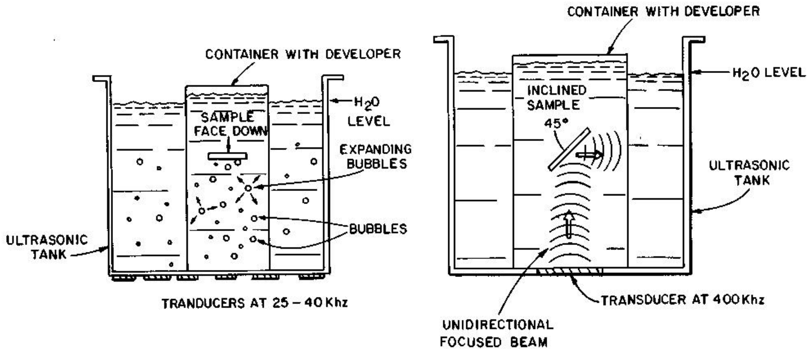

Ultrasonic agitation by cavitation

Ultrasonic agitation by narrowly focused beam

Figure 2.13 Modes of supplying ultrasonic agitation. Reprinted with permission from [165]. Copyright © 1997, American Vacuum Society.

two modes of agitation employing cavitation (collapse of bubbles) using 25 kHz ultrasound (Figure 2.13 (left)) and employing higher frequency 400 kHz directional pulses (Figure 2.13 (right)). Higher frequencies enable improved developer access to fine nanostructures. This is due to the fact that the developer viscous boundary layer ($\delta = \sqrt{2\nu/\omega}$) is viscosity ($\nu$) and frequency ($\omega = 2\pi f$) dependent. This has prompted the application of even higher frequency (> 1 MHz) “megasonic” assisted development for clearing narrow, high AR features [167]; however, such extremely high frequencies are rarely used.

Sonically assisted development increases the development rate significantly, enabling clearance in a fraction of the time as compared to regular development [128]. This helps to prevent swelling, which is a time dependent phenomenon [128,163]. Sonically assisted development is best used with short dip-development processes [165] and/or weaker developers [130,136] to enhance resolution. Moreover, sonically assisted development is helpful for scum removal [165] and minimizing process fluctuations [164]. Furthermore, sonically assisted development has been used together with surfactant addition for sensitivity improvements [164], and with cold development for further improvements in resolution and AR [128,168]. In this way, it may be stated that sonically assisted development is a complementary technique for kinetics enhancement, in addition to employing chemistry [150], electricity (voltage) [154], and temperature [107] as previously described.

2.1.4 Post-processing

The basic EBL process concludes with the development step. However, a number of further processing techniques have been employed to improve the quality and functionality of nanostructures. One class of post-processing techniques focuses on preventing pattern collapse in dense, high AR nanostructures caused by liquid development. During development the capillary forces strain the resist beyond the pattern separation and cause adjacent nanostructures to collapse (see Figure 2.14(a)). The stress (σ) caused by capillary forces is given by

$$\sigma = \frac{6\gamma_s \cos\theta}{D_s}\left(\frac{H}{W}\right)^2 \qquad (7)$$

where γ_s is the surface tension, θ is the liquid meniscus contact angle, D_s is the interline spacing, and H and W are the feature height and width, respectively [169]. One method of preventing pattern collapse is to conduct a post-develop

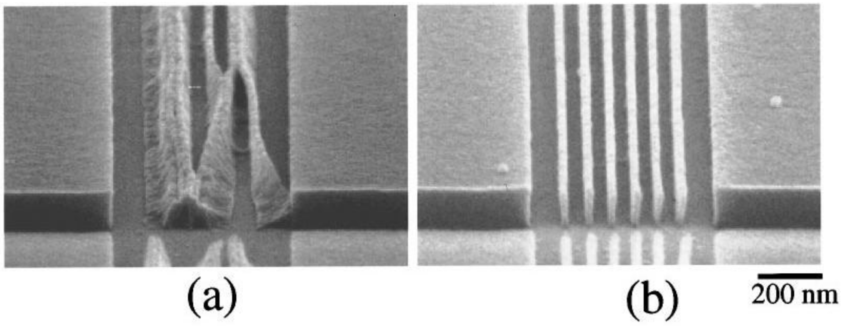

Figure 2.14 EBL patterned gratings in ZEP 7000B resist showing the results of (a) regular drying, and (b) supercritical drying. Reprinted with permission from [169]. Copyright © 2000, American Vacuum Society.

rinse in a low surface tension fluid before drying in air [170]. For example, Pentane (γ_s = 13.7 mN/m) has an approximately five times lower surface tension than water (γ_s = 73.1 mN/m) [170]. Another method to prevent pattern collapse is to conduct “supercritical drying” (see Figure 2.14(b)) [146,169,171,172]. In this method, drying is conducted in a fluid with a low supercritical point, such as carbon dioxide (CO_2), by avoiding the phase transition over the liquid-gas equilibrium line [169].In this way the surface tension during the drying is zero. Supercritical drying is also useful for preventing swelling [146], minimizing line edge roughness (LER) [171], and improving the fluctuations in AR due to line spacing [172]. Though pattern collapse is largely an unwanted effect, it has been harnessed for useful purposes such as forming nanofluidic channels [173].

Other post-processing techniques include curing the patterned resist to improve its etch resistance, or performing surface treatments to improve the CD. Cross-linked HSQ may be further densified, enhancing its etch resistance, by exposing it to 400 – 1200 °C heating (thermal curing) [174], or by flooding the pattern with electrons (electron-beam curing) [175]. As described previously, HF trimming [108] has been used as a post-processing step to improve the CD of HSQ nanostructures. The CD of positive-tone resist (UVIII) nanostructures may be improved by the SAFIER^{TM} process [176]. This process consists of a repeatable rinse-and-bake sequence which has demonstrated a three-fold improvement in resolution and a four-fold improvement in LER [176].

2.2 Process parameters and metrics

In section 2.1, the EBL process stages, various mechanisms, and process considerations were elucidated. Within the discussion of process considerations, a detailed set of parameters were introduced. These process parameters affect the process metrics (resolution, sensitivity, etc.) in a complex and synergistic fashion. A non-limiting set of these parameters and their impact on process metrics is provided in Table 1 (expanded from ref. [12]). This table does not contain certain parameters (e.g., substrate, resist chain length) and certain specialized process techniques (e.g., two-step development) to limit the discussion to process parameters directly relevant to this thesis. The objective of manipulating these parameters is to create sophisticated nanoscale EBL processes maximizing the desired positive outcomes (e.g., a high resolution and a high sensitivity). However, this requires an in-depth understanding of the interdependencies presented in Table 1.

Table 1. EBL parameters and their impact. An abridged version of this table was published in [12]. Copyright © 2012 Springer. Reprinted with permission.

Process Parameters	Impact (Process Metric, etc.)
Resist material	Sensitivity, Resolution, Contrast
Resist thickness	Sensitivity, Resolution, Pattern Quality
Pattern density	Pattern Quality, Proximity Effect
Exposure energy	Sensitivity, Resolution, Proximity Effect, AR
Exposure dose	Resolution, Pattern Quality, LER
Developer	Sensitivity, Resolution, Contrast, LER, SR, AR
Development time	Sensitivity, Resolution, LER
Development temperature	Sensitivity, Resolution, Contrast, LER
Sonic agitation	Resolution, AR, LER
Supercritical drying	Resolution, AR, LER, Pattern Quality

Successful EBL processes are judged based on a variety of metrics. One common set of metrics is known as 'SAR' – sensitivity, aspect ratio (AR), and resolution. Resolution is sometimes also referred to as CD. However, in reality there are many more such process metrics such as contrast (γ), line edge roughness (LER), line width roughness (LWR), surface roughness (SR), critical dimension uniformity (CDU), process window, process latitude, etc. Some of these metrics have already been defined previously, whereas others will be defined in the following sections. Through a survey (section 2.1) of the range of options present in each process parameter, it is clear that a thorough examination of the various combinations of all processing parameters and their impact on EBL process metrics is far too exhaustive to be covered herein. Nevertheless, process strategies and their results for major EBL resists PMMA, ZEP, and HSQ will be examined with emphasis on the development-stage parameters to pave the way for further research.

2.3 Advances in EBL processing

The EBL community has focused its efforts to develop processes, tools, and techniques to fabricate high resolution, high AR, and high density patterns using as high sensitivity (low dose) as possible. Groups that have exploited the interdependence of various process parameters have been successful at realizing elegant solutions to otherwise unviable or impossible tasks. In this section we study a few such examples and summarize key advances.

Advances in EBL processing have now enabled patterning a wide variety of materials below the 10 nm limit. Here we will restrict our survey to the resists selected in the preceding survey – PMMA, ZEP, and HSQ. Using 100 keV high voltage EBL, Chen and Ahmed have fabricated 5-7 nm wide isolated lines in PMMA using MIBK:IPA 1:3 developer [163]. Similarly, Grigorescu *et al.* have used 100 keV EBL to fabricate 6 nm lines in 20 nm thick HSQ on silicon using 2.38% TMAH developer [177]. Generally high voltage EBL has enabled the fabrication of smallest features; however, high voltage exposures have a significantly lower

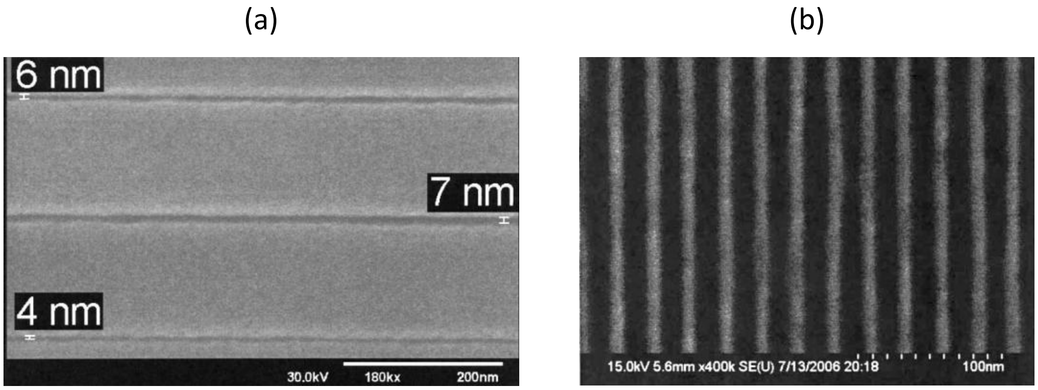

Figure 2.15 Nanoscale line patterns in (a) PMMA, and (b) HSQ developed at 6 °C and 45 °C temperatures respectively. Panels (a) and (b) reprinted with permission from [131] and [161], respectively. Copyright © 2004 and © 2007, American Vacuum Society.

sensitivity, which increases the exposure time and cost. By developing PMMA in IPA:Water 7:3 developer with sonic agitation, Yasin *et al.* have increased the sensitivity by 40% compared to regular MIBK:IPA 1:3 development [178]. Furthermore, with this process, they have fabricated isolated 4 nm lines in 40 nm thick resist and dense 32 nm periodic gratings at 80 keV [178]. Despite this sensitivity improvement, the dose requirement is still many times larger than what is needed using low voltage exposures.

In addition to the higher sensitivity, low voltage EBL systems offer a lower proximity effect and are easier to construct. For these reasons, any industrial HVM EBL solution is likely to employ low voltage, e.g., MAPPER uses thousands of 5keV columns [23]. The extraordinary resolution achieved with high voltage systems is still possible using low voltage systems by exploiting the interdependence of process parameters. For example, Hu *et al.* have fabricated

4-7 nm isolated lines in PMMA using 30 keV by cooling down MIBK:IPA 1:3 (with 1.5% MEK by volume) developer temperature to 6 °C (see Figure 2.15(a)) [131]. Similarly Ocola *et al.* [140] and Cord *et al.*[132] have developed this technique further to fabricate 20 nm wide ZEP features in 160 nm pitch with extremely low LER and 8 nm wide PMMA features in 60 nm pitch, respectively, using -4 °C and -15 °C developer temperatures, both exposed at 30 keV.

Employing 45 °C heated 25% TMAH developer, Choi *et al.* have fabricated 10 nm lines in dense 25 nm pitch using 25 nm thick HSQ resist exposed at 50 keV (see Figure 2.15(b)) [161]. Haffner *et al.* have managed to fabricate 40 nm pitch HSQ gratings using 25 keV exposures and 60 °C hot TMAH development [107]. They have also used a supercritical drying post processing step [107]. These and other similar techniques have enabled near 10 nm resolution patterning at 10-50 keV acceleration voltages.

As described previously, such cold or hot development processes work by respectively suppressing or enhancing the dissolution rates at the cost of 2× or more reduction in sensitivity. The cold or hot development processes improve the resolution by improving the resist contrast. Both sensitivity and contrast are graphically represented using contrast curves (see Figure 2.16 (a, b)). Contrast curves plot the remaining resist height vs. the dose after development of large, uniformly exposed areas of the resist, and may be used to compare the result of selecting various process parameters. Figure 2.16 (a) [179] & (b) [161] are

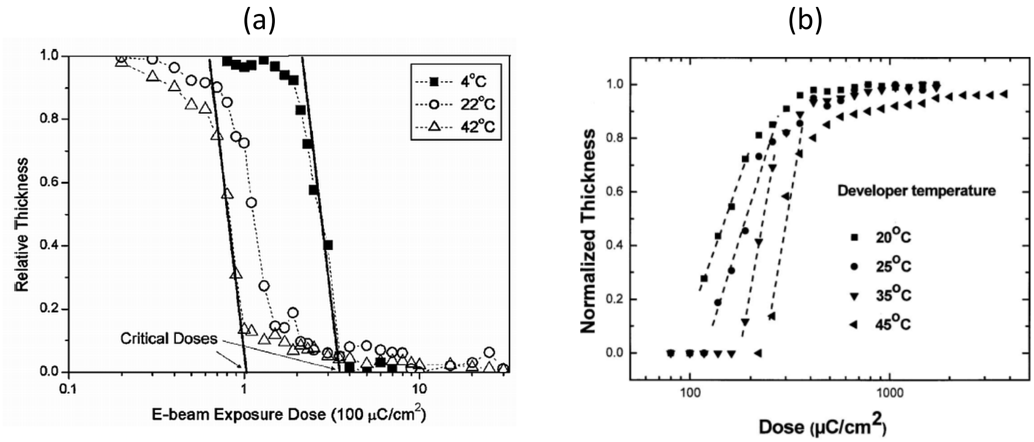

Figure 2.16 Contrast curves showing the impact of varying the developer temperature on sensitivity and contrast for (a) PMMA, and (b) HSQ. Panel (a) reprinted with permission from [179]. Copyright © 2005, IEEE. Panel (b) reprinted with permission from [161]. Copyright © 2007, American Vacuum Society.

examples of contrast curves, for PMMA and HSQ resists respectively, showing the effects of using various developer temperatures. Sensitivity may be read off contrast curves by selecting the clearance or cross-linking dose for a given process. Contrast (γ) is measured according to the standard definition $\gamma = [\log(d_0/d_1)]^{-1}$ [51] where the clearance (d_0) and onset (d_1) doses are determined by extending the tangent of the largest slope to the 0, 1 intercepts of the ordinate axis. In addition, contrast curves measured at different times can be used to calculate the development rate, and contrast curves measured at different temperatures can be used to obtain the activation energy through fitting, helping to understand EBL processes better [145,180].

Most of the above state-of-the-art results have been achieved using relatively thin (20 – 100 nm) resists. Generally, using thinner resists eases the

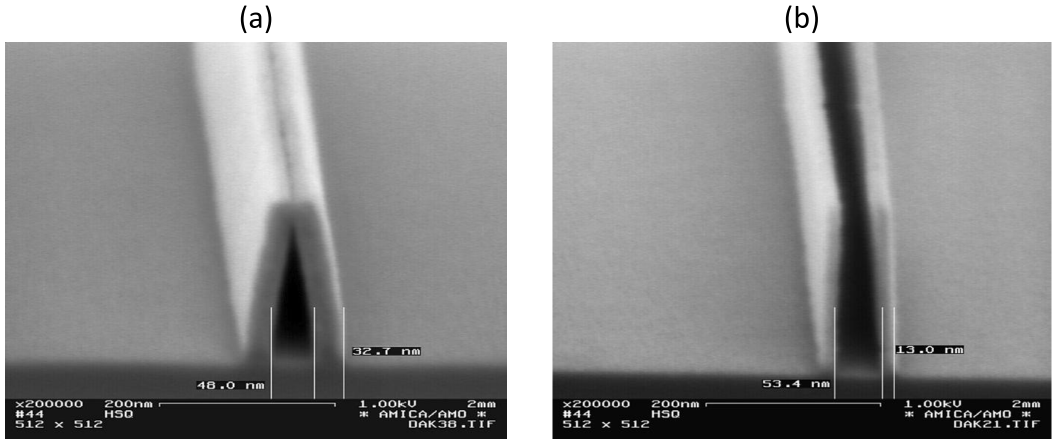

Figure 2.17 Regular (a) vs. supercritical (b) dried HSQ nanostructures. The AR improves from ~ 7 (H/W=220/33) to 17 (220/13) due to supercritical drying. Reprinted with permission from [172]. Copyright © 2007 Elsevier.

fabrication at the deep nanoscale due to reduced AR requirements. As mentioned previously, attempts to fabricate high AR structures result in pattern collapse due to the action of capillary forces at the time of drying. However, pattern transfer for device fabrication sometimes requires high AR patterning for which solutions such as supercritical (SC) drying have been devised. Compared to an AR of nearly 7 in HSQ using regular drying (see Figure 2.17(a)), Wahlbrink *et al.* have demonstrated the ability to nearly double their pattern AR to 17 using SC drying (see Figure 2.17(b)) [172]. These results were obtained using 100 keV exposure and room temperature 25% TMAH development. Rooks et al. achieved a similar AR of 13 in PMMA at 100 keV without using SC drying. They instead used cold 5 °C development in IPA:water 1:3 with ultrasonic (US) agitation [128]. As compared to PMMA and HSQ, the AR performance of ZEP has been very limited even at high voltages, albeit with a much higher sensitivity. Li *et al.* have

Table 2. EBL results showing selected metrics of interest

Resist	Voltage (keV)	Sensitivity (* µ/p)	CD † (nm)	AR	REF.	Notes
PMMA	30	1300 p	4-7	-	[131]	4 °C MIBK:IPA 1:3
PMMA	30	700 µ	8	-	[132]	-15 °C MIBK:IPA 1:3
PMMA	50	1600 µ	9	3	[133]	-10 °C MIBK:IPA 1:7
PMMA	80	740 µ	5-7	-	[163]	3:7 C:M ‡ + US
PMMA	100	4200 µ	111	13	[128]	5 °C IPA:H_2O 1:3 + US
ZEP	20	480 p	23	4	[168]	6 °C ZED-N50 + US
ZEP	30	200 µ	40	-	[140]	-4 °C Xylenes
ZEP	50	-	11	-	[142]	2 °C ZED-N50
ZEP	100	400 µ	50	7	[181]	ZED-N50
ZEP	100	20000 µ	9	-	[141]	IPA Developer
HSQ	10	420 p	10	-	[158]	50 °C 2.38% TMAH
HSQ	25	477 µ	20	-	[160]	60 °C 25% TMAH + SC
HSQ	50	-	10	2.5	[161]	45 °C 25% TMAH
HSQ	100	5500 µ	6	3	[177]	2.38 % TMAH
HSQ	100	-	13	17	[172]	25% TMAH + SC

(*µ/p) Units of dose – Area Dose µ = µC/cm^2 and Line Dose p = pC/cm.

† CD (Critical Dimension) used here as Resolution in nm.

‡ C:M – Cellosolve: Methanol developer

reported the highest ZEP AR of 7 at 100 keV using regular room temperature development in ZED-N50 [181].

The aforementioned significant advances in EBL processing provide a broad toolkit for further advances and applications development. Table 2 presents key advances in selected metrics of interest, summarizing some of the results presented in this section. It is clear that due to the complex relationships between various parameters and metrics, a systematic and quantitative understanding is required to apply and extend these processes effectively.

2.4 Role of EBL simulations

Due to the complexity and high costs associated with EBL, the necessity for predicting and rationally optimizing the required process parameters for patterning a particular nanostructure has been understood for a long time. Research groups world-wide have pursued the development of EBL simulators, some of which have been commercialized such as SELID [182,183], SCELETON$^{\text{TM}}$ [184], ProBEAM [185,186], and TRAVIT [187]. The exposure step, which involves electron transport and interaction with resist, has largely been represented by calculating the distributions of deposited energy in the resist with the Monte Carlo approach for describing the electron transport and scattering [184,185,186,187]. However, analytic approaches based on the Boltzmann equation for electron transport have also been used [182,183,188]. As compared to the exposure step, the development modeling studies lag significantly behind

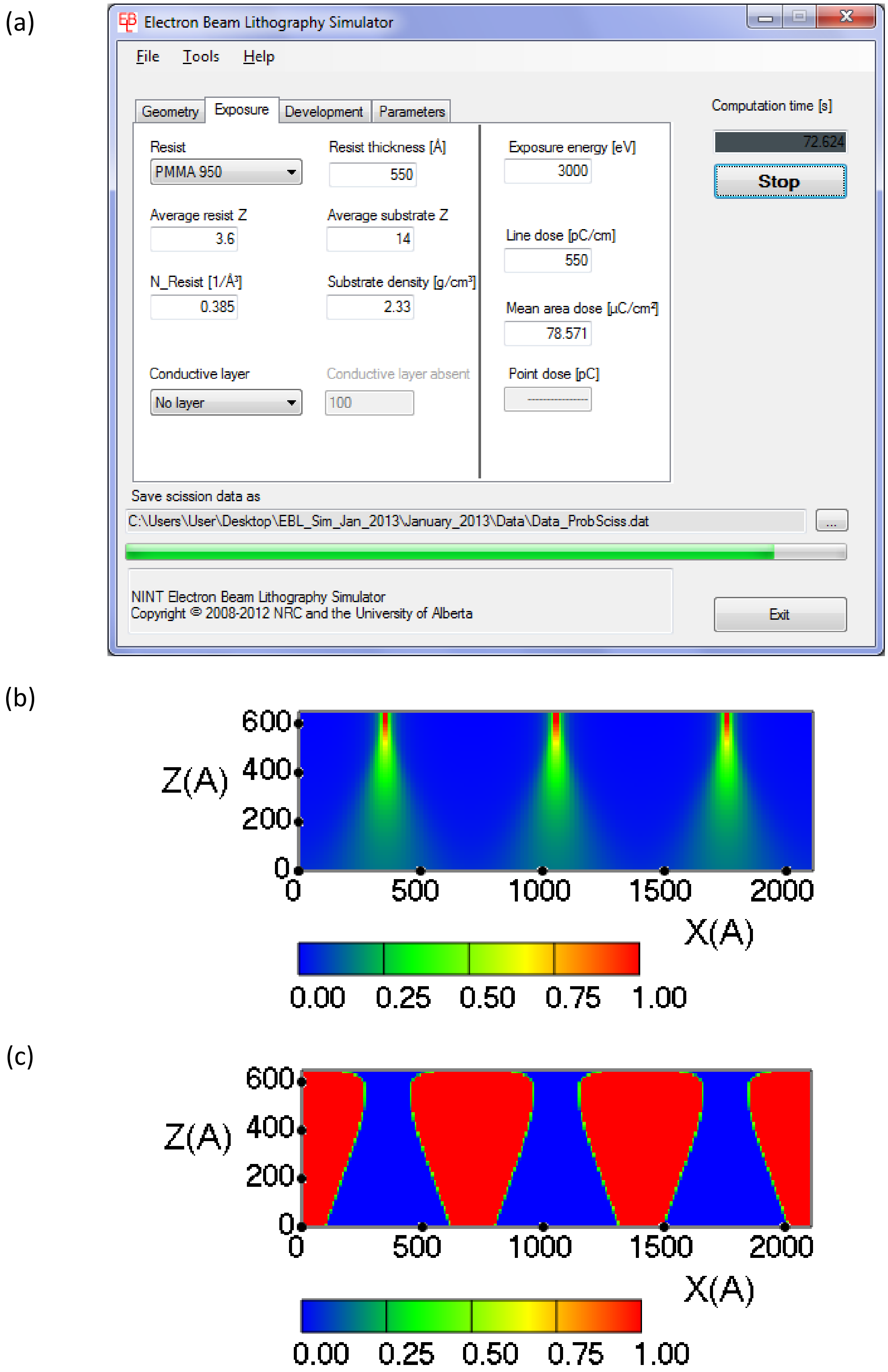

Electron Beam Lithography Simulator

Resist: PMMA 950

Resist thickness [Å]: 550

Average resist Z: 3.6

Average substrate Z: 14

N_Resist [1/Å³]: 0.385

Substrate density [g/cm³]: 2.33

Conductive layer: No layer

Conductive layer absent: 100

Exposure energy [eV]: 3000

Line dose [pC/cm]: 550

Mean area dose [µC/cm²]: 78.571

Point dose [pC]: ----------

Computation time [s]: 72.624

Save scission data as: C:\Users\User\Desktop\EBL_Sim_Jan_2013\January_2013\Data\Data_ProbSciss.dat

NINT Electron Beam Lithography Simulator
Copyright © 2008-2012 NRC and the University of Alberta

Figure 2.18 NINT EBL Simulator (a) GUI screenshot, (b) Post-exposure distribution of PMMA main-chain scission yield, and (c) Post-development resist profiles.

in the level of detail [112,113,68]. Raptis and Glezos [110] have recently reviewed various commercially available EBL simulators, electron transport simulators, and analytical tools.

Recently, a locally developed "NINT Electron Beam Lithography Simulator" has been commercially released [189]. In this simulator, the exposure step in a positive-tone resist is represented by the yield of the main-chain scission, avoiding uncertainties related to the mapping of deposited energy. The development step employs a recent kinetic model of polymer diffusion [85,190]. A screenshot of this simulator is shown in Figure 2.18(a) displaying the various tabs and options. Currently, the simulator can handle 1-100 keV exposures of PMMA and ZEP resists processed in popular developers. In addition to standard input parameters such as pattern geometry, voltage, dose, and development time, this simulator has the unique ability to handle development temperature and anti-charging top-coats [191].The simulator outputs 3D distributions of post-exposure resist scission yield (see Figure 2.18(b)) and complete post-development profiles (see Figure 2.18(c)) with a 1 nm resolution. The detailed treatment of polymeric resists and the ability to handle a wider variety of process parameters are key merits of interest. In this thesis, the NINT EBL Simulator has been used for analysis and prediction/testing of designs. In turn, some of the experiments reported in this thesis were employed by the simulator’s developers to parameterize and validate models used in the tool.

2.5 Research scope

In the following sections, the framework and thesis structure is presented. The objective of this thesis is to understand and control EBL processing at the molecular scale in the low voltage (3 - 30 keV) regime (see Figure 2.19). In particular, the post-exposure development stage has been investigated in greater detail. A better understanding of EBL processes will enable rational optimization of process parameters. By applying optimized processing strategies to fabricate functional devices, improved device dimensions and performance will be obtained.

Figure 2.19 Major themes of this research project.

2.5.1 EBL process windows

In order to compare the response of resists to various processing strategies, a graphical representation is often convenient. One such widely used and mature representation is to plot and compare contrast curves (see Figure 2.16(a, b)). Contrast curves provide quantitative information on the sensitivity and contrast of a process, and qualitative information about the resist-developer interaction strength and whether the resist may be used for 3D lithography. Furthermore, as explained in section 2.3, contrast curves can be used to obtain the development rate and activation energy. However, contrast curves provide no information regarding dense pattern resolution, pattern reproducibility, and processing limits as contrast curves are fundamentally generated by large area exposures.

For comparing processes used to fabricate dense patterns, process window plots can be used. For any process variable, a process window is the range of values for which fabricating a certain repeating nanoscale pattern is feasible. Process latitude plots, which focus on strict control of CD, are a subset of process window plots. Process window or latitude plots are seldom provided in the literature and, therefore, no single format for their axis ordering or graphical representation is followed. Examples of such plots from the literature are provided in Figure 2.20(a-d) studying the effects of voltage [68], CD [192], pitch [103,133], development temperature and molecular weight [133] for dense gratings in PMMA. The regions named on the above windows (see Figure 2.20(a, b)) refer to the various regimes encountered while patterning an array of lines (gratings) at various doses as shown in Figure 2.21(a) [100,193]. As the exposure dose is increased, there occurs a window of exposure doses for which quality gratings can be fabricated. This exposure dose window is the process window of interest which varies according to the conditions chosen e.g., development time

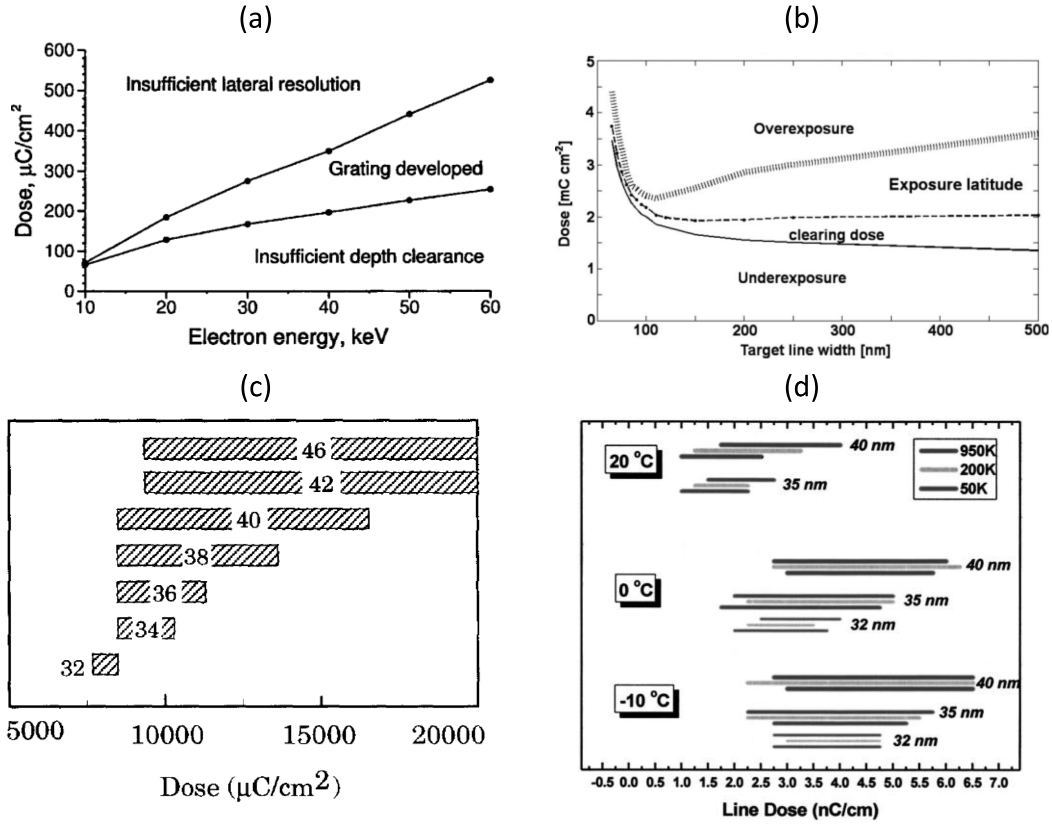

Figure 2.20 Theoretical (a) and experimental (b, c, d) process windows for PMMA resist under various conditions. Panel (a) reprinted with permission from [68]. Copyright © 2006, American Vacuum Society. Panel (b) reprinted from [192] (open access). Panel (c) reprinted with permission from [103]. Copyright © 1998 Elsevier. Panel (d) reprinted with permission from [133]. Copyright © 2008, American Vacuum Society.

(see Figure 2.21(b)). This arrangement enables studying and eventually predicting the dose required as a function of a given process parameter.

Process windows are a versatile, underexplored instrument that can be used to determine sensitivity, CD control, process robustness, and mapping of grating morphological regimes and their evolution, etc. An in-depth study of process windows provides an opportunity to quantify and understand the

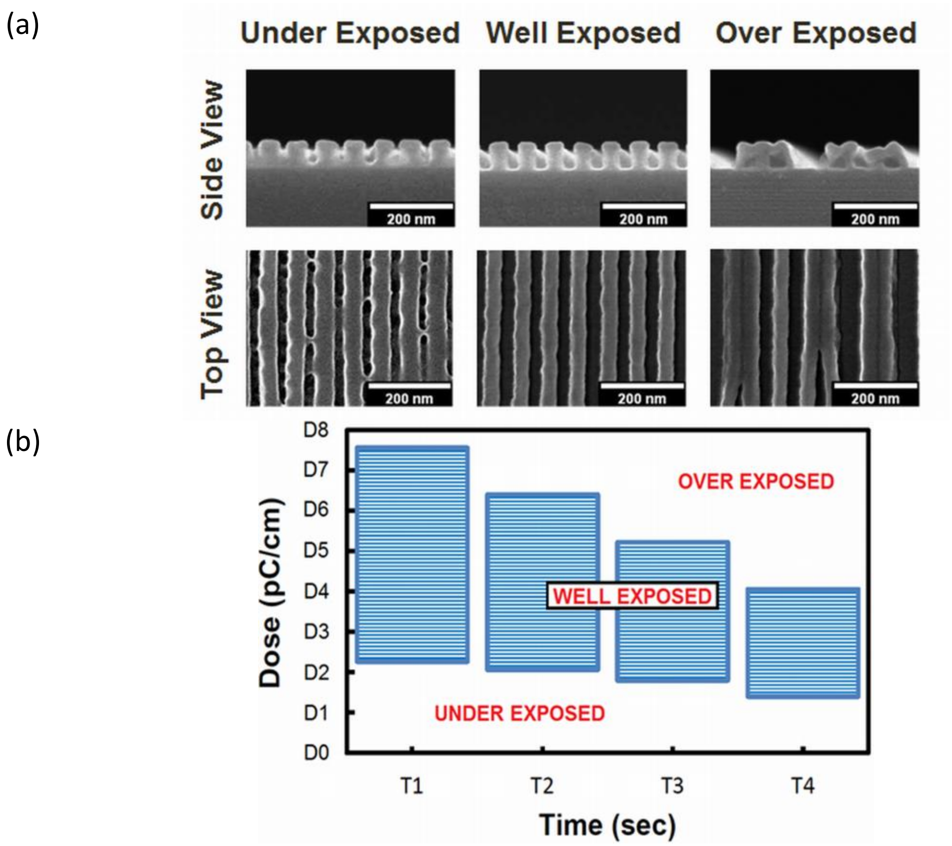

Figure 2.21 (a) Various regimes in grating fabrication [100,193], and (b) a typical process window plot. The shaded region is the process window for good gratings. Panel (a) reprinted with permission from [100]. Copyright © 2010 Elsevier.

intricate interdependence of numerous process parameters for dense grating fabrication and their impact on relevant process metrics. Understanding of process windows is essential for future industrial EBL processes that require very low tolerance control over CD and LER. Furthermore, process windows can be used for the fitting of development models and extracting model parameters.

In this thesis, the interplay of process parameters and their influence on process metrics is thoroughly examined using both process windows and contrast curves. Where applicable, one or both of these graphical representation methods are used for studying the effects of varying the grating pitch, exposure voltage, dose, developer, development time, temperature, etc., using PMMA and/or ZEP polymeric resists. In addition to improving the understanding of EBL and providing a roadmap for process optimization, this research is necessary for parameterizing and validating the NINT EBL Simulator.

2.5.2 Molecular study of development process

As established in section 2.1.3, the development stage is critical in the EBL process and can significantly influence the final process metrics. Consequently, understanding this stage is crucial for rational optimization of the EBL process. Efforts to probe the kinetics of resist development are well documented. For example, resist dissolution rates have been obtained through contrast curves [145], submerged quartz crystal microbalance (QCM) monitoring [154,155], and multi-wavelength interferometry [194]. However, research works addressing the resist dissolution at the molecular scale are relatively scarce. A major challenge in the experimental study of the resist dissolution is the very small size and low concentration of resist fragments in developer. Taking the case of exposed PMMA, most soluble fragments are less than 5 nm long at full stretch and their concentrations in solution are in the ng/ml to µg/ml range. This introduces the need for various modeling studies of the development process at the molecular level.

A viable modeling technique at the scale of PMMA fragments is to conduct molecular dynamics (MD) simulations. In an MD simulation, the equations of motion for a system of molecules are solved over a certain time interval to obtain a sequence of snapshots (trajectory file) containing dynamic position, velocity, energy, etc., data for all atoms in the system. A comprehensive overview of the MD techniques with discussion of simulation parameters and applications is provided in numerous references – one recent reference being [195]. MD techniques have been applied by the nanolithography community to study topics of interest in chemically amplified resists [196], scanning probe lithography [197], nanoimprint lithography (NIL) [198,199,200] and recently in electron beam lithography (EBL) [125,201].

With regards to polymer miscibility, MD techniques have been used in numerous studies. For example, the dissolution of relatively long (degree of polymerization $n \geq 1000$) unexposed PMMA chains have been studied in benzene [124]. In another study, the miscibility of various PMMA chain lengths ($n \sim 1, 2, 3, 100, 200$) in a low molecular mass liquid crystal has been investigated [202]. In this study [202], the BLENDS and DISCOVER software modules (Accelrys Materials Studio Package [203]) have been used to calculate the F–H interaction parameter χ (see equations (4-5)). In addition, the χ parameter values for various polymer blends [204,205] have also been obtained using the same software package. These examples demonstrate that polymer miscibility can be quantitatively studied using MD. Furthermore, MD also enables the study of kinetic aspects of polymer dissolution.

In order to obtain the χ parameter from MD simulations, the F-H equation (4) needs to be re-written using quantities obtainable from MD simulations [206]. In equation (4), ΔH_{mix} is related to the change in the computed energy of mixing ΔE_{mix} according to $\Delta H_{mix} = \Delta E_{mix} / N_{latt}$ where N_{latt} is the number of so-called F-H lattice sites in the simulated system. For a binary mixture of a polymer and developer $\Delta E_{mix} = E_{mix} - n_s E_{ss} - n_p E_{pp}$, where E_{mix}, E_{ss}, and E_{pp} are the energies of the mixture, the developer, and the polymer, respectively; and n_s and n_p are the number of developer and polymer molecules, respectively. It is to be noted that the number of polymer molecules here refer to PMMA chains of a chosen length (n). Substituting the equations for ΔH_{mix} and ΔE_{mix} provided above in equation (4), one obtains [206],

$$\chi = \frac{E_{mix} - n_s E_{ss} - n_p E_{pp}}{kTN_{latt}\varphi_s \varphi_p} \qquad (8)$$

Equation (8) contains only constants or quantities that can be acquired using MD simulations. This approach has been implemented by K. P. Santo [206] in a MATLAB code, which has been used in this thesis.

In order to parameterize the F-H model, the MD simulation strategy [206] has been employed as outlined in Figure 2.22. In these simulations, bulk systems of molecules of each specie (PMMA fragments, developers) are constructed and

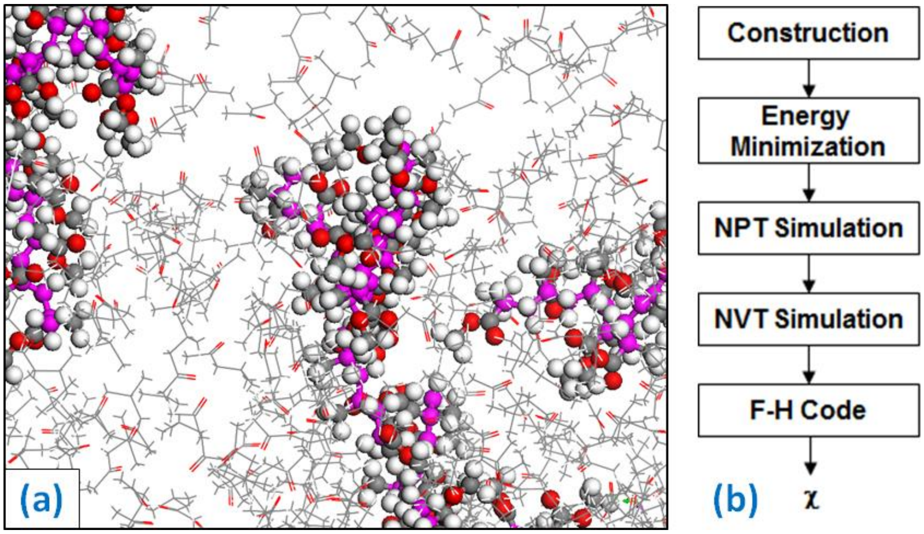

Figure 2.22 MD simulation of PMMA fragments in various developers: (a) sample screenshot, and (b) flowchart showing the simulation strategy to obtain interaction parameters of a binary mixture, inspired by ref. [206].

their energies are minimized. Further, each system is subjected to an isothermal–isobaric (NPT) ensemble dynamics simulation to obtain the system density, and subsequently subjected to a canonical (NVT) ensemble dynamics simulation to obtain the potential energies. After the properties of the individual species have been obtained, the same process is repeated for the fragment-developer binary mixtures. The computed properties of the individual species are also used to setup the mixture simulations. Finally, all relevant simulated quantities are used in the F-H model to calculate the respective fragment-developer χ parameters [206] and compared against χ_c in equation (6).

In this thesis, the miscibility of PMMA fragments (1-10 monomer chains) in MIBK and IPA developers is studied using MD simulations (Accelrys Materials Studio environment [203]). The simulated thermodynamic data is used to calculate the χ parameters for each fragment-developer pair. Furthermore, to understand various aspects of the dissolution process, the self-diffusivity, radii of gyration (R_g), and radial distribution functions (RDF) of PMMA fragments in both developers are calculated and compared.

2.5.3 Applications of EBL processing

The third aspect of this thesis is to utilize the understanding and knowledge of EBL processing and techniques towards improvement of sensitivity and resolution of nanoscale patterning in two specific applications.

High resolution and high AR patterning is a requirement in many nanoscale applications such as NIL templates, DRAM capacitors, X-ray zone plates (lenses), etc. However, standard positive-tone resists such as PMMA and ZEP have AR limited to 3-4 at 30 keV [52,128]. A novel EBL resist 'SML' (see Figure 2.23) has been recently [207] designed by the University of Manchester and marketed by *EM Resist Ltd.*, [208] with a claimed AR of 10:1 at 30 keV. This significant improvement is accompanied by a drawback – the sensitivity of SML resist is significantly less than PMMA using standard developers. Utilizing the methodologies learnt in the previous sections, an objective of my work has been to create a high sensitivity nanolithography process while maintaining the AR.

Nanomechanical doubly-clamped cantilevers (*aka* resonators) are devices used for chemical and biological sensing applications [209]. The sensing

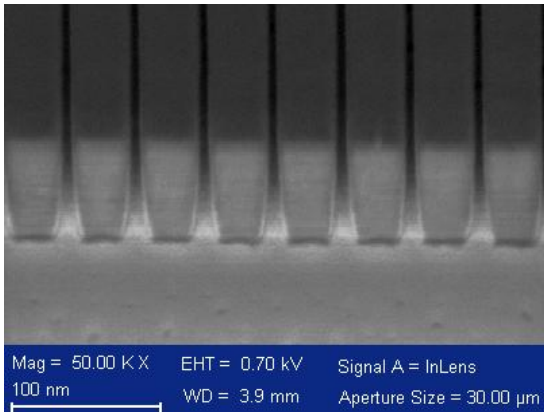

Figure 2.23 Cross-section micrograph of gratings fabricated in SML resist. Micrograph from *EM Resist Ltd.* website [208]. Reprinted with permission. Copyright © 2012 *EM Resist Ltd*.

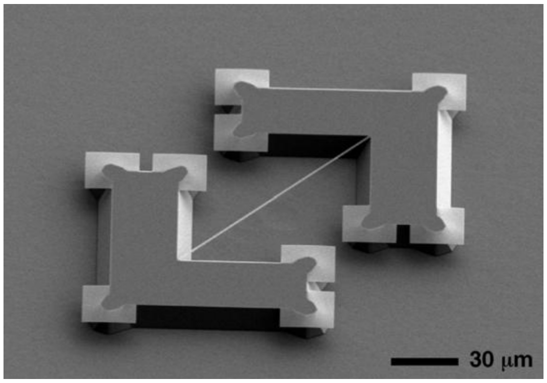

Figure 2.24 A 35 nm thick, 430 nm wide, and 40 micron long doubly-clamped SiCN cantilever. Reprinted with permission [212]. Copyright © 2008, Elsevier.

resolution of these resonators is improved as their dimensions are reduced [209] according to $\Delta m \propto wL^3$, where Δm is the mass sensitivity, and w and L are the resonator width and length, respectively. However, reducing the width poses various material and fabrication challenges. Fischer *et al.* from NEMSLAB [210] have developed glassy silicon carbon nitride (SiCN) for resonator fabrication [211], and demonstrated a hybrid surface-bulk nanomachining process for resonator fabrication (see Figure 2.24) [212]. The existing fabrication processes involve a long list of steps, increasing the complexity and reducing the final feature resolution. My objective has been to optimize and re-design the existing process for ultra-high resolution. Ultimately this work enabled the fabrication of uniform ultra-narrow sub-10 nm SiCN resonators – a task currently not possible with other NEMS materials and procedures.

2.6 Thesis structure

In this thesis, Chapters 1 and 2 provide a detailed introduction to EBL. In Chapter 1, the history of EBL development and its place among various lithographic techniques is presented. The role of EBL in industry and academia and the general need for further research is discussed.

Chapter 2 provides an in-depth coverage of the EBL process and an extensive literature review. The scientific mechanisms and processing conditions of each process stage are thoroughly covered. The reader is updated on the relevant processing advances. Chapter 2 concludes with outlining the avenues for research and establishing the scope of this research project.

In Chapter 3, a comprehensive experimental study of the effects of various EBL processing parameters on process windows, contrast curves, and nanostructure morphologies is provided for PMMA and ZEP resists. Special emphasis is placed on the development stage parameters. Relevant trends are discussed with the aid of the EBL simulator. The use of process windows for extraction of parameters of simulation models is demonstrated.

Chapter 4 presents a molecular study of PMMA fragment dissolution using MD simulations and Flory-Huggins solution theory. The thermodynamic, kinetic, and statistical mechanical aspects of dissolution of short PMMA chains in MIBK and IPA developers are examined. Model parameters for polymer dissolution are extracted and the simulation results are assessed in light of experimental observations.

The application of EBL processing techniques are presented in Chapters 5 and 6. In Chapter 5, an in-depth study of new and existing developers for SML resist pave the way for creating a high sensitivity EBL process. Carefully considered nanolithography processing enables fabrication of high AR and high resolution grating fabrication.

In Chapter 6, the fabrication of nanoscale SiCN resonators is discussed. An existing PMMA based fabrication approach developed by the Evoy NEMSLAB group is optimized for fabrication of sub-20 nm resonators. The EBL simulator is used for testing new and improved resonator anchor designs. Furthermore, a brand new HSQ based SiCN resonator fabrication approach is demonstrated for fabricating sub-10 nm resonators. Optimized development processes enable uniform resonator and anchor fabrication.

Finally, Chapter 7 summarizes the most important contributions and conclusions of the overall research project. In addition, recommendations for further research are provided.

CHAPTER 3

EBL PROCESS WINDOWS AND TRENDS

3.1 Introduction

The outcome of an EBL process is influenced by a wide range of (often interacting) process parameters. In chapter 2, various process variables and metrics of interest, and their mutual relationships, were identified through existing literature, and the scope for further research was described. In this chapter, a thorough investigation of the influence of process parameters on the characteristics of process windows, contrast curves, and nanostructure morphologies is conducted using PMMA and ZEP resists. This investigation leads to advancements in the overall understanding of EBL trends, nanofabrication strategies, and resist behavior. State-of-the-art ultrahigh resolution lithography results for dense gratings in both PMMA and ZEP are demonstrated.

3.1.1 Methods

The baseline experimental methodologies and parameters for all processes employed in chapter 3 are described in this section. The particular experimental parameters used to generate a given figure or data-set are specified when the results are discussed. Where differences from the primary methodologies exist, these are indicated at the relevant locations in the text.

The EBL trends are explored using two graphical representations, namely process windows and contrast curves. The data for these representations is acquired using similar fabrication parameters; however, the design layout and characterization procedures are very different. A summary of the fabrication procedure and parameters pertaining to this chapter are provided in Table 3.

The fabrication processes begin with a Piranha cleaning of diced Si (100) chips. These chips are baked to drive off any moisture and left to briefly cool. PMMA or ZEP resists are then spun-cast onto the Si chips followed by a resist soft-baking routine to drive off the resist's casting solvent. Detailed spinning parameters are provided in Appendix A1. The resist thickness varies from 55-65 nm for process window samples and from 145-330 nm for contrast curve samples. A thicker resist layer for contrast curves enables greater height resolution. The resists are then exposed according to the desired pattern (described in sections 3.1.1.1 and 3.1.1.2) and the desired exposure parameters such as voltage, dose, aperture size, and step size. After the exposure step, the samples are developed using a selected developer at a controlled development time and temperature. Subsequently, the development is quenched by dipping the samples in IPA for 20 sec. The development of ZEP samples may be quenched

Table 3. Fabrication steps and conditions for Chapter 3

Process Step	Parameters/Conditions	Apparatus
Substrate	Silicon (Si)	
Substrate Cleaning	Piranha (1:3 H_2O_2:H_2SO_4 15 min)	Wet Deck
Substrate Baking	5 min at 175 °C	Hot Plate
Resists	PMMA, ZEP	
Resist Spinning	(See Appendix A1)	Headway Spinner
Resist Baking	5 min at 175 °C	Hot Plate
Resist Thickness	55-65 nm (Process Windows) 145-330 nm (Contrast Curves)	Ellipsometer (VASE) or Filmetrics F50
Exposure Voltage	3-30 keV	Raith 150 or Raith 150^{TWO}
Exposure Dose	Variable (See data in chapter)	
Exposure Step Size	2-6 nm (Process Windows) 10-20 nm (Contrast Curves)	
Exposure Aperture	7.5-10 µm (Process Windows) 20-30 µm (Contrast Curves)	
Developer	MIBK:IPA 1:3, IPA:water 7:3, ZED-N50	Beaker (50 mL)
Development Time	2, 5, 10, 15, 20, 40 sec	
Development Temperature	-15 °C, -10 °C, -5 °C, 0 °C, 5 °C, 10 °C, 22 °C (room temperature)	Stir Kool SK-12D (See Appendix A2)
Quencher	IPA (PMMA, ZEP) MIBK (optional for ZEP)	Beaker
Quench Time	20 sec	
Ultrasonic Agitation	42 kHz, Power level 9 Time as above	Crest Powersonic or Branson Bransonic
Supercritical Drying	CO_2 Supercritical fluid, 30-60 min process time.	Tousimis autosamdri 815B

using MIBK. For samples developed in IPA:water 7:3, no quencher fluid is used. The setup required for performing development at cooler temperatures is shown in Appendix A2. The development may optionally take place in an ultrasonic bath. Following the development, most samples are dried by gently blowing gaseous N_2; however, some process window samples may be dried in a supercritical dryer. When supercritical drying is intended, the developed samples are transferred to the supercritical dryer in an IPA bath.

3.1.1.1 Process windows and grating morphologies

In order to obtain EBL process windows and perform high resolution nanolithography experiments, grating test structures of varying interline spacing (pitch) are employed. The process windows presented in this chapter have been obtained using two layout designs, (A) and (B), illustrated by Figures 3.1 and 3.2, respectively. Design (A) has been used to determine only the process window in section 3.2.1 [and in ref. 12,213,214], whereas design (B) has been used to determine all other process windows in this chapter [incl. ref. 12,100,180,190,214,215]. Each line in a grating was exposed in a single pass of the electron beam. This is also referred to as a single-pixel-line.

The layout of design (A) (used in paper [213]) consists of a 7 x 9 matrix of grating units, each unit having a particular exposure dose and pitch. Within the matrix, the dose increases from 25 to 150 $\mu C/cm^2$ on one *axis* and the pitch

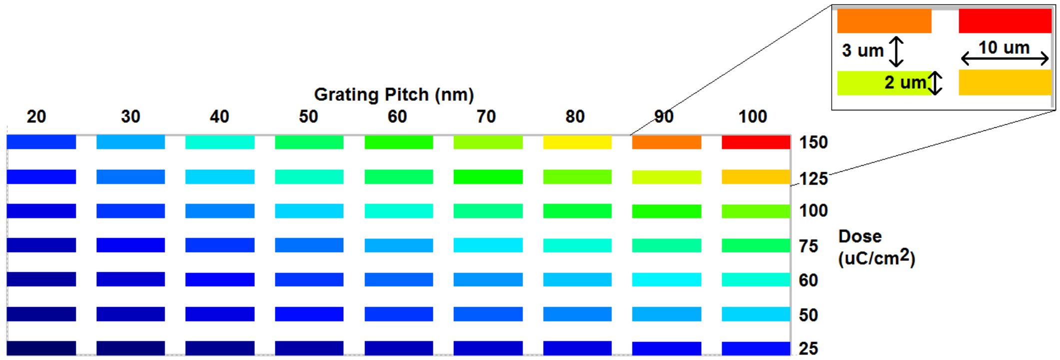

Figure 3.1 Dense gratings design (A) for measuring process windows and observing nanolithography results. The changing color shows increasing dose from low (blue) to high (red).

increases from 20 to 100 nm on the other *axis* (see Figure 3.1). In this way 63 different dose and pitch combinations are tested per exposure. Each grating unit in this matrix covers a 2 µm x 10 µm area and is separated from other grating units by 3 µm. The width of each grating unit (2 µm) has been chosen to be wide enough to ensure a uniform cumulative exposure due to backscattered electrons in the central portion of the unit. Similarly, the inter-unit spacing (3µm) has been chosen to be sufficient to limit any backscattered electron contribution from other units in the selected voltage regime.

In contrast with design (A) where an individual grating unit receives a uniform dose, the layout of design (B) [216,217] consists of grating units with a progressively increasing dose. Each grating unit (of a particular pitch) consists of a minimum of 2000 single-pixel-lines, with each line receiving an incrementally higher dose than the previous adjacent line (see Figure 3.2, this design has been

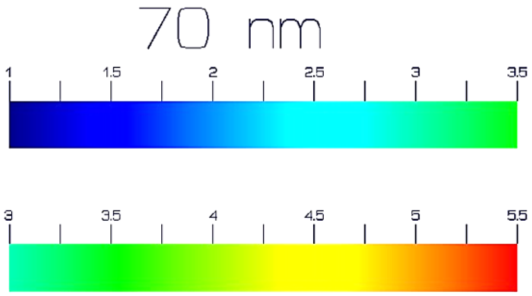

Figure 3.2 Dense gratings design (B) for measuring process windows and observing nanolithography results. The grating pitch in this design is 70 nm. The tick marks are part of the design and indicate (multiplicative) dose factors. The array has been broken in two to fit inside a 100 µm write-field. The changing color shows a gradually increasing dose from low (blue) to high (red) [216,217].

used in references [12,100,180,190,214,215,216,217]). The grating usually begins with a dose factor of 1.0 and ends with a dose factor of 5.5 with increments of 0.2%. By changing the original applied dose, a wide range of exposure doses can be tested. With increasing dose, the gratings generally proceed from under-exposed, to well-exposed, and finally over-exposed (see Figure 2.21(a) in section 2.5.1). The grating units in design (B) are 10 µm in length to capture the contribution of proximity effects. The width of each grating unit varies depending on pitch – the minimum width being 30 µm. The grating pitch was varied from 30 to 100 nm.

For both design (A) and (B), the dose window is the range of doses for which well-exposed gratings can be fabricated (see Figure 2.21(a)). The characterization of the gratings is performed through SEM imaging (Hitachi S-

4800 or Raith 150/150^{TWO}), which enables visualization and metrology of the process windows and nanostructure morphologies. Prior to SEM imaging, the resist samples are coated (Gatan 682 PECS or Kurt J. Lesker) with a thin (4-6 nm) chromium layer. This step is essential to avoid damage to the polymeric resists and prevent charging during SEM imaging.

Further characterization of nanostructure morphologies may be conducted by SEM imaging cross-sections of the patterned resist. To generate suitable samples for cross-section inspection, 2000 μm long grating units are fabricated and manually cleaved perpendicular to the pattern. This extraordinary length is intended to ensure that the cleave passes through the gratings. The EBL conditions used for generating these grating units are acquired after patterning and characterization of designs (A) and/or (B). To generate crisp cross-sections, the edge of a sample is scratched with a diamond scribe perpendicular to the patterns generated, as a seed location to guide the cleave. The sample is then held with two similar comb-tooth tweezers and immersed in liquid nitrogen (LN_2). After keeping the sample immersed in LN_2 for up to 30 sec., the sample is cleaved. The use of LN_2 allows the polymeric resists to become brittle and cleave without either stretching and deforming, or tearing and leaving residue that may obscure the cross-section of interest. An example of a poor and a high-quality grating cross-section is shown in Figure 3.3(a) and 3.3(b), respectively. The cross-sectioned resist samples are also coated with a thin layer of chromium prior to imaging; however, this coating is applied by tilting the sample 30-45 degrees.

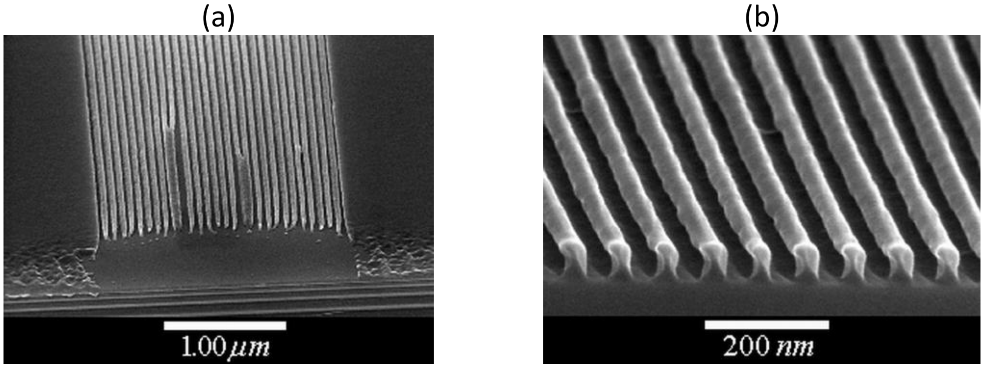

Figure 3.3 Examples of (a) poor [218], and (b) high-quality cross-sections of EBL defined grating nanostructures in PMMA. Panel (b) reprinted from [214] (Creative Commons Licence).

Further discussion on grating morphologies and high resolution nanolithography is provided in section 3.2.

3.1.1.2 Contrast curves

The design layout used to obtain contrast curves consists of an array of large squares or rectangles with a gradually increasing dose factor. Each member of the array is separated by a gap sufficient to minimize the proximity effect. After exposure and development, the resulting pattern is scanned by a suitable height measurement apparatus such as an atomic force microscope (AFM/Veeco Dimension 3100), a physical profilometer (AlphaStep IQ), or an optical profilometer (Zygo NewView 7300). The layout is varied according to characterization technology i.e., samples intended for AFM are exposed with an array of 1 μm squares separated by a 2 μm gap [180], whereas samples intended for both types of profilometers are exposed with an array of 20 x 75 μm

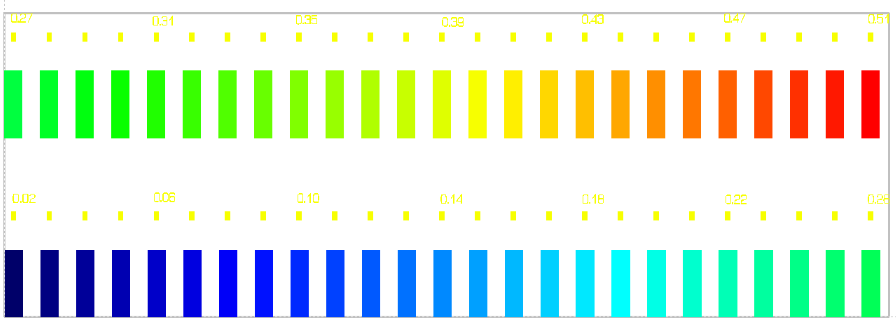

Figure 3.4 Design layout for measuring contrast curves with physical or optical profilometry. Each rectangle measures 20 x 75 µm and is spaced by 20 µm. The changing color shows dose increasing from low (blue) to high (red).

rectangles separated by a 20 µm gap (see Figure 3.4) [218]. The smaller features and gaps for AFM are due to its slower horizontal scan speed and higher resolution. Contrarily, the larger features and gaps for both types of profilometers are due to their faster horizontal scan speed and lower resolution. Except for samples measured with optical profilometry, a thin metallic top-coating is not required. The three height measurement techniques have been briefly compared in Appendix A3. Unless specified otherwise, the contrast curve patterns in this chapter have been measured with physical profilometry.

The dose factors of the design and applied dose are selected such that after patterning is complete, a gradual increase in depth is observed from onset to clearance. When scanned, these depth increases manifest as increasing step heights. These step heights are measured, normalized according to the original resist thickness, and plotted on a semi-log scale as contrast curves. The clearance dose is recorded as the sensitivity and the contrast value (γ) may be obtained as described in section 2.3 (also see Figure 2.16). In addition to obtaining contrast curves, the aforementioned patterns may be used for measuring resist surface roughness and for imaging fine details of partially exposed resist to learn more about the dissolution stage.

3.1.2 Contributions

Prior to discussing the data and interpretations, it is important to state the contributions of a few colleagues in our research group. Having worked on the same project, overall goals and even individual tasks were often jointly pursued. Due to this, there are some overlaps in data collection and analysis which are stated below.

Inspired by Raith's grating test design, Zsolt Szabo (2007-2009) drew the first version of design (B), a later version of which is shown in Figure 3.2 [216]. Jiang Chen (2008-2009) used this design to collect data on PMMA process windows, some parts of which have been utilized in Figures 3.10, 3.13, 3.14, 3.18, 3.19, and 3.24 [219]. Taras Fito (2008-2010, 2011-present) derived equations (9) and (10) which were jointly parameterized by J.C. and the author, and drawn as Figure 3.24 by the author [12, 100, 214, 215]. The aforementioned contributions have been jointly published and the appropriate journal permissions have been included wherever published data has been reprinted in this thesis.

3.2 Influence of parameters

In order to understand EBL processing, where applicable, both process window and contrast curve studies are conducted. In both of these studies, we undertake a systematic approach to understand the influence of process parameters. The parameters under consideration include grating pitch, exposure voltage, developer, development time, and development temperature. The influence of advanced processing techniques such as supercritical drying and ultrasonic agitation are also discussed. Practical nanofabrication results are presented to aid the discussion and, wherever applicable, demonstrate results of systematic optimization of process parameters.

3.2.1 Grating pitch

As discussed in section 2.3, controllably fabricating dense patterns is a significant challenge alongside high resolution and high sensitivity nanofabrication. Due to the proximity effect, nanofabrication of dense features is particularly demanding. Furthermore, the requirement for fabricating increasingly dense patterns is heavily sought by industry. In this regard, gratings serve as a useful benchmark for process studies.

The nanofabrication of gratings with increasing density (decreasing pitch) causes the grating quality and characteristics to vary significantly. Figure 3.5 presents a matrix of PMMA grating morphologies showing the effects of varying

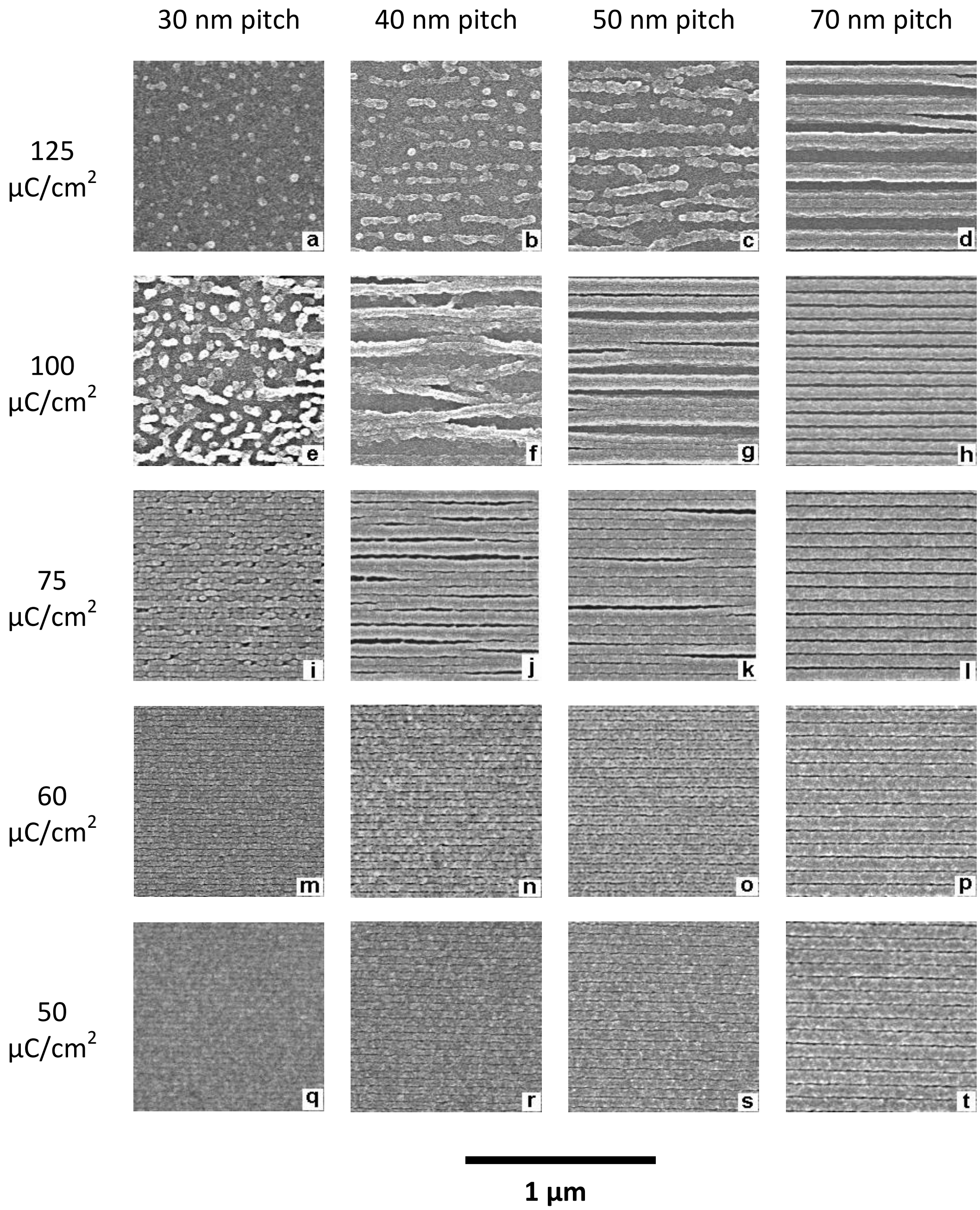

Figure 3.5 SEM images of 30-70 nm pitch nanoscale gratings in PMMA exposed to 50-125 μC/cm^2 area doses. The area doses are related to line doses by $d_{area} = d_{line}/\lambda$, where λ is the grating pitch. The exposure voltage was 10 keV and the patterns were developed at room temperature in MIBK:IPA 1:3 for 5 sec followed by a 20 sec IPA rinse. Reprinted with permission from [213]. Copyright © 2007, American Vacuum Society.

the grating pitch and exposure dose. The SEM images shown in this figure are a representative selection of grating morphologies imaged after EBL patterning of design (A) (shown in Figure 3.1). The exposure doses noted in Figure 3.5 are mean *area doses* which are useful to compare gratings of various periods as compared to *line doses*. Area doses can be related to line doses by $d_{area} = d_{line}/\lambda$, where λ is the grating pitch. A sample calculation showing the conversion of an area dose to a line dose for a grating geometry is given in Appendix A4.

It can be seen from Figure 3.5 that fabricating quality gratings is strongly dependent on both the grating pitch and the exposure dose. For example, quality 70 nm pitch gratings can be fabricated for all conditions except for the high 125 $\mu C/cm^2$ exposure dose condition shown in Figure 3.5(d). For 50 nm pitch gratings, promising morphologies are seen in Figures 3.5(k) and 3.5(o) corresponding to doses of 75 $\mu C/cm^2$ and 60 $\mu C/cm^2$, respectively. For 30 nm and 40 nm pitch gratings, only exposure at 60 $\mu C/cm^2$ in Figures 3.5(m) and 3.5(n), respectively, exhibits morphologies which could potentially yield quality grating patterns.

All other images in Figure 3.5 show poorly defined or damaged gratings and it is necessary to investigate the causes of this impact. This will enable the development of nanofabrication strategies to avoid fabricating such grating morphologies. In Figure 3.5, four causes of poor grating definition or damage have been identified namely (i) under-exposure, (ii) over-exposure, (iii) pattern collapse, and (iv) micellization. The first two causes are heavily influenced by the exposure stage and the second two causes are heavily influenced by the development stage.

In under-exposure, the grating patterns are not provided sufficient electron dose to clear the entire depth of the resist. Due to resist remaining at the bottom of the grating patterns, under-exposure is manifested by a low-contrast in SEM images. This can be seen in Figure 3.5(q) corresponding to the 30 nm pitch and 50 μC/cm^2 exposure dose case. In over-exposure, the grating patterns are provided an excessive electron dose. Due to electron scattering, this excessive dose results in clearance and removal of resist even from the locations not directly exposed. Figures 3.5(a), 3.5(b), and 3.5(c) demonstrate over-exposure due to application of high 125 μC/cm^2 dose to 30 nm, 40 nm, and 50 nm pitch gratings, respectively. Both under- and over-exposure are well-understood regimes.

The remaining two causes of grating damage occur at conditions intermediate to fabricating quality gratings and over-exposure. For gratings of 40 nm pitch and wider, exposed at relatively high exposure doses, pattern collapse occurs. The mechanisms [169,220] leading to pattern collapse and mitigation strategies [169,170,171] have been explained previously in section 2.1.4. Examples of collapsed grating morphologies at higher exposure doses (100-125 μC/cm^2) are shown in Figures 3.5(d), 3.5(f), and 3.5(g) and at a lower exposure dose (75 µC/cm^2) are shown in Figures 3.5(j) and 3.5(k). It will be shown in section 3.2.6 that despite employing pattern collapse mitigation strategies, this pattern degradation effect cannot be completely eliminated. The understanding, mitigation, and harnessing of pattern collapse is a subject of ongoing research.

The fourth cause of grating damage, denoted as micellization [213], occurs when the grating walls are destroyed and rearranged in the form of irregular globular droplets or networks. This is unlike pattern collapse, where the gratings are simply bent or misplaced from their initial locations. Examples of such micellized morphologies can be seen in Figures 3.5(e) and 3.5(i) corresponding to 30 nm pitch gratings exposed to 100 µC/cm^2 and 75 µC/cm^2 doses, respectively. Similar globular droplets or network structures are seen after phase separation of immiscible liquids [221]. It is possible that the micellization witnessed in Figures 3.5(e) and 3.5(i) is a result of phase separation between the EBL developer and insoluble PMMA resist fraction [222,223]. In addition to 30 nm pitch gratings, micellization can also be observed in less dense gratings (see Figures 3.5(b) and 3.5(c)) under strong over-exposure conditions. In relation to EBL processing, micellization is poorly understood, though there has been an effort [213,224] to explain the conditions under which micellization occurs for PMMA based on resist-solvent interaction and geometric factors.

All of the regimes mentioned above have been mapped in Figure 3.6 for 20-100 nm pitch and 25-150 µC/cm^2 exposure dose conditions. The process

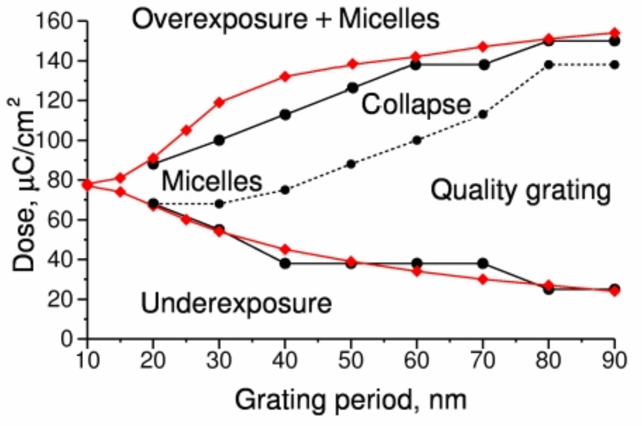

Figure 3.6 Process window of quality gratings and map of grating degradation regimes plotted for various grating periods and exposure doses. The experimental conditions are identical to those in Figure 3.5. Black circles and red diamonds indicate data points determined by experiment [213] and simulation [225], respectively. Solid lines indicate critical doses for under- and over-exposure and dashed lines indicate critical doses for resist degradation.

window for quality gratings can be seen in the central part of the plot. This window rapidly decreases as the grating pitch decreases. At low exposure doses, under-exposure is the limiting factor; whereas at high exposure doses, pattern collapse and micellization are the limiting factors. Generally, micellization is the dominant grating degradation factor for dense gratings; however, at very high exposure doses, over-exposure and micellization are observed simultaneously for all grating periods. Along with the experimentally determined data points, Figure 3.6 also contains computed data points [225]. The simulated data indicates the critical doses for under- and over-exposure. Examples of simulated grating cross-section morphologies as predicted by a recent version of the EBL Simulator [189] are provided in Figure 3.7. The panels represent under-exposed

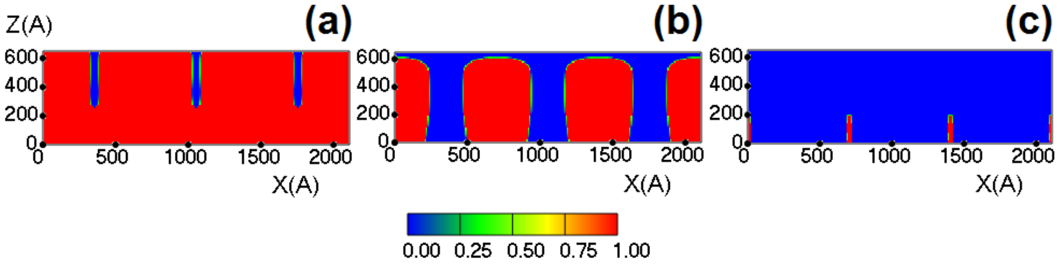

Figure 3.7 Simulated cross-sections representing (a) under-exposed, (b) well-exposed, and (c) over-exposed, 70 nm pitch gratings in PMMA resist on a Si substrate [218]. The resist and cleared areas are represented by red and blue, respectively.

(3.7(a)), well-exposed (3.7(b)), and over-exposed (3.7(c)) gratings, discussed previously in this section. The cross-section images representing pattern-collapse and micellization cannot yet be generated using the EBL Simulator.

In Figure 3.8(a), a cross-section SEM image of 70 nm pitch gratings developed for 20 seconds in MIBK:IPA 1:3 is shown. It can be seen that the pattern is not uniform across the exposed area. The gratings collapse in the centre of the array as compared to the outer parts of the array. Proximity effect results in a higher dose at the centre of the grating. This causes the grating lines to become narrower, less mechanically stable, and collapse due to capillary forces during the post-development drying stage. Structures at the edges of the pattern receive less proximity flux form neighboring regions and hence are in a different quality regime, even though the nominal dose is the same for each line. Furthermore, in Figure 3.8(b), critical dimension (CD) measurements for 70 nm pitch gratings developed for 5 seconds in MIBK:IPA 1:3 are compared to CD measurement for an isolated (single-) line and three 70 nm pitch (triple-) lines for

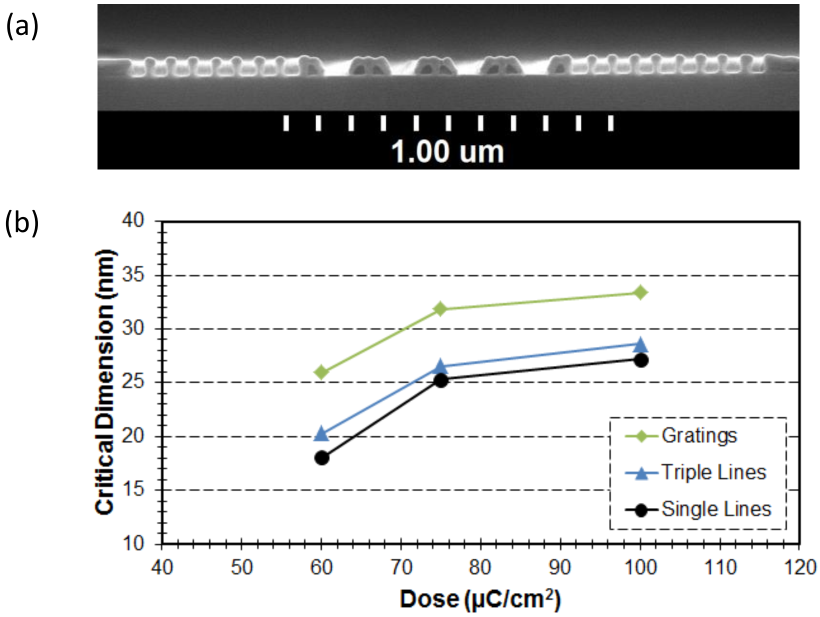

Figure 3.8 (a) Cross-section SEM image of 70 nm pitch gratings showing collapse in the centre [218]. Notice the symmetry of collapse. (b) CD measurements of 70 nm pitch gratings (diamonds) compared to isolated or single lines (circles) and three 70 nm pitch (triple-) lines (triangles). The samples have been developed in MIBK:IPA 1:3 for (a) 20 sec, and (b) 5 sec [218].

increasing exposure dose. For an identical dose, denser features will exhibit a larger CD than isolated or sparse features. This signifies the importance of acquiring measurements from the centre of the array. It is important to mention that all of the SEM images in Figure 3.5 have been taken from the centre of the grating array. This is to ensure accounting for the additional exposure contribution of proximity effect. In the upcoming sections, images for CD measurement are also taken from as close to the centre of the array as possible. Taking SEM images from the corner or edge of an array is strictly avoided unless for demonstration purposes.

3.2.2 Voltage

The role of exposure voltage in nanofabrication processes is significant. As detailed in Table 1 (Chapter 2), the exposure voltage impacts a large number of process metrics. The first impact studied here is sensitivity. Figure 3.9 presents contrast curves at 10 keV and 30 keV for PMMA and ZEP resists. The PMMA clearance dose at 30 keV (204 μC/cm^2) is a factor of 2.8 higher than at 10 keV (72 μC/cm^2). In other words, a 183% higher dose is required to clear PMMA at 30 keV as compared to at 10 keV. Similarly for ZEP, the clearance dose at 30 keV (66 μC/cm^2) is a factor of 2.9 lower than at 10 keV (23 μC/cm^2). This translates to a 187% higher dose requirement. These results are consistent with the understanding that the clearance dose increases roughly in proportion with increasing voltage and the trends observed are in agreement with literature [68,70,91]. Similarly, the sensitivity of PMMA is approximately 3.1 times lower than that of ZEP, which is also expected. Yet another observation from Figure 3.9 is that the contrast (γ) shows negligible change with voltage. This result is also expected as contrast is primarily influenced by the resist and development conditions (see Table 1).

The nearly proportional increase of exposure dose with voltage can also be observed using process windows. Figure 3.10 presents process windows for both PMMA and ZEP at 3 keV, 10 keV, and 30 keV [190] obtained by characterizing design (B) (see Figure 3.2). In both resists, the lower (clearance)

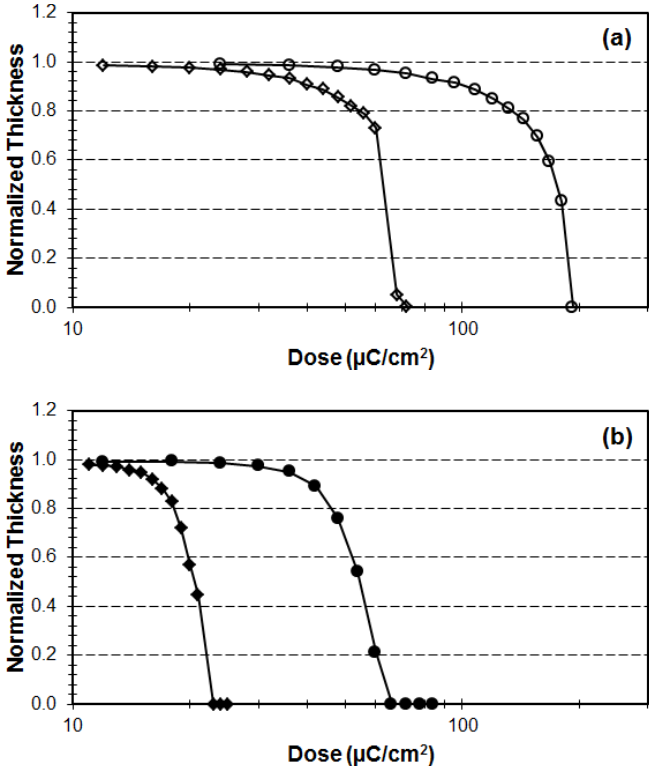

Figure 3.9 Contrast curves for (a) PMMA, and (b) ZEP exposed at 10 keV (diamonds) and 30 keV (circles) measured by optical profilometry. The PMMA sample was 276 nm thick and developed in MIBK:IPA 1:3 for 20 sec. The ZEP sample was 331 nm thick and developed in ZED-N50 for 20 sec. Both samples were rinsed in IPA for 20 sec [218].

and upper (collapse) boundaries of the process windows increase proportionally with voltage. As compared to the lower process window boundary (2.4x - 2.5x), the upper boundary exhibits a slightly larger (3.1x - 3.5x) proportional increase. This difference causes the process window to rapidly expand with increasing voltage. As the limiting factor at the upper process window boundary is pattern collapse, the process window increase is due to the 'delayed' collapse at higher voltages (explained ahead in this section). From Figure 3.10 we estimate that the process window of PMMA is 2.5x - 6.7x larger than that of ZEP. This implies that

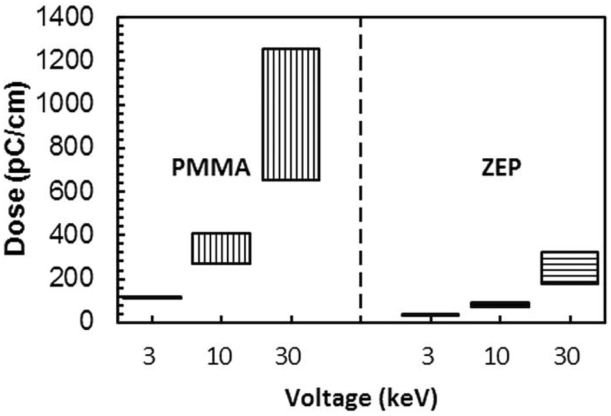

Figure 3.10 Process windows for 70 nm pitch gratings at 3, 10, 30 keV voltages for PMMA (bars) and ZEP (stripes). The PMMA samples were developed in MIBK:IPA 1:3 for 5 sec followed by a 20 sec rinse in IPA. The ZEP samples were developed in ZED-N50 for 30 sec followed by a 20 sec rinse in MIBK. All development and rinse processes were conducted at room temperature. Reprinted with permission from the Crown and reference [190]. Copyright Act (Canada), S. 12 and © 2011 American Vacuum Society.

the process for ZEP is less robust than that of PMMA. In addition to process robustness, a large process window enables more control over certain properties of the nanostructure, such as the aspect ratio (AR) [12,214]. By varying the dose within an applicable process window, the critical dimension (CD), and therefore the AR can be varied. This technique has shown that the AR may change by a factor of two within a process window [12,214].

The process windows in Figure 3.10 can also be used to estimate the sensitivity ratio. Comparing the clearance doses (lower process window boundary), a 3.7-4.1 times higher sensitivity is obtained for ZEP as compared to PMMA. Qualitatively, this sensitivity difference is in accordance with literature [70,139]. However, the scale of the sensitivity difference is higher than what has been observed using contrast curves in Figure 3.9. This can be explained by the differences in development time and the different rinse fluid used for ZEP. In the process window experiments, the rinse fluid was MIBK, as per the manufacturer specified standard procedure and the procedures in use by the scientific community at the time. Later, it was observed that MIBK actually develops ZEP, due to which IPA was used for any subsequent experiments. The impact of MIBK versus IPA rinse for ZEP has also recently been reported [168]. This shows that the sensitivity difference is also dependent on the development and rinse conditions (see next section 3.2.3).

The selection of exposure voltage heavily impacts the resist sidewall profile due to electron scattering and the resulting beam broadening [69,100]. Simulated sidewall profiles of 70 nm pitch gratings in PMMA resist at 3, 10, and 30 keV are presented in Figure 3.11. At low voltages, the strong forward scattering of electrons cause the gratings to have pronounced undercuts, such as in Figure 3.11(a). Such structures are more susceptible to pattern collapse, which leads to a narrower process window. However, the strongly undercut sidewall profiles created at low voltages may also be employed for creating 3D nanoscale profiles in the resist [92] and for efficient lift-off pattern transfer using a single resist layer [226]. At higher voltages, the sidewall profiles are almost vertical (see Figure 3.11(c)) due to decreased beam broadening, resulting in stable well-defined gratings over a large process window. In addition to decreased beam broadening, the decreased beam diameter [94] and increased penetration depth

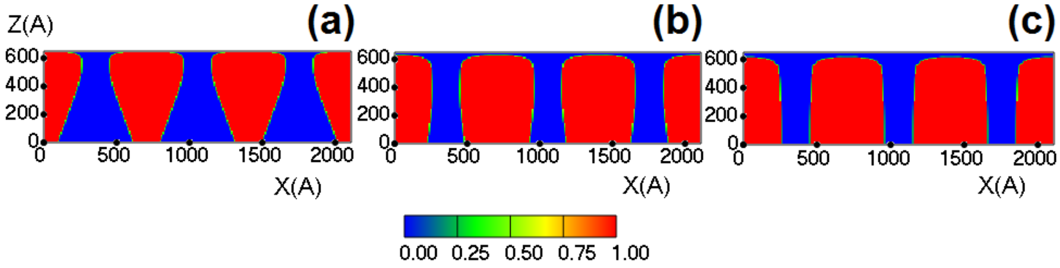

Figure 3.11 Simulated 70 nm pitch grating cross-sections generated at (a) 3 keV, (b) 10 keV, and (c) 30 keV. The resist and cleared areas are represented by red and blue, respectively [218]. Compare cross-section profiles to experimentally generated profiles in Figure 2.6.

[91,92] at higher voltages (see section 2.1.2 Exposure) are exploited to obtain a higher resolution and AR. However, at higher voltages, the increased electron penetration and lateral spread due to backscattering gives rise to significant proximity effect. Furthermore, the lower sensitivity at higher voltages, compounds this problem. The decreased sensitivity itself is also an unwanted effect as it reduces throughput resulting in increased nanofabrication costs.

3.2.3 Developer

In EBL processing, the developer is one of the most critical components. According to Table 1 (Chapter 2), the developer impacts the largest number of EBL process metrics. In this chapter, the role of developer is studied through EBL trends, and in further molecular-level detail in Chapter 4. Figure 3.12 presents contrast curves for PMMA and ZEP resists using two developers each. Comparing the sensitivity of PMMA developers, we observe that clearance using MIBK:IPA

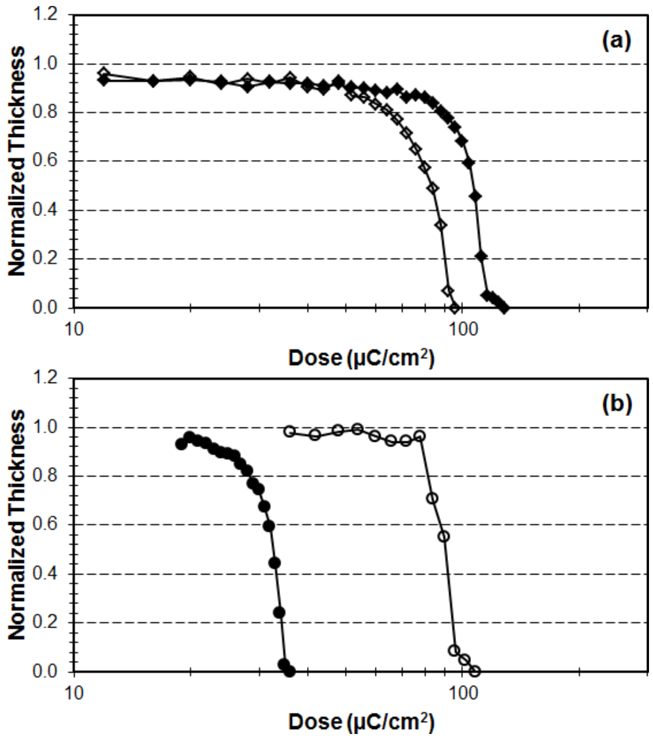

Figure 3.12 Contrast curves for (a) PMMA, and (b) ZEP exposed at 10 keV and developed for 5 sec in various developers and rinsed in IPA for 20 sec. The developers used for PMMA are MIBK:IPA 1:3 (filled diamonds) and IPA:water 7:3 (open diamonds). The developers used for ZEP are ZED-N50 (filled circles) and MIBK:IPA 1:3 (open circles). The samples were between 253-303 nm thick [218].

1:3 occurs at 128 μC/cm^2 whereas clearance using IPA:water 7:3 occurs at 96 μC/cm^2. This represents a 1.33 times (or 25%) improvement in sensitivity when using IPA:water 7:3 developer. These results are consistent with Yasin *et al.* [178] at 27% improvement; however, lower than the 40% improvement quoted by Olzierski and Raptis [127]. From Figure 3.12, the contrast values in both developers are very similar at 10 and 10.1 for MIBK:IPA 1:3 and IPA:water 7:3, respectively. Whereas Yasin *et al.* [178] have claimed a 19% higher contrast for IPA:water (6.4 vs. 5.4), Rooks *et al.* [128] have claimed a 12% lower contrast for

IPA:water (3.7 vs. 4.2), as compared to MIBK:IPA 1:3. Ozierski and Raptis [127] have also claimed that IPA:water 7:3 provides better contrast characteristics; however, they have not provided contrast values.

Comparing the sensitivity of ZEP developers in Figure 3.12, we observed that clearance using ZED-N50 occurs at 36 μC/cm^2 whereas clearance using MIBK:IPA 1:3 occurs at 108 μC/cm^2. This represents a 3 times (or 200%) decrease in sensitivity when using MIBK:IPA 1:3 developer. Despite the considerable sensitivity reduction, MIBK:IPA 1:3 exhibits a 14% improvement in contrast. The ZEP contrast values measured are 14.3 and 16.3 for ZED-N50 and MIBK:IPA 1:3 developers, respectively, and are clearly higher than the contrast values measured for PMMA. In addition, contrast curves for ZEP developed in IPA:water 7:3 were also generated (see Figure 3.27); however, they are not presented here as clearance was not achieved (20% thickness remaining) and the sensitivity is very low for the scale adopted in Figure 3.12. Moreover, using IPA:water 7:3, resist tone-inversion is observed at approx. 600 μC/cm^2. The IPA:water 7:3 contrast curves for ZEP will be presented and discussed further in section 3.3, while discussing the negative-tone behavior of ZEP.

The process windows for both PMMA and ZEP exposed at 10 keV and developed in ZED-N50, MIBK:IPA 1:3, and IPA:water 7:3 are presented in Figure 3.13. The usage of MIBK:IPA 1:3 and IPA:water 7:3 to develop ZEP, and the usage of ZED-N50 to develop PMMA, has not been reported in literature previously. All

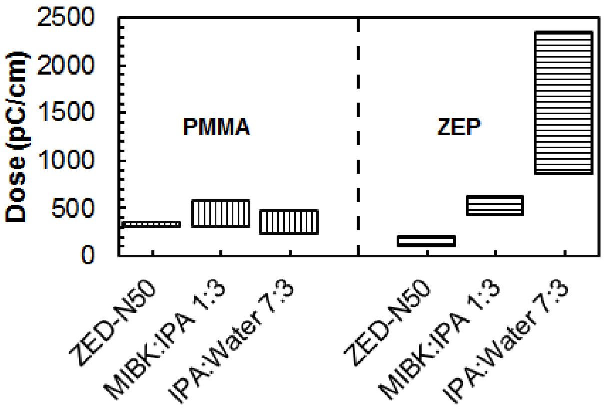

Figure 3.13 Process windows for PMMA (bars) and ZEP (stripes) 70 nm pitch gratings exposed at 10 keV and developed in various developers. All samples were developed for 5 sec at room temperature, except for PMMA in ZED-N50 (2 sec). No IPA rinse (20 sec) is required after development in IPA:water 7:3. Reprinted with permission from the Crown and reference [190]. Copyright Act (Canada), S. 12 and © 2011 American Vacuum Society.

of the process windows presented in this figure have been obtained for 5 sec room temperature development, except for PMMA in ZED-N50. ZED-N50 is a very strong developer for PMMA and no process window remains at 5 sec development, therefore this development was conducted for 2 sec only. From the process windows in Figure 3.13, a number of observations can be made regarding sensitivity and window sizes. Comparing the various developers employed here for PMMA, we observe that the standard MIBK:IPA 1:3 is the least sensitive developer. ZED-N50 is marginally (2.24%) more sensitive, whereas IPA:water 7:3 is significantly (22%) more sensitive than MIBK:IPA 1:3. The PMMA process window sizes for MIBK:IPA 1:3 and IPA:water 7:3 are roughly the same, whereas the process window size for ZED-N50 is 4.1-4.7 times smaller than either of the other two developers. The sensitivity observations regarding MIBK:IPA 1:3 and IPA:water 7:3 are in agreement with our previous contrast curve observations in Figure 3.12 and the observations by Yasin *et al.* [178].

Comparing the various developers employed here for ZEP, we observe that the standard ZED-N50 is the most sensitive developer. MIBK:IPA 1:3 is significantly (336% or 4.36 times) less sensitive than ZED-N50, whereas IPA:water 7:3 is the least sensitive among the group. The sensitivity of ZEP in IPA:water 7:3 is 763% (or 8.63 times) less than ZED-N50. Though ZED-N50's sensitivity is the highest, its corresponding process window is the smallest. The process windows of ZEP in MIBK:IPA 1:3, and in IPA:water 7:3, are roughly two and 14.2 times as large as ZED-N50, respectively.

Amongst the developers studied, an inverse dependence can be observed between sensitivity and process window for ZEP but not for PMMA. This strong dependence of ZEP's performance on developer formulation is unexpected and suggests a unique interaction between the resist and developer. Previously, it has been hypothesized that the higher sensitivity of ZEP may be due to the enhancement of main chain scission as a result of electron impact on side-groups [190,227]. This purely exposure-step-based explanation is challenged by the observation that the sensitivity significantly varies with developer formulation. The unique chemical composition of ZEP, which includes a chlorine and phenyl side-group (see Figure 2.1), may engage in complex physico-chemical interactions with the developers. Our results presented in Figure 3.13 strongly support the idea that the dissolution process plays an important role in ZEP's performance and molecular-level studies may be required for in-depth understanding of the resist-developer interaction mechanisms.

Our PMMA and ZEP dense grating fabrication results for the three developers studied above are presented in Figure 3.14. In the case of PMMA, the resolution varies significantly over a CD of 23-34 nm, whereas in the case of ZEP, the resolution remains roughly unchanged between 19-20 nm. The higher resolution observed in ZEP is consistent with the higher contrast measured in Figure 3.12(b). In both PMMA and ZEP, IPA:water 7:3 developer enables the highest resolution and least line edge roughness (LER). In general, the LER is better for weaker developers in ZEP; however, this observation does not apply to PMMA. In ZEP, the surface roughness has also been observed to be 2-3 times lower in the weaker developers. For example, the ZEP surface roughness has been measured at 3.1 nm in IPA:water 7:3 vs. 8.1 nm in ZED-N50 at room temperature conditions [180]. Such a correlation between LER and surface roughness has also been indicated previously [223]. In addition to the intuitive expectation that a stronger developer will cause a greater roughness due to aggregate extraction of resist molecules, it can be observed that the larger molecule (ZED-N50) is responsible for greater roughness (see tables by Zhao *et. al.* [228]). A correlation between ZEP surface roughness and van der Waals (vdW) volume of various alkyl-acetate developers of increasing molecular weight has

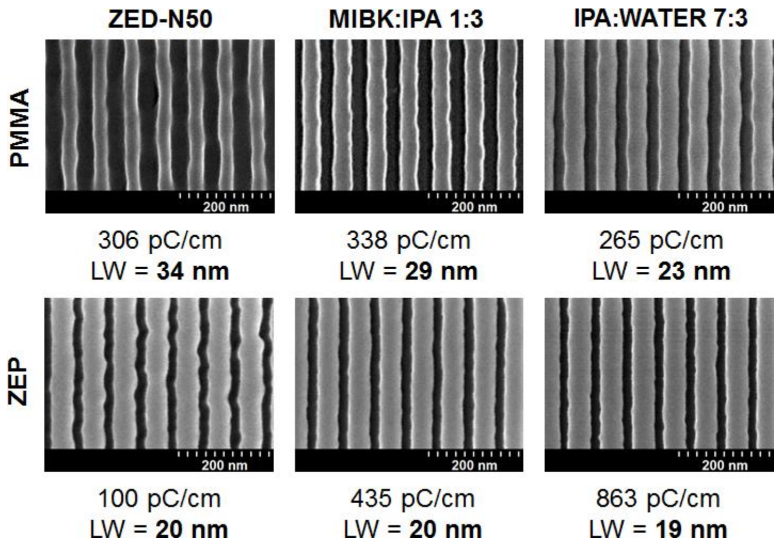

Figure 3.14 SEM images of 70 nm pitch PMMA and ZEP gratings exposed at 10 keV and developed in ZED-N50, MIBK:IPA 1:3, and IPA:water 7:3. The exposure doses and minimum line width (LW) are noted. The resists are 55-63 nm thick and fabricated patterns are coated with a 6 nm Cr layer. A version of this figure has been published elsewhere [219]. Reprinted with permission from the Crown and [219]. Copyright Act (Canada), S. 12 and © 2011 American Vacuum Society.

been demonstrated by Yamaguchi and Namatsu [106], supporting such a molecule-size based interpretation. However, due to the tremendous complexity of the ZEP development process [180,190], an interpretation based on vdW volumes alone would not be sufficient to explain the difference in ZEP resolution and roughness with different developers.

In the case of IPA:water 7:3 development of ZEP, clearance was not observed using contrast curve experiments (see also Figure 3.27). However, we observed clearance using process window (dense grating) experiments, which was confirmed by successful lift-off of an e-beam evaporated 12 nm thick chromium layer (not shown). This discrepancy may be explained by a number of conditions particular to process window experiments (versus contrast curve experiments) such as different exposure step-size (2 nm line-step vs. 20 nm area-step), pattern geometry (dense vs. sparse exposure), and proximity threshold (greater charge accumulation removes scum).

3.2.4 Development time

The next process parameter studied is the development time. Contrast curves for 5 sec and 20 sec development of PMMA in IPA:water 7:3 and ZEP in ZED-N50 developers are presented in Figure 3.15. In both resist-developer combinations, employing a larger development time increases the sensitivity and decreases the contrast. In PMMA, the sensitivity improves by 29.7% (from 94 μC/cm^2 to 66 μC/cm^2) at the expense of a 32.7% decrease (from 10.1 to 6.8) in contrast. Similarly, in ZEP, increasing the development time from 5 sec to 20 sec improves the sensitivity by 25% (from 36 μC/cm^2 to 27 μC/cm^2) at the expense of a 10.8% decrease (from 15.7 to 14.0) in contrast. In addition, increasing the development time causes a mild thickness loss due to the un-exposed or partly exposed resist dissolving. This thickness loss is visible in Figure 3.15(a) and has also been observed by us in contrast curves for other resist-developer combinations (not shown). In general, conducting longer development, though better for sensitivity, causes resolution and AR loss due to lower contrast and resist thinning.

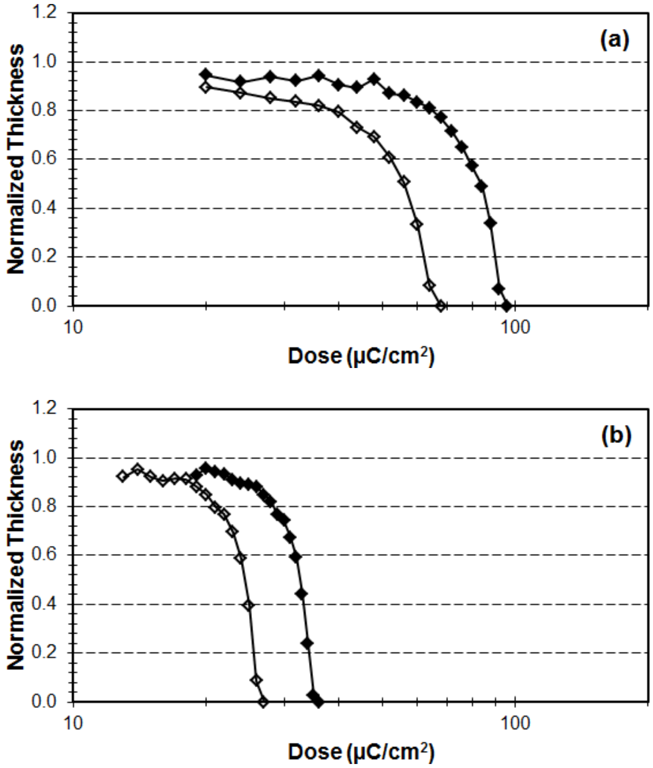

Figure 3.15 PMMA (a) and ZEP (b) contrast curves exposed at 10 keV and developed for 5 sec (filled symbols) and 20 sec (open symbols) in (a) IPA:water 7:3, and in (b) ZED-N50. The samples were between 253-294 nm thick [218].

Being a kinetic process, the dissolution of exposed positive-tone polymeric resists for longer times causes an increase in the gap-width [85]. For this reason, minimizing the development time is generally desired in both PMMA and ZEP to obtain as high a resolution as possible. Furthermore, depending on other factors such as pattern density, exposure voltage, dose, and developer strength, long development can cause resist pattern collapse. In Figure 3.16, cross-section SEM morphologies are presented for 70 nm pitch PMMA gratings exposed at 10 keV and developed for 5 sec and 20 sec in MIBK:IPA 1:3. As it has been discussed previously in section 2.1.3, the exposure dose and development

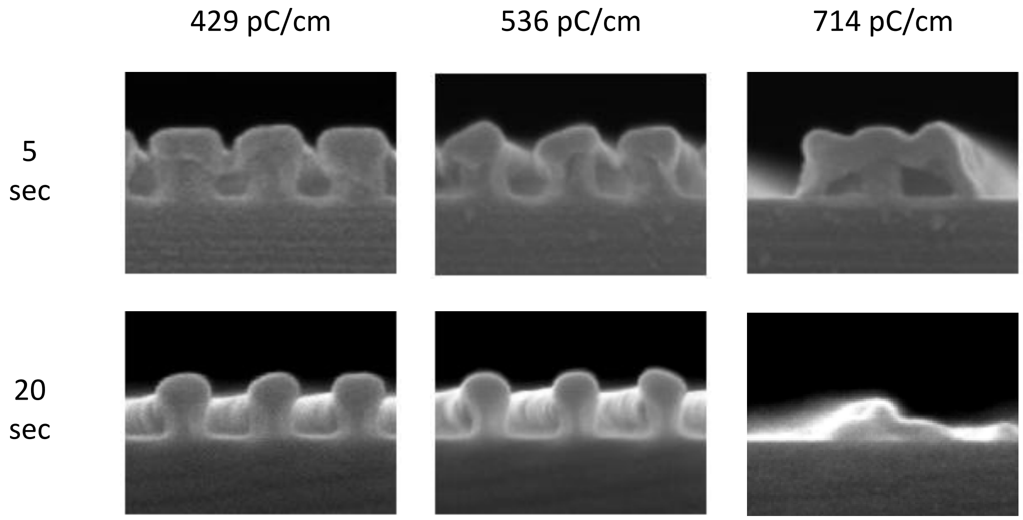

Figure 3.16 Cross-section SEM morphologies for 70 nm pitch PMMA gratings exposed at 10 keV for increasing exposure dose and development time. The width of each panel is 200 nm [218].

time show complementary behavior. In addition to showing the effect of increasing the exposure dose, the effect of increasing the development time is also shown in Figure 3.16. From Figure 3.16, it can be seen that the grating gap-

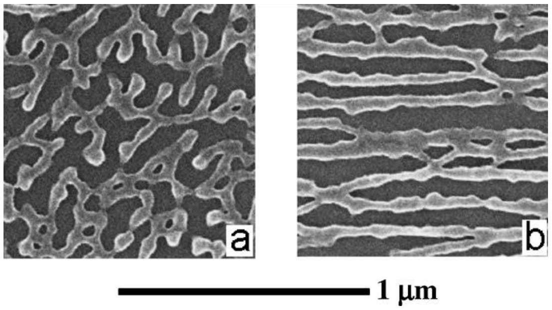

Figure 3.17 SEM morphologies of micellized (a) 30 nm, and (b) 40 nm pitch PMMA gratings developed for 40 sec in MIBK:IPA 1:3 at room temperature. The other exposure and development conditions are the same as in Figure 3.5(m) and 3.5(n). Reprinted with permission from [213]. Copyright © 2007 American Vacuum Society.

widths increase due to increasing both the exposure dose and development time. At high exposure doses, pattern collapse occurs; however this resist degradation behavior is worsened further due to increasing the development time. For example, at longer development times, pattern collapse occurs at a lower exposure dose (shown ahead in this section), reducing the fidelity of the process.

Furthermore, as described in section 3.2.1, micellization occurs in denser gratings allegedly due to phase separation between the insoluble resist fraction and the EBL developer. This polymer phase separation increases with increasing development time [221,222]. Figure 3.17 presents micellized 30 nm and 40 nm pitch PMMA grating morphologies developed in MIBK:IPA 1:3 for 40 sec at room temperature. The exposure conditions employed to generate Figure 3.17(a) and 3.17(b) are identical to those in Figure 3.5(m) and 3.5(n), respectively; however, the latter have been developed for 5 sec only. Comparing the micrographs from 5 sec and 40 sec development, the increased micellization behavior can clearly be observed when the development time increases.

Because of the described reasons, increasing the development time has a detrimental effect on the process window. Figure 3.18 presents process windows for 70 nm pitch gratings in ZEP resist exposed at 10 keV and developed at room temperature in ZED-N50 and in MIBK:IPA 1:3. Increasing the development time reduces the magnitude of the process window and also lowers both the upper

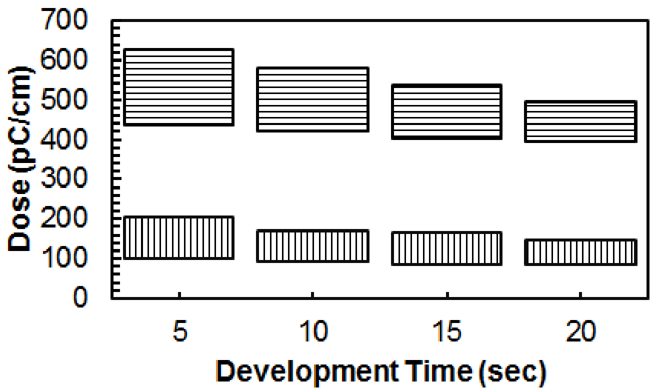

Figure 3.18 Process windows for 70 nm pitch ZEP gratings exposed at 10 keV and developed in ZED-N50 (bars) and in MIBK:IPA 1:3 (stripes). Both development and 20 sec IPA rinse have been conducted at room temperature [218].

and lower window boundaries. By increasing the development time from 5 sec to 20 sec, we observed that the process window shrinks by 39% and 47% in ZED-N50 and MIBK:IPA 1:3, respectively. The lower and upper process window boundaries shrink 17% and 28%, respectively, using ZED-N50 and 10% and 21% using MIBK:IPA 1:3. In both cases, we observe that the upper boundary shrinks almost twice as fast as the lower boundary over the selected time interval. This indicates that the primary cause of process window shrinkage, with increasing development time, is the early onset of pattern collapse. At the upper process window boundary, the higher exposure dose applied leads to smaller average fragment sizes which have higher diffusivities. Increasing the development time simply increases the dissolution of the partly-exposed gel layer resulting in rapid pattern degradation.

In Figure 3.18, it can be seen that the less sensitive developer, MIBK:IPA 1:3, has a consistently larger process window over the development times studied. In this way, the influence of the developer over the process window vs. time trend is also explored. The effect of other process parameters, on the process window vs. time plots, have also been explored such as voltage (not shown, see author refs. [12,100,214]) and developer temperature (see Figure 3.19 and author refs. [12,100,214,215]). In Figure 3.19, process windows for 70 nm pitch gratings in PMMA resist exposed at 10 keV, and developed at room temperature and -15 °C in MIBK:IPA 1:3 are presented. In both cases, the 20 sec IPA rinse is also conducted at the same temperature.

From Figure 3.19, a number of observations can be made. By decreasing the development temperature, the process window dramatically increases by 4.5-5.0 times (explored further in section 3.2.5). In addition, the magnitude of process window shrinkage drops significantly. We observe that by increasing the development time from 5 sec to 20 sec, the process window shrinkage is 23% at room temperature. In comparison, the shrinkage is only 10% at -15 °C development temperature. The upper boundary shrinkage (12%) at -15 °C is also nearly half the shrinkage (25%) observed at room temperature. At colder development temperatures, the development rate is reduced and therefore the effect of development time is suppressed. This is due to the fact that the colder developer has the effect of "freezing-out" [132] the resist fragments in the gel layer, reducing the diffusivity.

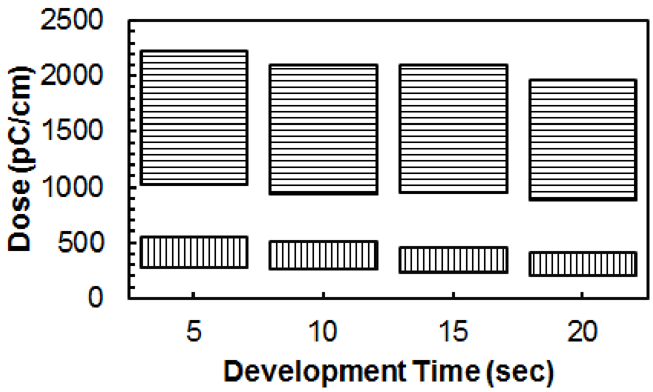

Figure 3.19 Process windows for 70 nm pitch gratings in PMMA resist developed in MIBK:IPA 1:3 at room temperature (bars) and at -15 °C (stripes) at various times. The exposure voltage is 10 keV and the development and rinse (20 sec IPA) both have been conducted at the same temperature [218].

The observation that the effect of development time is suppressed due to using lower development temperatures can also be seen in contrast curves. A unique example is shown in Figure 3.20 where no sensitivity decrease occurs when development time of PMMA changes from 5 sec to 20 sec using -15 °C IPA:water 7:3 developer. In comparison, the sensitivity changes by over 29.2% when room temperature development is employed. In addition, no significant thickness reduction occurs when cold development is used, indicating that improved AR can be obtained.

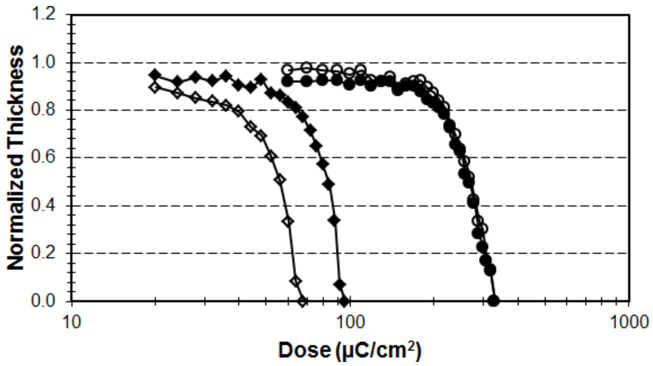

Figure 3.20 PMMA contrast curves exposed at 10 keV and developed for 5 sec (filled symbols) and 20 sec (open symbols) in IPA:water 7:3 at room temperature (diamonds) and -15 °C (circles). The resist thickness was 290-295 nm [218].

thickness reduction occurs when cold development is used, indicating that improved AR can be obtained.

3.2.5 Development temperature

The effect of lowering the development temperature on both PMMA and ZEP resists is illustrated by Figure 3.21. In both cases the contrast improves at the cost of decreased sensitivity. In PMMA, reducing the developer temperature from 22°C to -15 °C increases the contrast by 17% whereas the sensitivity decreases by 159% (or 2.6 times) from 117 μC/cm^2 to 302 μC/cm^2. Similarly, in ZEP over the same temperature range, the contrast increases by 13% at the cost of a 136% (or 2.4 times) sensitivity decrease from 35.1 μC/cm^2 to 82.7 μC/cm^2. In addition to improvement in contrast, there is less resist thickness loss observed when employing cold development (see Figure 3.21(a)). In addition, we have

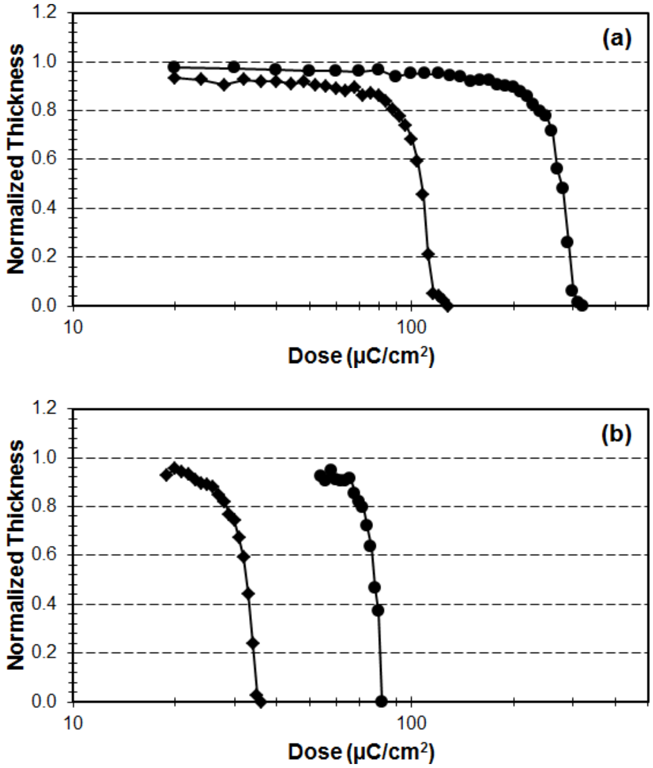

Figure 3.21 PMMA (a) and ZEP (b) contrast curves exposed at 10 keV and developed for 5 sec at 22 °C (diamonds) and at -15 °C (circles). The developers were (a) MIBK:IPA 1:3, (b) ZED-N50. The samples were 253-305 nm thick [218].

observed that when comparing MIBK:IPA 1:3 to IPA:Water 7:3 developers for PMMA at -15 °C, the clearance doses are nearly the same (not shown). Therefore, it may be noted that for very short development times and cold development temperatures, the effect of developer is suppressed. This is in addition to the already observed suppression of the effect of the development time by using cold development.

From a dense grating nanolithography perspective, the increase in contrast is manifested as improvements in resolution. Figure 3.22 presents top-

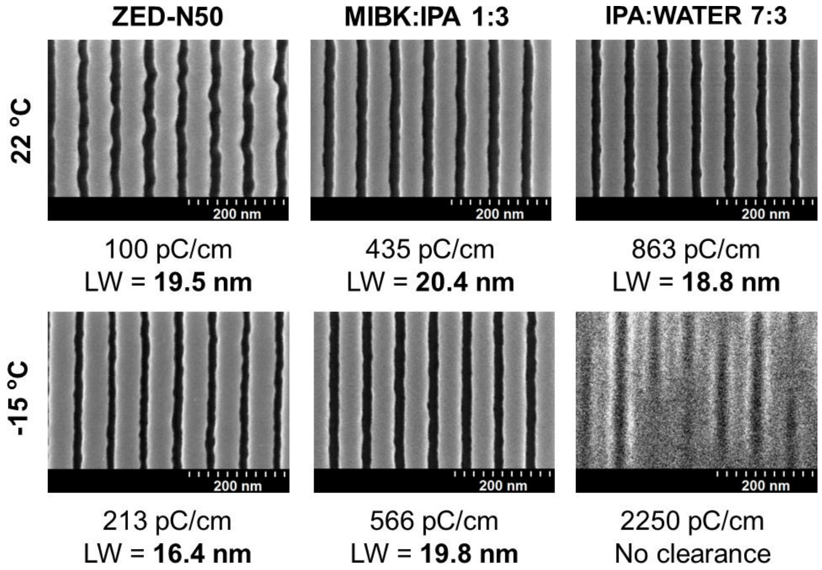

Figure 3.22 SEM images of 70 nm pitch ZEP gratings exposed at 10 keV and developed for 5 sec using various developers and development temperatures. The exposure doses and minimum line width (LW) are also noted. The resists were 55-63 nm thick and the gratings were coated with 6 nm Cr. A version of this figure has been published in [180]. Reprinted with permission from the Crown and [180]. Copyright Act (Canada), S. 12 and © 2012 The Japan Society of Applied Physics.

view SEM micrographs of 70 nm pitch ZEP gratings exposed at 10 keV and developed for 5 sec at both 22°C and -15 °C in ZED-N50, MIBK:IPA 1:3, and IPA:water 7:3 developers. The improvements in resolution with decreasing temperature are observed irrespective of the developer employed. The greatest resolution improvement (16%) has been observed in ZED-N50 developer where the line width (LW) is reduced from 19.5 nm (at 22°C) to 16.4 nm (-15 °C). This resolution improvement has been obtained at the cost of a 2.1 times lower sensitivity; however, the exposure dose required to achieve such high resolution gratings is still much less than any other condition in Figure 3.22. The resolution improvement is negligible in the case of MIBK:IPA 1:3 developer, and in the case of IPA:water 7:3 developer, clearance could not be obtained using -15 °C development (see also Figure 3.27). In order to obtain clearance with IPA:water 7:3 at cold developer temperatures, a significantly longer development time is required. For example, employing 120 sec development time for 10 °C IPA:water 7:3, clearance was obtained at 600 pC/cm, enabling 15 nm features in 60 nm thick ZEP (not shown). In addition to improving the resolution, the LER is visibly improved when using cold development.

Employing cold development also improves the pattern density. Using -15 °C development for 5 sec, 40 nm pitch ZEP gratings were fabricated in 60 nm thick ZEP resist. Figure 3.23 shows 40 nm pitch gratings with a critical dimension (CD) of 13.4 nm, representing an aspect ratio (AR) of 4.5. This is the best CD obtained in the polymeric resist work pursued here and it matches the previously reported value of 13 nm outermost zone plate fabrication using ZEP 7000 [33]. In fact, the experiments in ref. [33] employed a higher voltage (25 keV), colder development (-50 °C), and nitride membrane substrate, all of which act to significantly help to improve the resolution. In addition, the AR reported here also matches the best AR reported to date for up to 20 keV exposures [21].

The effect of cold development has been studied over various development temperatures and development times. We have consistently observed that decreasing the development temperatures and times yield the

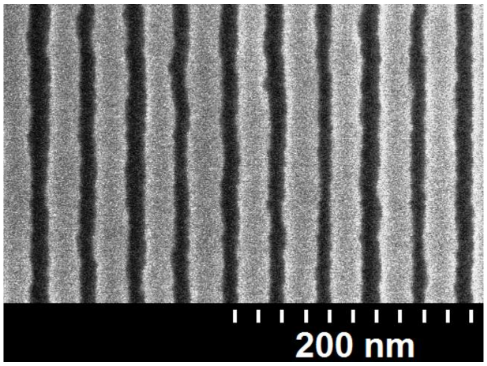

Figure 3.23 SEM image of 40 nm pitch ZEP gratings. The CD is 13.4 nm. The pattern was exposed at 10 keV, 180 pC/cm and developed for 5 sec at -15 °C in ZED-N50. Reprinted with permission from the Crown and [180]. Copyright Act (Canada), S. 12 and © 2012 The Japan Society of Applied Physics.

largest process windows at the cost of increasing clearance dose. The increased process window is due to the suppression of resist degradation mentioned earlier. The increase in sensitivity is due to the fact that in order to promote development at lower temperatures, mobile (and therefore smaller) fragments are required, and producing smaller average fragments requires higher exposure doses.

Figure 3.24 presents 70 nm pitch PMMA grating process windows as a function of temperature for 22 °C, -5 °C, -10 °C, and -15 °C at 5 sec and 20 sec development times. The windows here are shown as the regions between the pairs of similar symbols. The temperature dependence of the process window can be described by a simple kinetic model of resist dissolution accounting for the dose dependence of resist fragmentation. In refs. [100,214], it was shown that the diffusivity D of small PMMA fragments can be described as,

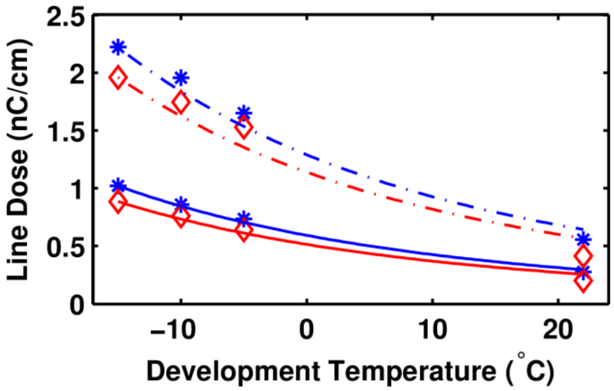

Figure 3.24 Comparison of experimental and theoretical temperature dependence of process window for 70 nm pitch PMMA gratings exposed at 10 keV. The upper and lower boundaries are shown by dashed and solid lines respectively. The development times used are 5 sec (stars) and 20 sec (diamonds). Reproduced with permission from [214]. Copyright © 2010 American Vacuum Society.

$$D = cd^{\alpha} \exp\left(\frac{-E_a}{kT}\right) \qquad (9)$$

where d is the exposure dose, α is a fragment size dependent exponent, and c is a constant of proportionality. Employing equation (9), colleague Taras Fito derived a function describing the lower ($d_{\min}$) and upper ($d_{\max}$) process window boundary doses, by assuming an equivalent D value independent of location, for a given development time [214].

$$d_{\min,\max} = d_{\min,\max}^{ref} \exp\left(-\frac{E_a}{\alpha k}\left(\frac{1}{T} - \frac{1}{T^{ref}}\right)\right) \qquad (10)$$

In equation (10), the 'ref' subscript indicates the reference (seed) value used for generating a process window. Figure 3.24 compares our experimental process windows with theoretical curves that we generated by equation (10), for two development times, showing a close fit. In Figure 3.24, the seed values were the data for the -15 °C condition. The above approach (and data) has been employed for parameterizing the EBL simulator. In addition, most of the contrast curves presented in this chapter were also used for parameterizing the EBL simulator [189].

3.2.6 Other factors

Process windows are influenced by a wide variety of process parameters and techniques. In this section, the influence of advanced process techniques, such as supercritical (SC) drying and ultrasonic development, on process windows is evaluated. SC drying is a well-known post-processing step designed to prevent pattern collapse in dense high aspect ratio nanostructures. In section 2.1.4, the mechanism and application of SC drying has been discussed. Figure 3.25 compares the differences in 70 nm pitch ZEP grating process windows as a result of regular and SC drying. It has been established that pattern collapse occurs beyond the upper boundary of the process window. The reader may observe that the region between dose factors 2.5-3.0 are not affected by pattern collapse in the SC dried sample (Figure 3.25(c & d)) as compared to the regular dried sample (Figure 3.25(a & b)). In quantitative terms, using SC drying, a nearly three times larger process window of 24 pC/cm (64-88 pC/cm) is observed as compared to a process window of 9 pC/cm (64-73 pC/cm) using regular drying.

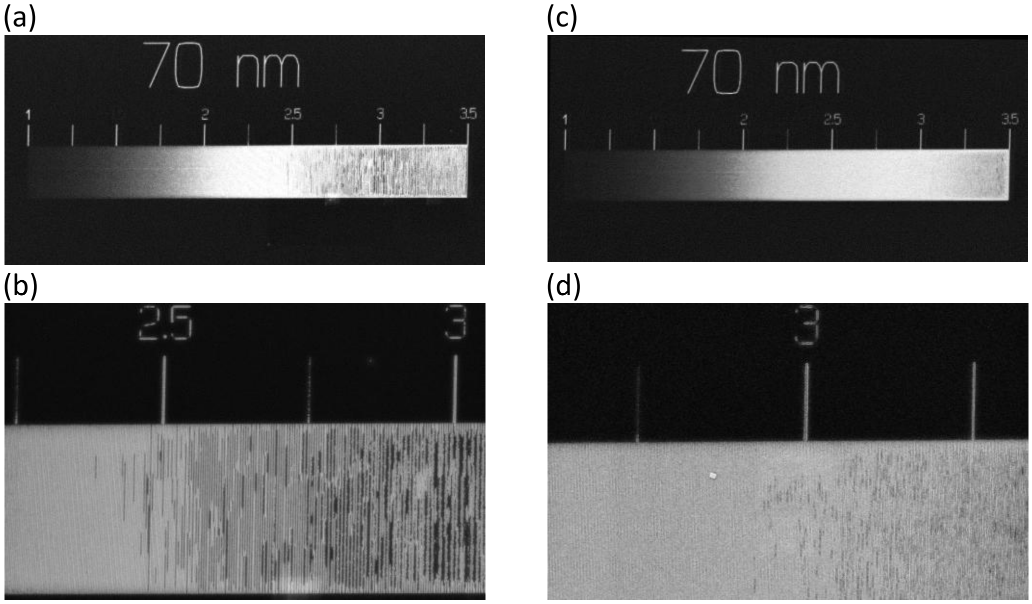

Figure 3.25 SEM images of patterned design (B) in ZEP exposed at 10 keV and developed for 30 sec in ZED-N50 and rinsed for 20 sec in MIBK. The images compare process windows as a result of (a & b) regular drying, and (c & d) supercritical drying. The width of the field is 90 µm in panels (a & c) and the distance between any two vertical line markers is 3 µm in panels (b & d) [218].

By employing supercritical drying, the upper boundary of the process window is raised, yielding a wider process window, although the same morphological regimes exist. This implies that pattern collapse is only deferred due to SC drying and not totally eliminated. In addition, no differences in grating quality (resolution, LER) are observed as a result of SC drying. Furthermore, the application of SC drying enables fabrication of denser 60 nm pitch gratings under the same exposure and development conditions (not shown) whereas this is not possible as a result of regular drying.

It is important to note that, under manufacturer specified conditions (see Table 3), SC drying does not work with PMMA . This is due to incompatibility of the transfer fluid. In SC drying, IPA is used as the transfer fluid; however, IPA happens to be a slow (weak) developer for PMMA [129]. During the ramp stage in SC drying, the extended period dip in IPA at high temperatures and pressures causes severe over-development and removal of any exposed PMMA (not shown). However, as shown in Figure 3.25, ZEP can withstand an extended period dip in IPA and is therefore compatible with SC processing.

Ultrasonic development is a well-known technique used to improve mass transport during the development stage. In section 2.1.3, the mechanism and application of ultrasonic development has been discussed. Figure 3.26 compares the differences in 70 nm pitch ZEP grating process windows as a result of regular and ultrasonic development. As ultrasonic development increases the development rate (see section 2.1.3), it was expected that the lower boundary (clearance) would shift down to lower doses, increasing the process window. However, observing the SEM images, it is not possible to discern any difference in process window size. Another observation from Figure 3.26 is the rapid cleaning-up of collapsed gratings. This indicates that the dissolution has indeed been promoted; however, perhaps not significantly enough to cause any difference in the process window. Further work is required to study the impact of sonically assisted development on process windows using greater power or

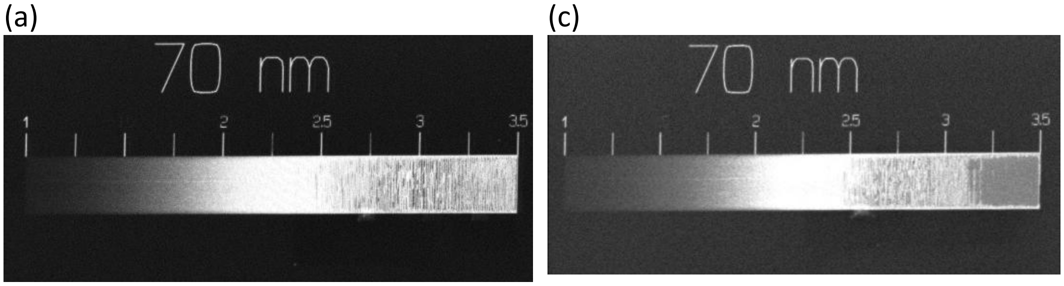

Figure 3.26 SEM images of patterned design (B) in ZEP exposed at 10 keV and developed for 30 sec in ZED-N50 and rinsed for 20 sec in MIBK. The images compare process windows as a result of (a) regular development, and (b) ultrasonic development. The width of the exposed field is 90 µm [218].

frequency. There is also need for further work studying the impact of other process parameters not considered in this chapter. For example, it is expected that the process windows would be influenced by substrate, resist thickness, resist top-coats, etc.

3.3 Negative-tone ZEP

In some polymeric resists, both chain-scission (positive-tone) and cross-linking (negative-tone) mechanisms may take place simultaneously. Depending on the exposure and development conditions, one of these mechanisms may be dominant or both may contribute equally. When cross-linking dominates, negative-tone behavior is observed. Such positive-to-negative 'tone inversion' has been observed in a number of positive-tone polymeric resists such as inPMMA [229,230] and in PMGI [231].

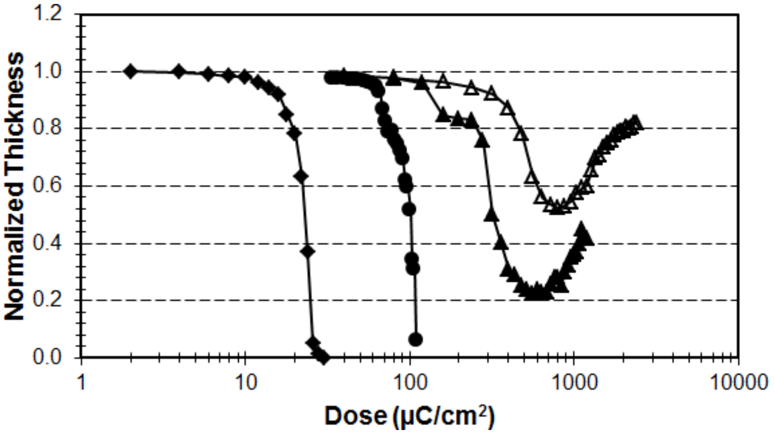

Figure 3.27 Contrast curves for ZEP exposed at 10 keV and developed for 20 sec in ZED-N50 (diamonds), MIBK:IPA 1:3 (circles), and IPA:water 7:3 (triangles). Closed symbols indicate 22 °C development whereas open symbols indicate -15 °C development. The resist thickness was between 145-160 nm and the samples were scanned using atomic force microscopy.

While performing development in IPA:water 7:3, tone inversion was also noticed in ZEP. Figure 3.27 presents contrast curves for ZEP exposed at 10 keV and developed for 20 sec in IPA:water 7:3, in addition to contrast curves for two other developers explored previously. It was observed that clearance does not occur using IPA:water 7:3 and resist tone inversion begins at approximately 600 µC/cm^2, leaving 20% un-cleared resist thickness. Furthermore, the negative-tone ZEP thickness does not approach the original resist thickness at room temperature conditions. When performing IPA:water 7:3 development at -15 °C, the resist tone inversion onset dose is shifted to 800 µC/cm^2 and over 50% un-cleared resist thickness remains. In addition, the negative-tone thickness approaches the original unexposed resist thickness to within 20%. The dose required for achieving this negative-tone condition at cold development

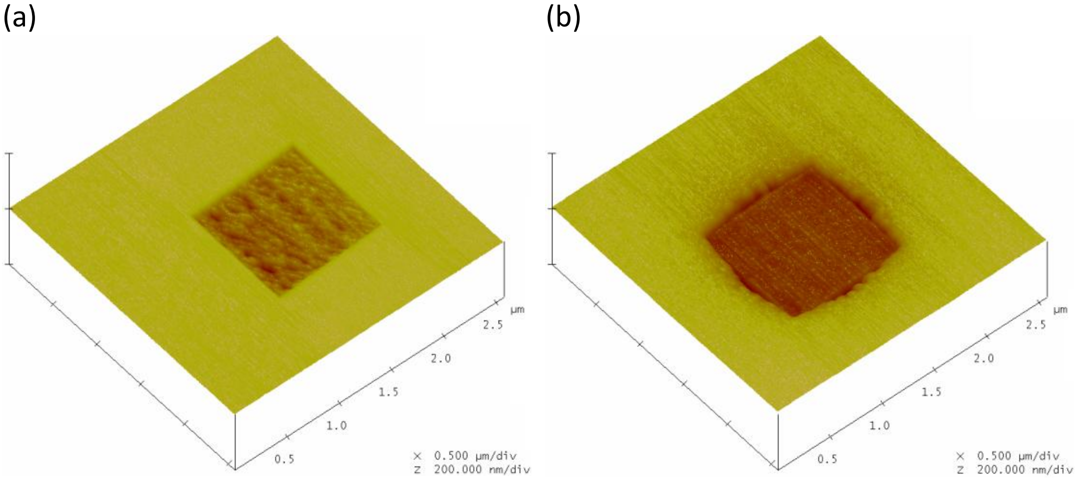

Figure 3.28 Atomic force micrographs of ZEP surface at 20-25 nm trench depth taken at conditions corresponding to (a) positive-tone, and (b) negative-tone regimes. Both samples were exposed at 10 keV and developed at -15 °C in IPA:water 7:3 for 20 sec [218].

temperature is in excess of 2000 µC/cm^2 (see Figure 3.27). However, this is still significantly lower than the negative-tone onset doses of 5800 µC/cm^2 [229] and 7891 µC/cm^2 [230] reported for PMMA and >17800 µC/cm^2 [231] reported for PMGI. Comparing the surface roughness of the positive- and negative-tone behavior (see Figure 3.28), we observe that the surface roughness of the negative-tone ZEP (0.9 nm) is nearly 3 times less than the surface roughness of the positive-tone behavior (2.6 nm) at equivalent depths.

The positive-to-negative tone inversion of ZEP was also recently observed by Oyama *et al.* [62]. They hypothesized that the ZEP tone inversion is due to abstraction of chlorine decreasing the cross-linking threshold. Generally, the tone inversion mechanism of polymeric resists has been a subject of debate within the community with focus on two alternative mechanisms namely cross-

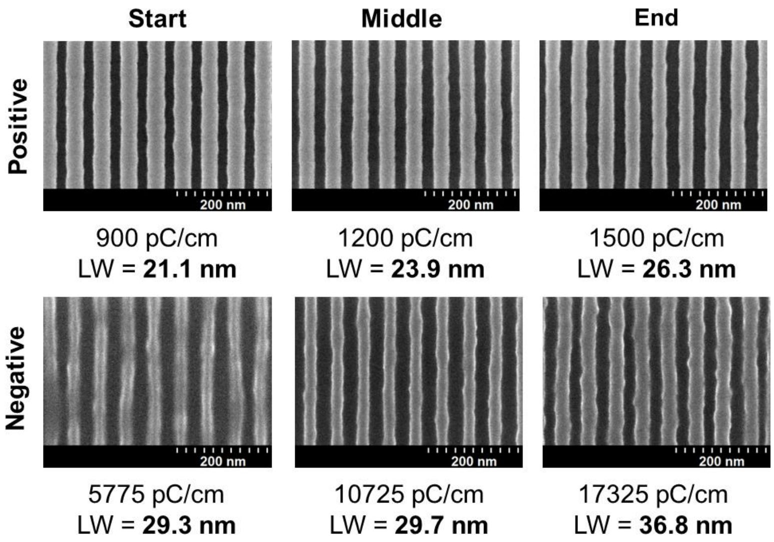

Figure 3.29 SEM images of 60 nm pitch ZEP gratings exposed at 10 keV and developed for 20 sec in IPA:water 7:3 at 22 °C. The SEM images are taken at the 'start', 'middle', and 'end' of the process window for both positive-tone and negative-tone behavior. The exposure doses and CD for each combination are noted. A version of this figure has been published in [180]. Reprinted with permission from the Crown and [180]. Copyright Act (Canada), S. 12 and © 2012 The Japan Society of Applied Physics.

linking, and carbonization. However, the recent results by Oyama *et al.* [62,88], suggest that the tone inversion witnessed in ZEP is indeed due to cross-linking behavior.

Further to observing the ZEP tone inversion, the fabrication of negative-tone dense gratings was also investigated. Figure 3.29 presents a representative set of 60 nm pitch positive- and negative-tone gratings exposed at 10 keV and developed for 20 sec in IPA:water 7:3 at room temperature. The critical dimension (CD) variation can be observed as the dose is increased from the start to the end of the process window. In the positive-tone behavior, the CD increases from 21.1 to 26.3 nm in a process window of 900-1500 pC/cm, whereas in the negative-tone behavior, the CD increases from 29.3-36.8 nm in a process window of 5775-17325 pC/cm. The negative-tone process window is significantly larger (d_{max}/d_{min} = 3.0) as compared to the positive-tone process window (d_{max}/d_{min} = 1.67). A common observation to both positive- and negative-tone behaviors is that the various grating metrics such as LER and CD uniformity (CDU) improve in the middle of the process window. Furthermore, the difference between positive- and negative-tone doses for ZEP (~6×) [180] is significantly less as compared to PMMA (>40×) [229,230] and comparable to PMGI (3-14×) [231]. The impact of the 'closeness' of exposure doses of both tones in ZEP is that both behaviors may be witnessed simultaneously, and this 'closeness' may be employed to perform density multiplication [54] of periodic patterns in ZEP at more favorable experimental conditions.

Figure 3.30 presents a detailed dependence of CD on exposure dose for 50, 60, and 70 nm pitch positive- and negative-tone gratings exposed at 10 keV and developed for 20 sec in IPA:water 7:3 at room temperature. It was observed that the CD is lower for denser gratings at identical exposure doses. Moreover this CD dependence on geometry (grating pitch) is stronger for negative-tone patterns. As compared to 70 nm pitch gratings, the 60 nm pitch grating CD is (on average) 1 nm smaller for positive-tone behavior and 2–3 nm smaller for negative-tone behavior. Perhaps the larger accessible area in wider grating

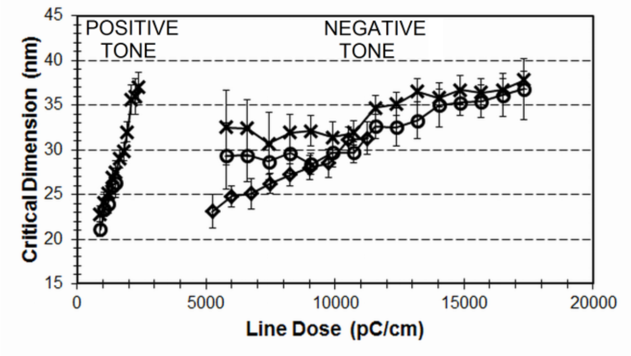

Figure 3.30 Variation in CD with increasing exposure dose for 50 nm (diamonds), 60 nm (circles), and 70 nm (crosses) pitch ZEP gratings at both positive-tone and negative-tone behavior. The exposure was conducted at 10 keV and the development at 22 °C in IPA:water 7:3 for 20 sec. Reprinted with permission from the Crown and [180]. Copyright Act (Canada), S. 12 and © 2012 The Japan Society of Applied Physics.

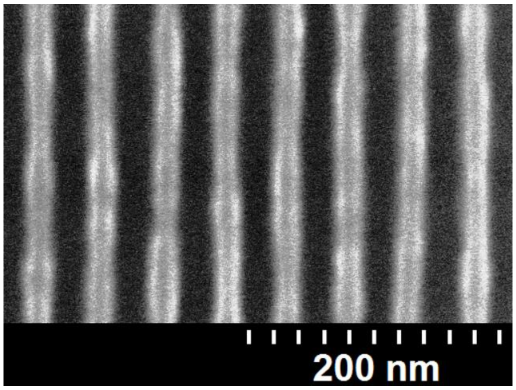

Figure 3.31 SEM image of 50 nm pitch negative-tone ZEP gratings. The CD is 23.1 nm. The pattern was exposed at 10 keV, 5250 pC/cm and developed for 20 sec at 22 °C in IPA:water 7:3. Reprinted with permission from the Crown and [180]. Copyright Act (Canada), S. 12 and © 2012 The Japan Society of Applied Physics.

periods allows for rapid diffusion, which may help explain the variation in CD. For the 50 nm pitch gratings, the positive-tone trend is not available at all, whereas a detailed negative-tone trend is available. As noticed in the contrast curves, the negative-tone gratings are expected to be 20% thinner, and hence have a less challenging aspect ratio (AR). This explains the availability of negative-tone dense 50 nm pitch gratings at room temperature conditions. The highest resolution negative-tone ZEP pattern has also been observed in 50 nm pitch gratings. In Figure 3.31, 23.1 nm lines were fabricated at an exposure dose of 5250 pC/cm using 20 sec development in IPA:water 7:3.

3.4 Summary

In this chapter, a comprehensive experimental study of the impact of a wide range of EBL processing parameters on various process metrics is presented for both PMMA and ZEP resists. Using process windows, contrast curves, and dense gratings, EBL processing strategies are investigated. Furthermore, through dense gratings fabrication, nanostructure morphologies, and high resolution processing limits of EBL in PMMA and ZEP are explored.

This work represents the most comprehensive examination of the influence of process parameters on process windows. The use of process windows for comparing process metrics and extraction of simulation model parameters is also demonstrated. In addition, this is the first report and detailed study of negative-tone ZEP gratings.

CHAPTER 4

SIMULATION OF PMMA FRAGMENT DISSOLUTION

4.1 Introduction

The exposure of PMMA during electron beam lithography (EBL) produces small polymer fragments that dissolve at varying rates during the development process. The chain length of the fragments that are dissolved and the dissolution behavior of these fragments varies greatly depending on the nature of the selected developer. The selection of the developer, in turn, influences the selection of EBL exposure parameters, such as the exposure dose. Understanding such relationships requires a molecular scale examination of the development process, as established in section 2.1.3. Furthermore, such an understanding is essential for rationally optimizing the EBL process as wet development is the most limiting step in nanolithography.

Previously, in sections 2.1.3 and 2.5.2, the Flory-Huggins (F-H) theory [114,115] was described as an appropriate molecular scale framework to investigate the miscibility of short-chain PMMA fragments in developers. In turn, molecular dynamics (MD) simulation allows for parameterizing the F-H equations

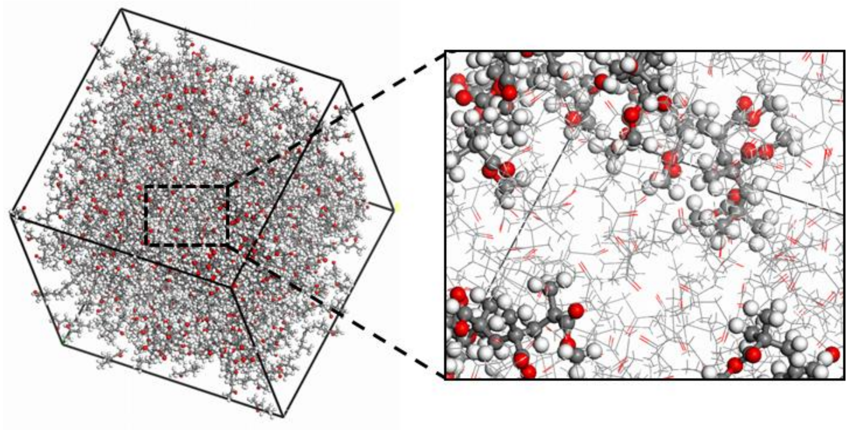

Figure 4.1. Visualization of a MD simulation box containing PMMA(10) chains in MIBK developer.

(section 2.5.2), thereby enabling the computation of the F-H interaction parameter (χ) for the fragment-developer binary mixtures. In addition to helping predict the fragment-developer miscibility, calculating the F-H χ parameter also enables the parameterization of statistical-mechanical and kinetic theories of resist dissolution [122] required for the rigorous modeling [85] of the development process. Furthermore, MD simulations of the fragment-developer interaction also enable the investigation of time-dependent properties such as fragment diffusivity, conformation, and aggregation.

In this chapter, the miscibility of short PMMA chains ($n \leq 10$) with MIBK and IPA developers is investigated by conducting MD simulations in the Accelrys Materials Studio [203] environment. Although the resist-developer interface is not included in these simulations explicitly (see Figure 4.1), the simulation setup is chosen such that both solute-solute and solute-solvent interactions occurring in the proximity of the resist-developer interface may be addressed [125]. The simulated data is used to calculate the F-H χ parameters for each fragment-developer pair. Furthermore, the differences in fragment gyration radii (R_g) and radial distribution functions (RDF) in MIBK and IPA are examined, and the fragment self-diffusion coefficients (self-diffusivities) are also evaluated. The behavior of PMMA fragments in both developers are compared in light of lithography observations.

4.2 Molecular Dynamics simulations

The simulation strategy employed in this thesis is summarized in Figure 4.2. The main simulations for miscibility and kinetic studies involve the binary mixtures PMMA(*n*):MIBK and PMMA(*n*):IPA for *n* = 1,2,3,4,6,8,10. However, prior to running simulations for the binary mixtures, simulations for each of the pure components MIBK, IPA, and PMMA(*n*) fragments of various size *n*, are performed. Where the physical properties of pure components are experimentally known (e.g., densities of MIBK and IPA), these known values are used to find the optimal simulation parameters and to compute the simulation system properties such as volume and potential energy. Where the physical properties are experimentally unknown (e.g., densities of PMMA(*n*)), these properties can be computed with confidence using the optimized MD simulation parameters obtained previously. The obtained quantities from the pure component simulations are further used as input data for simulating the mixtures PMMA(n):MIBK and PMMA(n):IPA.

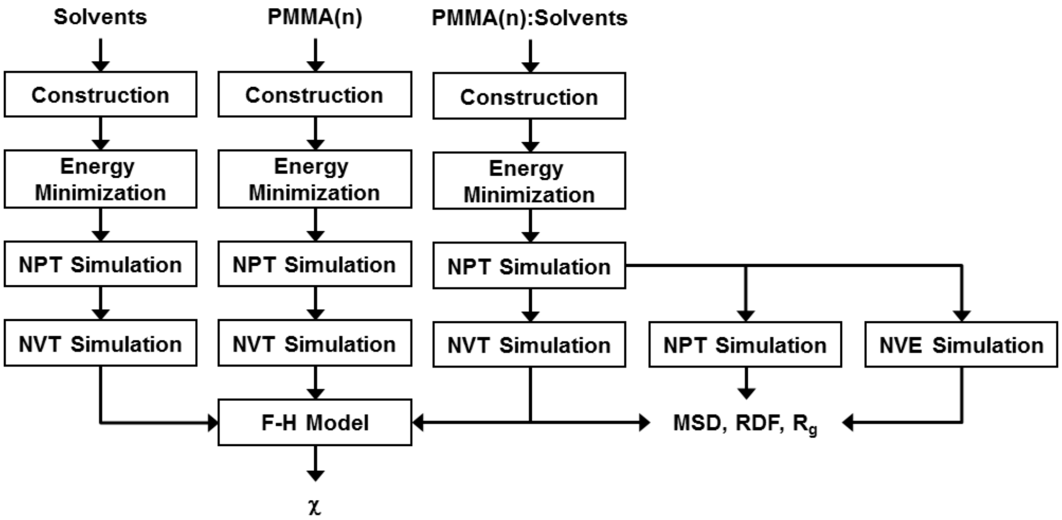

Figure 4.2. Simulation strategy used in this thesis (see also Figure 2.22 and inspired by ref. [206]). The acronyms have all been defined in section 2.5.2, except NVE (microcanonical ensemble).

Data from the pure component and mixture simulations are subsequently input into the F-H model [206] to compute the F-H χ parameters. The technical details of the simulations are provided below and in the following sections.

All of the MD simulations and analysis, except for the calculation of the F-H interaction parameters, are conducted using the Accelrys Materials Studio [203] package. All simulation systems are constructed at ambient conditions (295 K and 1 atm) with periodic boundary conditions using the AMORPHOUS CELL module. The default force-field used by Materials Studio is COMPASS [232], which is suitable for our systems. The AMORPHOUS CELL module is also used for the energy minimization (10,000 – 100,000 steps) using the conjugate gradient

[233] method. The DISCOVER module is used for all NPT (isothermal-isobaric), NVT (canonical), and NVE (microcanonical) ensemble dynamics runs.

The system energies, fragment mean squared displacement (MSD), gyration radii (R_g), and radial distribution functions (RDF) are obtained using the FORCITE module. Where applicable, the Andersen [234] thermostat (collision ratio 1.0) was used for the temperature control and the Berendsen [235] barostat (decay factor 0.08-0.09 ps) was used for the pressure control. Group-based summations were used for the non-bond (van der Waals and Coulomb) interactions and a cut-off of 12.5 Å (3 Å spline, 1 Å buffer, long range correction) was used [232]. The charge groups were assigned manually for the developers and automatically for the PMMA fragments (see Appendix A5). Constraint algorithms were not used. These simulation parameters were determined through extensive testing and verification, e.g., the Andersen thermostat and Berendsen barostat were found to be the most accurate in maintaining the temperature and pressure within desired limits (see Appendix A6). Moreover, the Andersen thermostat and Berendsen barostat have been employed by the COMPASS force-field paper [232] for calculating properties of non-crystalline systems. Similarly the simulation times for individual dynamics runs were carefully selected. Unless stated otherwise, the above parameters are kept constant in all simulations.

4.2.1 Developer simulations

The experimental densities of developers MIBK and IPA are known to be 0.801 g/cm^3 & 0.785 g/cm^3, respectively [236,237]. Two separate systems containing 500 molecules each of MIBK (9500 atoms) and IPA (6000 atoms) were constructed, energy minimized, and subjected to NPT dynamics for 1000 ps (1.0 fs step size) using the parameters described above (section 4.2). Information on the setup and NPT dynamics results for the developer systems are summarized in Table 4 [125]. The simulated densities were found to be 0.805 g/cm^3 and 0.803 g/cm^3, respectively, within 2.3 % of experimentally known values. Table 4 further shows that very good temperature control has been achieved around 295 K; however, the pressure has not settled close to 1.0 atm. Given the small size of the system and nature of intermolecular interactions, pressure may fluctuate significantly, yet providing accurate density values (see also examples in Appendix A6). The density equilibrated systems were further subjected to NVT dynamics for 1000 ps (1.0 fs step size) to determine the potential energies. The setup and NVT dynamics results are summarized in Table 5 [125].

4.2.2 PMMA fragment simulations

The experimental properties of bulk PMMA are well-known; however, properties of short-chain PMMA fragments are unknown. Therefore, the first step is to obtain the unknown densities of PMMA fragments by NPT dynamics.

Table 4. MD simulation (NPT ensemble) conditions and results – Developer liquids. A version of this table has been published in [125]. Reprinted with permission from the Crown and [125]. Copyright Act (Canada), S. 12 and © 2012 American Vacuum Society.

	Molecules	Atoms	Box Side (Å)	Sim. Density (g/cm^3)	Known Density (g/cm^3)	Pressure (atm)	Temp. (K)
MIBK	500	9500	49.2	0.805	0.801	0.65	295.0
IPA	500	6000	36.8	0.813	0.785	1.47	296.2

Table 5. MD simulation (NVT ensemble) conditions and results – Developer liquids. A version of this table has been published in [125]. Reprinted with permission from the Crown and [125]. Copyright Act (Canada), S. 12 and © 2012 American Vacuum Society.

	Molecules	Atoms	Potential Energy (kcal/mol)	Temp. (K)
MIBK	500	9500	-7600 ± 209	294.6
IPA	500	6000	-14800 ± 109	294.9

Table 6. MD simulation (NPT ensemble) conditions and results – PMMA fragments. A version of this table has been published in [125]. Reprinted with permission from the Crown and [125]. Copyright Act (Canada), S. 12 and © 2012 American Vacuum Society.

n	PMMA Molecules	Atoms	Box Side (Å)	Potential Energy (kcal/mol)	Temp. (K)	Pressure (atm)	Density (g/cm^3)
1	600	10200	48.1	25858	295.3	1.00	0.912 ± 0.004
2	300	9600	45.9	29292	294.7	0.96	1.039 ± 0.003
3	200	9400	45.5	31328	294.8	0.89	1.064 ± 0.003
4	150	9300	45.5	32451	294.8	0.97	1.062 ± 0.003
6	100	9200	45.6	33668	294.8	0.98	1.056 ± 0.004
8	150	18340	57.6	68683	295.1	0.95	1.048 ± 0.003
10	120	18240	57.4	69284	295.1	0.94	1.054 ± 0.002

Table 7. MD simulation (NVT ensemble) conditions and results – PMMA fragments. A version of this table has been published in [125]. Reprinted with permission from the Crown and [125]. Copyright Act (Canada), S. 12 and © 2012 American Vacuum Society.

n	PMMA Molecules	Residues	Atoms	Potential Energy (kcal/mol)	Temp. (K)
1	600	600	10200	16900 ± 198	294.7
2	300	600	9600	21000 ± 203	294.7
3	200	600	9400	23300 ± 194	294.8
4	150	600	9300	24500 ± 174	294.8
6	100	600	9200	25800 ± 208	294.7
8	150	1200	18340	52900 ± 290	295.0
10	120	1200	18240	53500 ± 744	295.8

In this work, only the isotactic conformations of PMMA fragments have been considered. Information on the simulation setup and results for all PMMA(*n*) systems are summarized in Table 6 [125]. In order to maintain uniformity in system size, we have attempted to keep the number of residues (monomers in system) constant; however, even more important was maintaining the minimum image convention. As a result, any particular unit cell's length is at least the length of the PMMA(*n*) molecule at full stretch + (2 × cut-off radius) + 5 Å. Therefore each unit cell has 9000 – 10000 atoms for PMMA(1) - PMMA(6) and approximately 18000 atoms for larger chain sizes corresponding to unit cell sizes of 45.5 – 57.4 Å. The total NPT simulation duration was 1250 ps (1.0 fs steps) which comprised a 1000 ps equilibration run and a 250 ps production run. From Table 6, we observe that excellent temperature and pressure control has been maintained near expected values. In addition, accurate density values have been obtained. The density shows a gradually increasing trend with increasing PMMA fragment size. This is consistent with the expectation that as the PMMA fragments become larger, the density of the PMMA(*n*) system would approach the PMMA bulk density of 1.19 g/cm^3.

Following NPT dynamics, the PMMA(*n*) systems were subjected to NVT dynamics for 1000 ps (at 1.0 fs step) to obtain the potential energies. The setup and NVT dynamics results are summarized in Table 7 [125]. From Table 7, we observe that very good temperature control has been maintained near 295 K. Furthermore, the simulated potential energies exhibit a gradually increasing trend with increasing PMMA fragment size.

4.2.3 PMMA fragment and developer mixture simulations

As described earlier in section 4.1, the MD simulations are setup such that the molecular mechanisms of dissolution in the proximity of the resist-developer interface region can be studied at the conditions when polymer fragments interact both with the developer and other fragments. Therefore, the PMMA fragment and developer mixture systems are constructed such that the polymer fraction is approximately 16.7% by mass. Such a polymer solution may be considered as semi-dilute. Simulating a significantly higher or lower concentration of polymer fragments would not represent the targeted environment. Moreover, if the polymer solution is too dilute, the criterion for uniform segmental density necessary for applicability of F-H theory will not be met, and alternative theories [238] would be required. The number of molecules in the PMMA(*n*):MIBK and PMMA(*n*):IPA binary mixtures is given ahead in Tables 8-9 (section 4.3) [125]. In both mixtures the number of PMMA(*n*) residues are kept constant while simultaneously maintaining the minimum unit cell size as described previously in section 4.2.2. The unit cell sizes for the PMMA(*n*):MIBK and PMMA(*n*):IPA mixtures range from 52.2 to 52.8 Å and from 52.5 to 53.0 Å, corresponding to 13324 – 13440 and 13824 – 14040 atoms, respectively.

After construction and energy minimization, the binary systems are subjected to NPT dynamics for 350 ps (at 0.5 fs step size for improved accuracy) including a 250 ps equilibration and a 100 ps production run. This is followed by NVT dynamics for 1000 ps (at 1.0 fs step size). The relevant information and results from the NPT and NVT binary mixture simulations are presented ahead in Tables 8-11 (section 4.3) [125]. The results from all binary mixture and pure component simulations are subsequently input into the F-H model (see Figure 4.2) to calculate the F-H χ parameters.

In addition to the above simulations primarily targeted at obtaining the F-H χ parameters, two further sets of simulations (see Figure 4.2) are conducted for each fragment-developer mixture. After the 350 ps NPT simulations, a further set of NPT (250 ps @ 0.5 fs step size) and NVE (100 ps @ 1.0 fs step size) simulations are performed in order to investigate various dynamic aspects of the fragment-developer mixing. As a result of these NPT, NVE, and the previous NVT simulations, the trajectory files containing sequential snapshots of fragment motions through the developer can be obtained and analyzed for studying the dynamic behavior of the PMMA fragments.

4.2.3.1 Self-diffusivity analysis

The self-diffusivity of a species in a mixture may be obtained using several routes – the two most popular ones being via computation of the (i) mean squared displacement (MSD), and the (ii) velocity autocorrelation function (VACF). In this work, the PMMA fragment self-diffusivities are obtained by calculating the MSD using the Materials Studio FORCITE module. Excluding the initial few snapshots where the fragments exhibit ballistic motion, the MSD vs. time plot would normally be linear. Calculating the slope of the linear region yields the fragment self-diffusivity *D* (hereinafter simply referred to as diffusivity),

$$D = \frac{1}{6N} \lim_{t \to \infty} \frac{d}{dt} \sum_{i=1}^{N} \left\langle \left[\vec{r}_i(t) - \vec{r}_i(0) \right]^2 \right\rangle \qquad (11)$$

where *N* is the number of atoms in the system, and $\vec{r}_i$ is the position vector of the *i*th atom at a time snapshot (simulation frame) *t*. Calculating the self-diffusivity of each fragment and plotting the self-diffusivity vs. the fragment size enables extraction of the exponent *α* which determines the fragment size dependence of the self-diffusivity, $D_0 \sim M_f^{-\alpha}$ discussed previously in chapters 2 and 3.

4.2.3.2 Conformation and aggregation analysis

When exposed to good solvents, polymers generally exhibit expanded conformations to maximize the number of molecular interactions with the solvent. Contrarily, in poor solvents, polymers adopt collapsed (folded) conformations and tend to aggregate in order to minimize the number of molecular interactions. The changes in polymer conformations may be characterized by calculating the radius of gyration (R_g). A polymer fragment with an expanded conformation is expected to have a large R_g, whereas a fragment with a folded conformation is expected to have a smaller R_g. In this research, the mass-weighted R_g [239] is calculated for PMMA fragments using the FORCITE module according to,

$$R_g = \sqrt{\left\langle \left(\sum_{i=1}^{N} m_i R_i^2 \right) \Big/ \sum_{i=1}^{N} m_i \right\rangle} \qquad (12)$$

where m_i is the mass of the atoms and R_i is the distance of each atom from the centre-of-mass of the particular polymer fragment.

The aggregation (or coming together) of PMMA fragments may be quantitatively assessed by computing the radial distribution functions (RDF) of the fragment centroids over different time intervals and comparing these RDFs against the average density of the simulated system. The standard definition of RDF [240] is given by,

$$g(R) = \frac{\langle n(R) \rangle}{4\pi\rho\, R^2 \Delta R} \qquad (13)$$

where $\langle n(R) \rangle$ is the average number of objects (atoms or centroids) at a distance $R + \Delta R$ from the reference object, and ρ is the average density of the system. The FORCITE module also enables computation of the RDF for centroids; however, the user is required to define a set of centroids as input. Therefore, a Perl [241] script has been written for (a) identifying the fragments of interest in the binary mixture, (b) calculating the fragment centroids, and (c) collecting the centroids in a set. Appendix A7 provides the various scripts used in this thesis.

4.3 Results and analysis

In this section, the results from the binary mixture simulations described above are presented and discussed. Relevant information on the simulation setup and results for all PMMA(*n*):MIBK and PMMA(*n*):IPA NPT simulations are summarized in Table 8 and Table 9, respectively. From both tables we observe that excellent temperature control has been maintained near the expected value of 295 K. The pressure control is also fairly good around 1 atm. In addition, accurate density values have been obtained for both sets of mixtures. The

Table 8. MD simulation (NPT ensemble) conditions and results – PMMA fragment and MIBK mixtures. A version of this table has been published in [125]. Reprinted with permission from the Crown and [125]. Copyright Act (Canada), S. 12 and © 2012 American Vacuum Society.

n	PMMA:MIBK Molecules	Atoms	Box Side (Å)	Potential Energy (kcal/mol)	Temp. (K)	Press-ure (atm)	Density (g/cm^3)
1	120:600	13440	52.8	-5753	295.1	0.70	0.819 ± 0.003
2	60:600	13320	52.3	-5004	295.3	1.01	0.839 ± 0.004
3	40:600	13280	52.2	-4630	295.1	0.73	0.845 ± 0.004
4	30:600	13260	52.2	-4486	294.9	0.96	0.848 ± 0.003
6	20:600	13240	52.3	-4320	294.7	1.01	0.853 ± 0.004
8	15:600	13230	52.3	-4163	295.2	0.87	0.854 ± 0.003
10	12:600	13224	52.5	-4089	295.2	0.94	0.854 ± 0.004

Table 9. MD simulation (NPT ensemble) conditions and results – PMMA fragment and IPA mixtures. A version of this table has been published in [125]. Reprinted with permission from the Crown and [125]. Copyright Act (Canada), S. 12 and © 2012 American Vacuum Society.

n	PMMA:IPA Molecules	Atoms	Box Side (Å)	Potential Energy (kcal/mol)	Temp. (K)	Press-ure (atm)	Density (g/cm^3)
1	120:1000	14040	53.0	-26233	295.1	0.96	0.823 ± 0.003
2	60:1000	13920	52.6	-25506	294.9	0.88	0.841 ± 0.003
3	40:1000	13880	52.5	-25047	295.4	0.94	0.847 ± 0.004
4	30:1000	13860	52.5	-24877	295.3	0.90	0.849 ± 0.003
6	20:1000	13840	52.5	-24708	295.0	0.96	0.854 ± 0.003
8	15:1000	13830	52.6	-24587	295.2	1.26	0.853 ± 0.004
10	12:1000	13824	52.5	-24549	295.1	1.06	0.855 ± 0.009

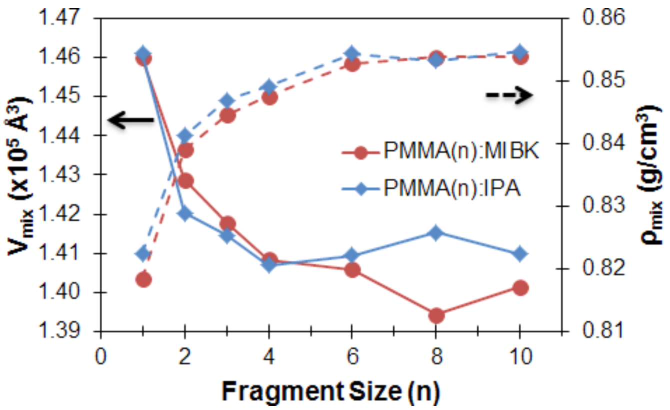

Figure 4.3. Volume and density of mixture for PMMA fragments containing *n* monomers in MIBK (circles) and IPA (diamonds) developers obtained after isothermal-isobaric (NPT) ensemble simulation. Reprinted with permission from the Crown and [125]. Copyright Act (Canada), S. 12 and © 2012 American Vacuum Society.

equilibrated volumes and densities for both PMMA(n):MIBK and PMMA(n):IPA mixtures after NPT dynamics have been plotted as a function of fragment size in Figure 4.3. We observe that as the PMMA fragments become larger, the volume and density rapidly change and subsequently tend to saturate. The gradual increase and saturation in mixture density with increasing PMMA fragment size is consistent with the single-component PMMA(*n*) NPT results in section 4.2.2.

4.3.1 PMMA fragment and developer affinity

The relevant simulation setup and results for all PMMA(*n*):MIBK and PMMA(*n*):IPA NVT simulations are summarized in Table 10 and Table 11, respectively. Comparing the NVT mixture volumes to the equilibrated NPT mixture volumes shown in Figure 4.3, we observe that excellent volume control

Table 10. MD simulation (NVT ensemble) conditions and results – PMMA fragment and MIBK mixtures. A version of this table has been published in [125]. Reprinted with permission from the Crown and [125]. Copyright Act (Canada), S. 12 and © 2012 American Vacuum Society.

n	PMMA:MIBK Molecules	Atoms	Potential Energy (kcal/mol)	Mixture Vol. ($Å^3$)
1	120:600	13440	-5557	145998
2	60:600	13320	-4807	142878
3	40:600	13280	-4436	141778
4	30:600	13260	-4320	140839
6	20:600	13240	-4099	140591
8	15:600	13230	-4050	139421
10	12:600	13224	-3905	140150

Table 11. MD simulation (NVT ensemble) conditions and results – PMMA fragment and IPA mixtures. A version of this table has been published in [125]. Reprinted with permission from the Crown and [125]. Copyright Act (Canada), S. 12 and © 2012 American Vacuum Society.

n	PMMA:MIBK Molecules	Atoms	Potential Energy (kcal/mol)	Mixture Vol. ($Å^3$)
1	120:1000	14040	-25993	146109
2	60:1000	13920	-25307	142028
3	40:1000	13880	-24907	141451
4	30:1000	13860	-24725	140686
6	20:1000	13840	-24522	140950
8	15:1000	13830	-24360	141527
10	12:1000	13824	-24323	140974

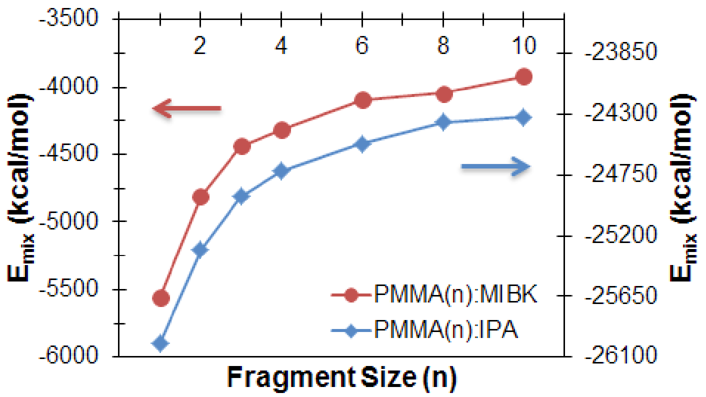

Figure 4.4. Energies of mixture for PMMA fragments containing *n* monomers in MIBK (circles) and IPA (diamonds) developers obtained after canonical (NVT) ensemble simulation. Reprinted with permission from the Crown and [125]. Copyright Act (Canada), S. 12 and © 2012 American Vacuum Society.

has been maintained during the NVT simulations. As the F-H theory assumes no volume change upon mixing, obtaining strict volume control is a condition for being able to utilize the potential energies of the binary mixtures. The potential energies of the PMMA(*n*):MIBK and PMMA(*n*):IPA mixtures after NVT dynamics are presented in Figure 4.4. These potential energies are taken as an average of the entire production trajectory and are not separated into various components. In Figure 4.4, the large negative energies of both mixtures suggest an exothermic (spontaneous) mixing process, consistent with expectations. Furthermore, the trend of lower negative energies for smaller fragments in both developers is also consistent with the conventional expectation that smaller fragments more readily mix with developers. However, the differences in the energies of mixing of PMMA fragments with MIBK and IPA are not directly representative of the relative affinities because of the different masses and volumes of the developers

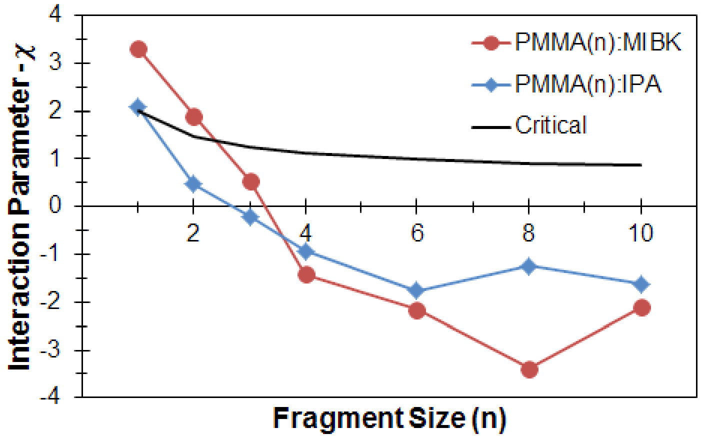

Figure 4.5. Flory-Huggins interaction parameters for PMMA fragments containing *n* monomers with MIBK (circles) and IPA (diamonds) developers. The critical interaction parameter, below which mixing is promoted, is also plotted. Reprinted with permission from the Crown and [125]. Copyright Act (Canada), S. 12 and © 2012 American Vacuum Society.

involved. In order to account for these factors while comparing the fragment-developer affinities, the F-H χ parameters are computed.

The Flory-Huggins χ parameters for the PMMA(*n*):MIBK and PMMA(*n*):IPA binary mixtures are presented in Figure 4.5 and compared with the critical interaction parameter χ_c (refer to eq. 6). With the exception of PMMA monomers (*n* = 1) and dimers (*n* = 2) in MIBK, all PMMA fragments exhibit a tendency to mix with both MIBK and IPA developers as their $\chi \leq \chi_c$. The behavior of PMMA monomers and dimers can be interpreted as limited miscibility with MIBK developer. Limited miscibility with a developer may be interpreted as very small fragments tending to aggregate when exposed to the developer. This hypothesis is investigated ahead. According to Figure 4.5, χ

decreases with increasing fragment size and tends to saturate beyond fragment sizes $n = 6$. PMMA fragments with $n > 3$ exhibit somewhat stronger attractive interaction with MIBK as compared to IPA; however, this trend does not fully explain the experimentally observed strong differences in sensitivities of more than 2.5 times between the developers and their mixtures [129]. PMMA fragments with $n \leq 3$ show relatively high χ parameters contrary to the expectation for smaller fragments to show greater affinity with developers as previously mentioned in section 2.1.3. In order to explain why the χ parameters are higher for smaller fragments, we hypothesize that larger fragments can adopt a larger variety of conformations so that particular functional groups are shielded, resulting in a “better” interaction with the developer. Because small fragments cannot adopt such conformations, the observed χ parameters are higher. In order to achieve more favourable conditions, aggregation of small fragments may be expected. Both of these hypotheses (conformation changes and aggregation) are investigated in section 4.3.3.

4.3.2 PMMA fragment self-diffusivity

The experimentally observed strong sensitivity differences of PMMA in MIBK versus IPA developers do not seem to be fully accounted for by the differences in the PMMA fragment-developer χ parameters presented above. I propose these may be due to kinetic rather than thermodynamic factors. For this reason, the self-diffusivities of PMMA fragments in both MIBK and IPA

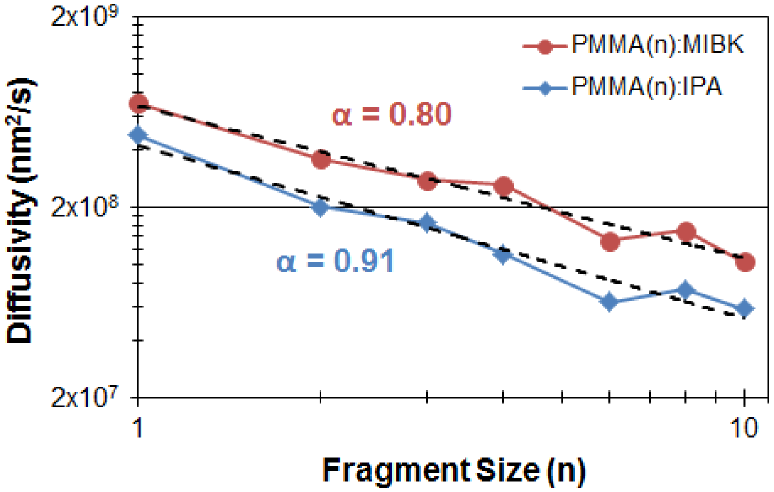

Figure 4.6. Self-diffusivity of PMMA fragments containing *n* monomers in MIBK (circles) and IPA (diamonds) developers computed from MSD obtained after an isothermal-isobaric (NPT) ensemble simulation. The power law (const. $\times n^{-\alpha}$) fitting parameters (α) are also presented for both developers [218].

Table 12. Power law (const. $\times n^{-\alpha}$) fitting equations for self-diffusivity (units: nm^2/s) calculated from various ensemble simulations

	Isothermal-isobaric NPT	Canonical NVT	Microcanonical NVE
MIBK	$(7\times10^{8})\times n^{-0.798}$	$(9\times10^{8})\times n^{-0.857}$	$(2\times10^{9})\times n^{-0.754}$
IPA	$(4\times10^{8})\times n^{-0.911}$	$(4\times10^{8})\times n^{-0.893}$	$(9\times10^{8})\times n^{-0.891}$

developers have been computed after NPT, NVT, and NVE ensemble simulations. The PMMA fragment self-diffusivities in both developers are plotted against the fragment length (number of monomers) in Figure 4.6 after NPT simulations. We observe that the self-diffusivity decreases with increasing fragment lengths, as expected, and the power law fitting parameter α varies between 0.8 and 0.9. In comparison, for low molecular weight polymers, α is theoretically expected to be ~0.6 in a good solvent (dilute solution) and 1.0 in a polymer melt [242]. Our simulated α values are intermediate to these theoretically expected values, which may be explained due to our use of a ~17% (semi-dilute) polymer concentration. From Figure 4.6 we also observe that the magnitude of the PMMA fragment self-diffusivities (between 6×10^{7} to 7×10^{8} nm^{2}/s) in both developers are compatible with the experimentally measured coefficients of self-diffusion of various compounds such as hydrocarbons, which are on the order of 10^{8} nm^{2}/s [243]. The self-diffusivities were also calculated from the other (NVT and NVE) ensemble simulations. The corresponding fitting parameters extracted from all simulation data are listed in Table 12. We observe that the exponent α extracted from the NVT and NVE ensemble runs are generally in agreement with the values extracted from the NPT simulations; however, the magnitude of the coefficient varies to some extent. In comparison to the NPT and NVT simulations, the pre-factor extracted from the NVE simulations are 2.2-2.9 times higher. On further inspection, this was found to be due to a gradual decrease in pressure in the NVE runs, suggesting that a higher confidence may be placed in the NPT and NVT data. In addition, the deviation from the fitting line is found to be the least (within ±20%) in the self-diffusivity values obtained from the NPT simulations.

However, the most significant observation from both Figure 4.6 and Table 12 is that the PMMA fragment self-diffusivities in MIBK are approximately two times higher than in IPA, regardless of the simulation ensemble used. This observation suggests that kinetic factors seem to be more significant as compared to thermodynamic factors when accounting for differences in EBL process sensitivities due to the developer selection. Although accounting for the two times lower self-diffusivity of PMMA fragments in IPA has not been pursued in this work, an examination of the weak molecular interactions during the simulation may yield further insight as it is known that hydrogen bonding retards the diffusivity during mixing [244,245]. Further comments on the subject of diffusivity are provided in section 4.4.

4.3.3 PMMA fragment conformations and aggregation

It was earlier (section 4.3.1) indicated that the unexpected intermolecular affinity behavior of smaller PMMA fragments in both MIBK and IPA developers may be explained by investigating the PMMA fragment conformation changes and possible fragment aggregation. Therefore, in order to study the conformation changes, the gyration radii (R_g) of PMMA fragments of various lengths have been computed. The corresponding distributions of R_g for n = 1, 2, 3, and 10 in MIBK and IPA developers are provided in Figure 4.7, after NPT simulations. For the monomer (Fig. 4.7(a)), the R_g distribution for both developers are identical, as one would expect; however, all other fragment sizes exhibit a different R_g distribution in IPA as compared to MIBK. Perhaps due to their small size, the R_g distributions for the PMMA dimers (Fig. 4.7(b)) and trimers (Fig. 4.7(c)) exhibit only minor differences from each other, although these differences are already sufficient to identify preferable R_g values. Generally,

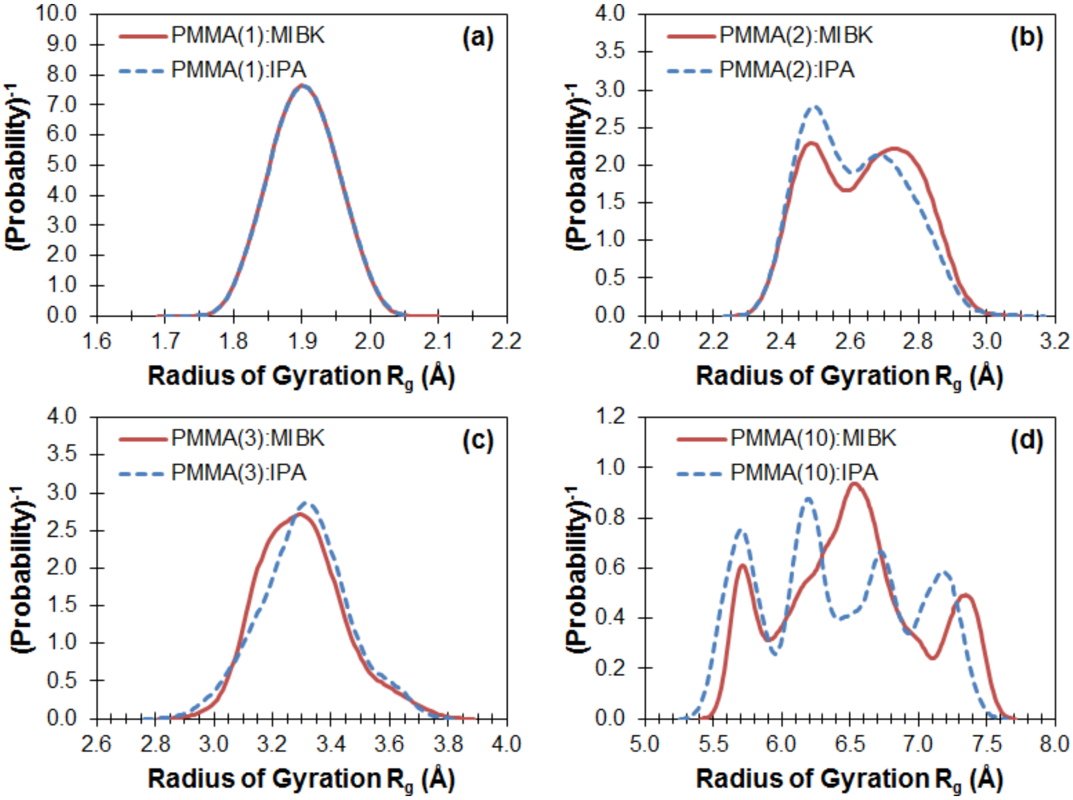

Figure 4.7. Radii of Gyration (R_g) for PMMA fragments in MIBK (solid lines) and IPA (dashed lines) developers obtained after NPT simulations [218].

the differences in R_g distributions between both developers tend to increase with increasing fragment size.

The R_g distribution for the largest PMMA(10) fragments (Fig. 4.7(d)) exposed to IPA exhibit four distinct maxima at 5.7 Å, 6.2 Å, 6.8 Å, and 7.2 Å. Comparing both developers, we observe that the most probable gyration radius in IPA (6.2 Å) is smaller than in MIBK (6.6 Å). Furthermore, we observe that the PMMA(10):IPA R_g distribution is shifted lower than the PMMA(10):MIBK distribution. These results may be interpreted as the PMMA fragments tending to adopt relatively collapsed conformations when exposed to IPA, a weaker developer than MIBK. This interpretation is compatible with the known dependence of the polymer chain conformation on the solvent strength. Nakamura *et al.* [246,247] and Nakata *et al.* [248] have performed experimental studies of dissolution of long PMMA chains (n ~ 16,000) in an alcohol and water mixture and found that both chain collapse (chain crumpling) and chain aggregation occurs in such mixtures of weak solvents. They also demonstrated that chain collapse tends to occur before the aggregation [248]. However, it is noteworthy to state that these phenomena depend on several factors such as the polymer molecular weight, concentration, and solvation time.

In order to investigate aggregation, the radial distribution functions (RDF) of PMMA fragments have been computed at various time intervals throughout the simulation trajectory files. The RDF plots for PMMA monomers, dimers, and trimers in MIBK and IPA developers are provided in Figure 4.8, after NVT simulations. Also included in each plot is the Wigner-Seitz radius $r_s = \sqrt[3]{3/(4\pi n_v)}$, where $n_v = N/V$ is the number of atoms per unit volume, N is the total number of atoms, and V is the system volume. The quantity r_s describes the average density of the simulated system and therefore is a benchmark quantity against which to compare the PMMA fragment RDFs. From Figure 4.8, we observe that except in the case of the PMMA monomers, all primary RDF peaks lie within the Wigner-Seitz radius. This suggests that for PMMA dimers and trimers, aggregation of these PMMA fragments may have occurred in both developers.

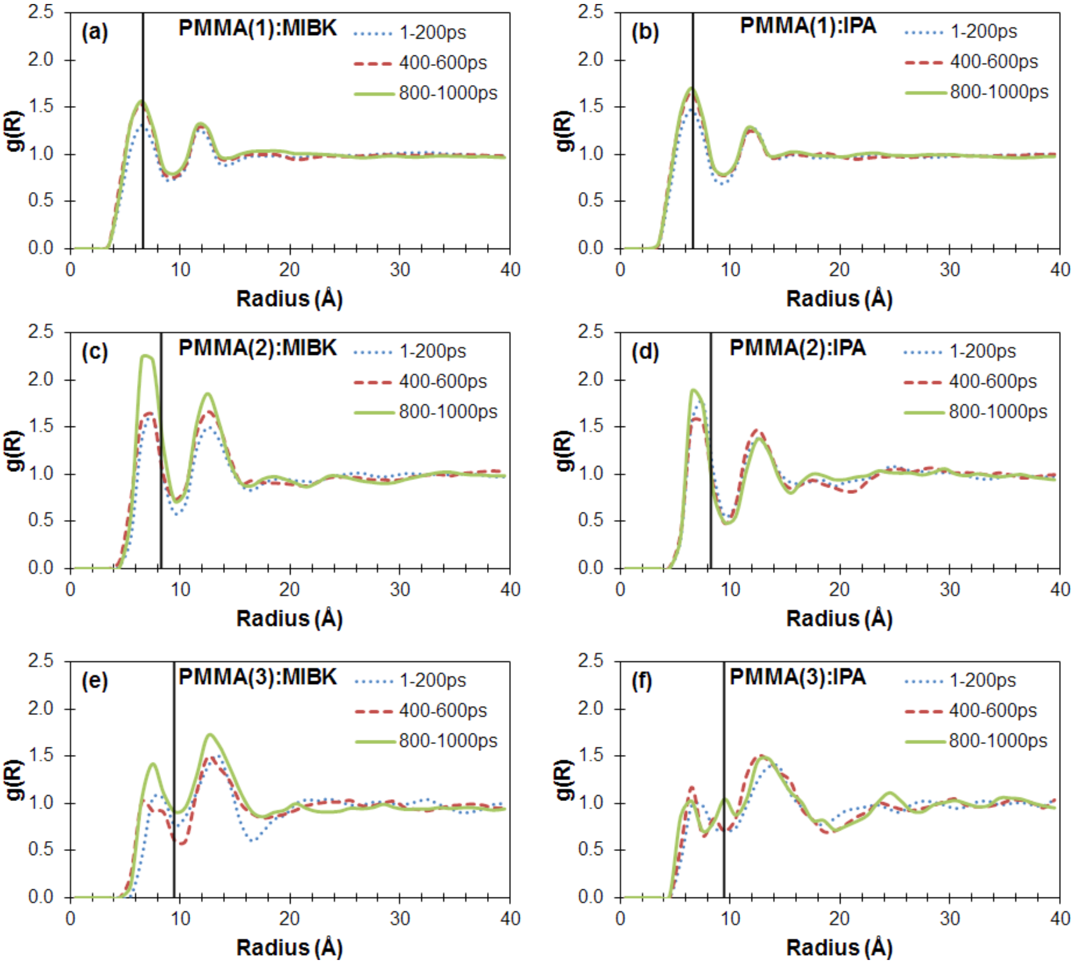

Figure 4.8. Radial distribution functions (RDF) at various time intervals for PMMA fragments in MIBK and IPA developers obtained after NVT simulations. The vertical line (Wigner-Seitz radius) describes the average system density [218].

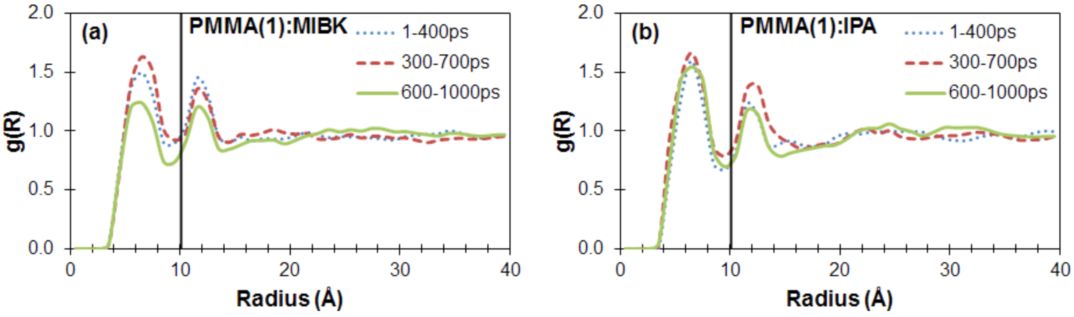

Figure 4.9. RDF at various time intervals for PMMA monomers in MIBK and IPA obtained after a NVT simulation using a four times lower PMMA fraction [218].

Furthermore, we observe that nearly all the primary peaks tend to increase in height over time, suggesting an increasing probability of the PMMA fragments to aggregate with time. The only exception to this observation are the PMMA trimers in IPA, where the position of the peaks remain unchanged throughout the trajectory. Moreover, the height increase in the primary peaks is more pronounced in the MIBK mixtures as compared to the IPA mixtures, consistent with our earlier hypothesis.

As for the PMMA monomers, it is not possible to be certain regarding the aggregation behavior by observing Figure 4.8(a) and 4.8(b). In this case, the distance of the first "shell" of neighboring fragments is very close to the average density of the system. In order to verify the aggregation behavior, simulations with a lower concentration have been performed. For this purpose, the radial distribution functions (RDFs) of PMMA monomers in both MIBK and IPA were acquired from simulations employing four times less PMMA fragments. These RDFs are presented in Figure 4.9. Studying both RDFs, the primary RDF peaks seem to be significantly within the Wigner-Seitz radius. Based on this criterion, we conclude that aggregation of PMMA fragments is observed in both MIBK (Fig. 4.9(a)) and IPA (Fig. 4.9(b)) mixtures.

4.4 Future research directions

The results presented in section 4.3.2 indicate that the kinetics of fragment dissolution is an important factor in order to predict the resist development trends. However, the approach based on calculating self-diffusivities addresses transport properties of individual particles and as such is accurate for dilute polymer solutions, whereas for solutions of higher concentration, an accounting for collective diffusion properties may be required [249]. In our research, we have used a semi-dilute PMMA fragment solution of approximately 17%. Such a concentration regime may warrant addressing collective diffusion properties.

For a binary mixture, collective diffusion properties may be represented by the mutual diffusivity D_{12} [249,250],

$$D_{12} = D_{12}^{M-S}\left(\frac{\partial \ln a_1}{\partial \ln x_1}\right) \qquad (14)$$

where D_{12}^{M-S} is the Maxwell-Stefan (M-S) diffusivity, x_1 is the mole fraction (or amount) fraction of component 1, and a_1 is the activity of component 1. The activity may be calculated using the equation $\ln a_1 = \ln \varphi_1 + ((r_2 - 1)/r_2)\varphi_2 + \chi\varphi_2^2$ [239], where φ_1 and φ_2 are the volume fractions of component 1 and 2, respectively, r_2 is the number of polymer segments, and χ is the Flory-Huggins interaction parameter. If the interactions between molecules are neglected, the

M-S diffusivity may be approximately estimated by the Darken relation [249,250] to be,

$$D_{12}^{M-S} = x_2 D_1 + x_1 D_2 \tag{15}$$

where D_1 and D_2 are the self-diffusivities of components 1 and 2, respectively. More rigorously, the M-S diffusivity D_{12}^{M-S} may be obtained through the Onsager coefficients Λ_{ij} [250,251,252] according to,

$$D_{12}^{M-S} = \frac{x_2}{x_1}\Lambda_{11} + \frac{x_1}{x_2}\Lambda_{22} - \Lambda_{12} - \Lambda_{21}. \tag{16}$$

The Onsager coefficients may be calculated by the Green-Kubo method (using velocity autocorrelation functions) [251],

$$\Lambda_{ij} = \frac{1}{3N}\int_0^\infty \left\langle \left(\sum_{k=1}^{N_i} \vec{V}_{i,k}(0) \bullet \sum_{m=1}^{N_j} \vec{V}_{j,m}(t) \right) \right\rangle dt \tag{17}$$

where N_i and N_j are the numbers of molecules of species i and j, respectively, $N = N_i + N_j$ is the total number of molecules in the system and $\vec{V}_{j,m}(t)$ is the centroid velocity vector of molecule m belonging to species j. Alternatively, the Onsager coefficients may be obtained through the equivalent [250,251,252,253] Einstein method (using molecule displacements),

$$\Lambda_{ij} = \frac{1}{6N}\lim_{t\to\infty}\frac{d}{dt}\left\langle \left(\sum_{k=1}^{N_i} \left(\vec{r}_{i,k}(t) - \vec{r}_{i,k}(0)\right) \right) \bullet \left(\sum_{m=1}^{N_j} \left(\vec{r}_{j,m}(t) - \vec{r}_{j,m}(0)\right) \right) \right\rangle \tag{18}$$

where $\vec{r}_{i,k}(t)$ is the centroid position vector of molecule k belonging to species i, and all other variables have the same meaning as defined previously. The Onsager coefficients satisfy the mass balance constraint $\sum_i M_i \Lambda_{ij} = 0$, where M_i is the molecular mass of the i^{th} species [250,251,252] and $\Lambda_{ij} = \Lambda_{ji}$ according to the Onsager reciprocal relations [250,252]. Therefore the Onsager coefficients for a binary mixture satisfy the following equations:

$$\frac{\Lambda_{11}}{\Lambda_{22}} = \left(\frac{M_2}{M_1}\right)^2 \qquad (19)$$

$$\frac{\Lambda_{11}}{\Lambda_{21}} = -\frac{M_2}{M_1}. \qquad (20)$$

Equation (18) together with equations (19) and (20) enables calculation and verification of the Onsager coefficients for obtaining the M-S diffusivities from molecular dynamics trajectories.

Employing the aforementioned approach, we have begun calculating the relevant quantities for our PMMA-developer solutions and obtained preliminary results for a PMMA(8):IPA system. In the discussion below, index ‘1’ refers to PMMA(8) and index ‘2’ refers to IPA. From our NPT simulations, the dependence of the mean dot product $\left\langle \left(\sum_{k=1}^{N_i} \left(\vec{r}_{i,k}(t) - \vec{r}_{i,k}(0) \right) \right) \bullet \left(\sum_{m=1}^{N_j} \left(\vec{r}_{j,m}(t) - \vec{r}_{j,m}(0) \right) \right) \right\rangle$ on time for $i = j = 1$ has converged to a linear dependence within approximately 20 ps,

Table 13. Preliminary results for Onsager coefficients and M-S diffusivity for PMMA(8) in IPA after an isothermal-isobaric (NPT) ensemble simulation [218].

Λ_{11} nm^2/s	Λ_{22} nm^2/s	$\Lambda_{12} = \Lambda_{21}$ nm^2/s	D_{12}^{M-S} (Onsager) nm^2/s	D_{12}^{M-S} (Darken) nm^2/s
3.410×10^5	6.088×10^7	-4.557×10^6	3.276×10^7	5.667×10^7

Note: D_{12}^{M-S} (Onsager) and D_{12}^{M-S} (Darken) refers to D_{12}^{M-S} calculation using equation (16) and (15) respectively.

which has allowed us to determine Λ_{11} from the slope in the interval 10-75 ps. Having determined Λ_{11}, the coefficients Λ_{22} and Λ_{12} were estimated using equations (19) and (20). Employing these Onsager coefficients, D_{12}^{M-S} was calculated using equation (16). These results are presented in Table 13. Furthermore, D_{12}^{M-S} has also been estimated using the Darken approximation (equation (15)) from the self-diffusivities of PMMA(8) and IPA centroids (equal to 5.317×10^7 nm^2/s and 2.900×10^8 nm^2/s respectively), and this D_{12}^{M-S} value is provided in Table 13 for the sake of comparison.

From the above results, we conclude that the two D_{12}^{M-S} values are reasonably close in magnitude, indicating that the previously calculated self-diffusivities are representative as approximate estimates of fragment mobilities. On the other hand, the fact that D_{12}^{M-S} obtained from Onsager's coefficients is less than the self-diffusivities of either mixture component, may indicate that the intermolecular interaction plays a non-negligible role. Based on this preliminary analysis, a more detailed follow up research on collective diffusion properties in our PMMA fragment-developer mixtures is in progress.

4.5 Summary

In this chapter, the dissolution of small PMMA fragments in MIBK and IPA developers are studied using molecular dynamics simulations. The fragment-developer interactions are characterized using Flory-Huggins theory, and the interaction parameters are calculated. In addition, using the MD simulations, the fragment self-diffusivities are extracted and the fragment gyration radii and radial distribution functions are examined. We observe differences in miscibility, kinetics, and statistical-mechanical properties of PMMA between MIBK and IPA developers. In summary,

- Larger PMMA fragments ($n > 3$) exhibit a slightly stronger affinity to MIBK as compared to IPA;
- Smaller PMMA fragments tend to aggregate in both developers with slightly stronger preference for aggregation in MIBK developer;
- When exposed to IPA, PMMA fragments tend to adopt smaller gyration radii than in MIBK. Preferred gyration radii have been identified.
- The self-diffusivity of PMMA fragments is nearly two times higher in MIBK as compared to IPA.

We conclude that the difference in experimentally observed dissolution behavior of PMMA resist in the various developers can largely be attributed to the kinetic factor (difference in self-diffusivities). The tendency of PMMA fragments to collapse and/or aggregate could also play a role. The tendency of smaller fragments to aggregate is a plausible consequence of the weaker fragment-developer affinity observed in PMMA monomers, dimers, and trimers.

CHAPTER 5

EBL PROCESSING APPLICATIONS – SML RESIST

5.1 High aspect ratio resist patterning

The need for high aspect ratio (AR) patterning for a wide range of applications was described previously in section 2.5.3. Furthermore, the processing conditions required for improved AR, resolution, sensitivity, etc., were also discussed for PMMA, ZEP, and HSQ resists (sections 2.1 and 2.3). Generally, higher AR patterning is enabled by employing a higher exposure voltage; however, increasing the voltage also leads to a decrease in the sensitivity, and consequently, a decrease in the throughput. The sensitivity and throughput are further reduced due to processing strategies aimed at enhancing the resolution and reducing the LER, such as employing weaker developers, cold development, etc. However, by utilizing novel SML resist, and applying the understanding of EBL processing strategies and parameters gained through previous research, the aforementioned trade-offs between various process metrics can be considerably improved.

The well-known positive-tone resists PMMA and ZEP-520 can be patterned with sub 20 nm resolution for dense grating patterns. However, the achievable ARs of PMMA on solid substrates are limited to 2:1 to 4:1 at 25 keV [128,254], to approximately 5:1 at 50 keV [128,133], and to 12:1 to 20:1 at 100 keV [128,255,256]. Similarly, ZEP resist has ARs limited to 4:1 at 20 keV [168] and to 7:1 at 100 keV [181], albeit with over three times higher sensitivity than PMMA. Another positive-tone resist, PMGI has been patterned with an AR of over 2:1 at 30 keV [257] and extremely high AR of 38:1 at 100 keV [231] using an optimized development process. However, the sensitivity of PMGI is four to nine times lower than that of PMMA, requiring up to 18,000 μC/cm^2 [231] to expose a single line.

Similar trends are observed for negative-tone resists such as HSQ. Reported ARs for HSQ are 4:1 at 10 keV [258], 7:1 at 50 keV [148], and 25:1 at 100 keV [259,260]. HSQ's main attraction is its extremely high resolution; however, its sensitivity is usually an order of magnitude lower than that of PMMA. Other negative-tone resists such as AZ nLOF 2020 [261] and high molecular weight polystyrene (PS) [262] also have sensitivities a fraction of that of PMMA; however, their AR performance is limited to 4:1 to 5:1 at 100 keV for AZ nLOF 2020 [261] and to less than 2:1 at 20 keV for PS [262,263].

EM Resist Ltd. have recently introduced an EBL resist 'SML' [208] in thicknesses ranging from 50 to 2,000 nm. SML is a positive-tone, organic resist that has been designed for high AR patterning. The resist is anticipated to yield ARs of up to 10:1 at 30 keV and exceeding 50:1 at 100 keV [208]. This represents a greater than two times improvement over benchmark PMMA resist; however, its sensitivity and resolution are lower than those of PMMA and ZEP using supplier-recommended conditions. Similar to other positive-tone resists such as PMMA [213], PMGI [257], and ZEP [190], SML may be developed in MIBK:IPA 1:3 and rinsed in IPA [207].

While developing nanolithography processes for SML, the challenge is to improve the sensitivity without sacrificing its inherent high AR capability. In this research [264], a systematic experimental study of SML as a high-performance EBL resist at 30 keV is conducted with the aim of co-optimizing sensitivity, contrast, and AR. A total of six developers (both single- and binary-component) are evaluated by generating the contrast curves and comparing their respective sensitivities and contrast values. After selecting the developer with desired characteristics, high AR grating patterns at various pitch values are fabricated to obtain a dense, high AR, and high sensitivity nanolithography process. The pattern transfer performance of SML is also explored by lift-off experiments. At each stage of this research, the performance of SML resist is compared to that of PMMA, and other resists as well.

5.2 Methods

The samples used in this research [264] were provided courtesy of EM Resist Ltd. [208] as pre-spun and baked SML coated silicon chips. The experimental work with SML resist began using supplier-recommended conditions [208,207] to fabricate grating structures in 300- and >1,500 nm thick resist samples. The overall strategy for grating fabrication and characterization followed the procedures given in section 3.1.1.1. However, the grating pitch for these preliminary experiments was extended up to 500 nm. In addition, a combination of single-pixel-line gratings and gratings with thin 100 nm rectangles were used. These variations in strategy (from section 3.1.1.1) were due to the thicker resist used in this chapter. Based on the understanding of the SML resist gained through these preliminary experiments, the majority of the work was conducted in three sequential steps: (a) generation of SML contrast curves with six different developers, followed by (b) fabrication and characterization of high AR gratings using a selected developer, and (c) evaluation of lift-off performance.

5.2.1 Contrast curves

To generate the SML contrast curves, the approach described in section 3.1.1.2 was used. The array of 20 × 75 µm rectangular pads (see Figure 3.4) was exposed to 30 keV EBL (Raith 150^{TWO}) on 300-330 nm thick SML resist samples.

The exposed samples were developed for 20 sec at ambient temperature in six developers: MIBK, MIBK:IPA 1:3, IPA:water 7:3, n-amyl acetate, xylene, and xylene:methanol 3:1. The developed samples were quickly dried in a nitrogen flow, and no post-development rinsing was performed. The resulting resist surfaces were scanned using physical profilometry. The depth resolution of the physical profilometer (KLA-Tencor Alpha-Step IQ) used is 10 nm.

5.2.2 Dense gratings

To fabricate dense, high AR gratings, large arrays of 50-200 nm pitch grating patterns were exposed at 30 keV on 300-330 nm thick SML samples. An exposure voltage of 30 keV (the highest voltage on the Raith 150^{TWO}) was selected to maximize the AR while achieving high sensitivity through the development process. The width of the grating arrays was kept sufficient for capturing the contribution of proximity effects. The exposure current was 23-24 pA (7.5 µm aperture), and an exposure step size of 2 nm was used. The exposed samples were developed ultrasonically for 20 sec in IPA:water 7:3 (developer selected after contrast curve study). Before drying the samples in flowing nitrogen, the developed samples were briefly (approximately 2 sec) immersed in a low surface tension fluid (pentane or hexane) to reduce the probability of pattern collapse. Prior to SEM imaging, the samples were coated with a 6 nm chromium layer (Gatan PECS). Cleaved samples were coated at a 45° tilt with the sample cross section facing the target. The SEM imaging (Hitachi S-4800) was conducted at 5 keV, 20 µA, and 4 mm working distance. To evaluate the pattern transfer capability of SML resist, metal lift-off was performed. By electron beam evaporation, 50 nm of chromium was deposited on nanoscale SML gratings and the resulting stack was lifted-off by immersing for 1 min, in an ultrasonic acetone bath.

5.3 Discussion

Within the introductory attempts, it was possible to readily fabricate SML gratings with an AR better than PMMA in both 300 and >1,500 nm thick films. Figure 5.1 presents cross-sectional micrographs of cleaved gratings fabricated in SML using the supplier recommended developer, MIBK:IPA 1:3. In Figure 5.1(a), a uniform 5 µm wide array of 200 nm pitch gratings is shown. This array has been patterned at an exposure line dose of 3600 pC/cm. In comparison, similar PMMA gratings can be fabricated using an approximately three times lower dose. Figure 5.1(b) shows a magnified image from the center of the array measuring a thickness of 282 nm and line widths ranging from 45 to 67 nm (from top to base of gratings), resulting in ARs of 4.2 to 6.3. From Figure 5.1(a) and 5.1(b), it was evident from these preliminary experiments that proximity effect is of minor importance in SML. In contrast resists such as PMMA, at comparable conditions, exhibit wider patterned features and/or collapse in the center of the grating

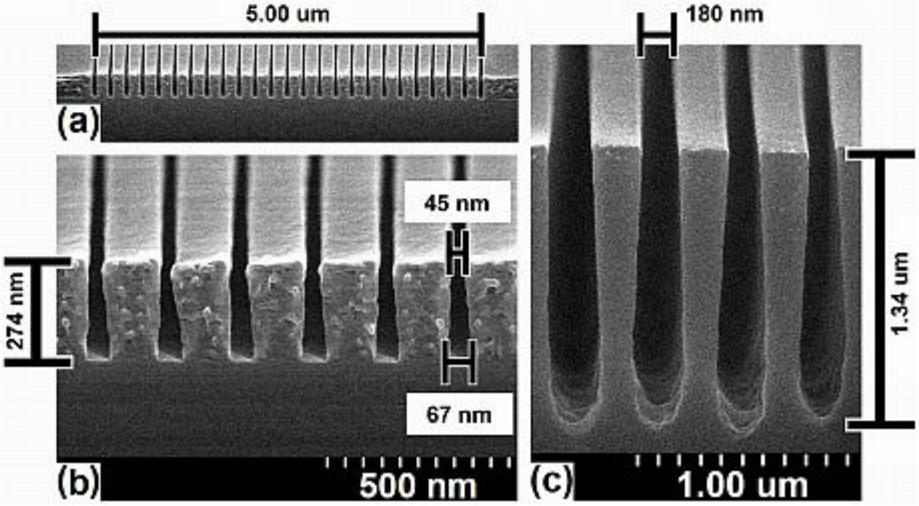

Figure 5.1 Cross-sectional micrographs of SML exposed at 30 keV and developed in MIBK:IPA 1:3 for 20 sec. The panels show (a) a 5 µm array of 200 nm pitch gratings in nominally 300 nm thick resist, (b) magnified image with thickness of 282 nm and denoted line widths, and (c) 400 nm pitch gratings in >1,500 nm thick resist (no clearance) with the achieved depth of 1,380 nm and line widths of 180 to 220 nm from top to bottom of gratings. The exposure doses were (a, b) 3600 pC/cm and (c) 700 µC/cm^2. See also reference [264].

arrays (see earlier Figure 3.8(a)) as compared to the sides.

In Figure 5.1(c), an array of 400 nm pitch gratings is patterned to a depth of 1,380 nm (no clearance) using an exposure area dose of 700 µC/cm^2. From top to bottom, the line widths range from 180 to 220 nm, resulting in ARs of 6.3 to 7.7. The AR results achieved using MIBK:IPA 1:3 are not optimized and can be significantly improved; however, the much lower sensitivity compared to PMMA requires a higher sensitivity developer that maintains or even improves the AR performance.

5.3.1 Study of SML developers

The SML contrast curves for the six developers: MIBK, MIBK:IPA 1:3, IPA:water 7:3, n-amyl acetate, xylene, and xylene:methanol 3:1 are presented in Figure 5.2. The contrast (γ) was measured as described in section 2.3 (see also Figure 2.16). Comparing the contrast curves of the supplier recommended MIBK:IPA 1:3 to MIBK, it was found that using undiluted MIBK yields a 54% higher sensitivity (180 μC/cm^2 vs. 390 μC/cm^2) at the cost of a similar 53% contrast loss (3.7 vs. 7.8). The other four developers exhibit a sensitivity and contrast performance between those of MIBK:IPA 1:3 and MIBK. In particular, two developers, n-amyl acetate (ZED-N50) and IPA:water 7:3, provide a relatively high sensitivity and contrast as compared to the other developers.

The surfaces of the developed patterns were also inspected by optical microscopy, and it was found that all of the developers provide a uniform thickness loss with increasing dose except for xylene:methanol 3:1. Using xylene:methanol 3:1, the dissolution is non-uniform with certain exposed areas dissolving more rapidly than others, leaving a porous resist surface. Perhaps a technique such as ultrasonic agitation may be useful in this regard.

In Figure 5.3, comparing the contrast curves of SML and PMMA, both developed in MIBK:IPA 1:3 for 20 sec, it was found that SML is 71% less sensitive (390 μC/cm^2 vs. 228 μC/cm^2) than PMMA and has a 7% higher contrast (7.8 vs.

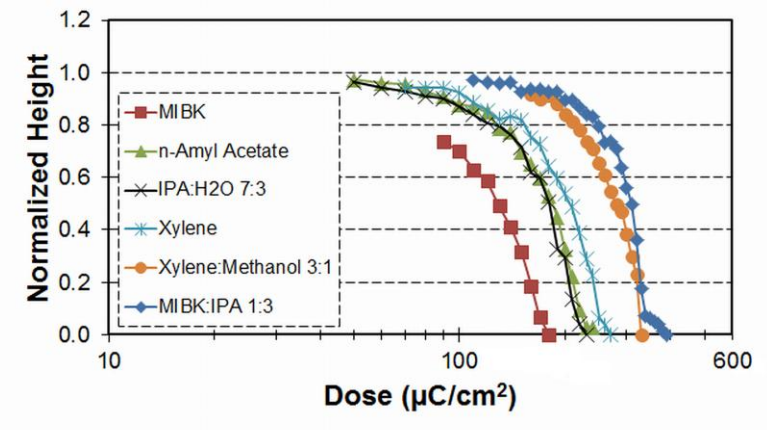

Figure 5.2 SML contrast curves generated using 30 keV on 300-330 nm thick resist. The development was performed for 20 sec in MIBK (squares), n-amyl acetate (triangles), IPA:water 7:3 (crosses), xylene (stars), xylene:methanol 3:1 (circles), and MIBK:IPA 1:3 (diamonds). Reprinted from [264] with the permission of the Crown. Copyright Act (Canada), S. 12 © 2013.

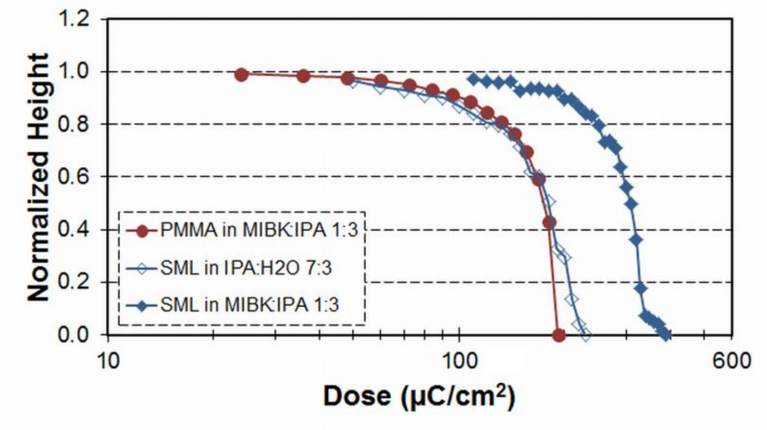

Figure 5.3 Comparison of SML (triangles) and PMMA (circles) contrast curves exposed at 30 keV and developed for 20 sec in MIBK:IPA 1:3 (filled symbols) and IPA:water (open symbols). Reprinted from [264] with the permission of the Crown. Copyright Act (Canada), S. 12 © 2013.

7.3). However, when SML is developed in IPA:water 7:3, a 41% sensitivity improvement (230 μC/cm^2 vs. 390 μC/cm^2) is realized as compared to SML in

MIBK:IPA 1:3, enabling the sensitivity of SML to be comparable to that of PMMA in MIBK:IPA 1:3. This behavior is similar to PMMA – the sensitivity of PMMA developed in IPA:water 7:3 improves by 30% as compared to PMMA developed in MIBK:IPA 1:3 [136]. The sensitivity improvement of SML is achieved with a minor trade-off in contrast – SML in IPA:water 7:3 has a 13% lower contrast (6.8 vs. 7.3) than SML in MIBK:IPA 1:3.

Furthermore, the IPA:water 7:3 mixture provides the highest contrast versus sensitivity trade-off. By arranging SML developers with increasing clearance dose as shown in Figure 5.4, it was found that IPA:water 7:3 has a higher than average contrast and the best (lowest) contrast-weighted-sensitivity. The quantity contrast-weighted-sensitivity has been introduced as a figure of merit (FOM) to factor in the sensitivity while selecting the developer with the best contrast. In Table 14, the contrast-weighted-sensitivity of SML in IPA:water 7:3 is compared to the six other resists cited in section 5.1.1 [264,265]. Analyzing the information in Table 14, we notice that only positive-tone ZEP resist (3.2-7.0) and negative-tone AZnLOF resist (4.2-18.3) have a lower contrast-weighted-sensitivity value than SML resist (33.8). In addition to the above analysis, the IPA:water 7:3 developer has other merits including cost, safety, and experience of the EBL community using it as a developer for PMMA [128] and ZEP [190] at both ambient and cold development conditions. In addition to the aforementioned developers, the development of SML in MIBK:IPA 1:3 at -15°C

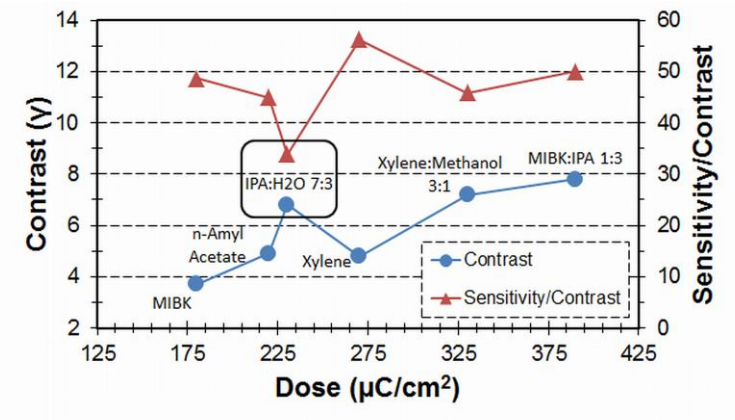

Figure 5.4. Comparison of SML contrast (circles) and contrast-weighted-sensitivity (triangles) for various developers. The quantity contrast-weighted-sensitivity has units of dose (μC/cm^2). Reprinted from [264] with the permission of the Crown. Copyright Act (Canada), S. 12 © 2013.

Table 14. Comparison of contrast-weighted-sensitivity (S/γ) of various resists. Reprinted from [264] with the permission of the Crown. Copyright Act (Canada), S. 12 © 2013.

Resist	Tone + / -	Voltage [keV]	Sensitivity (S) [μC/cm^2]	Contrast (γ)	S/γ	Ref.
PMMA	+	50	500	3.0	166.7	[3]
PMMA	+	50	1600	8.0	200.0	[3]
ZEP	+	20	30	4.3	7.0	[6]
ZEP	+	20	80	25.1	3.2	[6]
PMGI	+	30	631	6.7	94.2	[8]
PMGI	+	50	6310	3.3	1889.2	[9]
PMGI	+	100	12600	12.0	1049.1	[9]
HSQ	-	50	500	7.0	71.4	[11]
AZnLOF	-	100	22	5.2	4.2	[14]
AZnLOF	-	100	42	2.3	18.3	[14]
PS	-	20	250	1.5	166.7	[15]
PS	-	20	8000	4.4	1818.2	[16]
SML	+	30	230	6.8	33.8	[21]

cold development conditions was also attempted; however, due to the extremely low sensitivity (clearance onset >1,000 μC/cm^2), it was abandoned.

5.3.2 Dense grating fabrication

Based on the analysis of contrast curves, IPA:water 7:3 was selected as the preferred developer for fabricating dense, high AR gratings. Similar to PMMA, both IPA and water alone are poor or non-developers for SML resist but are effective in combination. The usage of ultrasonic agitation during development was chosen to help promote the dissolution of SML fragments as inspired by Yasin's work [136]. Since resist fragments tend to coil in poor solvents and exhibit a smaller radius of gyration, ultrasonic agitation may be expected to promote the rapid removal of these fragments, enabling a narrower grating trench [136]. As described in section 5.2.2, a brief rinse in low surface tension fluid was used to reduce the probability of pattern collapse. The surface tension of pentane (approximately 16 dyn/cm) and hexane (approximately 18 dyn/cm) is at least four times less than that of water (approximately 73 dyn/cm).

Figure 5.5 presents top-view grating micrographs of 70 nm pitch SML gratings in a 300-330 nm thick resist showing the effect of increasing line dose. The line width increases from 25 nm at 550 pC/cm (Figure 5.5(a)) to 32 nm at 750 pC/cm (Figure 5.5(b)) and to 40 nm at 950 pC/cm (Figure 5.5(c)) just prior to pattern collapse. Observing the top-view grating micrographs, clearance cannot

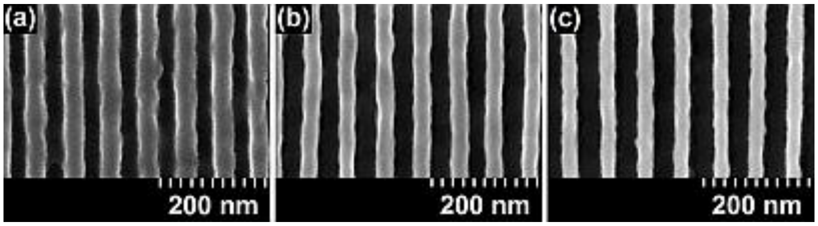

Figure 5.5 Micrographs of 70 nm pitch gratings patterned by 30 keV on 300-330 nm thick SML. Effect of dose on increasing line width (a) 550 pC/cm, 25 nm gap, (b) 750 pC/cm, 32 nm gap, and (c) 950 pC/cm, 40 nm gap. Data obtained for 20 sec ultrasonic development in IPA:water 7:3 and 2 sec pentane rinse. Reprinted from [264] with the permission of the Crown. Copyright Act (Canada), S. 12 © 2013.

be conclusively ascertained; however, this question is explored through cross-sectional micrographs ahead. Based on the observations from Figure 5.5, it is estimated that as low as 25 nm resolution with SML is readily achievable without resolution enhancement techniques. Furthermore, the gratings show relatively low LER.

The resolution limits (with thinner resists) were not explicitly pursued as this research focused on maximizing the AR, pattern density, and sensitivity by co-optimizing the exposure and development conditions. Given that the proximity effect appears to be of minor importance, if present at all (see Figure 5.1(a)), the results in Figure 5.5 are representative of the resist performance even without clearance and can be employed to co-optimize the resist thickness and process conditions if so desired.

In Figure 5.6, micrographs of cleaved SML resist are presented showing the effect of reducing the grating pitch from 150 (Figures 5.6(a) and 5.6(b)) to

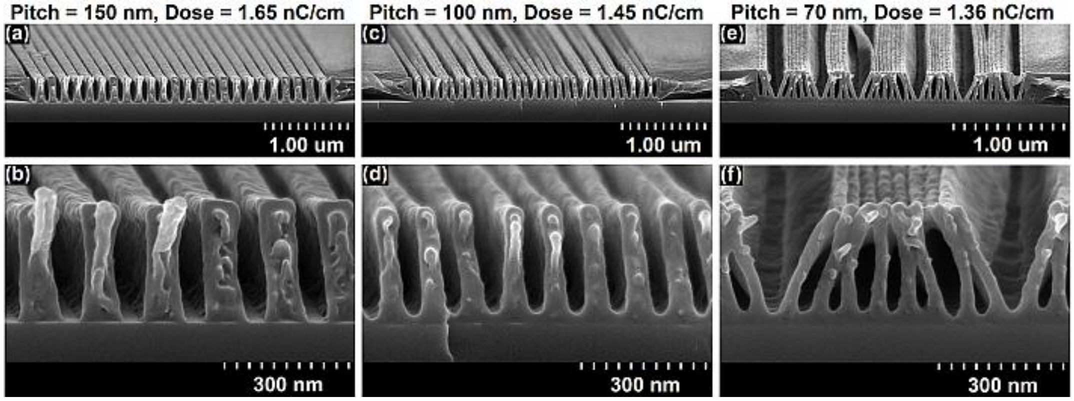

Figure 5.6 Cross-sectional micrographs of SML exposed at 30 keV on 300-330 nm thick resist. Achievable line width and pitch (a, b) 36-40 nm gaps in 150 nm pitch, (c, d) 33-40 nm gaps in 100 nm pitch, and (e, f) 30 nm sidewall in 70 nm pitch, yielding an approximate AR of 9:1 in all cases. The development procedure is identical to that in Figure 5.5. The resist was cleaved and coated with a 6 nm Cr layer before imaging. Reprinted from [264] with the permission of the Crown. Copyright Act (Canada), S. 12 © 2013.

100 nm (Figures 5.6(c) and 5.6(d)) and finally to 70 nm (Figures 5.6(e) and 5.6(f)). All micrographs are captured at a SEM tilt of 14° from normal. The upper row of micrographs (Figures 5.6(a), 5.6(c), and 5.6(e)) shows the complete patterned arrays, and the lower row of micrographs (Figures 5.6(b), 5.6(d), and 5.6(f)) shows zoomed-in micrographs taken near the center of the grating arrays. Observing the complete arrays, the gratings are uniform and no proximity effect can be noticed. It was observed that denser gratings require a higher dose for clearance and the resolution also improves. The highest density gratings that could be fabricated before pattern collapse were of 100 nm pitch in a 300-330 nm thick resist. In addition, 80 nm pitch gratings were also patterned (not shown); however, those also collapsed. From the micrographs in Figures 5.6(a-f),

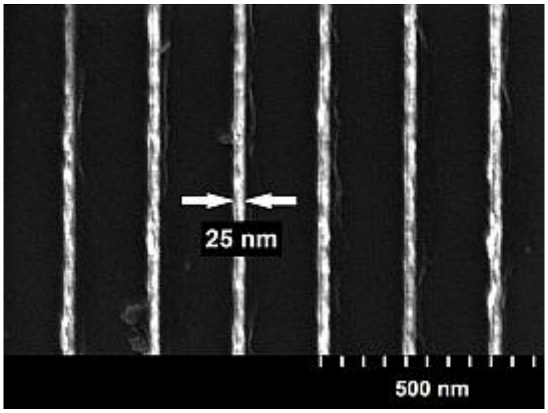

Figure 5.7 Micrograph of 25 nm wide lifted-off chromium gratings on silicon. The metallization (50 nm thickness) was performed by e-beam evaporation. Reprinted from [264] with the permission of the Crown. Copyright Act (Canada), S. 12 © 2013.

feature sizes between 30 and 40 nm are observed yielding a best case AR of 9:1 at 30 keV for all pitch values. It is clear that for 30 keV exposures, this AR is two to five times better than the resists reviewed in section 5.1.1. In some panels in Figure 5.6 (c, b, d), deformed resist profiles are observed. These deformations (bending, shrinkage) are a result of the imaging process due to the fragility of the resist [264] and not a result of the EBL exposure.

Finally, the lift-off results for SML are presented in Figure 5.7. The lift-off procedure using SML was found to be very efficient. Un-patterned SML may be readily stripped by acetone when rinsed with a wash bottle for a few seconds. Patterned SML with 50 nm of chromium metal was fully removed by acetone by immersing in an ultrasonic bath for 1 min. Figure 5.7 shows 25 nm wide chromium lines in a 200 nm pitch grating pattern exposed at 1,650 pC/cm. Considering that the chromium was deposited on a 300-330 nm thick resist film, this result implies that an even higher AR (=12:1) may have been obtained previously than observed (=9:1) during cross-sectional SEM due to the fragility of the resist.

5.4 Summary

In this chapter, a detailed characterization of SML electron beam resist has been presented with emphasis on high AR nanopatterning at high sensitivity. SML contrast curves were generated for a range of developers and through various analyses, an optimal developer was identified as IPA:water 7:3. Using this formulation, the sensitivity of SML was improved considerably over existing SML results (40%) and found to be comparable to benchmark PMMA resist without affecting the AR performance. Employing 30 keV EBL and ultrasonic development in IPA:water 7:3, an AR of 9:1 in 50 nm half-pitch dense grating patterns was achieved, representing over 100% improvement as compared to PMMA or ZEP. Through Cr metal lift-off, fabrication of 25 nm features (through 300-330 nm thick resist) was demonstrated.

A version of this chapter has been published in reference [264] (Mohammad et. al. 2013. Nanoscale Research Letters 8, 139 (7 pages)). Reprinted with permission. Copyright governed by Copyright Act (Canada), S. 12.

CHAPTER 6

EBL PROCESSING APPLICATIONS – SiCN RESONATORS

6.1 Nanomechanical resonators

Nanomechanical resonant devices and systems are used for a wide variety of applications in communications, signal processing, microfluidics, and ultrasensitive mass detection and analysis. In recent years, MEMS and NEMS resonators of the singly- and doubly-clamped cantilever configuration have attracted significant attention as platforms for chemical and biological sensing in both liquid and gas phases [209,266]. Such nanomechanical resonant devices have been used for sensing numerous gases, organic vapors, self-assembled monolayers, bacteria, viruses, DNA molecules, etc., [266] which paves the way for their use in applications of great contemporary importance such as the detection of pathogens, drugs, and explosives, among others. Furthermore, top-down (lithographic) machining approaches have allowed for the fabrication of large arrays of such resonant devices, with precise control over device positioning and dimensions, thereby enabling rapid, inexpensive, and highly-sensitive detection in the aforementioned applications.

6.1.1 Scale challenges

Resonators designed for chemical and biological sensing often require mass sensitivities down to a few zeptograms (few kDa). One approach for sensing such ultra-low masses is to employ ultra-fine resonators. Fabricating ultra-fine resonators requires that all dimensions of the cantilever portion be reduced as small as possible [266,267]. The sensing resolution (Δm) of cantilever-type resonators improves according to $\Delta m \propto w \times L^3$, where w & L are the resonator width and length, respectively [209]. However, reducing the dimensions is accompanied by various performance trade-offs. As the resonator lengths are reduced, the resonant frequency increases, and clamping (anchor) losses become significant as well [268]. Similarly, as the resonator widths are reduced, the *Q*-factor decreases [269]. Nevertheless, whereas reducing the resonator length is straightforward using high resolution lithographic approaches such as EBL, reducing the resonator width has been a prevailing fabrication challenge. This is due to the inherent resolution limitations of EBL and also due to the limited response of conventional resonator materials to demanding nano-machining processes. From a fabrication perspective, in order to reduce the resonator width and find solutions to energy loss mechanisms (e.g., anchor losses), a thorough understanding of high resolution EBL is required. Co-optimizing the exposure and development conditions with the assistance of numerical simulations can help to achieve ultra-narrow resonators as well as minimize the factors leading to energy loss.

6.1.2 Material challenges

In order to fabricate resonators at the deep nanoscale, selecting the resonator material is very important. A wide variety of materials have been used in this regard such as monocrystalline Si, poly-Si, Si_3N_4, SiC, AlN, TiN, etc. Resonators fabricated with crystalline materials (e.g., Si) are the easiest to measure; however, they are brittle and prone to mechanical failure. Silicon resonators as narrow as 45 nm (100 nm thick) have been fabricated [270]; however, the yield of these devices drops to near zero at lengths exceeding a few µm [269]. Similarly, polycrystalline materials (e.g., poly-Si) are also not resilient to processing requirements as these materials are prone to rapid etching and crack propagation at grain boundaries [271]. As compared to crystalline and polycrystalline materials, recent studies have shown that glassy materials have advantages for the fabrication of ultra-narrow resonators [269,272]. Silicon nitride (SiN) resonators as narrow as 50 nm (220 nm thick) have been fabricated with a 98% yield [272]. Similarly, titanium nitride (TiN) resonators as narrow as 30 nm (72 nm thick) have also been very recently fabricated [273]. These results indicate that employing glassy materials for the fabrication of ultra-narrow resonators is more promising.

6.2 SiCN resonator fabrication

Fischer *et al.* from the Evoy NEMSLAB [210] group recently reported the development and microstructural characterization of novel silicon carbon nitride (SiCN) thin films for the fabrication of nanomechanical resonators [211]. SiCN is a glassy material with a number of mechanical and processing benefits. For example, through a post deposition anneal, the thin film stress of SiCN can be controlled to access a broad range of compressive and tensile stress regimes [211]. In the same paper, Fischer *et al.* reported a surface micromachining process using which micron-scale (0.8-1.0 µm wide) singly- and doubly-clamped cantilevers were fabricated. These cantilevers achieved high *fQ* products exceeding the performance of silicon [211].

Fischer *et al.* further reported the development of a resonator nanomachining process combining both surface and bulk micromachining techniques [212]. Using this hybrid process, 430 nm wide (35 nm thick) SiCN resonators (revisit Figure 2.24) were fabricated with a high yield, and their corresponding mass sensitivities were reported to be in the low attogram (MDa) range while detecting proteins. This novel process enabled the resonators to be suspended several microns above the silicon surface and also eliminated the need for critical point drying (CPD), a key advantage for applications requiring repeated immersion in liquids [212]. Furthermore, employing an almost identical process as ref. [212], Guthy et al. [269] managed to fabricate SiCN resonators as narrow as 16 nm, indicating the excellent performance of the material.

The hybrid nanofabrication process developed by Fischer *et al.* [212] has been summarized in Figure 6.1 and briefly described herein. A 35 nm layer of SiCN was deposited on piranha cleaned silicon (100) wafers employing plasma enhanced chemical vapor deposition (PECVD by Trion Tech.) using ammonia (NH_3) and diethylsilane (DES) precursors. The films were annealed (MiniBrute furnace) for 5-8 hours at 500 °C to change the stress from compressive to tensile. Following a secondary piranha cleaning and a buffered hydrofluoric (BHF) etch, a 160 nm bi-layer stack of PMMA 950k/495k was spun cast. The PMMA bi-layer is patterned using 10 keV EBL, and the resist is subsequently developed at room temperature in MIBK:IPA 1:3 and rinsed in IPA. Following the EBL steps, the lower resolution PMMA 495k yields a comparatively wider base, which facilitates the lift-off pattern transfer process. A 30 nm layer of chromium is deposited using electron beam evaporation and the resulting Cr/PMMA bi-layer stack is lifted-off by immersing the samples for 5 min in acetone under ultrasonic agitation. The chromium patterns are further used as a masking layer while the SiCN 'device' layer is dry-etched using a 4:1 sulfur hexafluoride (SF_6) and oxygen (O_2) recipe for 30 sec (Trion Phantom II). The chromium masking layer is stripped by immersing the samples for 20 min in 'chrome etch', a stock solution comprising of ceric ammonium nitrate, nitric acid, and water. Finally, the SiCN

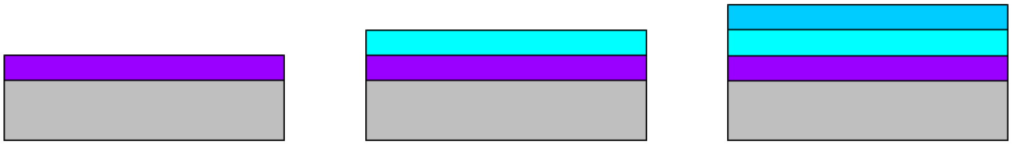

(1) PECVD 35 nm SiCN on Si 4:1 NH_3:DES 300 °C + 5-8 hr anneal at 500 °C

(2) Spin PMMA 495k

(3) Spin PMMA 950k – Total bi-layer thickness 160 nm

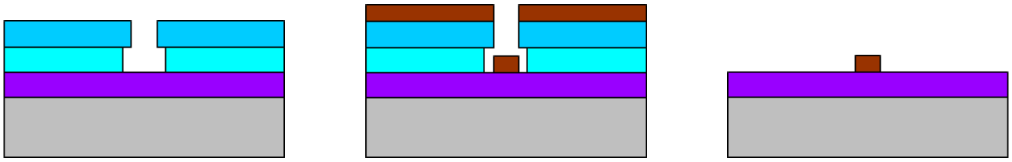

(4) EBL exposure 10 keV 20 µm and development MIBK:IPA 1:3 at 22 °C

(5) 30 nm chromium evaporation

(6) Acetone lift-off (5 min ultrasonic)

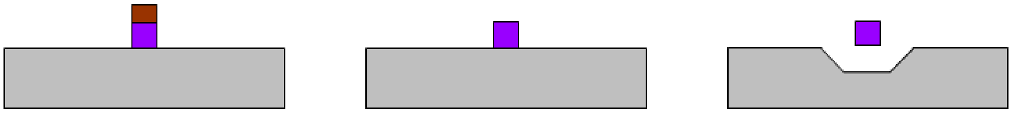

(7) SiCN RIE using 4:1 SF_6:O_2 (30 sec)

(8) Chromium etching (20 min)

(9) Si etch 35% KOH at 75 °C saturated with IPA

Figure 6.1 Original process flow for fabricating nanoscale SiCN resonators developed by NEMSLAB. Drawn based on process described in ref. [212].

resonators are released after a bulk silicon etch step conducted at 75 °C in IPA saturated potassium hydroxide (KOH) 35% solution. The released resonators are briefly rinsed in deionized water and gently blow-dried in a nitrogen flow.

In this work, we advanced further the process described above in collaboration with NEMSLAB [210]. Two resonator fabrication processes have been developed. First, we modified the above PMMA-based process to employ a single resist layer exposed using a low voltage and developed in chilled liquids [226]. This modified process enabled optimized fabrication of uniform sub-20 nm

SiCN resonators while reducing one processing step [226]. Second, we thoroughly redesigned the fabrication process to employ HSQ resist and the metal pattern transfer steps were eliminated [274]. This novel process enabled the fabrication of uniform sub-10 nm SiCN resonators while reducing three processing steps, as compared to the process summarized in Figure 6.2 [274]. Both of these latest SiCN resonator development efforts are discussed below.

6.3 PMMA resist fabrication approach

Aspect ratio (AR) considerations fundamentally limit the resolution achievable using a 160 nm PMMA bi-layer [269,212]. For this reason, a significantly thinner PMMA single layer has been used in this fabrication approach. In addition to reducing the AR requirement and improving resolution, a single PMMA layer simplifies the exposure and development co-optimization. In order to create the re-entrant profiles needed for lift-off within a single resist layer, low voltage exposures have been employed. The severe undercut pattern using 3 keV EBL has been shown previously in Figure 2.6(a) which enables replacement of bi-layer resist schemes with a single resist layer, as shown in Figure 6.2. Furthermore, cold development has been used to enhance the resolution further. In this way, a methodology has been developed for precisely controlling the resonator widths in the ultra-narrow regime of 11–20 nm. Figure 6.3 shows examples of high density chromium gratings fabricated with the above

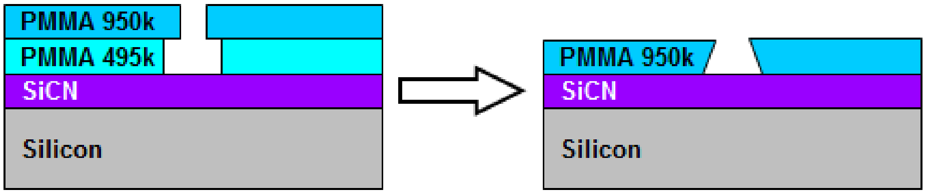

Figure 6.2 Undercut pattern created by using low voltage EBL exposure enables replacement of bi-layer resist schemes (left) with a single resist layout (right).

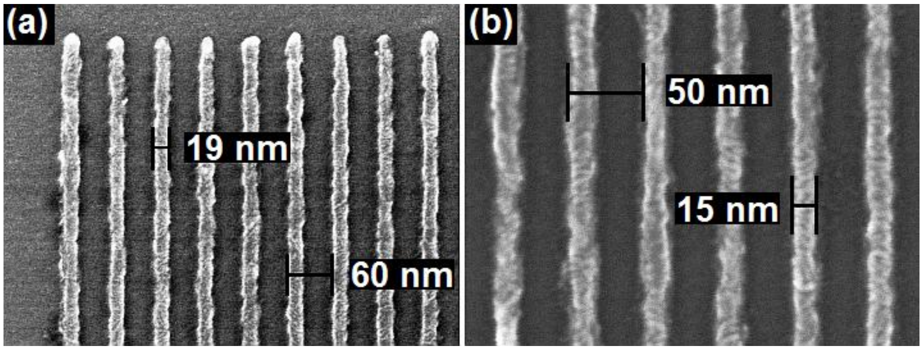

Figure 6.3 Lift-off results showing (a) 20 nm wide chromium lines in a 60 nm pitch grating, and (b) 15 nm wide chromium lines in a 50 nm pitch grating, both fabricated using 3 keV exposure of a single PMMA 950k resist layer and developed at -15 °C in MIBK:IPA 1:3. Reprinted with permission [12]. Copyright © 2012 Springer.

low voltage and cold development approach. Additionally, as part of this work, various alternative anchor designs have been modeled (using the EBL Simulator [189]) and fabricated, in pursuit of reduced anchor losses.

6.3.1 Resonator fabrication process (1)

Figure 6.4 summarizes the first fabrication process employed in this research. Similarly to the process described in Figure 6.1, a 50 nm thick SiCN device layer was deposited on a silicon wafer using PECVD. The thickness

(1) PECVD 50 nm SiCN on Si 4:1 NH_3:DES 300 °C + 5-8 hr anneal at 500 °C

(2) Spin PMMA 950k thickness 45 nm

(3) EBL exposure 3 keV 10 µm and development MIBK:IPA 1:3 at -15 °C

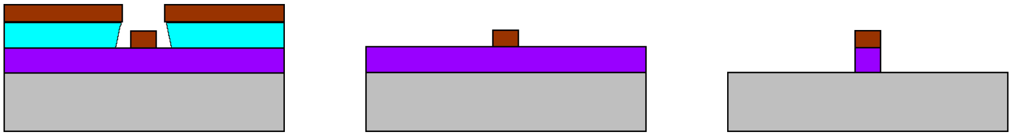

(4) 12 nm chromium evaporation

(5) Acetone lift-off (3 min ultrasonic)

(6) SiCN RIE using 4:1 SF_6:O_2 (30 sec)

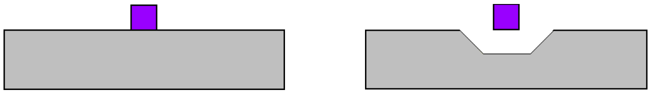

(7) Chromium etching (20 min)

(8) Si etch 32% KOH at 75 °C saturated with IPA

Figure 6.4 Process flow for fabricating nanoscale SiCN resonators using a PMMA-based process employing low keV exposures and cold development. Drawn based on process described in reference [226].

variation of the SiCN device layer was measured (Filmetrics F-50) to be within 10% across the wafer. The SiCN coated wafer was annealed, resulting in a stress of 100-150 MPa (as measured by Flexus 2320) and subsequently diced into small (1x1 cm^2) chips. Each chip was piranha cleaned and baked. In distinction to the process described in Figure 6.1, the chips were spin-coated with a single 45 nm thick PMMA 950k resist layer using a 1% PMMA solution in anisole. An array of doubly-clamped resonators were patterned using a Raith 150^{TWO} EBL system at 3 keV, 10 µm aperture. The resonator supporting pads were exposed at 600 µC/cm^2, and the desired resonator line widths were achieved by varying the single pixel line (SPL) dose from 1.4 to 3.0 nC/cm and by varying the Raith CAD defined line widths from 0 (SPL) to 110 nm. The exposed resist was then developed for 5 sec in MIBK:IPA 1:3 at a decreased temperature of -15 °C and rinsed for 15 sec in -15 °C IPA.

In addition to the shape and resolution of the resulting nanostructures, the usage of the combined low voltage, cold development EBL approach has several other merits. Employing low voltage exposures improves the process throughput [68,97,100] which is important for fabricating large resonator arrays. Additionally, employing cold development [128,131,140,132,133,215] improves the line edge roughness (LER), and increases the resistance of the patterned PMMA against post-exposure degradation such as wall collapse and fusion, thereby increasing the process window and robustness.

Following the EBL exposure and development steps, a 12 nm thick chromium film was deposited by electron beam evaporation. The resulting chromium/PMMA stack was lifted-off using a 3 min immersion in acetone under the influence of ultrasonic agitation. The re-entrant resist profiles and significantly thinner chromium layer enable the acetone solvent to access all areas of the trench and lift-off the metal/resist stack without leaving any resist scum sticking to the SiCN or deposited metal. The thinner chromium layer is sufficient to act as a masking layer for the SiCN RIE and easily removed afterwards using chrome etchant. There were no changes to the SiCN RIE or chrome etching steps. Finally, the SiCN resonators are released by etching the silicon substrate in a hot (75 °C) 32% KOH etch saturated with IPA for 40-100 sec etch durations. The slightly weaker [275] KOH solution is used for increased control over the etching step.

6.3.2 Sub-20 nm resonator structures

As a result of the nanofabrication process described above, arrays of nanoscale SiCN resonators were fabricated with lengths between 1-20 µm, and widths ranging from 11-280 nm. A representative micrograph of one such resonator is provided in Figure 6.5 [12]. In this micrograph, the resonator cantilever portion is 5 µm long, 50 nm thick, and is 16 ± 2 nm wide over the entire length. We observed that the minimum achievable line widths of the resonators depends on the desired length. In general, the narrowest resonators with sub-15 nm widths could only be fabricated for resonator lengths of up to 2 µm; resonators with widths between 14-18 nm could only be fabricated for lengths of up to 10 µm; and beyond 10 µm lengths, resonator widths of 20-28 nm were required. Resonators with larger length-to-width aspect ratios were prone to mechanical failure predominantly near the clamping points. However, we believe that resist and EBL limitations contribute greatly to this 'mechanical' failure, as described ahead.

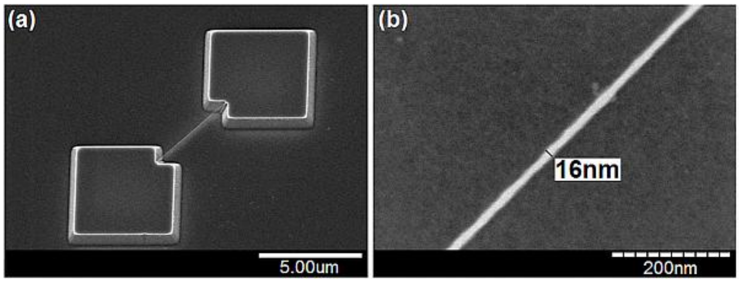

Figure 6.5 Top-view micrographs of (a) a sub-20 nm wide, 5 µm long SiCN resonator, and (b) a magnified image of the bridge portion showing a width of 16 ± 2 nm, fabricated using a PMMA-based process. Reprinted with permission [12]. Copyright © 2012 Springer.

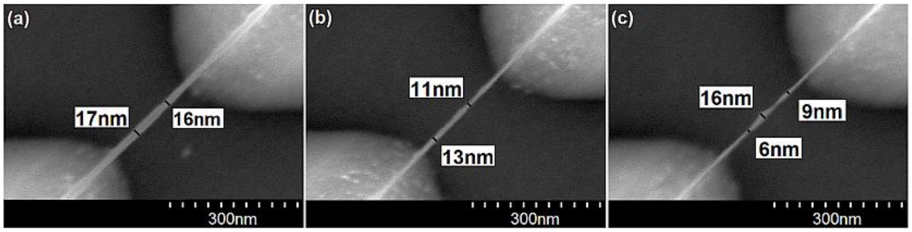

Figure 6.6 Top-view micrographs of 1 µm long SiCN resonators measuring (a) 16 ± 2 nm exposed at 2.0 nC/cm, (b) 13 ± 3 nm exposed at 1.6 nC/cm, and (c) 11 ± 5 nm exposed at 1.5 nC/cm. Reprinted with permission [226]. Copyright © 2010 American Vacuum Society.

The resonator widths may be controlled by two different methods. For the narrowest resonators (up to 30 nm wide), the line widths are controlled by varying the SPL line exposure doses; whereas for the wider resonators (40-280nm), the line widths are controlled by applying a single exposure dose while varying the Raith CAD designed feature widths. Precise line width control by SPL line doses is demonstrated for 1 µm long resonators in Figure 6.6 [12]. By applying a dose of 2.0 nC/cm, a 16 ± 2 nm resonator width can be fabricated as shown in Figure 6.6(a). Gradually reducing the dose to 1.6 nC/cm and 1.5 nC/cm, resonators measuring 13 ± 3 nm (Figure 6.6(b)) and 11 ± 5 nm (Figure 6.6(c)), respectively, were fabricated. As the line dose during exposure is decreased, the resonator width after release also decreases as expected. However, when approaching approximately 10 nm widths, the line width non-uniformity visibly increases. This resonator 'edge roughness' increases the probability of mechanical failure in ultra-narrow resonators. In the case of wider resonators, the Raith software-defined feature widths are varied from 10 to 110 nm, while the line dose is kept constant at 2.0 nC/cm. This enables the width of the resonators to vary in the range of 40-280 nm (not shown) [226].

The resonant characteristics of a large set of the fabricated resonators, with varying dimensions, were investigated by C. Guthy from NEMSLAB [226]. The detailed measurement setup has been described elsewhere [269]. In brief, the resonators were actuated with a piezoelectric disk in low vacuum (10^{-2} Torr), and the resonant characteristics were measured using optical interferometry. Depending on the device length, resonance frequencies between 7-40 MHz were measured. Each resonance spectrum was used to extract the Q-factor, which measured between 12,000-17,400. These and other results have been described in detail in ref. [226]. Based on a large set of measurements, surface and anchor losses were identified as the dominant energy loss mechanisms. In pursuit of lower anchor losses, various alternative anchor designs were modeled with the EBL simulator [189] and subsequently fabricated [226].

6.3.3 Modeling and fabrication of anchor designs

The anchor point is a major factor in determining mechanical losses for relatively short resonators; therefore, its optimal fabrication is key to ensuring high resonator performance. A sketch of a typical anchor area is shown in Figure 6.7(a). The orientation of the anchor is designed such that the silicon etch planes are matched, and undercut (at the time of release-etch) is minimized [269,212]. The exposure and development of the resonator anchor area has been simulated using the EBL simulator [189] for our 3 keV, -15 °C cold development conditions. As described previously, the EBL simulator allows the user to visualize the results after both exposure and development stages. The anchor area post-exposure and post-development simulated profiles are shown in Figures 6.7(b) and 6.7(c), respectively.

The simulated results in Figure 6.7(c) accurately resemble the experimentally developed PMMA resist profile shown in Figure 6.7(d). The contribution of backscattered electron proximity effects is considerably less at the low voltages employed; however, proximity effects due to forward scattered electrons cause rounding of the anchor point. After the final release etch, the effect of the anchor rounding is to increase the overhanging area, which contributes toward anchor losses. This overhanging area is the high-contrast region (due to thinner material) around the anchor point shown in Figure 6.7(e).

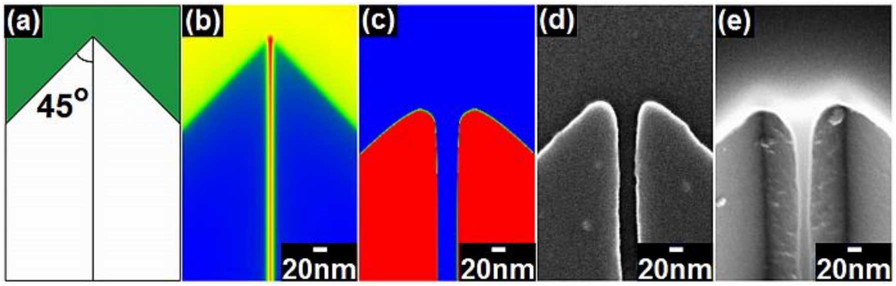

Figure 6.7 (a) Sketch of a typical anchor design, (b) the computed yield of scission (*exposure plot*), (c) the computed dissolution profile (*development plot*), (d) a micrograph of the developed PMMA resist, and (e) a micrograph of the released anchor portion. Reprinted with permission [12]. Copyright © 2012 Springer.

The exposure and development conditions in Figure 6.7 have already been optimized, and therefore a different strategy is required to reduce the overhanging area. One strategy is to use proximity effect correction (PEC) [276], an approach used to optimize the doses when complex structures involving multiple length scales, and in proximity of each other, are being fabricated. However, PEC routines require the definition of a large set of parameters, and do not provide the flexibility to change the geometry of the anchor area. Furthermore, considering the complexity and time-consuming serial nature of EBL, expensive trial-and-error search of optimal anchor geometry and process parameters is ruled out. Therefore, we proceed towards the EBL simulator assisted fabrication of alternative anchor designs.

A number of alternative anchor designs were modeled and tested with the aid of the EBL simulator [189]. Two of the most promising anchor designs are

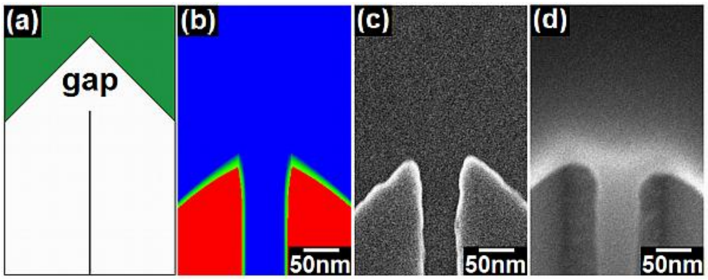

Figure 6.8 (a) Diagram of an alternative anchor design with an optimized pad-resonator gap of 170 nm, (b) the corresponding computed dissolution profile, compared with micrographs of (c) the developed PMMA resist showing sharper corners as compared to Fig. 6.7(d), and (d) the released SiCN anchor point. Reprinted with permission [226]. Copyright © 2010 American Vacuum Society.

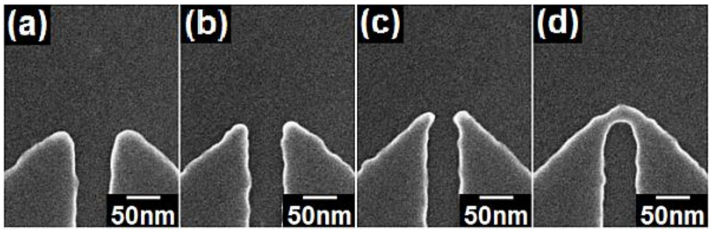

Figure 6.9 Top-view micrographs of the developed PMMA resist at the anchor point using the alternative anchor design described in Fig. 6.8(a) for various pad-resonator gaps: (a) 155, (b) 170, (c) 190, and (d) 200 nm. Reprinted with permission [226]. Copyright © 2010 American Vacuum Society.

presented here. The first alternative anchor design aims to sharpen the anchor point by defining a gap between the pad and resonator at the design stage, as shown in Figure 6.8(a). This design exploits the movement of the resist-developer interface (the dissolution front) at the development stage such that the pad and resonator *just connect*, yielding a sharp anchor point. However, in order to yield a sharp anchor point, the pad-resonator gap needs to be optimized. An optimized gap of 170 nm was obtained by modeling, as shown in Figure 6.8(b), and experimentally validated, as shown in Figure 6.8(c). However, as shown in Figure 6.8(d), after the release etch there is some rounding in the SiCN layer as compared to the otherwise sharp corners seen at the resist stage (Figure 6.8(c)). One hypothesized explanation for this rounding may be the effect of the etchant contact angle and surface area minimization effects at the release etch stage. Regardless of the slight rounding, the amount of overhanging mass has been visibly reduced as compared to Figure 6.7(e).

This particular anchor design also provides insight into the exposure and development process as well as a way of fine tuning the anchor geometry as shown in Figure 6.9. Gaps of 155, 170, and 190 nm cause the anchor geometry to change in a controllable manner from round to straight and to a cusp, as shown in Figures 6.9(a), 6.9(b), and 6.9(c), respectively. Finally, at a gap of 200 nm, the size of the gap overcomes the resist-developer interface diffusion rate, and the pad separates from the resonator, as shown in Figure 6.9(d).

The second alternative anchor design aims to isolate the resonator from the overhanging mass of the anchor point, and therefore overcome the issue of anchor rounding. This design is shown in Figure 6.10(a) and resembles an empty region in the shape of a barn-top or an inverted "V". This approach of 'removing material' is opposite to the idea of 'adding serfs' [277] to gain fine control over design characteristics. The two sides of the anchor design are related by the

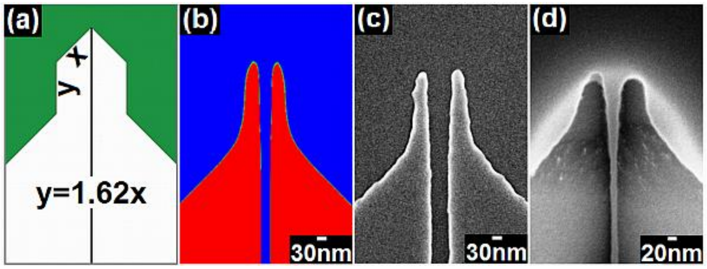

Figure 6.10 (a) Diagram of an alternative anchor design with an optimized side width of x = 165 nm, (b) the corresponding computed dissolution profile, compared with micrographs of (c) the developed PMMA resist, and (d) the released SiCN anchor point. Reprinted with permission [226]. Copyright © 2010 American Vacuum Society.

golden ratio y = 1.618x. Using the EBL simulator, an optimized value of x = 165 nm was obtained and experimentally verified as shown in Figure 6.10(c) and 6.10(d). The micrograph for the released resonator (Figure 6.10(d)) demonstrates that the overhanging mass (higher contrast area) is clearly disconnected from the resonator. In terms of reducing the overhanging mass, this inverted "V" design is clearly superior. The amount of reduced overhanging mass shown in Figure 6.10(d) is approximately 50 nm per anchor. In this work, the resonant characteristics of the devices fabricated with alternative anchor designs were not measured; however, this research forms a suitable foundation for studying the impact of anchor losses on nanoscale resonators.

6.4 HSQ resist fabrication approach

The SiCN resonator fabrication processes described thus far employ positive-tone PMMA resist and hence require a metal layer to (i) invert the EBL-defined pattern, and to (ii) function as an etch mask. At the deep nanoscale, metal lines develop a pronounced roughness as the feature dimensions approach the grain size of the metal. This limitation challenges the process uniformity and reproducibility. Moreover, at sub-10 nm dimensions, we approach the PMMA resist nodule size, which adds to the aforementioned challenge. To circumvent this problem, the SiCN resonator fabrication process has been thoroughly redesigned employing HSQ as both EBL resist and SiCN etch mask. In this way, the metal layer (and the corresponding process steps) have been eliminated yielding a much simpler process. Various development strategies have been investigated, and a combined hot and HF-trimming assisted development process has been employed, yielding resolution and process advantages. In this way, a methodology has been developed for precisely controlling the resonator widths in the sub-10 nm regime.

6.4.1 Resonator fabrication process (2)

Figure 6.11 summarizes the redesigned SiCN resonator fabrication process employing HSQ resist. An approx. 50 nm thick SiCN layer was deposited on silicon and annealed according to the processes described previously in sections 6.2 and 6.3.1. As deposited, the SiCN films exhibited compressive stress (-646 MPa); however after the annealing process, the films average stress changed to tensile (390 MPa). Following piranha cleaning and baking of the SiCN

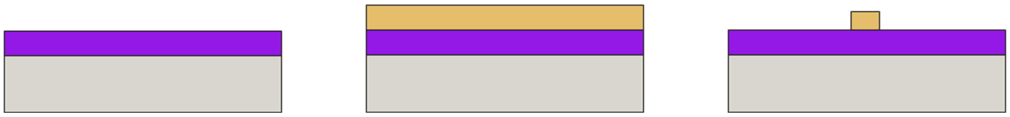

(1) PECVD 48 nm SiCN on Si 4:1 NH_3:DES 300 °C + 5-8 hr anneal at 500 °C

(2) Spin HSQ (1% XR-1541) thickness 26 nm

(3) EBL exposure 30 keV 10 µm and 25% TMAH development

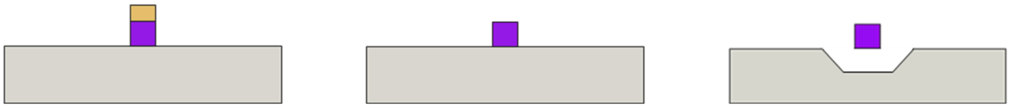

(4) SiCN RIE using 4:1 SF_6:O_2 (14 sec)

(5) BHF HSQ strip (30 sec) followed by H_2O rinse

(6) Si etch 28.3% KOH at 75 °C saturated with IPA

Figure 6.11 Process flow for fabricating nanoscale SiCN resonators using a HSQ-based process employing moderate keV exposures and hot development. Drawn based on process described in references [274,12].

samples, a single 26 nm thick HSQ layer was spun cast on the SiCN layer using a 1% XR-1541 solution in MIBK. An array of doubly clamped resonators were patterned using a Raith 150^{TWO} EBL system at 30 keV using 10 µm aperture. The doses used to expose the resonators and pads varied from 3.0-16.0 nC/cm and from 1.0-5.0 mC/cm^2, respectively. To avoid rastering artefacts [12] due to the higher inherent resolution of HSQ, relatively small line and area exposure step sizes of 2 nm and 10 nm, respectively, were used. The exposed samples were developed using three different recipes as outlined in Table 15.

Following exposure and development, the cross-linked HSQ patterns were used as an etch mask for the SiCN RIE step. The 4:1 SF_6:O_2 RIE duration was reduced to 14 sec, from 30 sec used in previous recipes. This RIE duration

Table 15. HSQ development recipes used in this research. Reprinted with permission [274]. Copyright © 2011 Elsevier.

Recipe	Developer Formulation
(A)	75 sec dip in 25% TMAH
(B)	75 sec dip in 50 °C 25% TMAH
(C)	75 sec dip in 50 °C 25% TMAH + 30-60 sec dip in 2000:1 H_2O:BHF + 75 sec dip in 50 °C 25% TMAH

reduction was necessitated by the etch rate selectivity of SiCN over HSQ, which was found to be approximately 2.5:1. A 30 sec BHF etch (10:1 HF:NH_4F) was used to strip the cross-linked HSQ layer which was followed by a 150 sec safety rinse in deionized (DI) water. The resonators were finally released by wet etching in IPA saturated hot (75 °C) 28.3% KOH solution for etch durations ranging from 30-45 sec. Using this wet etch recipe, an silicon etch rate of approx. 13 nm/s is obtained yielding an etch depth ranging between 400-600 nm.

Table 15 summarizes the development recipes used in this work. All of the recipes use 25% tetra methyl ammonium hydroxide (TMAH) developer in water. Recipe (A) is a standard room temperature process, recipe (B) uses hot 50 °C TMAH development [107,156,158,161,162] and recipe (C) is a modified multi-step development process adapted from Lee et al. [109]. Lee et al. used a multi-step development process where a very dilute HF (4000:1 H_2O:HF) dip is incorporated between two room temperature 25% TMAH development steps

[109]. The changes in recipe (C) with respect to the recipe of Lee et al. include (i) replacing room temperature TMAH with hot 50 °C TMAH development, (ii) increasing the HF concentration, and (iii) employing BHF instead of HF. All of the developed samples were rinsed in DI water and dried in flowing N_2.

As described previously, the key advantage of this process is using HSQ as both resist and SiCN etch mask. However, to employ HSQ as the etch mask, the HSQ cross-link density must be sufficient to withstand the RIE process. For properly cross-linking HSQ, merely exposing the sample at the minimum onset dose is insufficient, and a higher dose is necessary [107]. At the same time, over-exposing HSQ creates partly cross-linked low molecular mass siloxane-line ($HSiO_x$) scum [109] on pattern sidewalls and around dense features. This siloxane-line scum is insoluble in TMAH and is unwanted because it negatively affects the uniform, accurate, and high resolution RIE pattern transfer from HSQ to SiCN. In Figure 6.12(a), this scum can be seen around the anchor point and on the resonator device sidewalls, after the sample was developed in recipe (A) and subjected to RIE.

Developing HSQ in hot TMAH (recipe (B)) is helpful in the removal of this scum [107] in addition to improving the resonator resolution. However, these improvements come at the cost of sensitivity. As this scum consists of a non-stoichiometric silicon oxide, it can also be etched away using a dilute BHF rinse. Therefore, recipe (C) can be used as an alternative to remove this scum. In fact,

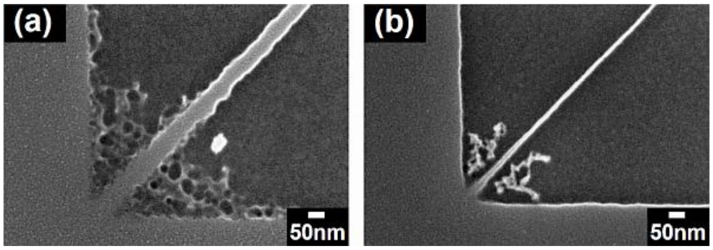

Figure 6.12 (a) Top-view micrographs of the un-released SiCN resonator at the anchor point developed using (a) recipe (A) with resonator width 48 ± 5 nm, and (b) with recipe (C) with resonator width 15 ± 2 nm. The pad dose used in both cases was 3.0 mC/cm^2. Reprinted with permission [274]. Copyright © 2011 Elsevier.

due to the usage of dilute BHF, recipe (C) provides a number of other process advantages such as (i) it prevents the development process from saturating which improves contrast [109], and (ii) it also trims the patterns [108] which further enhances the resolution. In light of these reasons, recipe (C) was used for the production samples.

The anchor area after development with recipe (C) and RIE is shown in Figure 6.12(b). It is clear that using recipe (C) helps to clean the unwanted siloxane-like scum, which prevents overhanging material in the anchor area. In addition, recipe (C) reduces the line edge roughness and provides ample line width trimming. The resonator widths measured in Figure 6.12(a) and 6.12(b) are 48 ± 5 nm and 15 ± 2 nm, respectively. From our survey of numerous samples, the trimming rate in our process is estimated to be as high as 20 nm/min. This is considerably higher than previously reported values [109] and [108]; however, this can be explained in light of our modified recipe (C) using (i) BHF instead of

HF, and (ii) hot development in place of room temperature development; both of which remove partly exposed HSQ rapidly.

6.4.2 Sub-10 nm resonator structures

Utilizing the above processes, arrays of SiCN resonators of various lengths and widths were fabricated. Figure 6.13(a) shows a sub-10 nm wide, 5 µm long doubly-clamped SiCN resonator. The pad and resonator doses were 2.5 mC/cm^2 and 9 nC/cm, respectively, and development recipe (C) was used. Figure 6.13(b) shows a magnified top-view micrograph from the centre of the resonator measuring 9 ± 1 nm. Additional micrographs of the anchor area of this resonator are provided in Figure 6.14. Both Figure 6.14(a) and 6.14(b) show that little or no residual scum is visible at the anchor point, and the surfaces and edges are very clean. The areas around the anchor point show very minor overhang. Finally, both figures show that the resonator width is uniform and less than 10 nm along the entire length. These results demonstrate that by co-optimization of exposure and development conditions, proximity effects can be avoided or compensated without the use of complicated correction algorithms. Resonators of similar resolution can also be obtained using single step room temperature recipe (A) by over-etching (etch biasing) in the RIE step. However, any approach incorporating etch biasing is generally not preferred as the process uniformity is difficult to control. Moreover, with recipe (A) the siloxane-like scum is not removed contributing to non-uniformity and overhanging material at the anchor area.

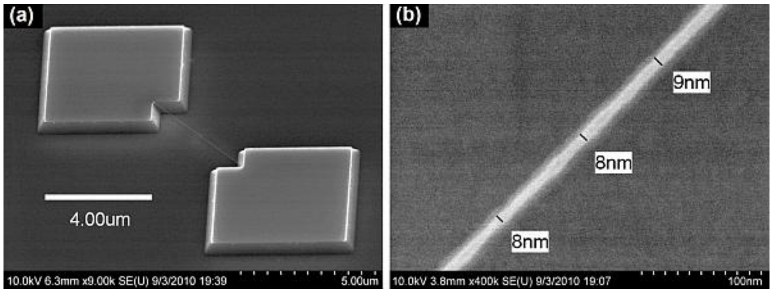

Figure 6.13 Micrographs of a sub-10 nm wide, 5 µm long, and 48 nm thick doubly-clamped resonator: (a) profile image, and (b) magnified top-view image measuring 9 ± 1 nm. The pad and resonator doses were 2.5 mC/cm^2 and 9 nC/cm, respectively. Reprinted with permission [12]. Copyright © 2012 Springer.

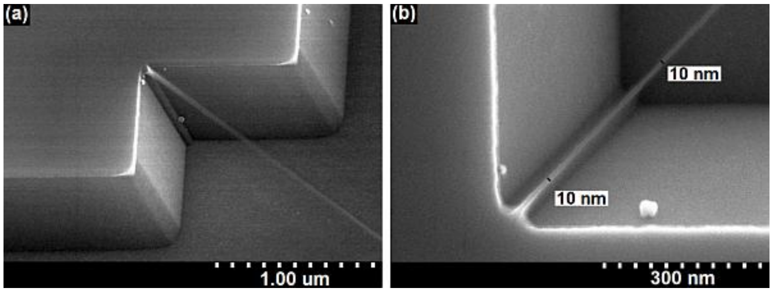

Figure 6.14 Micrographs of the anchor area: (a) tilt-view showing anchor features, minimal overhang, and clearance, and (b) top-view showing resonator uniformity. Reprinted with permission [12]. Copyright © 2012 Springer.

Similarly, using recipe (B), sub-10 nm features can be obtained; however, a higher dose is required and full removal of siloxane-like scum is not guaranteed.

Figure 6.15(a) and 6.15(b) show SiCN lines of 7 nm and 5 nm widths fabricated using recipes (B) and (C), with line doses of 13.0 and 5.0 nC/cm, respectively. The two times longer development time made possible by recipe (C) allows for a significantly lower dose to be applied. The structures in Figure 6.15

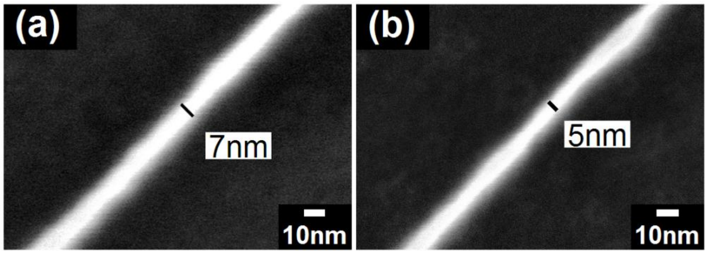

Figure 6.15 Micrographs of the un-released SiCN resonator masking layer showing the minimum width achieved using (a) hot TMAH recipe (B), and (b) using hot TMAH-BHF-TMAH recipe (C). Reprinted with permission [274]. Copyright © 2011 Elsevier.

are from samples different to those used in Figure 6.13 and 6.14. These figures demonstrate the narrowest patterns detected before the KOH release etch, representing the high potential of our process. In practice, however, the 9 ± 1 nm bridge shown in Fig. 6.13 and 6.14 represents the tiniest structures that we successfully released at this time, whereas the narrower structures did not release properly and would collapse. Critical point drying, a non-essential step for the present process, may help to fabricate approximately 5 nm wide resonator structures in the future; however, we may also be reaching the mechanical limit of the SiCN material for the current length regime which spans over several microns. In addition to fabricating even narrower resonators, a key challenge would be measuring the resonance characteristics of sub-10 nm wide resonators – a task not pursued in this work.

6.5 Summary

In this chapter, our research on doubly-clamped cantilever resonator fabrication methods at the deep nanoscale using novel SiCN material [211] is presented. Initially an existing PMMA-based process was enhanced by incorporating low voltage electron beam exposures and cold development. Using this modified process, precise control over resonator line widths in the sub-20 nm scale was demonstrated. In addition the resonator anchor point was thoroughly investigated with the aid of the EBL simulator and two new anchor designs were proposed. Based on modeling and experimental validation, an inverted "V" shaped anchor point design was considered optimal.

However, the first process was limited with regards to the uniform fabrication of resonators below 15 nm dimensions. Therefore, a second and thoroughly redesigned, HSQ-based process was introduced. In this process, the HSQ layer served both as the resist and SiCN etch mask, and novel HSQ hot- and multi-step development strategies were employed. This simplified and highly optimized process enabled the fabrication of uniform sub-10 nm wide and 5 µm long resonators with the demonstrated potential to fabricate even narrower resonators at the 5 nm scale. To the best of our knowledge, these are the narrowest suspended structures of such length fabricated to-date using a direct write lithographic technique.

CHAPTER 7

CONCLUSIONS

7.1 Significant contributions

Electron beam lithography (EBL) is an enabling technology for numerous applications of interest in academia and industry. Development of fabrication strategies at the deep nanoscale is central to advancing EBL technology; however, processing at such length scales requires an in-depth understanding of the relevant molecular mechanisms. The focus of this thesis is on understanding, optimizing, and applying EBL for nanoscale patterning. As part of this research, both experimental and modeling efforts were undertaken.

This work represents the most comprehensive examination of the influence of EBL process parameters on dense grating process windows for both PMMA and ZEP resists. Special emphasis is laid on studying the impact of the development stage parameters in order to understand the post-exposure development process. The EBL development stage is further investigated using molecular dynamics (MD) simulation, and the PMMA fragment-developer interactions are analyzed using the Flory-Huggins theory. Optimized processing strategies for dense grating fabrication are applied towards (i) the development of a high sensitivity and high aspect ratio nanopatterning process for novel SML resist, and for (ii) the development of an ultra-high resolution SiCN resonator fabrication process. The significant contributions and outcomes of this thesis can be summarized as follows:

- The impact of a wide range of EBL process parameters and their intricate interdependencies on process window fidelity and sensitivity is thoroughly investigated, and compared to the results obtained from contrast curves. Through the study of process windows and contrast curves, EBL processing strategies are developed and high resolution processing limits in PMMA and ZEP resists are explored. Uniform, sub-20 nm features in both PMMA and ZEP resists are obtained in 60 nm thick resist with 13 nm features in 40 nm pitch ZEP being our best and state-of-the-art results for a positive-tone resist.

- Through the study of dense grating process windows, various pattern degradation mechanisms and nanostructure morphologies are explored. The micellization pattern degradation mechanism and the conditions leading to this phenomenon have been identified for the first time. In addition, the study of process windows has led to the first reporting of negative-tone ZEP gratings. Negative-tone ZEP has been found to be interesting because of its quicker (higher sensitivity) tone reversal as compared to other positive-tone resists and its ability to be patterned at the deep nanoscale (23 nm features demonstrated).

- The process window data obtained in this work is used to fit a semi-empirical dissolution model (in collaboration with Dr. Taras Fito) with the goal of parameterizing an in-house developed EBL simulator.
- A unique application of the MD simulation technique to study the EBL dissolution process is presented. In this work, the thermodynamic, kinetic, and statistical-mechanical aspects of the dissolution of small PMMA fragments in MIBK and IPA developers are examined. By employing Flory-Huggins solution theory, the PMMA fragment-developer interaction parameters are calculated using data obtained from MD simulations. These calculations reveal that PMMA fragments larger than three monomers exhibit a slightly stronger attractive interaction with MIBK as compared to IPA, in line with expectation; however, this observation is reversed in the case of PMMA monomers, dimers, and trimers. In the case of these very small fragments, a stronger tendency to aggregate in MIBK as compared to IPA was observed, in agreement with their relatively weaker affinity to MIBK. In addition, the diffusivity of all PMMA fragments was found to be nearly two times higher in MIBK as

compared to IPA. This observation suggests that kinetic factors play a major role in the dissolution behavior of PMMA in various developers.

- An in-depth study of various developers for novel SML resist is conducted using contrast curves and dense gratings tests. IPA:water 7:3 was found to be the best developer, improving the sensitivity of SML by 40% as compared to existing results without affecting the aspect ratio (AR) performance of the resist. Employing a carefully considered process, an AR of 9:1 in 100 nm pitch dense gratings is achieved at a sensitivity comparable to PMMA. Through chromium metal lift-off, fabrication of 25 nm features (through 300-330 nm thick resist) is also demonstrated. All of these achievements with SML have not been previously reported.
- Two highly optimized SiCN resonator fabrication approaches are presented. Employing a PMMA-based, low voltage exposure and cold development process, sub-20 nm wide SiCN resonators are fabricated. To further improve the resonator dimensions, a simplified HSQ-based, medium voltage exposure and hot multi-step development process is designed. This process enables the fabrication of uniform sub-10 nm wide and 5 µm long SiCN resonators, constituting a world record! In addition, the resonator anchor point is thoroughly investigated with the aid of the EBL simulator and two new anchor designs are proposed. Based on

modeling and experimental validation, an inverted "V" shaped anchor point design is considered optimal.

7.2 Recommended future work

Building on this research work, a number of further developments in each of the above projects can be proposed.

- The research on EBL process windows can be extended to include the impact of a number of other process parameters such as substrate, resist thickness, anti-charging top-coatings, etc. Such an investigation can further our understanding of EBL process windows in addition to helping compare various processing strategies. The concept of EBL process windows can also be extended to negative-tone resists and such an effort is expected to yield significant insight into negative-tone resist morphologies and degradation mechanisms.
- The research on MD simulations of PMMA fragment dissolution in MIBK and IPA can facilitate (i) MD dissolution studies in binary-component developers such as MIBK:IPA, IPA:water, etc., using modified Flory-Huggins equations, and (ii) the study of PMMA fragment transport away from the resist surface using multi-scale modeling techniques. These developments can enhance our understanding of the development process at the molecular scale.

- To further improve the novel SML resist sensitivity and dissolution characteristics, a stronger developer (stronger than MIBK) could be identified and combined with a small molecule non-solvent (such as methanol) to form a potent binary-component developer. In addition, pattern collapse prevention techniques such as supercritical drying need to be developed for SML, which could utilize an SML-inert exchange liquid such as hexane. Additionally, given the sensitivity of SML to SEM imaging, conditions or techniques for damage-free electron microscopy need to be explored.
- The resonance characteristics of 16 nm wide SiCN resonators have already been conducted. Further efforts are required to measure sub-10 nm wide SiCN resonators. In addition, the experimental validation of improved anchor designs through Q-factor measurements is desired.

References

---

1 R. F. Pease and S. Y. Chou, Lithography and other patterning techniques for future electronics, Proc. IEEE 96, 248 (2008). DOI: 10.1109/JPROC.2007.911853

2 H. Lan and Y. Ding, Nanoimprint lithography, In: Michael Wang, Ed., Lithography, *InTech*, Rijeka, 2010, pp. 457-494, ISBN 9789533070643. DOI: 10.5772/8189

3 A. Flores and M. R. Wang, Soft lithographic fabrication of micro optic and guided wave devices, In: Michael Wang, Ed., *Lithography*, InTech, Rijeka, 2010, pp. 379-402, ISBN 9789533070643. DOI: 10.5772/8185

4 K. Salaita, Y. Wang, and C. A. Mirkin, Applications of dip-pen nanolithography, Nature Nano. 2, 145 (2007). DOI: 10.1038/nnano.2007.39

5 X. Yang, L. Wan, S. Xiao, Y. Xu, and D. K. Weller, Directed block copolymer assembly versus electron beam lithography for bit-patterned media with areal density of 1 terabit/inch2 and beyond, ACS Nano 3, 1844 (2009). DOI: 10.1021/nn900073r

6 M. A. McCord and M. Rooks, Electron beam lithography. In: P. Rai-Choudury, Ed., *Handbook of microlithography, micromachining and microfabrication (vol. 1)*, SPIE, Bellingham, 1997, pp. 139-250, ISBN 9780819423788. [www.cnf.cornell.edu/cnf_spietoc.html]

7 J. A. van Kan, P. Malar, and A. B. de Vera, The second generation Singapore high resolution proton beam writing facility, Rev. Sci. Instrum. 83, 02B902 (2012). DOI: 10.1063/1.3662205

8 H. D. Wanzenboeck and S. Waid, Focused ion beam lithography, In: Bo Cui, Ed., *Recent advances in nanofabrication techniques and applications,* InTech, Rijeka, 2011, pp. 27-50, ISBN 9789533076027. DOI: 10.5772/22075

9 J. G. Skinner, T. R. Groves, A. Novembre, H. Pfeiffer, and R. Singh, Photomask fabrication procedures and limitations, In: P. Rai-Choudury, Ed., *Handbook of microlithography, micromachining and microfabrication (vol. 1)*, SPIE, Bellingham, 1997, pp. 380-476, ISBN 9780819423788.

10 B. J. Enyon, Jr., Introduction, In: B. Eynon and B. Wu, Eds., *Photomask fabrication technology (1st Ed.)*, McGraw-Hill, New York, 2005, p. 6. ISBN 9780071445634. DOI: 10.1036/0071445633

11 MolecularImprints Perfecta TR1100, Precision Nanoimprint Lithography System for Template Replication [http://www.molecularimprints.com/products/template_replication.php]

12 M. A. Mohammad, M. Muhammad, S. K. Dew, and M. Stepanova, Fundamentals of electron beam exposure and development, In: Maria Stepanova and Steven Dew, Eds., *Nanofabrication*, Springer, Vienna, 2012, pp. 11-41, ISBN 9783709104248. DOI: 10.1007/978-3-7091-0424-8_2

13 J. Nabity, L. A. Campbell, M. Zhu, and W. Zhou, E-beam nanolithography integrated with scanning electron microscope, In: W. Zhou and Z. L. Wang, Eds., *Scanning microscopy for nanotechnology: techniques and applications (1st Ed.)*, Springer, New York, 2007, pp. 120-151, ISBN 9781441922090. DOI: 10.1007/978-0-387-39620-0_5

14 D. R. Herriott, R. J. Collier, D. S. Alles, and J. W. Stafford, EBES: a practical electron lithographic system, IEEE Trans. Electron Devices 21, 385 (1975). DOI: 10.1109/T-ED.1975.18149

15 H. C. Pfeiffer, Variable spot shaping for electron-beam lithography, J. Vac. Sci. Technol. 15, 887 (1978). DOI: 10.1116/1.569621

16 M. G. R. Thomson, R. J. Collier, and D. R. Herriott, Double-aperture method of producing variably shaped writing spots for electron lithography, J. Vac. Sci. Technol. 15, 891 (1978). DOI: 10.1116/1.569622

17 L. H. Veneklasen, H. M. Kao, S. A. Rishton, S. Winter, V. Boegli, T. Newman, G. Bertuccelli, G. Howard, P. Le, Z. Tan, and R. Lozes, High-throughput electron-beam lithography with a raster-scanned, variably shaped beam, J. Vac. Sci. Technol. B 19, 2455 (2001). DOI: 10.1116/1.1414117

18 L. R. Harriott, Scattering with angular limitation projection electron beam lithography for suboptical lithography, J. Vac. Sci. Technol. B 15, 2130 (1997). DOI: 10.1116/1.589339

19 H. C. Pfeiffer, R. S. Dhaliwal, S. D. Golladay, S. K. Doran, M. S. Gordon, *et al.*, Projection reduction exposure with variable axis immersion lenses: Next generation lithography, J. Vac. Sci. Technol. B 17, 2840 (1999). DOI: 10.1116/1.591080

20 Y. Sohda, H. Ohta, F. Murai, J. Yamamoto, H. Kawano, H. Satoh, H. Itoh, Recent progress in cell-projection electron-beam lithography, Microelectron. Eng. 67-68, 78 (2003). DOI: 10.1016/S0167-9317(03)00062-5

21 J. A. Liddle, H. A. Huggins, S. D. Berger, J. M. Gibson, G. Weber, R. Kola, and C. W. Jurgensen, Mask fabrication for projection electron-beam lithography incorporating the SCALPEL technique, J. Vac. Sci. Technol. B. 9, 3000 (1991). DOI: 10.1116/1.585357

22 T. H. Newman, R. F. W. Pease, and W. DeVore, Dot matrix electron beam lithography, J. Vac. Sci. Technol. B 1, 999 (1983). DOI: 10.1116/1.582722

23 Mapper Lithography, Delft, The Netherlands [www.mapperlithography.com]

24 P. Petric, C. Bevis, A. Carroll, H. Percy, M. Zywno, K. Standiford, A. Brodie, N. Bareket, and L. Grella, REBL: A novel approach to high speed maskless electron beam direct write lithography, J. Vac. Sci. Technol. B 27, 161 (2009). DOI: 10.1116/1.3054281

25 A. Yamada, H. Yasuda, and M. Yamabe, Evaluation of each electron beam and exposure results with four column cells in multicolumn e-beam exposure system, J. Vac. Sci. Technol. B 27, 2518 (2009). DOI: 10.1116/1.3253614

26 S. M. Kennedy, C. X. Zheng, J. Fu, W. X. Tang, D. M. Paganin, and D. E. Jesson, Electron caustic lithography, AIP Advances 2, 022152 (2012). DOI: 10.1063/1.4730139

27 IMS Nanofabrication, Vienna, Austria [www.ims.co.at]

28 ADVANTEST E-Beam Lithography Products, Tokyo, Japan [www.advantest.co.jp/products/EB/en-index.shtml]

29 JC Nabity Lithography Systems, Bozeman, Montana, USA [www.jcnabity.com]

30 Raith GmbH, Dortmund, Germany [www.raith.com]

31 Vistec EBL GmbH, Jena, Germany [www.vistec-semi.com]

32 Crestec, Tokyo, Japan [http://www.crestec8.co.jp/englishF]

33 Elionix, Tokyo, Japan [http://www.elionix.co.jp/english/]

34 JEOL EBL, Tokyo, Japan [www.jeol.com/PRODUCTS/SemiconductorEquipment/ElectronBeamLithography/tabid/99/Default.aspx]

35 NanoBeam Ltd., Cambridge, UK [www.nanobeam.co.uk]

36 C. Mack, *Fundamental principles of optical lithography (1st Ed.)*, Wiley, West Sussex, 2007, p. 12, ISBN 9780470018934

37 P. Clarke, *TSMC set to receive matrix 13,000 e-beam litho machine*, EE Times, Feb. 2012 [www.eetimes.com/electronics-news/4236492/TSMC-set-to-receive-Matrix-13-000-e-beam-litho-machine]

38 Mapper company press release: *MAPPER Lithography signs deal for financing round of € 80 million* (Aug. 23, 2012) [http://www.mapperlithography.com/news/2012/89-mapper-lithography-signs-deal-for-financing-round-of-80-million]

39 M. LaPedus, *Optical Lithography, Take Two*, Semiconductor Manufacturing and Design Community, Feb. 2013 [http://semimd.com/blog/tag/nikon]

40 K. M. Palmer, *EUV faces its most critical test*, IEEE Spectrum Jan. 2012 [www.spectrum.ieee.org/semiconductors/devices/euv-faces-its-most-critical-test]

41 J. Holmes and R. Hobbs, High Resolution Lithography for Germanium, [http://techtransfer.ucc.ie/industry/documents/HighResLitho_FG_May12Copy.pdf]

42 A. Notargiacomo, E. Giovine, F. Evangelisti, V. Foglietti, R. Leoni, EBL- and AFM-based techniques for nanowires fabrication on Si/SiGe, Mater. Sci. Eng. C 19, 185 (2002). DOI: 10.1016/S0928-4931(01)00483-0

43 W. J. Mitchell and E. L. Hu, *In situ* electron-beam lithography on GaAs substrates using a metal alkoxide resist, Appl. Phys. Lett. 74, 1916 (1999). DOI: 10.1063/1.123712

44 A. Turala, P. Regreny, P. Rojo-Romeo, and M. Gendry, Localized growth of InAs quantum dots on nanopatterned InP(001) substrates, Appl. Phys. Lett. 94, 051109 (2009). DOI: 10.1063/1.3078275

45 H. Park, H. M. Chan, and R. P. Vinci, Patterning on sapphire substrates via a solid state conversion process, J. Mater. Res. 20, 417 (2005). DOI: 10.1557/JMR.2005.0050

46 M. Muhammad, S. C. Buswell, S. K. Dew, and M. Stepanova, Nanopatterning of PMMA on insulating surfaces with various anticharging schemes using 30 keV electron beam lithography, J. Vac. Sci. Technol. B 29, 06F304 (2011). DOI: 10.1116/1.3636367

47 M. L. Schuette and W. Lu, Simple technique for beam focusing in electron beam lithography on optically transparent substrates, J. Vac. Sci. Technol. B 27, 2612 (2009). DOI: 10.1116/1.3237102

48 A. L. Koh, D. W. McComb, S. A. Maier, H. Y. Low, and J. K. W. Yang, Sub-10 nm patterning of gold nanostructures on silicon-nitride membranes for plasmon mapping with electron energy-loss spectroscopy, J. Vac. Sci. Technol. B 28, C6O45 (2010). DOI: 10.1116/1.3501351

49 G. W. Gale, R. J. Small, K. A. Reinhardt, 4 - Aqueous Cleaning Surface Conditioning Processes, In: Karen A. Reinhardt and Werner Kern, Eds.,

Handbook of Silicon Wafer Cleaning Technology (2nd Ed.), William Andrew Publishing, Norwich, NY, 2008, pp. 201-265, ISBN 9780815515548. DOI: DOI: 10.1016/B978-081551554-850007-0

50 ShinEtsu MicroSi, Inc. Adhesion Promoters [http://www.microsi.com/AdhesionPromoters.aspx]

51 W. Hu, Ultrahigh resolution electron beam lithography for molecular electronics, Ph.D. Thesis, University of Notre Dame (2004). [http://www.utdallas.edu/~walter.hu/research/publications/Hu%20dissertation.pdf]

52 A. E. Grigorescu and C. W. Hagen, Resists for sub-20-nm electron beam lithography with a focus on HSQ: state of the art, Nanotechnology 20, 292001 (2009). DOI:10.1088/0957-4484/20/29/292001

53 B. Bilenberg, M. Schøler, P. Shi, M. S. Schmidt, P. Bøggild, M. Fink, C. Schuster, F. Reuther, C. Gruetzner, and A. Kristensen, Comparison of high resolution negative electron beam resists, J. Vac. Sci. Technol. B 24, 1776 (2006). DOI: 10.1116/1.2210002

54 A. P. Adeyenuwo, M. Stepanova, and S. K. Dew, Density multiplication of nanostructures fabricated by ultralow voltage electron beam lithography using PMMA as positive- and negative-tone resist, J. Vac. Sci. Technol. B 29, 06F312 (2011). DOI: 10.1116/1.3657512

55 I. Haller, M. Hatzakis, and R. Srinivasan, High-resolution positive resists for electron-beam exposure, IBM J. Res. Dev. 12, 251 (1968). DOI: 10.1147/rd.123.0251

56 MicroChem Corp., PMMA positive resists, U.S.A. [http://www.microchem.com/Prod-PMMA.htm]

57 T. Nishida, M. Notomi, R. Iga, and T. Tamamura, Quantum wire fabrication by e-beam lithography using high-resolution and high-sensitivity e-beam resist ZEP-520, Jpn. J. Appl. Phys. 31, 4508 (1992). DOI: 10.1143/JJAP.31.4508

58 ZEONREX Electronic Chemicals, Japan [http://www.zeon.co.jp/business_e/enterprise/imagelec/imagelec.html#ie1-1]

59 ZEONREX Electronic Chemicals ZEP520A - High Resolution Positive Electron Beam Resist, Technical Report Apr. 2003

60 T. Yamaguchi and H. Namatsu, Impact of developers on roughness of dissolution front in electron-beam resists, J. Photopolym. Sci. Technol. 17, 557 (2004). DOI: 10.2494/photopolymer.17.557

61 ZEONREX Electronic Chemicals ZEP7000 - High Resolution Positive Electron Beam Resist, Technical Report Jun. 2000

62 T. G. Oyama, A. Oshima, H. Yamamoto, S. Tagawa, and M. Washio, Study on positive-negative inversion of chlorinated resist materials, Appl. Phys. Express 4, 076501 (2011). DOI: 10.1143/APEX.4.076501

63 H. Namatsu, Y. Takahashi, K. Yamazaki, T. Yamaguchi, M. Nagase, and K. Kurihara, Three-dimensional siloxane resist for the formation of nanopatterns with minimum linewidth fluctuations, J. Vac. Sci. Technol. B 16, 69 (1998). DOI: 10.1116/1.589837

64 Dow Corning XR-1541 E-Beam Resist, U.S.A [http://www.dowcorning.com/content/publishedlit/11-1547e-01.pdf]

65 M. Morgen, E. T. Ryan, J.-H. Zhao, C. Hu, T. Cho, and P. S. Ho, Low dielectric constant materials for ULSI interconnects, Annu. Rev. Mater. Sci. 30, 645 (2000). DOI: 10.1146/annurev.matsci.30.1.645

66 X.-G. Feng and L.-C. Sun, Mathematical model of spin-coated photoresist on a spherical substrate, Opt. Express 13, 7070 (2005). DOI: 10.1364/OPEX.13.007070

67 N. Arjmandi, L. Lagae, and G. Borghs, Enhanced resolution of poly(methyl methacrylate) electron resist by thermal processing, J. Vac. Sci. Technol. B 27, 1915 (2009). DOI: 10.1116/1.3167367

68 M. Aktary, M. Stepanova, and S. K. Dew, Simulation of the spatial distribution and molecular weight of polymethylmethacrylate fragments in electron beam lithography exposures, J. Vac. Sci. Technol. B 24, 768 (2006). DOI: 10.1116/1.2181580

69 Y.-H. Lee, R. Browning, N. Maluf, G. Owen, and R. F. W. Pease, Low voltage alternative for electron beam lithography, J. Vac. Sci. Technol. B 10, 3094 (1992). DOI: 10.1116/1.585935

70 H. Yang, L. Fan, A. Jin, Q. Luo, C. Gu, Z. Cui, Low-energy electron-beam lithography of ZEP-520 positive resist, Nano/Micro Engineered and Molecular Systems, 2006. NEMS '06. 1st IEEE Intl. Conf., pp. 391-394 (2006). DOI: 10.1109/NEMS.2006.334765

71 D. F. Kyser and N. S. Viswanathan, Monte Carlo simulation of spatially distributed beams in electron-beam lithography, J. Vac. Sci. Technol. 12, 1305 (1975). DOI: 10.1116/1.568524

72 D. A. Czaplewski and L. E. Ocola, 100 keV electron backscattered range and coefficient for silicon, J. Vac. Sci. Technol. B 30, 021604 (2012). DOI: 10.1116/1.3693985

73 G. Brewer, Ed., *Electron-beam technology in microelectronic fabrication*. New York: Academic, 1980. ISBN 978-012-133-550-2

74 M. Kamp, M. Emmerling, S. Kuhn, and A. Forchel, Nanolithography using a 100 kV electron beam lithography system with a Schottky emitter, J. Vac. Sci. Technol. B 17, 86 (1999). DOI: 10.1116/1.590520

75 T. H. P. Chang, Proximity effect in electron-beam lithography, J. Vac. Sci. Technol. 12, 1271 (1975). DOI: 10.1116/1.568515

76 C. W. Lo, M. J. Rooks, W. K. Lo, M. Isaacson, and H. G. Craighead, Resists and processes for 1 kV electron beam microcolumn lithography, J. Vac. Sci. Technol. B 13, 812 (1995). DOI: 10.1116/1.587859

77 L. K. Mun, D. Drouin, E. Lavallée, and J. Beauvais, The impact of charging on low-energy electron beam lithography, Microsc. Microanal. 10, 804 (2004). DOI: 10.1017/S1431927604040711

78 B. Wu and A. R. Neureuther, Energy deposition and transfer in electron-beam lithography, J. Vac. Sci. Technol. B 19, 2508 (2001). DOI: 10.1116/1.1421548

79 A. Raghunathan and J. G. Hartley, Influence of secondary electrons in high-energy electron beam lithography, J. Vac. Sci. Technol. B 31, 011605 (2013). DOI: 10.1116/1.4774114

80 D. Joy, An introduction to Monte Carlo simulations, Scanning Microsc 5, 329 (1991).

81 M. Dapor, Monte Carlo simulation of backscattered electrons and energy from thick targets and surface films, Phys. Rev. B 46, 618 (1992). DOI: 10.1103/PhysRevB.46.618

82 C. A. Mack, Electron beam lithography simulation for mask making, Microelectron. Eng. 46, 283 (1999). DOI: 10.1016/S0167-9317(99)00082-9

83 I. Raptis, N. Glezos, and M. Hatzakis, Use of the Boltzmann transport equation for the evaluation of energy deposition in the case of electron sensitive resist films over composite substrates, Microelectron. Eng. 21, 289 (1993). DOI: 10.1016/0167-9317(93)90075-G

84 B. K. Paul, An analytical model of the diffusive scattering of low-energy electrons in electron-beam resists, Microelectron. Eng. 49, 233 (1999). DOI: 10.1016/S0167-9317(99)00444-X

85 M. Stepanova, T. Fito, Zs. Szabó, K. Alti, A. P. Adeyenuwo, K. Koshelev, M. Aktary, and S. K. Dew, Simulation of electron beam lithography of nanostructures, J. Vac. Sci. Technol. B 28, C6C48 (2010). DOI: 10.1116/1.3497019

86 J. O. Choi, J. A. Moore, J. C. Corelli, J. P. Silverman, and H. Bakhru, Degradation of poly(methylmethacrylate) by deep ultraviolet, x-ray, electron beam, and proton beam irradiations, J. Vac. Sci. Technol. B 6, 2286 (1988). DOI: 10.1116/1.584071

87 V. Bermudez, Low-energy electron-beam effects on poly(methyl methacrylate) resist films, J. Vac. Sci. Technol. B 17, 2512 (1999). DOI: 10.1116/1.591134

88 T. G. Oyama, K. Enomoto, Y. Hosaka, A. Oshima, M. Washio, and S. Tagawa, Electron-beam-induced decomposition mechanisms of high-sensitivity

chlorinated resist ZEP520A, Appl. Phys. Express 5, 036501 (2012). DOI: 10.1143/APEX.5.036501

89 B. A. Miller-Chou and J. L. Koenig, A review of polymer dissolution, Prog. Polym. Sci. 28, 1223 (2003). DOI: 10.1016/S0079-6700(03)00045-5

90 D. L. Olynick, B. Cord, A. Schipotinin, D. F. Ogletree, and P. J. Schuck, Electron-beam exposure mechanisms in hydrogen silsesquioxane investigated by vibrational spectroscopy and in situ electron-beam-induced desorption, J. Vac. Sci. Technol. B 28, 581 (2010). DOI: 10.1116/1.3425632

91 K.-D. Schock, F. E. Prins, S. Strähle, and D. P. Kern, Resist processes for low-energy electron-beam lithography, J. Vac. Sci. Technol. B 15, 2323 (1997). DOI: 10.1116/1.589638

92 W. Brünger, E.-B. Kley, B. Schnabel, I. Stolberg, M. Zierbock, R. Plontke, Low energy lithography; energy control and variable energy exposure, Microelectron. Eng. 27, 135 (1995). DOI: 10.1016/0167-9317(94)00073-4

93 T. Borzenko, C. Gould, G. Schmidt, L. W. Molenkamp, Metallic air-bridges fabricated by multiple acceleration voltage electron beam lithography, Microelectron. Eng. 75, 210 (2004). DOI: 10.1016/j.mee.2004.05.005

94 B. Cord, J. Yang, H. Duan, D. C. Joy, J. Klingfus, and K. K. Berggren, Limiting factors in sub-10 nm scanning-electron-beam lithography, J. Vac. Sci. Technol. B 27, 2616 (2009). DOI: 10.1116/1.3253603

95 B. H. Koek, T. Chisholm, A. J. v. Run, J. Romijn, and J. P. Davey, An electron beam lithography tool with a Schottky emitter for wide range applications, Microelectron. Eng., 23, 81 (1994). DOI: 10.1016/0167-9317(94)90109-0

96 S. W. H. K. Steenbrink, B. J. Kampherbeek, M. J. Wieland, J. H. Chen, S. M. Chang, M. Pas, J. Kretz, C. Hohle, D. van Steenwinckel, S. Manakli, J. Le-

Denmat, and L. Pain, High throughput maskless lithography: low voltage versus high voltage, Proc. SPIE 6921, 69211T (2008). DOI: 10.1117/12.771971

97 M. Bolorizadeh and D. C. Joy, Effects of fast secondary electrons to low-voltage electron beam lithography, J. Micro/Nanolith. MEMS MOEMS. 6, 023004 (2007). DOI: 10.1117/1.2728899

98 J. Bönisch, V. Kudryashov, R.E. Burge, The experimental study of the main technical parameters influencing the possible resolution of electron beam lithography, Microelectron. Eng. 17, 33 (1992). DOI: 10.1016/0167-9317(92)90010-O

99 D. A. Z. Zheng, M. A. Mohammad, S. K. Dew, and M. Stepanova, Developer-free direct patterning of PMMA/ZEP 520A by low voltage electron beam lithography, J. Vac. Sci. Technol. B 29, 06F303 (2011). DOI: 10.1116/1.3634017

100 M. A. Mohammad, T. Fito, J. Chen, S. Buswell, M. Aktary, M. Stepanova, and S. K. Dew, Systematic study of the interdependence of exposure and development conditions and kinetic modelling for optimizing low-energy electron beam nanolithography, Microelectron. Eng. 87, 1104 (2010). DOI: 10.1016/j.mee.2009.11.047

101 J. Goldstein, D. Newbury, D. Joy, C. Lyman, P. Echlin, E. Lifshin, L. Sawyer, J. Michael, *Scanning electron microscopy and x-ray microanalysis*, New York: Springer, 2003. ISBN 978-030-647-292-3

102 Raith NanoSuite Software Operation Manual, © 2010 by Raith GmbH, Dortmund.

103 S. Thoms, D. S. Macintyre, and M. McCarthy, Sub - 35 nm metal gratings fabricated using PMMA with high contrast developers, Microelectron. Eng. 41–42, 207 (1998). DOI: 10.1016/S0167-9317(98)00047-1

104 V. A. Harmandaris, V. G. Mavrantzas, D. N. Theodorou, M. Kröger, J. Ramírez, H. C. Öttinger, and D. Vlassopoulos, Crossover from the rouse to the entangled polymer melt regime: Signals from long, detailed atomistic molecular dynamics simulations, supported by rheological experiments, Macromolecules 36, 1376 (2003). DOI: 10.1021/ma020009g

105 L. Masaro and X. X. Zhu, Physical models of diffusion for polymer solutions, gels and solids, Prog. Polym. Sci. 24, 731 (1999). DOI: 10.1016/S0079-6700(99)00016-7

106 T. Yamaguchi and H. Namatsu, Effect of developer molecular size on roughness of dissolution front in electron-beam resist, J. Vac. Sci. Technol. B 22, 1037 (2004). DOI: 10.1116/1.1736647

107 M. Häffner, A. Haug, A. Heeren, M. Fleischer, H. Peisert, T. Chassé, and D. P. Kern, Influence of temperature on HSQ electron-beam lithography, J. Vac. Sci. Technol. B 25, 2045 (2007). DOI: 10.1116/1.2794324

108 R. Tiron, L. Mollard, O. Louveau, E. Lajoinie, Ultrahigh-resolution pattern using electron-beam lithography HF wet etching, J. Vac. Sci. Technol. B 25, 1147 (2007). DOI: 10.1116/1.2743653

109 H.-S. Lee, J.-S. Wi, S.-W. Nam, H.-M. Kim, and K.-B. Kim, Two-step resist-development process of hydrogen silsesquioxane for high-density electron-beam nanopatterning, J. Vac. Sci. Technol. B 27, 188 (2009). DOI: 10.1116/1.3049482

110 I. Raptis and G. P. Patsis, Simulation of electron beam exposure and resist processing for nano-patterning, In: Maria Stepanova and Steven Dew, Eds., Nanofabrication, Springer, Vienna, 2012, pp. 43-91, ISBN 9783709104248. DOI: 10.1007/978-3-7091-0424-8_3

111 J. González-Benito and J. L. Koenig, Nature of PMMA dissolution process by mixtures of acetonitrile/alcohol (poor solvent/nonsolvent) monitored by FTIR-imaging, Polymer 47, 3065 (2006). DOI: 10.1016/j.polymer.2006.02.086

112 J. S. Greeneich, Developer characteristics of poly-(methyl methacrylate) electron resist, J. Electrochem. Soc. 122, 970 (1975). DOI: 10.1149/1.2134380

113 F. J. Pantenburg, S. Achenbach and J. Mohr, Influence of developer temperature and resist material on the structure quality in deep x-ray lithography, J. Vac. Sci. Technol. B 16, 3547 (1998). DOI: 10.1116/1.590494

114 P. J. Flory, *Principles of Polymer Chemistry* (Cornell University Press, New York, 1953), p. 495. ISBN: 978-0-8014-0134-3

115 M. Rubinstein and R. H. Colby, *Polymer Physics* (Oxford University Press, New York, 2003), pp. 137–170. ISBN: 978-0-1985-2059-7

116 J. H. Hildebrand, The term ‘Regular Solution’, Nature 168, 868 (1951). DOI: 10.1038/168868a0

117 V. K. Sharma, S. Affrossman, and R. A. Pethrick, Electron beam lithography — influence of molecular characteristics on the performance of positive resists, Br. Polym. J. 16, 73 (1984). DOI: 10.1002/pi.4980160205

118 D. G. Hasko, S. Yasin, and A. Mumtaz, Influence of developer and development conditions on the behavior of high molecular weight electron

beam resists, J. Vac. Sci. Technol. B 18, 3441 (2000). DOI: 10.1116/1.1319834

119 Q. Hang, D. A. Hill, and G. H. Bernstein, Efficient removers for poly(methylmethacrylate), J. Vac. Sci. Technol. B 21, 91 (2003). DOI: 10.1116/1.1532734

120 D. L. Olynick, P. D. Ashby, M. D. Lewis, T. Jen, H. Lu, J. A. Liddle, and W. Chao, The link between nanoscale feature development in a negative resist and the Hansen solubility sphere, J. Polym. Sci., Part B: Polym. Phys. 47, 2091 (2009). DOI: 10.1002/polb.21806

121 S. Patel, A. Lavasanifar, and P. Choi, Application of molecular dynamics simulation to predict the compatability between water-insoluble drugs and self-associating poly(ethylene oxide)-b-poly(ε-caprolactone) block copolymers, Biomacromolecules 9, 3014 (2008). DOI: 10.1021/bm800320z

122 S. M. Scheinhardt-Engels, F. A. M. Leermakers, and G. J. Fleer, Lattice mean-field method for stationary polymer diffusion, Phys. Rev. E 68, 011802 (2003). DOI: 10.1103/PhysRevE.68.011802

123 P. G. de Gennes, Dynamics of entangled polymer solutions. I. The rouse model, Macromolecules 9, 587 (1976). DOI: 10.1021/ma60052a011

124 U. M. Apel, R. Hentschke, and J. Helfrich, Molecular Dynamics Simulation of Syndio- and Isotactic Poly(methyl methacrylate) in Benzene, Macromolecules 28, 1778 (1995). DOI: 10.1021/ma00110a009

125 M. A. Mohammad, K. P. Santo, S. K. Dew, and M. Stepanova, Study of the interaction of polymethylmethacrylate fragments with methyl isobutyl ketone and isopropyl alcohol, J. Vac. Sci. Technol. B 30, 06FF11 (2012). DOI: 10.1116/1.4766318

126 R. W. Johnstone, Self-sacrificial surface-micromachining using poly(methyl methacrylate), Ph.D. Thesis, Simon Fraser University (2008). [http://www.ece.ualberta.ca/~rj/phd-thesis.html]

127 A. Olzierski and I. Raptis, Development and molecular-weight issues on the lithographic performance of poly (methyl methacrylate), Microelectron. Eng. 73-74, 244 (2004). DOI: 10.1016/j.mee.2004.02.048

128 M. J. Rooks, E. Kratschmer, R. Viswanathan, J. Katine, R. E. Fontana, and S. A. MacDonald, Low stress development of poly(methylmethacrylate) for high aspect ratio structures, J. Vac. Sci. Technol. B 20, 2937 (2002). DOI: 10.1116/1.1524971

129 J.-S. Wi, H.-S. Lee, and K.-B. Kim, Enhanced development properties of IPA (isopropyl alcohol) on the PMMA electron beam resist, Electron. Mater. Lett. 3, 1 (2007). URL [http://www.e-eml.org/upload/04218154.pdf]

130 S. Yasin, D. G. Hasko, M. N. Khalid, D. J. Weaver, and H. Ahmed, Influence of polymer phase separation on roughness of resist features, J. Vac. Sci. Technol. B 22, 574 (2004). DOI: 10.1116/1.1651106

131 W. Hu, K. Sarveswaran, M. Lieberman, and G. H. Bernstein, Sub-10 nm electron beam lithography using cold development of poly(methylmethacrylate), J. Vac. Sci. Technol. B 22, 1711 (2004). DOI: 10.1116/1.1763897

132 B. Cord, J. Lutkenhaus, and K. K. Berggren, Optimal temperature for development of poly(methylmethacrylate), J. Vac. Sci. Technol. B 25, 2013 (2007). DOI: 10.1116/1.2799978

133 M. Yan, S. Choi, K. R. V. Subramanian, and I. Adesida, The effects of molecular weight on the exposure characteristics of

poly(methylmethacrylate) developed at low temperatures, J. Vac. Sci. Technol. B 26, 2306 (2008). DOI: 10.1116/1.3002562

134 A. Schleunitz, V. A. Guzenko, A. Schander, M. Vogler, and H. Schift, Selective profile transformation of electron-beam exposed multilevel resist structures based on a molecular weight dependent thermal reflow, J. Vac. Sci. Technol. B 29, 06F302 (2011). DOI: 10.1116/1.3634013

135 O. Dial, C. C. Cheng, and A. Scherer, Fabrication of high-density nanostructures by electron beam lithography, J. Vac. Sci. Technol. B 16, 3887 (1998). DOI: 10.1116/1.590428

136 S. Yasin, D. G. Hasko, and H. Ahmed, Fabrication of <5 nm width lines in poly(methylmethacrylate) resist using a water:isopropyl alcohol developer and ultrasonically-assisted development, Appl. Phys. Lett. 78, 2760 (2001). DOI: 10.1063/1.1369615

137 G. H. Bernstein, D. A. Hill, and W. -P. Liu, New high-contrast developers for poly(methyl methacrylate) resist, J. Appl. Phys. 71, 4066 (1992). DOI: 10.1063/1.350831

138 W. H. Teh, C.-T. Liang, M. Graham, and C. G. Smith, Cross-linked PMMA as a low-dimensional dielectric sacrificial layer, J. Microelectromech. S. 12, 641 (2003). DOI: 10.1109/JMEMS.2003.817891

139 H. Namatsu, M. Nagase, K. Kurihara, K. Iwadate, K. Murase, 10-nm silicon lines fabricated in (110) silicon, Microelectron. Eng. 27, 71 (1995). DOI: 10.1016/0167-9317(94)00058-3

140 L. E. Ocola and A. Stein, Effect of cold development on improvement in electron-beam nanopatterning resolution and line roughness, J. Vac. Sci. Technol. B 24, 3061 (2006). DOI: 10.1116/1.2366698

141 X.-M. Yang, S. Xiao, W. Wu, Y. Xu, K. Mountfield, R. Rottmayer, K. Lee, D. Kuo, and D. Weller, Challenges in 1 Teradot/in.2 dot patterning using electron beam lithography for bit-patterned media, J. Vac. Sci. Technol. B 25, 2202 (2007). DOI: 10.1116/1.2798711

142 H. Wang, G. M. Laws, S. Milicic, P. Boland, A. Handugan, M. Pratt, T. Eschrich, S. Myhajlenko, J. A. Allgair, and B. Bunday, Low temperature ZEP-520A development process for enhanced critical dimension realization in reactive ion etch etched polysilicon, J. Vac. Sci. Technol. B 25, 102 (2007). DOI: 10.1116/1.2426976

143 J. Reinspach, M. Lindblom, O. von Hofsten, M. Bertilson, H. M. Hertz, and A. Holmberg, Cold-developed electron-beam-patterned ZEP 7000 for fabrication of 13 nm nickel zone plates, J. Vac. Sci. Technol. B 27, 2593 (2009). DOI: 10.1116/1.3237140

144 J. Reinspach, M. Lindblom, M. Bertilson, O. von Hofsten, H. M. Hertz, and A. Holmberg, 13 nm high-efficiency nickel-germanium soft x-ray zone plates, J. Vac. Sci. Technol. B 29, 011012 (2011). DOI: 10.1116/1.3520457

145 T. Okada, J. Fujimori, M. Aida, M. Fujimura, T. Yoshizawa, M. Katsumura, and T. Iida, Enhanced resolution and groove-width simulation in cold development of ZEP520A, J. Vac. Sci. Technol. B 29, 021604 (2011). DOI: 10.1116/1.3569892

146 H. Namatsu, Supercritical resist drying for isolated nanoline formation, J. Vac. Sci. Technol. B 19, 2709 (2001). DOI: 10.1116/1.1418411

147 D. Lauvernier, J.-P. Vilcot, M. François, D. Decoster, Optimization of HSQ resist e-beam processing technique on GaAs material, Microelectron. Eng. 75, 177 (2004). DOI: 10.1016/j.mee.2004.05.002

148 W. Henschel, Y. M. Georgiev, and H. Kurz, Study of a high contrast process for hydrogen silsesquioxane as a negative tone electron beam resist, J. Vac. Sci. Technol. B 21, 2018 (2003). DOI: 10.1116/1.1603284

149 F. Fruleux-Cornu, J. Penaud, E. Dubois, M. François, and M. Muller, An optimal high contrast e-beam lithography process for the patterning of dense fin networks, Mater. Sci. Eng. C 26, 893 (2006). DOI: 10.1016/j.msec.2005.09.017

150 J. K. W. Yang and K. K. Berggren, Using high-contrast salty development of hydrogen silsesquioxane for sub-10-nm half-pitch lithography, J. Vac. Sci. Technol. B 25, 2025 (2007). DOI: 10.1116/1.2801881

151 J. K. W. Yang, B. Cord, H. Duan, K. K. Berggren, J. Klingfus, S.-W. Nam, K.-B. Kim, M. J. Rooks, Understanding of hydrogen silsesquioxane electron resist for sub-5-nm-half-pitch lithography, J. Vac. Sci. Technol. B 27, 2622 (2009). DOI: 10.1116/1.3253652

152 J. Kim, W. Chao, B. Griedel, X. Liang, M. Lewis, D. Hilken, D. Olynick, Understanding the base development mechanism of hydrogen silsesquioxane, J. Vac. Sci. Technol. B 27, 2628 (2009). DOI: 10.1116/1.3250261

153 S.-W. Nam, M. J. Rooks, J. K. W. Yang, K. K. Berggren, H.-M. Kim, M.-H. Lee, K.-B. Kim, J. H. Sim, and D. Y. Yoon, Contrast enhancement behavior of hydrogen silsesquioxane in a salty developer, J. Vac. Sci. Technol. B 27, 2635 (2009). DOI: 10.1116/1.3245991

154 K. J. Harry, S. Strobel, J. K. W. Yang, H. Duan, and K. K. Berggren, In situ study of hydrogen silsesquioxane dissolution rate in salty and electrochemical developers, J. Vac. Sci. Technol. B 29, 06FJ01 (2011). DOI: 10.1116/1.3644339

155 S. Strobel, K. J. Harry, H. Duan, J. K. W. Yang, V. R. Manfrinato, and K. K. Berggren, Electrochemical development of hydrogen silsesquioxane by applying an electrical potential, Nanotechnology 22, 375301 (2011). DOI: 10.1088/0957-4484/22/37/375301

156 Y. Chen, H. Yang, and Z. Cui, Effects of developing conditions on the contrast and sensitivity of hydrogen silsesquioxane, Microelectron. Eng. 83, 1119 (2006). DOI: 10.1016/j.mee.2006.01.167

157 G. M. Schmid, L. E. Carpenter, and J. A. Liddle, Nonaqueous development of silsesquioxane electron beam resist, J. Vac. Sci. Technol. B 22, 3497 (2004). DOI: 10.1116/1.1825014

158 H. Yang, A. Jin, Q. Luo, C. Gu, Z. Cui, Comparative study of e-beam resist processes at different development temperature, Microelectron. Eng. 84, 1109 (2007). DOI: 10.1016/j.mee.2007.01.053

159 M. Yan, J. Lee, B. Ofuonye, S. Choi, J. H. Jang, and I. Adesida, Effects of salty-developer temperature on electron-beam-exposed hydrogen silsesquioxane resist for ultradense pattern transfer, J. Vac. Sci. Technol. B 28, C6S23 (2010). DOI: 10.1116/1.3504497

160 M. Häffner, A. Heeren, M. Fleischer, D. P. Kern, G. Schmidt, L. W. Molenkamp, Simple high resolution nanoimprint-lithography, Microelectron. Eng. 84, 937 (2007). DOI: 10.1016/j.mee.2007.01.020

161 S. Choi, N. Jin, V. Kumar, I. Adesida, and M. Shannon, Effects of developer temperature on electron-beam-exposed hydrogen silsesquioxane resist for ultradense silicon nanowire fabrication, J. Vac. Sci. Technol. B 25, 2085 (2007). DOI: 10.1116/1.2794315

162 L. E. Ocola and V. R. Tirumala, Nanofabrication of super-high-aspect-ratio structures in hydrogen silsesquioxane from direct-write e-beam lithography and hot development, J. Vac. Sci. Technol. B 26, 2632 (2008). DOI: 10.1116/1.3021395

163 W. Chen and H. Ahmed, Fabrication of 5–7 nm wide etched lines in silicon using 100 keV electron-beam lithography and polymethylmethacrylate resist, Appl. Phys. Lett. 62, 1499 (1993). DOI: 10.1063/1.109609

164 T. Iwamoto, H. Shimada, S. Shimomura, M. Onodera and T. Ohmi, High-reliability lithography performed by ultrasonic and surfactant-added developing system, Jpn. J. Appl. Phys. 33, 491 (1994). DOI: 10.1143/JJAP.33.491

165 K. L. Lee, J. Bucchignano, J. Gelorme, and R. Viswanathan, Ultrasonic and dip resist development processes for 50 nm device fabrication, J. Vac. Sci. Technol. B 15, 2621 (1997). DOI: 10.1116/1.589696

166 S. Yasin, D. G. Hasko, and H. Ahmed, Comparison of sensitivity and exposure latitude for polymethylmethacrylate, UVIII, and calixarene using conventional dip and ultrasonically assisted development, J. Vac. Sci. Technol. B 17, 3390 (1999). DOI: 10.1116/1.591016

167 D. Küpper, D. Küpper, T. Wahlbrink, J. Bolten, M. C. Lemme, Y. M. Georgiev, and H. Kurz, Megasonic-assisted development of nanostructures, J. Vac. Sci. Technol. B 24, 1827 (2006). DOI: 10.1116/1.2214709

168 L. Y. M. Tobing, L. Tjahjana, and D. H. Zhang, Large contrast enhancement by sonication assisted cold development process for low dose and ultrahigh resolution patterning on ZEP520A positive tone resist, J. Vac. Sci. Technol. B 30, 051601 (2012). DOI: 10.1116/1.4739053

169 H. Namatsu, K. Yamazaki, and K. Kurihara, Supercritical resist dryer, J. Vac. Sci. Technol. B 18, 780 (2000). DOI: 10.1116/1.591276

170 J.-H. Jang, C. K. Ullal, M. Maldovan, T. Gorishnyy, S. Kooi, C. Koh, E. L. Thomas, 3D micro- and nanostructures via interference lithography, Adv. Funct. Mater. 17, 3027 (2007). DOI: 10.1002/adfm.200700140

171 T. Wahlbrink, D. Küpper, Y. M. Georgiev, J. Bolten, M. Möller, D. Küpper, M. C. Lemme, H. Kurz, Supercritical drying process for high aspect-ratio HSQ nano-structures, Microelectron. Eng. 83, 1124 (2006). DOI: 10.1016/j.mee.2006.01.026

172 T. Wahlbrink, D. Küpper, J. Bolten, M. Möller, M. C. Lemme, H. Kurz, Supercritical drying for high aspect-ratio HSQ nano-structures, Microelectron. Eng. 84, 1045 (2007). DOI: 10.1016/j.mee.2007.01.142

173 S. Choi, M. Yan, and I. Adesida, Fabrication of triangular nanochannels using the collapse of hydrogen silsesquioxane resists, Appl. Phys. Lett. 93, 163113 (2008). DOI: 1.1063/1.3006322

174 S. Choi, M. J. Word, V. Kumar, and I. Adesida, Comparative study of thermally cured and electron-beam-exposed hydrogen silsesquioxane resists, J. Vac. Sci. Technol. B 26, 1654 (2008). DOI: 10.1116/1.2960565

175 J. K. W. Yang, V. Anant, and K. K. Berggren, Enhancing etch resistance of hydrogen silsesquioxane via postdevelop electron curing, J. Vac. Sci. Technol. B 24, 3157 (2006). DOI: 10.1116/1.2395949

176 X. Yang, H. Gentile, A. Eckert, and S. R. Brankovic, Electron-beam SAFIER™ process and its application for magnetic thin-film heads, J. Vac. Sci. Technol. B 22, 3339 (2004). DOI: 10.1116/1.1815309

177 A. E. Grigorescu, M. C. van der Krogt, C. W. Hagen, P. Kruit, 10 nm lines and spaces written in HSQ, using electron beam lithography, Microelectron. Eng. 84, 822 (2007). DOI: 10.1016/j.mee.2007.01.022

178 S. Yasin, D. G. Hasko, and H. Ahmed, Comparison of MIBK/IPA and water/IPA as PMMA developers for electron beam nanolithography, Microelectron. Eng. 61–62, 745 (2002). DOI: 10.1016/S0167-9317(02)00468-9

179 W. Hu, K. Sarveswaran, M. Lieberman, and G. H. Bernstein, High-resolution electron beam lithography and DNA nano-patterning for molecular QCA, IEEE Trans. Nanotechnol. 4, 312 (2005). DOI: 10.1109/TNANO.2005.847034

180 M. A. Mohammad, K. Koshelev, T. Fito, D. A. Z. Zheng, M. Stepanova, and S. Dew, Study of development processes for ZEP-520 as a high-resolution positive and negative tone electron beam lithography resist, Jpn. J. Appl. Phys. 51, 06FC05 (2012). DOI: 10.1143/JJAP.51.06FC05

181 Q. Li, L. Zhang, M. Chen, and S. Fan, A process study of electron beam nano-lithography and deep etching with an ICP system, Sci. China, Ser. E: Technol. Sci. 52, 1165 (2009). DOI: 10.1007/s11431-009-0156-7

182 A. Rosenbusch, N. Glezos, M. Kalus, and I. Raptis, SELID: a new 3D simulator for e-beam lithography, Proc. SPIE 2884, 435 (1996). DOI: 10.1117/12.262829

183 A. Rosenbusch, Z. Cui, E. DiFabrizio, M. Gentili, N. Glezos, G. Meneghini, B. Nowotny, G. Patsis, P. Prewett, and I. Raptis, Simulation of chemically amplified resist processes for 150 nm e-beam lithography, Microelectron. Eng. 46, 379 (1999). DOI: 10.1016/S0167-9317(99)00111-2

184 SCELETON^{TM} Simulator, Synopsys, Mountain View, California, USA, [http://www.synopsys.com/Tools/Manufacturing/MaskSynthesis/CATS/Pages/ProximityEffectCorrection.aspx#Scelton]

185 ProBEAM 3-D Electron Beam Lithography Optimization, KLA Tencor, Milpitas, California, USA [http://www.kla-tencor.com/lithography-modeling/probeam.html]

186 C. A. Mack, Electron beam lithography simulation for mask making, Microelectron. Eng. 46, 283 (1999) DOI: 10.1016/S0167-9317(99)00082-9

187 TRAVIT EBL, aBeam Technologies, Castro Valley, California, USA [http://www.abeamtech.com/index.php?dir=products/TRAVIT%20EBL&pg=index]

188 N. Glezos, I. Raptis, and M. Hatzakis, LITHOS: A fast electron beam lithography simulator, Microelectron. Eng. 23, 417 (1994). DOI: 10.1016/0167-9317(94)90186-4

189 NINT Electron Beam Lithography Simulator, Edmonton, Alberta, Canada [http://www.flintbox.com/public/project/7272/]

190 K. Koshelev, M. A. Mohammad, T. Fito, K. L. Westra, S. K. Dew, and M. Stepanova, Comparison between ZEP and PMMA resists for nanoscale electron beam lithography experimentally and by numerical modeling, J. Vac. Sci. Technol. B 29, 06F306 (2011). DOI: 10.1116/1.3640794

191 Electron Beam Lithography Simulator – Manual and Case Studies, 3rd Ed. January 2013, 37 pages © 2013 NINT-NRC & University of Alberta, Edmonton, Alberta, Canada.

192 S. Gorelick, J. Vila-Comamala, V. A. Guzenko, R. Barrett, M. Salomé, and C. David, High-efficiency fresnel zone plates for hard x-rays by 100 keV e-

beam lithography and electroplating, J. Synchrotron Rad. 18, 442 (2011). DOI: 10.1107/S0909049511002366

193 M. van Dalfsen, Cold development of gratings in PMMA photoresist, 40 pages (unpublished report, the University of Alberta), Jan. 2008.

194 A. Kokkinis, E. S. Valamontes, D. Goustouridis, Th. Ganetsos, K. Beltsios, and I. Raptis, Molecular weight and processing effects on the dissolution properties of thin poly(methyl methacrylate) films, Microelectron. Eng. 85, 93 (2008). DOI: 10.1016/j.mee.2007.04.141

195 C. Lorenz and N. L. Doltsinis, Molecular Dynamics Simulation: From “Ab Initio” to “Coarse Grained”, In: Jerzy Leszczynski, Ed., Handbook of Computational Chemistry, Springer Netherlands, 2012, pp. 195-238, ISBN 9789400707108. DOI: 10.1007/978-94-007-0711-5_7

196 G. P. Patsis and N. Glezos, Molecular dynamics simulation of gel formation and acid diffusion in negative tone chemically amplified resists, Microelectron. Eng. 46, 359 (1999) DOI: 10.1016/S0167-9317(99)00104-5

197 T.-H. Fang, C.-I. Weng, and J.-G. Chang, Molecular dynamics simulation of nano-lithography process using atomic force microscopy, Surf. Sci. 501, 138 (2002). DOI: 10.1016/S0039-6028(01)01938-0

198 A. Taga, M. Yasuda, H. Kawata, and Y. Hirai, Impact of molecular size on resist filling process in nanoimprint lithography: Molecular dynamics study, J. Vac. Sci. Technol. B 28, C6M68 (2010). DOI: 10.1116/1.3511434

199 K. Tada, M. Yasuda, G. Tan, Y. Miyake, H. Kawata, M. Yoshimoto, and Y. Hirai, Atomic step patterning in nanoimprint lithography: Molecular dynamics study, J. Vac. Sci. Technol. B 29, 06FC11 (2011). DOI: 10.1116/1.3659712

200 M. Yasuda, K. Araki, A. Taga, A. Horiba, H. Kawata, and Y. Hirai, Computational study on polymer filling process in nanoimprint lithography, Microelectron. Eng. 88, 2188 (2011). DOI: 10.1016/j.mee.2011.01.016

201 M. Yasuda, H. Sakai, R. Takai, H. Kawata, and Y. Hirai, Molecular simulation of pattern formation in electron beam lithography, Microelectron. Eng. (2013). DOI: 10.1016/j.mee.2013.03.119 (In Press)

202 S. S. Patnaik and R. Pachter, A molecular simulations study of the miscibility in binary mixtures of polymers and low molecular weight molecules, Polymer 43, 415 (2002). DOI: 10.1016/S0032-3861(01)00432-3

203 Accelrys Materials Studio Software, San Diego, California, USA. [http://accelrys.com/products/materials-studio/]

204 I. M. de Arenaza, E. Meaurio, B. Coto, and J.-R. Sarasua, Molecular dynamics modelling for the analysis and prediction of miscibility in polylactide/polyvinilphenol blends, Polymer 51, 4431 (2010). DOI: 10.1016/j.polymer.2010.07.018

205 Y. Fu, L. Liao, Y. Lan, L. Yang, L. Mei, Y. Liu, and S. Hu, Molecular dynamics and mesoscopic dynamics simulations for prediction of miscibility in polypropylene/polyamide-11 blends, J. Mol. Struct. 1012, 113 (2012). DOI: 10.1016/j.molstruc.2011.12.026

206 K. P. Santo, Analysis of PMMA fragment-developer interaction in electron beam lithography, 19 pages (unpublished report, NINT-NRC and the University of Alberta), Nov. 14, 2010.

207 S. Lewis, D. Jeanmaire, V. Haynes, P. McGovern, L. Piccirillo, Characterization of an ultra high aspect ratio electron beam resist for nano-lithography, In NSTI-Nanotech 2010: NanoFab: Manufacture,

Instrumentation. 13th Nanotech Conference & Expo, June 2010; Anaheim. Cambridge: CRC Press; 2010:195. [http://www.emresist.com/Papers/nanotech2010.pdf]

208 EM Resist Ltd., Macclesfield, UK [http://www.emresist.com/]

209 K. Eom, H. S. Park, D. S. Yoon, and T. Kwon, Nanomechanical resonators and their applications in biological/chemical detection: Nanomechanics principles, Phys. Reports 503, 115 (2011). DOI: 10.1016/j.physrep.2011.03.002

210 NEMSLAB, Edmonton, Alberta, Canada [http://www.ece.ualberta.ca/~nemslab/index.htm]

211 L. M. Fischer, N. Wilding, M. Gel, and S. Evoy, Low-stress silicon carbonitride for the machining of high-frequency nanomechanical resonators, J. Vac. Sci. Technol. B 25, 33 (2007). DOI: 10.1116/1.2402153

212 L. M. Fischer, V. A. Wright, C. Guthy, N. Yang, M. T. McDermott, J. M. Buriak, and S. Evoy, Specific detection of proteins using nanomechanical resonators, Sens. Actuators B 134, 613 (2008). DOI: 10.1016/j.snb.2008.06.003

213 M. A. Mohammad, S. K. Dew, K. Westra, P. Li, M. Aktary, Y. Lauw, A. Kovalenko, and M. Stepanova, Nanoscale resist morphologies of dense gratings using electron-beam lithography, J. Vac. Sci. Technol. B 25, 745 (2007). DOI: 10.1116/1.2731330

214 M. A. Mohammad, T. Fito, J. Chen, S. Buswell, M. Aktary, S. K. Dew, and M. Stepanova, The interdependence of exposure and development conditions when optimizing low-energy EBL for nano-scale resolution, In: Michael

Wang, Ed., Lithography, InTech, Rijeka, 2010, pp. 293-318, ISBN 9789533070643. DOI: 10.5772/8182

215 M. A. Mohammad, T. Fito, J. Chen, M. Aktary, M. Stepanova, and S. K. Dew, Interdependence of optimum exposure dose regimes and the kinetics of resist dissolution for electron beam nanolithography of polymethylmethacrylate, J. Vac. Sci. Technol. B 28, L1 (2010). DOI: 10.1116/1.3268131

216 Z. Szabo’, Activity outline, 7 pages (unpublished report, NINT-NRC and the University of Alberta), Mar. 27, 2009.

217 M. A. Mohammad, Z. Szabo’, T. Fito, J. M. Lee, J. Chen, M. Aktary, S. K. Dew, and M. Stepanova, “Systematic study of nanoscale resolution for low-energy electron beam lithography,” poster presentation at the 12th Nanotechnology Conference and Trade Show NSTI Nanotech, (Houston, TX, USA), May 3-7, 2009.

218 M. A. Mohammad, unpublished material.

219 J. Chen, Experimental protocol: Sub-50 nm grating fabrication and imaging, 10 pages (unpublished report, NINT-NRC), June 9, 2009.

220 T. Tanaka, M. Morigami, and N. Atoda, Mechanism of resist pattern collapse during development process, Jpn. J. Appl. Phys. 32, 6059 (1993). DOI: 10.1143/JJAP.32.6059

221 H. Tanaka, Viscoelastic phase separation, J. Phys.: Condens. Matter 12, R207 (2000). DOI: 10.1088/0953-8984/12/15/201

222 M. N. Khalid, S. Yasin, and M. R. Khan, Effects of development time on polymer phase separation in a PMMA resist, Turk. J. Phys. 28, 271 (2004).

[http://journals.tubitak.gov.tr/physics/issues/fiz-04-28-4/fiz-28-4-8-0401-5.pdf]

223 S. Yasin, M. N. Khalid, D. G. Hasko, and S. Sarfraz, Correlation of surface roughness with edge roughness in PMMA resist, Microelecton. Eng. 78-79, 484 (2005).

224 Y. Lauw, On the model of poly(methyl methacrylate) resist structure after development, 16 pages (unpublished report, NINT-NRC and the University of Alberta), Nov. 14, 2006.

225 The simulation data in Figure 3.6 are from the model presented in ref. [68] as obtained by Maria Stepanova. Simulation data of Maria Stepanova reprinted with permission. Copyright © 2006, Maria Stepanova.

226 M. A. Mohammad, C. Guthy, S. Evoy, S. K. Dew, and M. Stepanova, Nanomachining and clamping point optimization of silicon carbon nitride resonators using low voltage electron beam lithography and cold development, J. Vac. Sci. Technol. B 28, C6P36 (2010). DOI: 10.1116/1.3517683

227 H. Ikeura-Sekiguchi, T. Sekiguchi, and M. Koikea, Characterization and degradation of ZEP520 resist film by TOF-PSID and NEXAFS, J. Electron Spectrosc. Relat. Phenom. 144-147, 453 (2005). DOI: 10.1016/j.elspec.2005.01.152

228 Y. H. Zhao, M. H. Abraham, and A. M. Zissimos, Fast calculation of van der Waals volume as a sum of atomic and bond contributions and its application to drug compounds, J. Org. Chem. 68, 7368 (2003). DOI: 10.1021/jo034808o

229 H. Duan, D. Winston, J. K. W. Yang, B. M. Cord, V. R. Manfrinato, and K. K. Berggren, Sub-10-nm half-pitch electron-beam lithography by using poly(methyl methacrylate) as a negative resist, J. Vac. Sci. Technol. B 28, C6C58 (2010). DOI; 10.1116/1.3501353

230 E. van der Drift and D. J. Maas, Helium ion lithography, In: Maria Stepanova and Steven Dew, Eds., Nanofabrication, Springer, Vienna, 2012, pp. 93-116, ISBN 9783709104248. DOI: 10.1007/978-3-7091-0424-8_4

231 G. Karbasian, P. J. Fay, H. Xing, D. Jena, A. O. Orlov, and G. L. Snider, High aspect ratio features in poly(methylglutarimide) using electron beam lithography and solvent developers, J. Vac. Sci. Technol. B 30, 06FI01 (2012). DOI: 10.1116/1.4750217

232 H. Sun, COMPASS: An ab initio force-field optimized for condensed-phase applications - Overview with details on alkane and benzene compounds, J. Phys. Chem. B 102, 7338 (1998). DOI: 10.1021/jp980939v

233 J. R. Shewchuk, An introduction to the conjugate gradient method without the agonizing pain, 64 pages (1994). [http://www.cs.cmu.edu/~quake-papers/painless-conjugate-gradient.pdf]

234 H. C. Andersen, Molecular dynamics simulations at constant pressure and/or temperature, J. Chem. Phys. 72, 2384 (1980). DOI: 10.1063/1.439486

235 H. J. C. Berendsen, J. P. M. Postma, W. F. van Gunsteren, A. DiNola, and J. R. Haak, Molecular dynamics with coupling to an external bath, J. Chem. Phys. 81, 3684 (1984). DOI: 10.1063/1.448118

236 4-Methyl-2-pentanone (MIBK) chemical properties, Chemical Book [http://www.chemicalbook.com/ChemicalProductProperty_EN_CB8691781.htm]

237 Isopropanol (IPA) chemical properties, Chemical Book[http://www.chemicalbook.com/ProductChemicalPropertiesCB8854102_EN.htm]

238 J. R. Fried, Conformation, Solutions, and Molecular Weight, Chapter 3, *Polymer Science and Technology*, 2nd Ed., (2003) Prentice Hall, Upper Saddle River, ISBN 9780130181688. p. 102.

239 A. Rudin and P. Choi, *The Elements of Polymer Science and Engineering*, 3rd Ed. (Elsevier Science Publishing, San Diego, USA, 2013). ISBN: 978-0-1238-2178-2.

240 A. S. Côté, B. Smith, and P. J. D. Lindan, The Radial Distribution Function, in A Molecular Dynamics tutorial (2001). [http://www.compsoc.man.ac.uk/~lucky/Democritus/Theory/rdf.html]

241 The Perl Programming Language [www.perl.org]

242 I. Teraoka, *Polymer Solutions – An Introduction to Physical Properties*, (John Wiley & Sons, New York, USA, 2002). ISBN: 978-0-4712-2451-0

243 M. Holz, S. R. Heil, A. Sacco, Temperature-dependent self-diffusion coefficients of water and six selected molecular liquids for calibration in accurate 1H NMR PFG measurements, Phys. Chem. Chem. Phys. 2, 4740 (2000). DOI: 10.1039/b005319h

244 J. G. Lu, R. Kong, and T. C. Chan, Effects of molecular association on mutual diffusion: A study of hydrogen bonding in dilute solutions, J. Chem. Phys. 110, 3003 (1999). DOI: 10.1063/1.477895

245 J. T. Su, P. B. Duncan, A. Momaya, A. Jutila, and D. Needham, The effect of hydrogen bonding on the diffusion of water in n-alkanes and n-alcohols measured with a novel single microdroplet method, J. Chem. Phys. 132, 044506 (2010). DOI: 10.1063/1.3298857

246 Y. Nakamura, T. Nakagawa, N. Sasaki, A. Yamagishi, and M. Nakata, Chain aggregation and chain collapse of poly(methyl methacrylate) in a mixed solvent, Macromolecules 34, 5984 (2001). DOI: 10.1021/ma010064+

247 Y. Nakamura, N. Sasaki, and M. Nakata, Chain aggregation process of poly(methyl methacrylate) in the mixed solvent tert-butyl alcohol + water, Macromolecules 35, 1365 (2002). DOI: 10.1021/ma011225c

248 M. Nakata, Y. Nakamura, N. Sasaki, and Y. Maki, Transition from a chain-collapse process to a chain-aggregation process of poly(methyl methacrylate) in a mixed solvent, Phys. Rev. E 76, 041805 (2007). DOI: 10.1103/PhysRevE.76.041805

249 D. N. Theodorou, Molecular simulations of sorption and diffusion in amorphous polymers, chapter 2 in: P. Neogi, Ed., Diffusion in Polymers, Marcel Dekker, New York, 1996, pp. 67-142, ISBN 978-0-8247-9530-6.

250 R. Krishna and J. M. van Baten, The darken relation for multicomponent diffusion in liquid mixtures of linear alkanes: An investigation using molecular dynamics (MD) simulations, Ind. Eng. Chem. Res. 44, 6939 (2005). DOI: 10.1021/ie050146c

251 M. Garcia-Ratés, J.-C. de Hemptinne, J. B. Avalos, and C. Nieto-Draghi, Molecular modeling of diffusion coefficient and ionic conductivity of CO_2 in aqueous ionic solutions, J. Phys. Chem. B 116, 2787 (2012). DOI: 10.1021/jp2081758

252 B. Chakraborty, J. Wang, and J. Eapen, Multicomponent diffusion in molten LiCl-KCl: Dynamical correlations and divergent Maxwell-Stefan diffusivities, Phys. Rev. E 87, 052312 (2013). DOI: 10.1103/PhysRevE.87.052312

253 D. R. Wheeler and J. Newman, Molecular dynamics simulations of multicomponent diffusion. 1. Equilibrium method, J. Phys. Chem. B 108, 18353 (2004). DOI: 10.1021/jp047850b

254 S. Lewis and L. Piccirillo, Influence of nanocomposite materials for next generation nano lithography, In: Boreddy Reddy, Ed., Advances in diverse industrial applications of nanocomposites, InTech, Rijeka, 2011, pp. 475-500, ISBN: 978-9-5330-7202-9, DOI: 10.5772/15624.

255 S. Gorelick, J. Vila-Comamala, V. Guzenko, R. Mokso, M. Stampanoni, and C. David, Direct e-beam writing of high aspect ratio nanostructures in PMMA: A tool for diffractive X-ray optics fabrication, Microelectron. Eng. 87, 1052 (2010). DOI: 10.1016/j.mee.2009.11.091

256 S. Gorelick, V. A. Guzenko, J. Vila-Comamala, and C. David, Direct e-beam writing of dense and high aspect ratio nanostructures in thick layers of PMMA for electroplating, Nanotechnology 21, 295303 (2010). DOI: 10.1088/0957-4484/21/29/295303

257 B. Cui and T. Veres, High resolution electron beam lithography of PMGI using solvent developers, Microelectron. Eng. 85, 810 (2008). DOI: 10.1016/j.mee.2008.01.008

258 H. Yang, A. Jin, Q. Luo, C. Gu, Z. Cui, and Y. Chen, Low-energy electron beam lithography of hydrogen silsesquioxane, Microelectron. Eng. 83, 788 (2006). DOI: 10.1016/j.mee.2006.01.004

259 M. M. Mirza, H. Zhou, P. Velha, X. Li, K. E. Docherty, A. Samarelli, G. Ternent, and D. J. Paul, Nanofabrication of high aspect ratio (~50:1) sub-10 nm silicon nanowires using inductively coupled plasma etching, J. Vac. Sci. Technol. B. 30, 06FF02 (2012). DOI: 10.1116/1.4755835

260 J. Vila-Comamala, S. Gorelick, V. A. Guzenko, and C. David, 3D nanostructuring of hydrogen silsesquioxane resist by 100 keV electron beam lithography, J. Vac. Sci. Technol. B 29, 06F301 (2011). DOI: 10.1116/1.3629811

261 E. Herth, E. Algre, P. Tilmant, M. Francois, C. Boyaval, and B. Legrand, Performances of the Negative Tone Resist AZnLOF 2020 for Nanotechnology Applications, IEEE Transactions on Nanotechnology 11, 854 (2012). DOI: 10.1109/TNANO.2012.2196802

262 C. Con, R. Dey, M. Ferguson, J. Zhang, R. Mansour, M. Yavuz, and B. Cui, High molecular weight polystyrene as very sensitive electron beam resist, Microelectron. Eng. 98, 254 (2012). DOI: 10.1016/j.mee.2012.07.005

263 S. Ma, C. Con, M. Yavuz, and B. Cui, Polystyrene negative resist for high-resolution electron beam lithography, Nanoscale Res. Lett. 6, 446 (2011). DOI: 10.1186/1556-276X-6-446

264 M. A. Mohammad, S. K. Dew, and M. Stepanova, SML resist processing for high-aspect-ratio and high-sensitivity electron beam lithography, Nanoscale Res. Lett. 8, 139 (2013). DOI: 10.1186/1556-276X-8-139

265 Most sensitivity values quoted in the table have been extracted from graphs and, therefore, are estimates.

266 P. S. Waggoner and H. G. Craighead, Micro- and nanomechanical sensors for environmental, chemical, and biological detection, Lab Chip 7, 1238 (2007). DOI: 10.1039/B707401H

267 N. V. Lavrik, M. J. Sepaniak, and P. G. Datskos, Cantilever transducers as a platform for chemical and biological sensors, Rev. Sci. Instrum. 75, 2229 (2004). DOI: 10.1063/1.1763252

268 D. M. Photiadis and J. A. Judge, Attachment losses of high Q oscillators, Appl. Phys. Lett. 85, 482 (2004). DOI: 10.1063/1.1773928

269 C. Guthy, R. Das, B. Drobot, and S. Evoy, Resonant characteristics of ultranarrow SiCN nanomechanical resonators , Appl. Phys. Lett. 108, 014306 (2010). DOI: 10.1063/1.3428394

270 D. W. Carr, S. Evoy, L. Sekaric, J. M. Parpia, and H. G. Craighead, Measurement of mechanical resonance and losses in nanometer scale silicon wires, Appl. Phys. Lett. 75, 920 (1999). DOI: 10.1063/1.124554

271 D. H. Alsem, B. L. Boyce, E. A. Stach, and R. O. Ritchie, Effect of post-release sidewall morphology on the fracture and fatigue properties of polycrystalline silicon structural films, Sens. Actuators, A 147, 553 (2008). DOI: 10.1016/j.sna.2008.05.027

272 L. Sekaric, D. W. Carr, S. Evoy, J. M. Parpia, and H. G. Craighead, Nanomechanical resonant structures in silicon nitride: fabrication, operation and dissipation issues, Sens. Actuators, A 101, 215 (2002). DOI: 10.1016/S0924-4247(02)00149-8

273 N. Nelson-Fitzpatrick, C. Guthy, S. Poshtiban, E. Finley, K. D. Harris, B. J. Worfolk, and S. Evoy, Atomic layer deposition of TiN for the fabrication of

nanomechanical resonators, J. Vac. Sci. Technol. A 31, 021503 (2013). DOI: 10.1116/1.4790132

274 M. A. Mohammad, S. K. Dew, S. Evoy, and M. Stepanova, Fabrication of sub-10 nm silicon carbon nitride resonators using a hydrogen silsesquioxane mask patterned by electron beam lithography, Microelectron. Eng. 88, 2338 (2011). DOI: 10.1016/j.mee.2010.11.045

275 KOH Etching, Brigham Young University Cleanroom [http://www.cleanroom.byu.edu/KOH.phtml]

276 F. Robin, S. Costea, G. Stark, R. Wüest, P. Strasser, H. Jäckel, A. Rampe, M. Levermann, and G. Piaszenski, Accurate proximity-effect correction of nanoscale structures with NanoPECS, Raith Application Note (2006). [http://www.first.ethz.ch/infrastructure/equipment/EBL/NanoPECS_2006.pdf]

277 L. E. Ocola, Nanoscale geometry assisted proximity effect correction for electron beam direct write nanolithography, J. Vac. Sci. Technol. B 27, 2569 (2009). DOI: 10.1116/1.3237135

APPENDICES

APPENDIX A1

RESIST SPINNING PARAMETERS

In this thesis, four electron beam resists were used namely, PMMA, ZEP, HSQ, and SML. Of these, PMMA, ZEP, and HSQ were spun locally according to the parameters provided below. The spin curve data for PMMA was obtained by colleague Jiang Chen, and the spin curve data for ZEP and HSQ were obtained by the author.

Prior to spinning, the piranha cleaned substrates were baked at 150 °C for 5 min on a hot plate. The resist spinning was conducted using a Headway spinner and the samples were subsequently pre-baked without any delay. The resist thickness measurements were conducted using a VASE ellipsometer.

<u>PMMA</u>

Formulation: Dilute PMMA in Anisole 1% and 1.5% (by volume)

Spread cycle: RPM = 100, RAMP = 2 sec, Time = 10 sec

Spin cycle: RPM = see Figure A1–1, RAMP = 4 sec, Time = 40 sec

Pre-bake: 175 °C for 5 min on a hot plate.

Optical constants: $\alpha = 1.49$, $\beta = 0.003$, $\gamma = 0.0002$

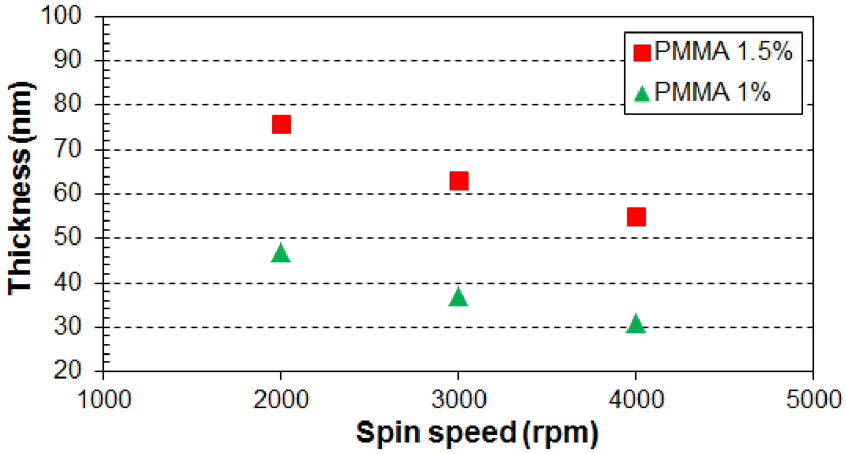

Figure A1–1. Spin curves for various PMMA formulations 1% in Anisole (red squares) and 1.5% in Anisole (green triangles).

ZEP

Formulation: Dilute ZEP-520A in Anisole 1:1, 1:2, and 1:3 (by volume)

Spread cycle: RPM = 100, RAMP = 1 sec, Time = 10 sec

Spin cycle: RPM = see Figure A1–2, RAMP = 1-5 sec, Time = 40 sec

Pre-bake: 170 °C for 10 min on a hot plate (set-point 270 °C)

Optical constants: c1 = 1.54, c2 = 0.005, c3 = 0.0002

Detailed ZEP spinning instructions and guidelines are provided elsewhere (http://www.nanofab.ualberta.ca/wp-content/uploads/downloads/2011/02/ZEP_Spin_Curves1.pdf).

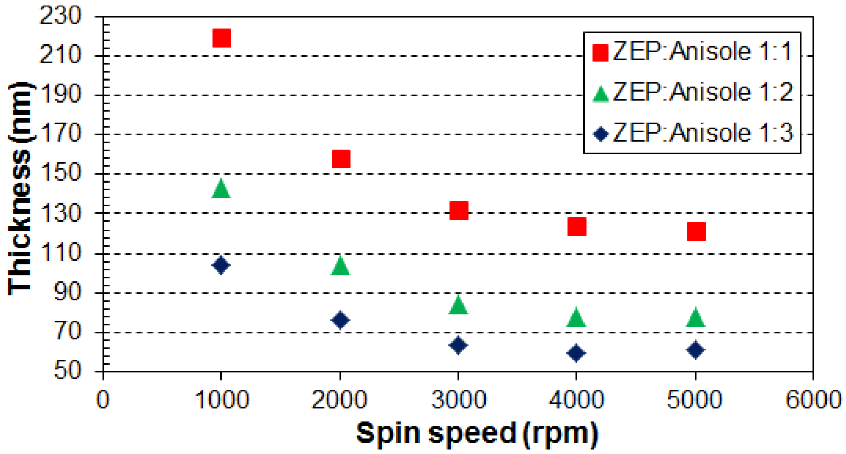

Figure A1–2. Spin curves for various ZEP-520A:Anisole formulations 1:1 (red squares), 1:2 (green triangles), and 1:3 (blue diamonds). A constant ramp rate of 1000 rpm/sec was used therefore the ramp time increases from 1-5 sec as the spin speed is increased from 1000-5000 rpm.

<u>HSQ</u>

Formulation:	Dilute HSQ in MIBK 1%, 2%, and 3% (by volume)
Spread cycle:	RPM = 100, RAMP = 1 sec, Time = 10 sec
Spin cycle:	RPM = see Figure A1–3, RAMP = 2 sec, Time = 40 sec
Pre-bake:	90 °C for 5 min on a hot plate (set-point 135 °C)
Optical constants:	c1 = 1.42, c2 = 0.004, c3 = 0.00006

Detailed HSQ spinning instructions and guidelines are provided elsewhere (http://www.nanofab.ualberta.ca/wp-content/uploads/downloads/2011/04/HSQ_Spin_Curves.pdf).

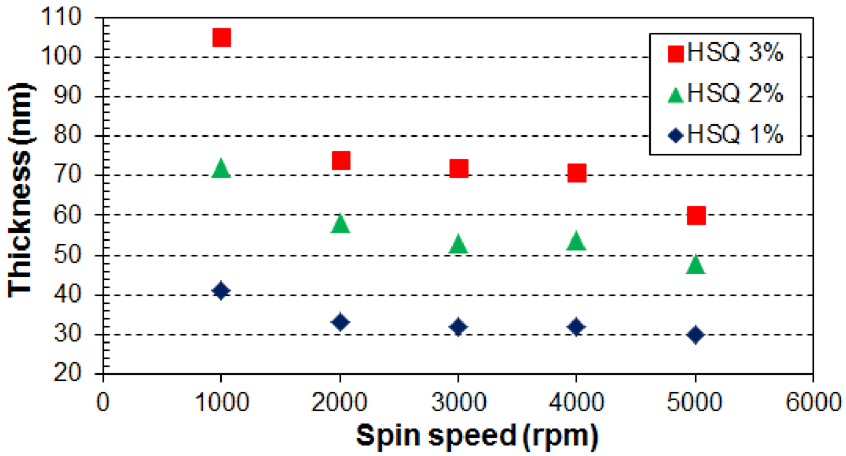

Figure A1–3. Spin curves for various HSQ formulations 1% in MIBK (red squares), 2% in MIBK (green triangles), and 3% in MIBK (blue diamonds). Due to the rapid evaporation of MIBK casting solvent, a constant 2 sec ramp time was used.

Spinning more than one layers of resist (on top of an existing resist layer) is possible in order to achieve thicker resist layers than obtainable using a given concentration. However, for this, a baking step is necessary after each spin process. For example, to obtain a 120 nm thick PMMA film, two 3000 rpm spin cycles of PMMA 1% (yields 60 nm film) can be conducted with a pre-bake after each spin. If the pre-bake is not conducted after the first spin, the total resist thickness will be considerably less than the sum of both thicknesses.

APPENDIX A2

COLD PLATE SETUP

In order to perform cold development after electron beam lithography (EBL) exposures, a Stir-Kool SK-12D (21485) cold plate (Ladd Research) was used. The SK-12D is a very accurate and sophisticated thermoelectric cooler capable of cooling small (<250 mL) amounts of liquid very rapidly to 40 °C below the tap water temperature. Figure A2–1 below shows our setup for cooling both the

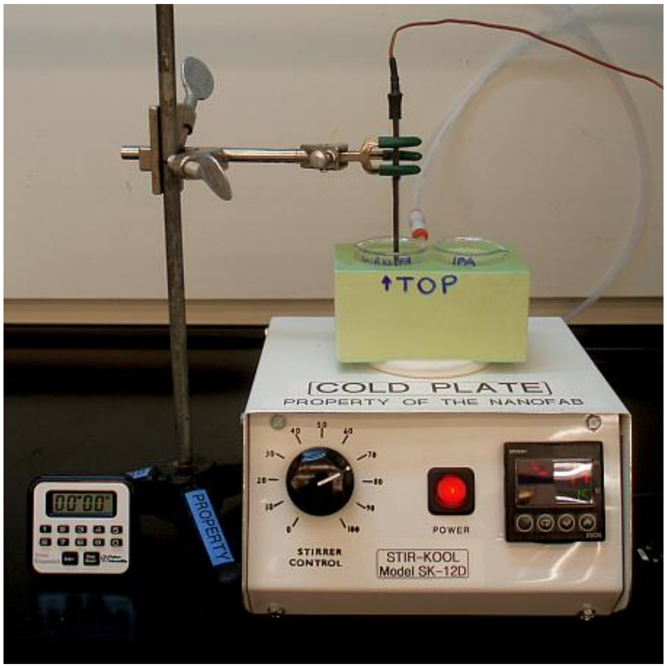

Figure A2–1. Stir-Kool SK-12D cold plate in action.

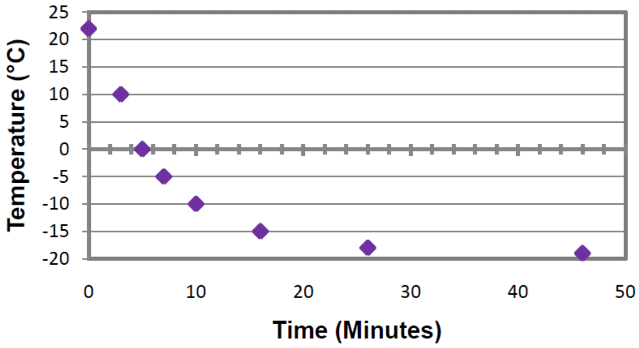

Temperature (°C)	22	10	0	-5	-10	-15	-18	-19
Time (Minutes)	0	3	5	7	10	16	26	46

Figure A2–2. Time required to cool 30 mL MIBK:IPA 1:3 developer using SK-12D and 3 L/min room temperature water flow rate.

developer and stopper simultaneously. Both beakers contain a stirring rod and approximately 30 mL of liquid. The beakers are insulated with a foam jacket. Before the beakers are placed, five drops of silicone oil are applied to the surface of the cold plate to improve thermal conduction and prevent frost from accumulating on the plate. Detailed setup instructions and guidelines for optimal liquid cooling are provided in a standard operating procedures (SOP) document, written by the author, at the following URL (http://www.nanofab.ualberta.ca/wp-content/uploads/downloads/2011/04/Cold_Plate_SOP.pdf). The performance of the SK-12D cold plate in our setup is demonstrated by a cooling curve provided in Figure A2–2. This figure plots the developer temperature against duration for cooling 30 mL of MIBK:IPA 1:3 using a 3 L/min room temperature water flow rate. The set point temperature was -20 °C.

APPENDIX A3

COMPARING PROFILE MEASUREMENT TECHNIQUES

While collecting data for this thesis, three different profile measurement techniques have been used. These are atomic force microscopy (AFM), optical profilometry, and physical profilometry. The images of the various instruments used are presented in Figure A3–1.

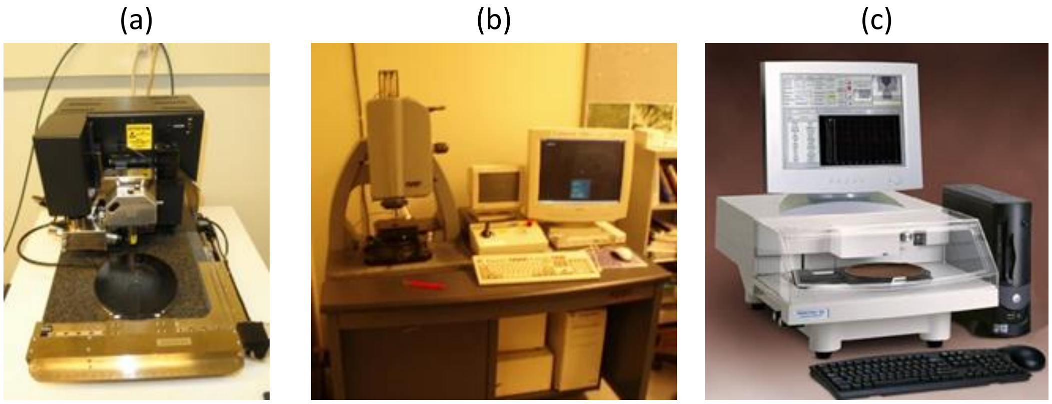

Figure A3–1. Images of profile measurement instruments (a) Veeco Dimension 3100 AFM, (b) Zygo NewView 7300 optical profilometer, (c) KLA-Tencor AlphaStep IQ physical profilometer.

Even though all three of these techniques have been used for measuring contrast curves, the majority of the contrast curve data presented in this thesis has been acquired using physical profilometry. In addition to contrast curves, surface profiles of various patterned samples were studied, for which AFM was used. The various merits and limitations of each of these techniques (as observed by the author) have been summarized in Table A3–A.

TABLE A3–A. Comparing profile measurement techniques.

Category	AFM	Optical Profilometry	Physical Profilometry
Convenience	2nd	3rd	1st
Resolution (nm)	1	0.1	10
Cost ($/hr)	20-120	15	10
Time (hr/sample)	2.0	1.0	0.5-1.0
Information	3D	3D	2D
Surface Analysis	Yes	Yes	No
Limitations	Sample height limited, field of view limited	Sample roughness limited, field of view limited	Tip size limited

Additional details are provided below:

Convenience	Optical profilometry requires samples to be coated with a reflective top-coating (e.g., chromium) increasing the cost and sample preparation time.
Resolution	The vertical (height) resolution of the optical profilometer is the highest; however, this is highly dependent on the calibration and user proficiency.

Cost	AFM cost is increased due to the following factors: (i) cost of AFM tip, and (ii) cost of being assisted by professional AFM operator.
Time	AFM and physical profilometry are serial scan techniques whereas optical profilometry scans the whole field at once (i.e., in parallel).
Information	Physical profilometry provides line scans at high speed.
Surface Analysis	Both AFM and optical profilometry acquire 3D information and have surface analysis features such as measuring surface roughness, etc. Physical profilometry does not have this feature; however, post processing options such as profile leveling exist in this technology.
Limitations	Large height variations in the sample and operation speed restrict AFM. Rough surfaces cause information loss (dark zones) in the optical profilometer. The tip size limits the type of samples that can be measured using physical profilometer.

For the purpose of generating contrast curves, physical profilometry is the best choice in terms of accuracy, cost, efficiency, and ease of use. However, the samples should have sufficient step heights (depth) and trench width.

APPENDIX A4

CONVERTING AVERAGE AREA DOSES TO LINE DOSES

The process for converting electron beam lithography (EBL) average area doses (units: µC/cm^2) to line doses (units: pC/cm) employed by this thesis is described with the aid of an example. Consider a sample 50 nm pitch grating structure (see Figure A4–1) that is to be exposed using 10 keV EBL. An average area dose of 60 µC/cm^2 is selected as sufficient to obtain well-exposed gratings. What is the equivalent dose in pC/cm?

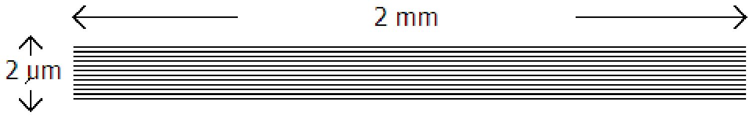

Figure A4–1. A sample 50 nm pitch grating with 2 µm × 2000 µm dimensions.

The formula for converting average area doses to line doses is given by:

$$Line\ Dose = \frac{Average\ Area\ Dose \times Area}{\#\ of\ lines\ over\ the\ area}$$

The exposed area in Figure A4–1 is 2 µm × 2000 µm = 4000 µm^2. Converting units from µm^2 to cm^2, we obtain the following grating area:

$$\text{Exposed area in cm}^2 = 4000\mu m^2 \times \frac{1cm^2}{10^8 \mu m^2} = 4 \times 10^{-5} cm^2$$

As the grating width and pitch is specified, the number of lines over the area is simply width/pitch = 2000 nm / 50 nm = 40 lines. Now employing the previously described relationship,

$$Line\ Dose = \frac{\left(60\mu C / cm^2\right) \times \left(4 \times 10^{-5} cm^2\right)}{40\ lines} = 6 \times 10^{-11} C = 60 pC$$

However, to obtain the line dose in pC/cm, we need to divide by the length of the exposed area. The length of the grating in Figure A4–1 is 2 mm = 0.2 cm, therefore,

$$Line\ Dose = \frac{60 pC}{0.2 cm} = 300 pC / cm .$$

In this way, average area doses can be conveniently converted into line doses. Converting doses is particularly useful for calculating dose factors (for input into Raith EBL software) when large patterns employing many gratings are to be exposed.

APPENDIX A5

CHARGE GROUP ASSIGNMENTS

A charge group is a set of atoms in a molecule with a net charge of zero. In molecular dynamics (MD) simulations, defining charge groups enhances the simulation speed at the cost of some reduction in accuracy. However, defining charge groups may also help to improve accuracy in other circumstances. For example, when atom based (intermolecular interaction) cut-offs are used, sometimes split dipoles (–O–H) are created artificially, giving incorrect energies.

Accelrys Materials Studio provides the option of either manually or automatically defining charge groups. Automatic definition of charge groups is understood to work really well with polymers; however, using automatic charge group definition is not advised for small molecules. In order to manually define charge groups some rules and steps are to be followed, as under.

Rules

- Charge groups need to be smaller than the cut-off radius. As a general rule, a whole molecule should not be defined as a charge group.

- For any charge group, the partial charges should add up to zero. If this is not possible, the net charges may be between -0.1e and 0.1e.
- Charge groups cannot be used for ionic systems.

<u>Steps</u>

- Select the molecule of interest. If the point charges are not already defined, perform a single point energy calculation to get point charges.
- Identify and select a group of 2-5 atoms with a net charge of zero. Define this group as a charge group and calculate the net charge values.
- Repeat the above process until each atom of a molecule is assigned to a charge group.

For the MD simulations used in this thesis, charge groups were manually defined for the developer molecules methyl isobutyl ketone (MIBK) and isopropyl alcohol (IPA). For the polymethylmethacrylate (PMMA) fragments, charge groups were automatically defined. Figure A6–1 and A6–2 present charge group definition for both developers.

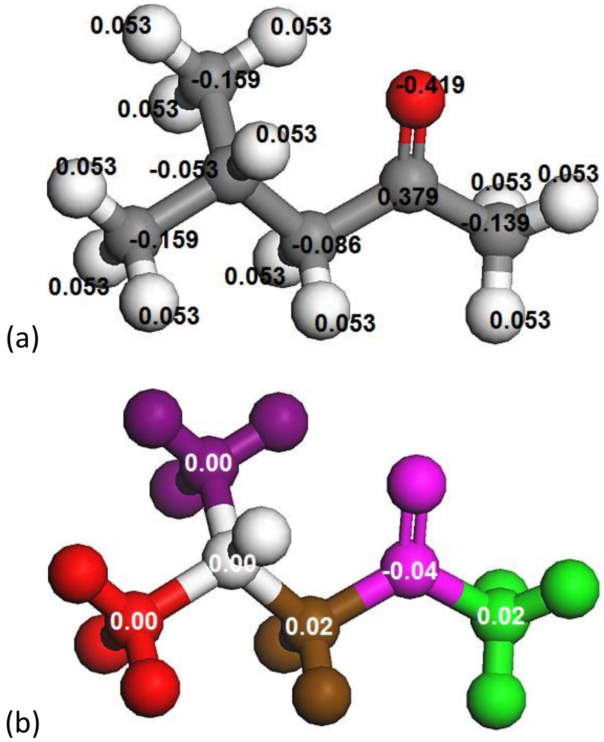

Figure A5–1. A MIBK molecule showing (a) point charges, and (b) color coded charge groups with net charge labels.

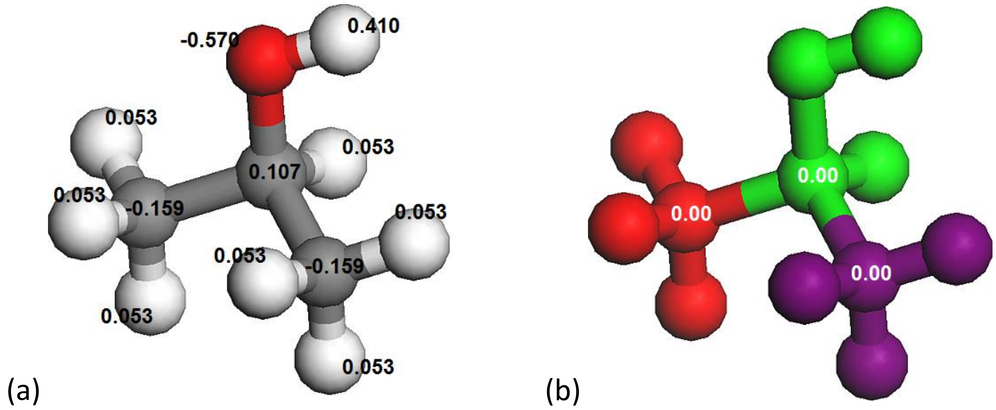

Figure A5–2. An IPA molecule showing (a) point charges, and (b) color coded charge groups with net charge labels.

The typical (automatic) charge group definition for PMMA fragments is shown through an example of a PMMA(4) molecule in Figure A5–3.

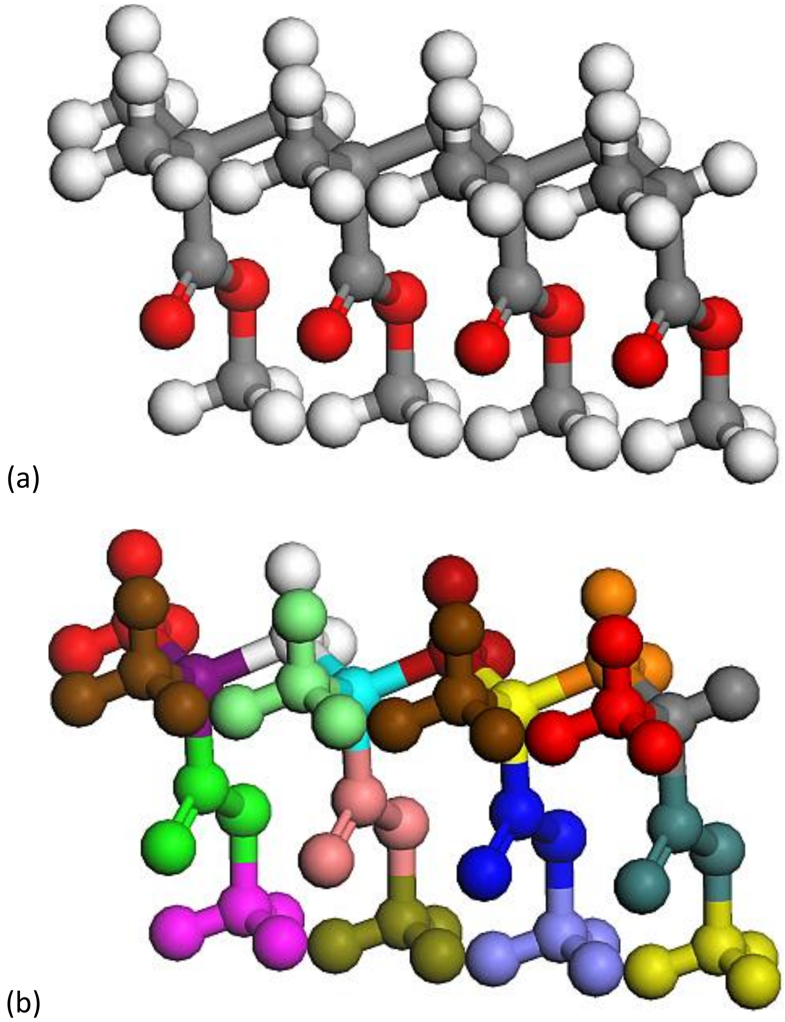

Figure A5–3. An isotactic (a) PMMA(4) molecule, and the corresponding (b) automatically defined charge groups.

APPENDIX A6

THERMOSTAT AND BAROSTAT SELECTION

This appendix provides some supplementary results that formed the basis for deciding which thermostat and barostat to use in our MD simulations. The thermostat and barostat for the equilibration and production runs were determined subsequently in two iterations. Initially the Andersen thermostat (target temperature 300 K) and Andersen barostat (target pressure 1 atm) were used. MD simulations using this combination of thermostat and barostat provided good temperature control; however, the pressure control was not satisfactory. For example, after a 350 ps NPT simulation of PMMA(2) molecules, the following average values were obtained (see Table A6–A):

TABLE A6–A. Initial equilibration run control

Quantity	Value	Comments
Temperature (K)	300.15	Excellent
Pressure (GPa)	-0.035 (-345 atm)	Poor
Density (g/cm^3)	1.0043	Excellent

Clearly, further work could be done to improve the pressure control. Accelrys Materials Studio provides three barostats namely Andersen, Berendsen, and Parrinello. Employing each of these barostats for 500ps PMMA(2) NPT simulations yielded the following average values (see Table A6–B):

TABLE A6–B. Improved equilibration run control

Barostat	Density (g/cm^3)	Temp. (K)	Pressure (GPa)	Comments
Andersen	1.0043	300	-0.035	Poor
Berendsen	1.0228	298	0.00003 (0.3 atm)	Good
Parrinello	1.0040	299	-0.036	Poor

The Berendsen barostat provided the most promising results. Without adversely affecting the temperature control, the pressure control was further improved to 0.00098 GPa (0.97 atm) using a smaller Berendsen decay constant of 0.6 ps, after several trial runs.

Having determined the parameters required for the equilibration, further test simulations were conducted to determine the parameters required for the production runs. In the following example, a PMMA(4) NPT equilibration is conducted at first using the previously determined parameters. The target temperature and pressure were 295 K and 1.0 atm, respectively, and the equilibration was run for 1000 ps. The control over the initial conditions is demonstrated in Table A6–C.

TABLE A6–C. Equilibration run control on new system using Andersen thermostat and Berendsen barostat.

Quantity	Value	Comments
Temperature (K)	294.6	Excellent
Pressure (GPa)	0.000086 (0.85 atm)	Very Good
Density (g/cm^3)	1.0532	Excellent

Following successful equilibration, three NPT test simulations were conducted using a combination of various thermostats and barostats. The temperature, pressure, and density control of these simulations is summarized in Table A6–D.

TABLE A6–D. Production run control using combinations of various thermostats and barostats. Each simulation duration was 250 ps.

Thermostat	Barostat	Density (g/cm^3)	Temp. (K)	Pressure (GPa)
Andersen	Berendsen	1.0623	294.8	0.000098 (0.97 atm)
Andersen	Parrinello	1.0536	295.0	-0.03547 (-350 atm)
Nose	Parrinello	1.0626	272.2	-0.03094 (-305 atm)

These results demonstrate that the combination of Andersen thermostat and Berendsen barostat provide the best temperature and pressure control, respectively, though a very slight (<1 %) increase in density is witnessed. Moreover, the COMPASS forcefield paper employs the same thermostat and barostat combination. Due to the aforementioned reasons, we conduct our MD simulations with Andersen thermostat and Berendsen barostat.

APPENDIX A7

PERL SCRIPTS

This appendix contains a few scripts in Perl programming language written by the author for use in this thesis. The choice of Perl language is dictated by the programming environment in Accelrys Materials Studio.

The following script creates centroids of all molecules of a certain type (depending on name label) and then creates a set of all centroids. For example, the PMMA(1):MIBK NVT simulation has 120 PMMA(1) molecules, so 120 centroids are created and then one set is created with 120 members. This set is subsequently used as input data for analysis by various Accelrys modules.

```
#!perl

use strict;
use MaterialsScript qw(:all);

#Select trajectory of interest
my $doc = $Documents{"pmma1_NVT.xtd"};

#Delete existing centroids (disable if unwanted!)
$doc->UnitCell->Centroids->Delete;

#Update screen view
```

```
$doc->UpdateViews;

#Loop over all molecules in trajectory file
for (my $i=$doc->UnitCell->Molecules->Count-1 ; $i>=0 ;
--$i)
{
     #Select each molecule
     my $molecule = $doc->UnitCell->Molecules($i);

     #Select name of each molecule
     my $nameMolecule = $molecule->Name;

          #If name of molecule matches pmma1
          if($nameMolecule =~ m/^pmma1.*/ )
          {
                #Create centroid of that molecule
                $doc->CreateCentroid($molecule->Atoms);
          }
}

#Update screen view
$doc->UpdateViews;

#Create a set of all newly created centroids and name
the set PMMA_Centroids
$doc->CreateSet("PMMA_Centroids", $doc->UnitCell->
Centroids);

#Update screen view
$doc->UpdateViews;
```

```
#SECTION FOR VERIFICATION
#========================

#Print total number of centroids created
printf "Total centroids created: %f \n", $doc->
UnitCell->Centroids->Count;

#Print name of set created and number of members
my $sets = $doc->UnitCell->Sets;

foreach my $set (@$sets)
{
     printf "Name and members of set created: %f %f
     \n",$set->Name,$set->NumItems;

}
```

The following script calculates the Wigner-Seitz radius used to describe the density of the system. This script uses the centroid count to quickly obtain the number of PMMA molecules in the system and is therefore run after the previous script has been run.

```
#!perl

use strict;
use MaterialsScript qw(:all);

#Definition of PI
use constant PI => 4*atan2(1, 1);
```

```
#Select trajectory of interest
my $doc = $Documents{"pmma1_NVT.xtd"};

#Number of molecules in system (one centroid per
molecule)
my $numMolec = $doc->UnitCell->Centroids->Count;

#Cell volume
my $cellVolume = $doc->Lattice3D->CellVolume;

#Value of 'n' in Wigner-Seitz radius
my $density = $numMolec/$cellVolume;


my $wigner = 3/(4*PI*$density);

printf "Number of molecules %f \n", $numMolec;
printf "Cell volume %f Angstroms^3 \n", $cellVolume;
printf "Wigner-Seitz radius is %f Angstroms",
$wigner**(1/3);
```

The following is a brief script used to delete sets. This script is useful to reset a trajectory file in which other sets may have been previously created.

```
#!perl

use strict;
use MaterialsScript qw(:all);
```

```
my $doc = $Documents{"pmma1_NVT.xtd"};

#Find number of sets created previously
my $sets = $doc->UnitCell->Sets;

foreach my $set (@$sets)
{
     print $set->Name;
     $set->Delete;
}
```

In addition to the above scripts, some other scripts were written for use in this research (but not directly for use in this thesis). These scripts had the following purposes:

- Export the XYZ coordinates of a centroid for all trajectory frames
- Export the XYZ coordinates of an atom for all trajectory frames
- Export the gyration radii of a molecule for all trajectory frames
- Export individual frames from a trajectory (as xsd, pdb)
- Export individual frames with only selected atoms, molecules (as pdb)
- Import, export, and analysis of data present in Accelrys study tables

The above scripts can be obtained by contacting the author at the following e-mail address: mam20@ualberta.ca.